HIGH-ENERGY GAMMA-RAY OBSERVATIONS OF SOLAR FLARES WITH THE FERMI LARGE AREA TELESCOPE

A DISSERTATION
SUBMITTED TO THE DEPARTMENT OF PHYSICS
AND THE COMMITTEE ON GRADUATE STUDIES
OF STANFORD UNIVERSITY
IN PARTIAL FULFILLMENT OF THE REQUIREMENTS
FOR THE DEGREE OF
DOCTOR OF PHILOSOPHY

Alice Allafort

December 2018

This dissertation is online at: http://purl.stanford.edu/kp476kd8769

I certify that I have read this dissertation and that, in my opinion, it is fully adequate in scope and quality as a dissertation for the degree of Doctor of Philosophy.

Peter Michelson, Primary Adviser

I certify that I have read this dissertation and that, in my opinion, it is fully adequate in scope and quality as a dissertation for the degree of Doctor of Philosophy.

Vahe Petrosian

I certify that I have read this dissertation and that, in my opinion, it is fully adequate in scope and quality as a dissertation for the degree of Doctor of Philosophy.

Philip Scherrer

I certify that I have read this dissertation and that, in my opinion, it is fully adequate in scope and quality as a dissertation for the degree of Doctor of Philosophy.

Nicola Omodei,

Approved for the Stanford University Committee on Graduate Studies.

Patricia J. Gumport, Vice Provost for Graduate Education

This signature page was generated electronically upon submission of this dissertation in electronic format. An original signed hard copy of the signature page is on file in University Archives.

Abstract

Solar flares are the most energetic events in our Solar System. They consist of sudden energy release from reconfiguration of magnetic fields, leading to acceleration of particles to relativistic energies. The Fermi Large Area Telescope (LAT) gamma-ray observations of the Sun present a unique opportunity to explore the mechanisms of high-energy emission as well as particle acceleration and transport in solar flares.

I will present the results of the first 9 years of observations of the active Sun by the Fermi-LAT, which represents the largest sample to date of detected solar flares with emission greater than 30 MeV. Some of the new detections confirm the standard models for solar flares based on observations from past missions in the 1980s and 90s, but new behaviors have also been identified: detections of delayed gamma-ray emission lasting up to 20 hours and the first detection of gamma-ray emission above 100 MeV from three solar flares originating from behind the visible part of the Sun.

Considering all of the 45 flares detected by the Fermi-LAT, I will describe the characteristics of the first gamma-ray solar flare catalog covering Solar Cycle 24, exploring trends and correlations with the most relevant solar events: X-ray emission, coronal mass ejections, and direct detection of solar energetic particles.

Résumé

Les éruptions solaires sont les évènements les plus énergétiques de notre système solaire. Elles sont provoquées par la soudaine libération d'énergie magnétique accumulée dans l'atmo-sphère solaire au dessus des taches solaries. Cela conduit à l'accélération de particules à des vitesses relativistes et à l'émission de radiation sur l'ensemble du spectre électromagnétique, du domaine radio jusqu'aux rayons gammas. Les observations du Soleil par le Fermi Large Area Telescope (Fermi-LAT) présentent une unique opportunité d'explorer les processus d'accélération et de transport des particules au cours d'éruptions solaires.

Je présente les résultats des 9 premières années d'observation de l'activité solaire par le Fermi-LAT, qui constituent le catalogue le plus complet d'éruptions solaires détectées au dessus de 30 MeV. Ces nouvelles détections confirment en partie le model standard des éruptions solaires mais ont aussi permit d'en étendre notre compréhension : émission différée de rayons gammas pouvant durer jusqu'à 20 heures, observations de hausse et déclin de l'intensité ainsi que les premières observations d'émission gamma au-dessus de 100 MeV provenant d'éruptions occultées.

Grâce au Fermi-LAT, mon travail a permit l'élaboration du premier catalogue de 45 éruptions solaires en rayons gamma au cours du 24ème cycle solaire. Je présente les caractéristiques temporelles, spectrales et spatiales de ces éruptions, ainsi qu'une étude comparative avec d'autres type d'évènements solaires: rayons X, éjections de masses coronales et particules énergétiques solaires.

Acknowledgements

I would like to thank all the people in my life who encouraged me and made this Dissertation possible.

First and foremost thanks to my husband Aurélien who has been supporting me every step of the way, helping me celebrate the successes and mourn the losses. I am forever grateful to have him in my life.
To my mother who taught me curiosity and wonder, always rooting for me from a continent away. To my family who always showed great interest in my research, absorbed by my late night tales under the stars. To my friends who were there to listen and cheer me along, Jasmine, Maria, Gaëlle, Adèle, Carrie, Tuom, Sarah, Dima, Norbert, Shizuka, Fabio, Philipp, Pierre, Thomas and so many others.

My path to the study solar flares at high energies started with my work with the Fermi Large Area Telescope. After a taste of the study of supernovae remnants, TeV sources and the flaring sky, it was through the Flare Advocate monitoring work that a solar flare bursted into my life and became the subject of my thesis.

This research would simply not be without an amazing group of scientists that decided to make the Fermi telescope a reality and a success. I want to recognize the tremendous support of the Fermi-LAT collaboration whose members have provided important guidance throughout this thesis research: Rolf Buehler, Marco Ajello, Jim Chiang, Seth Digel, Rob Cameron, Eric Charles, Matthew Wood, Terri Brandt, Anna Franckowiak, Luigi Tibaldo, Tobias Jogler, Simona Murgia, David Paneque, Markus Ackermann, Eugenio Bottacini, Elena Orlando, Matthew Kerr, Peter den Hartog, Yasunobu Uchiyama. A particular thanks to Nicola Omodei, Giacomo Vianello and Giovanna Senatore who welcomed me to the Stanford Fermi group in the last part of my PhD. I also want to thank the Fermi-LAT solar team for their interest in my work, our many conversations and their feedback which helped guide my research, in particular Melissa Pesce-Rollins and Francesco Longo. A large part of the original work in this Dissertation was made in collaboration with members of the Fermi-LAT team and I will use 'we' in the following text to acknowledge this effort, in the

same manner as in the publications I worked on.

The KIPAC institute is an extremely rich environment to conduct research in astrophysics and I feel lucky and proud having been a part of it. Thanks to my fellow graduate students who helped my navigate Stanford and the start of a research career, I learned a lot from you: Sarah Kernasovskiy, Josh Lande, Keith Bechtol, Alex Drlica-Wagner, Helen Craig, Warit Mitthumsiri, Josh Cogan, Paul Simeon and many others. I am grateful to have been part of the KIPAC outreach group with the help of Mandeep Gill, and be a SLAC tour guide which I enjoyed very much. Thanks to the staff of KIPAC and the Physics Department for their continuous help: Maria Frank, Martha Siegel, Chris Hall, John Skinner, Christine Aguilar, Stuart Marshall, Ken Zhou, Ziba Mahdavi, Elva Carbajal, Violet Catindig, Bob Khan, David Stricker and Dana Volponi. My work with the Petrosian group would not have been the same without the presence of Fatima Rubio da Costa, Frederic Effenberger, Maria Dainoti, Qingrong Chen as well as Wei Liu and Monica Bobra from the solar group.

Through my PhD at Stanford I discovered a passion for teaching Physics, in large part thanks to the support and encouragement of Chaya Nanavati, Rick Pam, Professors Pat Burchat and Carl Wieman, as well as the staff of the Vice Provost for Teaching and Learning. I also want to acknowledge the guidance of my early Physics Professors Silvie Berger from Lycée Joffre and Emmanuelle Deleporte from Ecole Normale Supérieure de Cachan who are great role models for women in Physics. I continued to be encouraged and mentored at Stanford by my contacts with Professors Sarah Church, Risa Wechsler, Pat Burchat and Persis Drell who always showed great leadership. Thanks to Roger Blandford and Phil Scherrer for sharing their expertise and answering my questions on high-energy and solar Physics, as well as sitting on my Dissertation committee. Writing this Dissertation took effort and time, and I want to thank the Stanford Hume Center staff and tutors for the amazing support they provide to all graduate students who struggle with this task. Thanks to my writing fellows who shared my frustrations: James Dennedy-Frank, Sarah Polk, Shenglan Qiao and the bootcampers.

And finally I want to thank my advisors and mentors throughout my PhD who made this research possible. Stefan Funk welcomed me in his group and the Fermi collaboration. He always showed great faith in me and gave me the freedom necessary for me to find an area of research I was most interested in. I continued my work with Vahe Petrosian and would like to thank him for his support. He taught me the fundamentals of Solar flares Physics, allowing me to put my work in perspective and open up new avenues to explore. A lot of the skills required to analyze Fermi data come from the close collaboration with Nicola Omodei.

I benefited greatly from his deep knowledge of the instrument in order to carefully consider the complexity of gamma-ray astronomy data. He was always available for me, generously spending countless hours brainstorming, solving bugs and patiently answering the many questions I had along the way. Last but not least, Peter Michelson was instrumental in the finishing of this work, meticulously reviewing this Dissertation and providing great feedback. He always encouraged me in digging deeper into my data, asking insightful questions and prompting me to new ideas.

To all, I am deeply grateful for the time and support you have given me over the years.

Alice Allafort (Stanford, Dec. 2018)

Contents

List of Tables

List of Figures

Chapter 1

Introduction

Gamma-ray photons are the most energetic form of electromagnetic radiation. By observing the Universe at high-energies with gamma rays, new physics can be explored by testing theories and observing processes which are not possible to produce in earth-bound laboratories. Although it was long been suspected that high-energy processes occur in the Universe, the field of gamma-ray astronomy started when scientists were able to send detectors above the Earth's atmosphere, which absorbs these high-energy photons, onboard balloon and spacecraft. The first observations started in the early 1960s and continued in part with defense satellites designed to detect possible nuclear blasts. Their results yielded the unexpected discovery of gamma-ray bursts which, after being ruled out as coming from Earth or the Sun, were eventually associated with sources in distant galaxies. We now know a lot more about a variety of gamma-ray sources in our galaxy as well as in the distant Universe: from Terrestrial Gamma-ray Flashes to Solar Flares, Pulsars, Pulsar Wind Nebulae, Supernova Remnants, Globular Clusters, Binaries, Novae, Star-forming Regions, Galactic Diffuse emission, Blazars, Gamma-Ray Bursts and the nearly uniform Extragalactic Background.

Launched in 2008, the Fermi Gamma-ray Space Telescope (Fermi[1]) is the latest major advance in the field of high-energy gamma-ray astronomy. Fermi brings together a large community in Astrophysics and Particle Physics, and provides public data analyzed both by the instrument teams and the general community. It was named after the famous physicist Enrico Fermi in recognition of his work on cosmic rays. The Fermi NASA mission consists of two instruments: the Large Area Telescope (LAT) detecting high-energy gamma rays from 20 MeV to more than 300 GeV, and the Gamma-ray Burst Monitor (GBM) observing the entire unocculted sky from hard X-ray to soft gamma-rays. The Fermi-LAT instrument has an much larger field of view relative to other telescopes, similar to our own eyes: about 1/6 of an entire sphere, and an effective area almost 10 times that of

[1] `https://www.nasa.gov/content/fermi-gamma-ray-space-telescope`

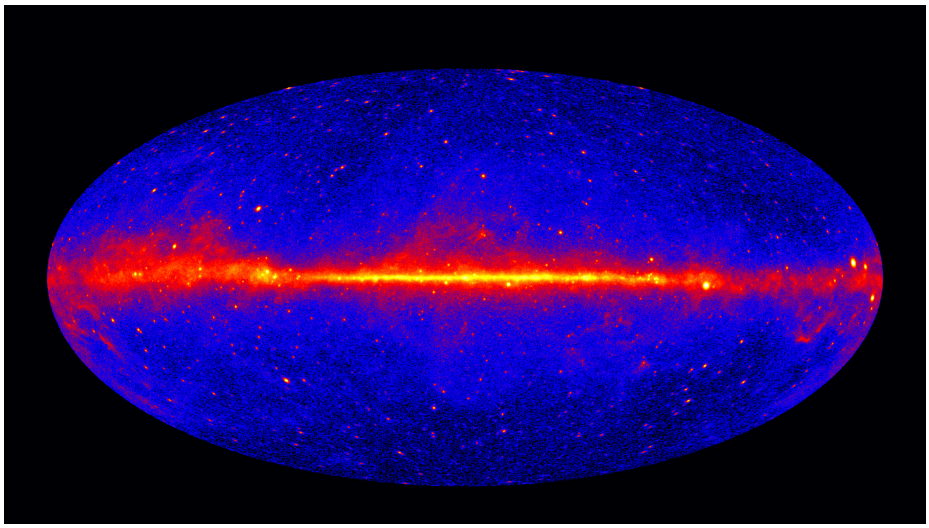

Figure 1.1: The Fermi-LAT 60-month full-sky map (> 1 GeV).

previous observatories (Atwood et al. 2009). The combination of those features leads to 30 times more sensitivity that its predecessor EGRET (Energetic Gamma-Ray Experiment Telescope) onboard the Compton Gamma Ray Observatory. It also has a better angular precision, better background rejection and better energy resolution (Abdo et al. 2010).

As a result, the third Fermi-LAT source catalog lists 3033 objects detected above 100 MeV, whereas the third EGRET catalog contains 271 sources (Acero et al. 2015, Hartman et al. 1999, Michelson et al. 2010). Figure 1.1 shows the 5-year view of the entire sky by the Fermi-LAT: it is dominated by the galactic plane emission due to the interaction of cosmic rays with the diffuse interstellar gas and interstellar radiation field. Most of the bright point sources close to the galactic plane are pulsars or supernova remnants, but above the plane most point sources correspond to blazars and, at a lower level, the isotropic extragalactic diffuse emission.

This thesis focuses on Fermi-LAT observations of solar flares, the most energetic events in our Solar System. They consist of explosive phenomena that emit electromagnetic radiation extending from radio to gamma rays. It is generally agreed that magnetic energy stored in the solar corona around sunspots and released through reconnection is the source of acceleration of electrons and ions to relativistic energies on time scales as short as a few seconds. Large solar flares are observed emitting up to $\sim 10^{32}$ erg in radiation over the entire electromagnetic spectrum on timescales of minutes to hours. The number of sunspots and associated flares vary with the 11-year activity cycle of the Sun. Observations in hard X-rays, microwaves, gamma rays, and direct detection of Solar Energetic Particles (SEPs) have supported the evidence of flare-accelerated particles interacting in the solar atmosphere

(Fletcher et al. 2011).

Coronal Mass Ejections (CMEs) are another component of solar activity, consisting of the eruption of billion-ton clouds of solar atmospheric material being transported away from the Sun at velocities of hundreds to thousands of km/s. Both flares and CMEs are two aspects of a large-scale magnetic reconfiguration and energy release. However, not all flares, even large ones, are associated with CMEs and the exact connection between these two phenomena is still unclear. The total energy of a CME ranges from 10^{29} to 10^{32} erg, which is similar to the electromagnetic radiation released by flares. The motion of fast CMEs through the interplanetary material at speeds much greater than the solar wind creates a shock front, efficient at accelerating particles called Solar Energetic Particles (SEPs).

1.1 Outline

Before the Fermi-LAT was launched in 2008, when the Sun was going through one of the deepest minimum in solar activity in almost a century. The activity only ramped up in 2010, and since then the Fermi-LAT has proven its remarkable sensitivity to observe new behaviors of solar flares at high energies, opening a unique window in understanding the properties of the acceleration processes occurring in solar flares.

This dissertation focuses on the analysis and discussion of solar flares observations by the Fermi-LAT during the first 9 years of scientific operations, which began in early August 2008.

In Chapter 2, I will first present the basics of the physics involved in the solar flare processes, followed by a description of the solar flare standard model and the characteristics of the multi-messenger observations. I will then review the past high-energy observations of solar flares by previous missions and summarize the understanding drawn from those.

Chapter 3 provides a description of the Fermi-LAT and its performance, followed by Chapter 4 presenting the details of the methodology for the analysis of solar flare observations usingFermi-LAT data.

Through the continuous monitoring of the solar activity during Cycle 24 by the Fermi-LAT, a total of 45 Fermi-LAT Solar Flares (FLSFs) were detected at energies greater than 60 MeV, extending the sample of known high-energy gamma-ray flares by a factor of ~ 4.

About 40% of all FLSFs exhibit gamma-ray emission lasting longer than 2 hours which was previously thought to be a rare occurrence. A few even show a rise and decay behavior that had never been observed with past missions. A new class discovered above 60 MeV by the Fermi-LAT are gamma-ray "Behind-the-limb" solar flares, challenging the question of the location of the production of high-energy gamma rays, and in turn the location of

the particle acceleration. Chapter 5 presents the detailed analysis of some of the most important flares observed in March 2012 and September 2017.

Chapter 6 applies a comprehensive temporal, spectral and spatial analysis for each flare in the FLSF catalog. It is found that the FLSF detections are not limited to the most powerful flares. This work suggests that efficient particle acceleration might be a phenomena more common than previously thought, even for relatively modest flares.

Chapter 7 presents a comparison of gamma-ray results with broadband ground-based and space-based observations across the electromagnetic and charged-particle spectrum. This can shed new light on the particle acceleration mechanisms at play in solar flares and elsewhere as well.

Chapter 2

Past High-Energy Observations of Solar Flares

During solar flares, the Sun is capable of accelerating electrons and ions to relativistic energies on time scales as short as a few seconds. Observations in hard X-rays, microwaves, gamma rays, and direct detection of particles have all supported the evidence of flare-accelerated particles interacting in the solar environment (Fletcher et al. 2011). They offer a unique window in understanding the properties of the acceleration processes acting in solar flares. The Gamma Ray Spectrometer (GRS) aboard the Solar Maximum Mission (SMM, Forrest et al. 1980) and the high-energy instrument Energetic Gamma-Ray Experiment Telescope (EGRET, Kanbach et al. 1988, Esposito et al. 1999) observed the maxima of solar cycles 21 and 22 at energies up to the GeV scale. The Solar Maximum Mission was launched in February 1980 and ended in December 1989. The satellite suffered a critical attitude failure nine months into its mission and was repaired in 1984 by the Challenger space shuttle, making it the first orbiting unmanned satellite to be serviced in space. However, this failure did not affect the results by the GRS which detected 258 gamma-ray solar flares above 300 keV Vestrand et al. (1999). The EGRET instrument was the highest energy detector onboard the Compton Gamma-Ray Observatory (CGRO), named in honor of Arthur Compton. It was launched on 1991 April 5 and re-entered the Earth's atmosphere on 2000 June 4, after a planned de-orbit maneuver. The CGRO carried four instruments covering the photon energy range from 30 keV to 30 GeV: BATSE, OSSE, COMPTEL and EGRET, in order of increasing energy. Several flares were observed in gamma rays and showed puzzling behavior not correlated with other wavelength.

In this Chapter, I will describe the physics of the high-energy processes at play in solar flares and eruptive events. I will also provide an overview of the first detections of those processes in the past 35 years and the current models that have been proposed to explain

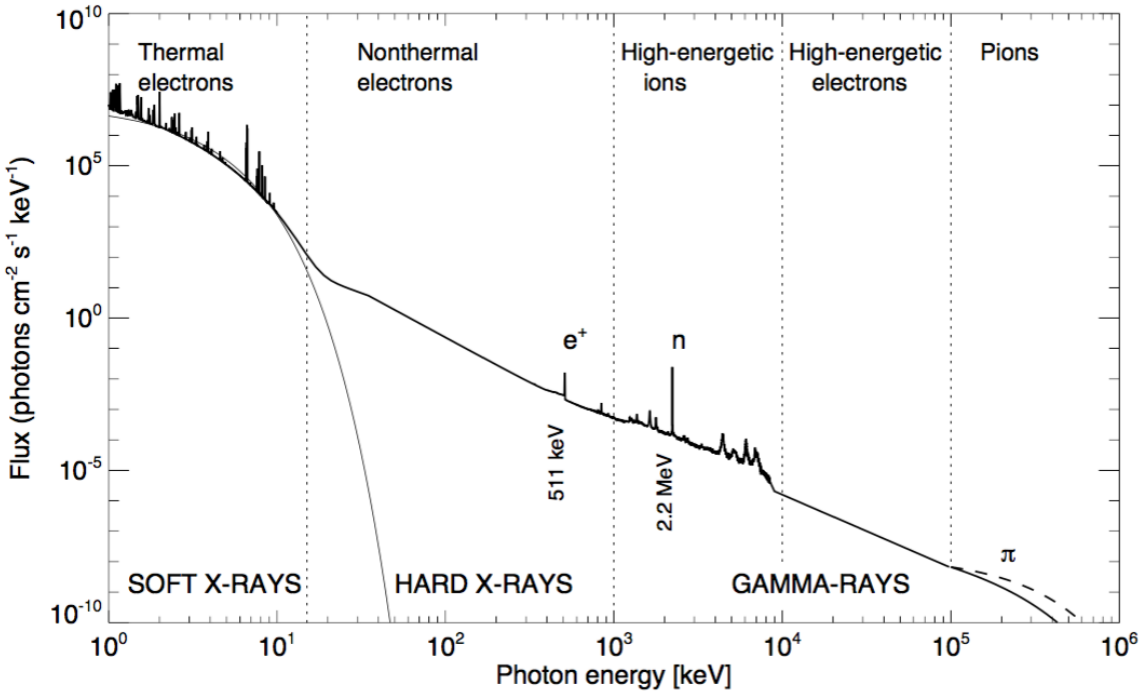

Figure 2.1: Photon spectral distribution for a large solar flare from Soft X-rays to high-energy gamma rays, with each of the high-energy components (although few flares exhibit all those signatures, Aschwanden 2005).

the observations.

2.1 Physical Processes at Play in Solar Flares

The solar flare environment is complex, with a large number of physical processes determining the behavior of particles and of their electromagnetic emission. I will focus on those processes relevant to the high-energy aspects of solar flares.

At high energies, the main emission process from high-energy electrons is bremsstrahlung seen in X-Rays, but their presence is also supported by detection of synchrotron emission in the microwave range. High-energy protons and ions interact through a number of nuclear processes: nuclear lines, neutron capture, annihilation of positrons produced by ions in the 1-100 MeV range, decay of pions produced in nuclear collisions.

Figure 2.1 shows an example of an extended solar flare spectrum from soft X-rays to gamma-rays and I will present the different features below:

- Relativistic Electron Bremsstrahlung Continuum:

  In the solar plasma environment, charged particles are free to move and a common

interaction consists of a free electron being scattered by the field of an ion. The electron loses a small amount of kinetic energy, which is converted into a photon. Bremsstrahlung, first introduced by Bohr, Bethe and Heitler from the german *bremsen* "to brake" and *Strahlung* "radiation" (i.e. "braking radiation") is sometimes referred to as free-free emission, as both electron and ion interacting are free. Thermal bremsstrahlung refers to the emission of colliding electrons with similar energies as the ambient plasma. For higher-energy particles, the emission is referred as non-thermal bremsstrahlung, for which quantum effects need to be accounted for (as well as relativistic effects depending on the energy of the particle).

Bremsstrahlung is largely the main process for high-energy electrons to produce Hard X-rays (HXR) extending in some cases to Soft Gamma Rays (SGR) in solar flares (see Kontar et al. 2011 for review).

The rate of bremsstrahlung emission depends largely on the energy of the energetic electron and the characteristics of the medium it moves through. Two main assumptions have been used to facilitate the modeling: thick and thin target. Thick target emission assumes that the energetic electrons loose all their energy, mostly through Coulomb collisions and emit bremsstrahlung X-rays with progressively softer frequencies that can be characterized as thermal bremsstrahlung. Thin target assumes that electrons loose some energy via bremsstrahlung emission but the energy loss process minimally affects the energy of the particle. In the context of solar flares, a combination of these two cases can happen (Veronig & Brown 2004, Park et al. 1997).

- Synchrotron Radiation:

  Synchrotron radiation is the name given to the radiation which occurs when charged particles move in magnetic fields. Particles propagating in magnetic fields gyrate along the field lines and their constant change of momentum causes synchrotron emission. Particle energy and characteristics of the magnetic field determine the spectrum of the emitted radiation. In the context of solar flares, gyrosynchrotron radiation is observed in the GHz range, which can give valuable information on the properties of the energetic particles (see review by Kaufmann, 2009).

  Whether the high-energy electrons loose more energy to bremsstrahlung or to synchrotron emission depends on the local density n and magnetic field strength B as: n/B^2.

- Inverse Compton Scattering:

In the radiation field of the Sun, high-energy elections can up-scatter optical/UV photons to gamma rays. For energetic electrons accelerated during solar flares, this process is usually negligible compared to other energy loss processes like bremsstrahlung and synchrotron emission, although it is relevant to the interactions of cosmic rays with the solar environment.

- Coulomb cooling:

  The processes above cover the non-thermal processes high-energy electrons can loose their energy to. However the main process for energetic particles loosing their energy is through the interaction with the ambient material by way of Coulomb cooling (Emslie 1978). A large fraction of the radiation energy emitted during a flare is thermal emission from the heated material at the Sun.

Relevant processes for **energetic protons and ions** are:

- Proton interactions with ions from ambient medium, producing nuclear de-excitation lines between 4 and 7 MeV:

  Sharp features are created by accelerated protons or alpha particles impacting higher densities site, most likely the chromosphere, and exciting heavy elements like: Be, Li, C, O, Ne, Si, Mg, Fe. Broader features are obtained by accelerated heavy ions impacting the ambient material and producing the same de-excitation lines which are Doppler broadened.

- Positrons annihilation in flight, 511 keV line:

  Positrons can be produced through a variety of nuclear reactions. The proton + proton interaction can yield the production of π^+ which in turns decay to positrons. These can annihilate when interacting with free ambient electrons to produce 511 keV photons.

- Neutron capture line emission at 2.2 MeV:

  Some nuclear reactions between accelerated hadrons produce high-energy neutrons, mainly in (p, p), (p, α), and (α, p) reactions (Hua & Lingenfelter 1987) These can be captured by ambient protons to form deuterium with the release of 2.223 MeV photon of binding energy from the mass excess. This emission is very often slightly delayed compared to the other high-energy signatures because of the time required for the neutrons to slow down in the solar atmosphere and photosphere and be captured. The nuclear line emission implies the presence of accelerated ions up to at least 50 MeV/nucleon (Ackermann et al. 2012b).

- Pion decay:

  Protons, or heavier ions with energies above 300 MeV/nucleon can produce π mesons in collisions. The charged pions decay to muons which then decay to electrons and positrons, contributing to bremsstrahlung continuum and 511 keV line emission. Neutrinos are also produced in the decay of charged pions and decay of muons. Neutral pions decay to a photon pair. The resultant spectrum is a gamma-ray Doppler-broadened line centered on 67.5 MeV, which is half of the π^0 rest mass (135 MeV). More details can be found in Murphy et al. (1987).

Figure 2.1 shows the features of the main nuclear lines and indications of a pion decay component. More details on hadronic interactions can be found in Table 2.1.

Comparing the different multi-messenger observations provides information on the maximum energies of accelerated charged particles, electron to ion ratios and thus acceleration efficiencies. This helps put constraints on the mechanism of acceleration, the site where it takes place and the timescales of acceleration, possible trapping, timescales of transport and the emission site.

Table 2.1: High-energy photon and neutron emissions from high-energy processes in solar flares (Ramaty & Mandzhavidze 1994, Chupp & Ryan 2009).

Emission	Processes	Observed photons or neutrons	Primary ion or electron energy range
Continuum	Primary electron bremsstrahlung	20 keV - 1 MeV > 10 MeV	20 keV — 1 GeV
Nuclear De-excitation Lines	Accelerated ion interactions	Lines at e.g., 1.634 MeV 4.448 MeV 6.129 MeV	1—100 MeV/nucl
Neutron Capture Line	Neutron production by accelerated ions	Line at 2.223 MeV (Photosphere)	1—100 MeV/nucl
Positron Annihilation	β^+ emitter or π^+ production by accelerated ions	Line at 0.511 MeV	1—100 MeV/nucl
Pion Decay Radiation	π^0 and $\pi^\pm$ production by accelerated particles $\pi^0 \rightarrow 2\gamma$, $\pi^\pm \rightarrow \mu^\pm \rightarrow e^\pm$	10 MeV — 3 GeV (Peak at 67.5 MeV)	0.2 — 5 GeV
Neutron Production	Accelerated particles interactions (e.g., p + 4He = p + n +3 He)	Neutron in space (10 — 500 MeV) Neutron induced atmospheric cascades (0.1 — 10 MeV)	10 MeV — 1 GeV 0.1 MeV — 10 GeV

2.2 Solar Flare Standard Model

The basis for the standard model rests on a sudden release of stored magnetic energy. Most of the energy is used to accelerate a very large number of particles to high energies. Flares happen close to active regions of the Sun with complex magnetic field configurations, where it is thought that the motion at the photosphere and emergence of magnetic flux create distortion and stress in the field and increase the energy stored. The field evolves to a non-equilibrium state and suddenly reconfigures itself to a lower energy equilibrium. Models for solar flares always include reconnection between field lines as an initial process to transfer magnetic energy into kinetic energy of accelerated particles. From this first release of energy a wealth of electromagnetic emission follows (see Benz 2008 or Fletcher et al. 2011 for reviews). Reconnection must happen on short timescales, as the observed signature of high-energy particles in HXR during the impulsive phase can happen on timescales as short as seconds to minutes with a bursting variability of order of 0.1 seconds.

The precise mechanism for the acceleration of high-energy particles is still a matter of debate, although most models place the acceleration in the corona, in or close to the reconnection region. Once accelerated, high-energy particles can follow open field lines and escape, but most follow the closed magnetic field lines to interact with the chromosphere. Signatures of non-thermal emission can be observed at the footpoints but also at the looptop.

Coronal Mass Ejections (CMEs) consist of the eruption of a large cloud of solar atmospheric material being transported away from the Sun at velocities of several hundreds to thousands km/s. Howard & Tappin (2009) and Webb & Howard (2012) review the theory and observation of CMEs. Both flares and CMEs are two aspects of a large-scale magnetic reconfiguration and energy release. However big flares are not associated with CMEs in 40% of the cases. The exact connection between these two phenomena is still unclear (Yashiro et al. 2005).

CMEs are usually characterized by their speeds and accelerations as well as the opening angle. Fast CMEs with speeds larger than the solar wind can create a shock front, efficient at accelerating particles. CMEs starting on the western limb carry particles that can generally reach the earth, because particles, even if energetic, travel along field lines of the Parker spirals (Parker 1958). There are two types of CMEs: the gradual ones that evolve at speeds of 400-600 km/s and show signs of sustained acceleration; the impulsive CMEs, that are associated with flares with speed of order of 1000km/s or more and move at constant velocities or decelerating.

The total energy of a CME ranges from 10^{29} to 10^{32} erg, which is similar to the energy budget released by flares in non-thermal energies. The total energy going into a CME comes from the magnetic energy stored and the energy released in the corona. As the

CME develops, part of the energy budget goes to kinetic energy and potential energy. The mass of a CME is estimated from white light brightness. For slow CMEs the magnetic energy contained in the CME volume is decreasing as the CME expands, and corresponds to the increase in kinetic energy. For fast CMEs (speed > 600 km/s) the magnetic energy is significantly less than the kinetic energy. This indicates a initial influx of energy in the corona during the impulsive phase of the flare, and then the total energy contained in the CME decreases and the expansion decelerates.

2.2.1 High-Energy Electrons

Proof of the acceleration of electrons to high energies comes most directly from the bremsstrahlung emission detected for many solar flares in HXR.

In large solar flares, a bremsstrahlung continuum can be observed from soft X-rays all the way to the gamma-ray range which traces electrons that can be accelerated up to tens of MeV. The X-ray spectrum can be fitted by thermal component at low energies and a non thermal power law tail at energies above about 15 keV. At energies greater than tens of MeV, the electrons are highly relativistic and the full relativistic treatment of bremsstrahlung is necessary to describe the process. An example of X-ray emission during a bright solar flare is shown in Figure 2.2 (Lin 2011) with the two components of bremsstrahlung emission fitted together.

Numerous observations point to electrons interaction taking place with the denser material of the chromosphere at the loop footpoints emitting thick target bremsstrahlung. Interestingly, dimer HXR sources have been observed above the looptop most likely from thin target bremsstrahlung emission produced by electrons accelerated in a region close-by the acceleration site, first reported by Masuda et al. (1994), shown in Figure 2.3. More sensitive observations have now shown that this is a common feature (Krucker et al. 2008, Krucker et al. 2008).

Bright footpoints emission is generally seen in HXR as well as in microwaves, tracing the gyro synchrotron (5-17 GHz) emission from high-energy electrons in the solar magnetic field (see for example Lee & Gary 2000 for coincident intensity maps of microwave and HXR).

In the case of the occulted Dec 31, 2007 flare, Krucker et al. (2010) showed that the sources above the loop detected in HXR and microwave were temporally and spatially correlated, signatures of the presence high-energy electrons. The intensity of the bremsstrahlung emission is directly related to the target material density, so the intensity of the HXR footpoint source is greater than at the looptop. This is why the intensity of the coronal looptop

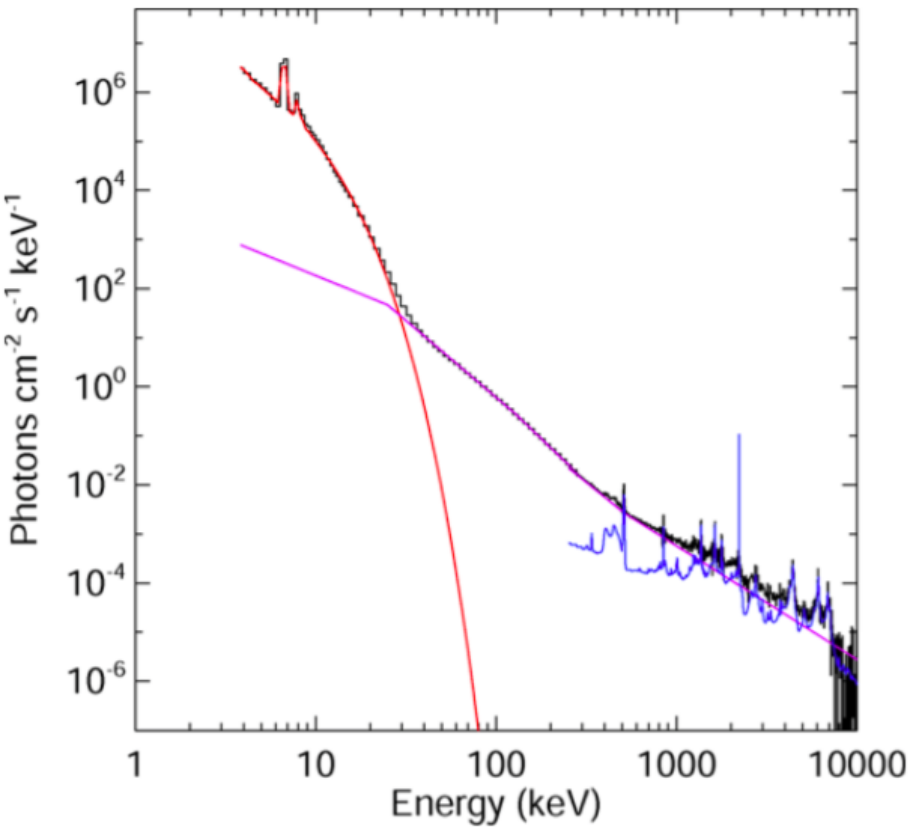

Figure 2.2: Typical spectral distribution for a bremsstrahlung emission with a thermal and a non-thermal component seen by RHESSI for a bright solar flare. The red line fits the thermal emission from plasmas with temperatures up to 40 MK, the magenta fits the non-thermal component as a power law with a cutoff. At higher energies the blue lines fits the gamma-ray lines that will be described below.

HXR source puts significant constrains on the need for a large number of accelerated electrons and the efficiency of the acceleration. The efficiency of the energy of the electron population going into bremsstrahlung emission, compared to Coulomb energy losses is actually the same as they are both proportional to the medium density. A second source has been observed even higher in the corona and is thought to come from above the acceleration region (Liu et al. 2008).

From the X-rays observations, models have been developed to infer the electron population distribution (see Raymond et al. 2012, for a review and references therein). Most models fit the electron population as a broken power law in the non-thermal range, with indices varying from 2 to 6. For some large flares, a flattening above 100 keV with a cutoff above tens of MeV has been observed, which could directly reflect the properties of the acceleration mechanism (Trottet et al. 1998; Petrosian et al. 1994).

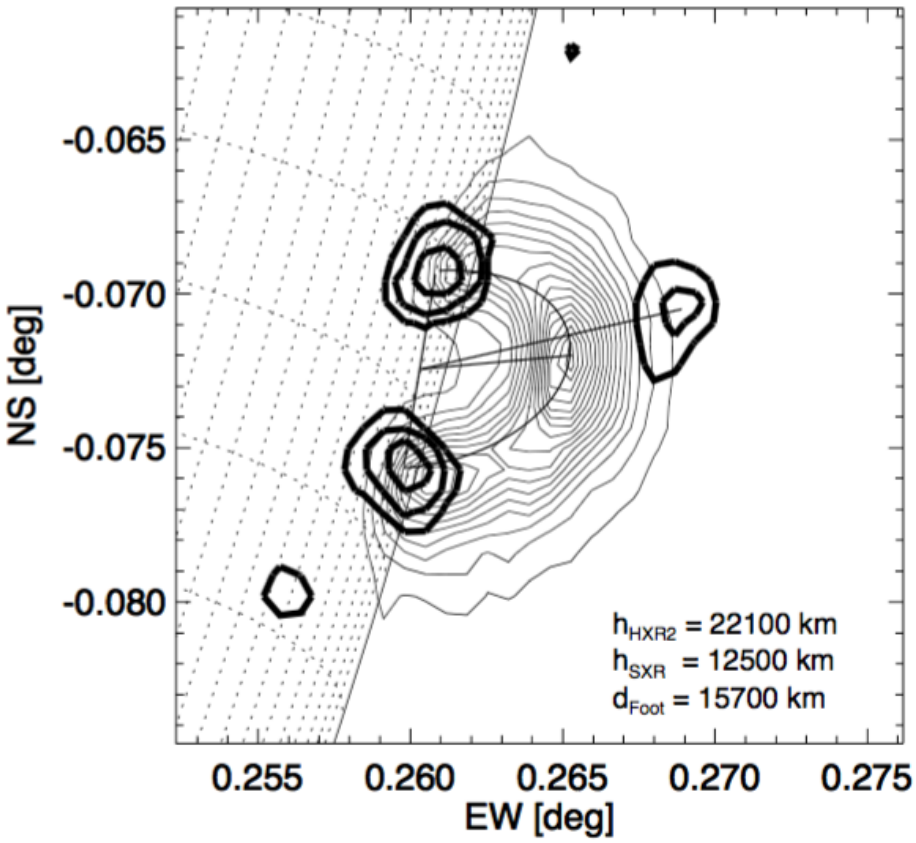

Figure 2.3: RHESSI imaging of the so-called Masuda flare in Jan.13, 1992 (black contour in the 22-33 keV channel for the non-thermal bremsstrahlung, thin contour from ultra-hot material in soft X-rays observed by Yohkho SXT) (Aschwanden et al. 1996).

Fast (down to sub-seconds) pulses in the HXR light curve are signatures of the acceleration of particles by fast reconnection bursts occurring, most likely, in the corona above the loop. The rise time of these bursts is energy dependent, which traces the direct transport of the high-energy particles with different time-of-flight to the chromosphere where the thick target bremsstrahlung occurs. A signature of this phenomenon is the **softening** of the spectrum: high-energy particles interact first. From those time-of-flight measurement, the acceleration site is thought to be about 50% higher than the height of the loop, most likely where the reconnection operates (see simple cartoon for flare mechanism in Figure 2.4).

Some of the high-energy particles could end up trapped by mirroring in the magnetic loop, and only collisions and pitch angle diffusion will cause their precipitation. This induces a delay up to ten seconds, which is also energy dependent but in the opposite way: higher energy particles will stay trapped longer than the lower energy ones (Krucker et al. 2008). This trapping-precipitation model causes a **hardening** of the spectrum at high energies and gamma-ray emission from electron bremsstrahlung can slightly outlast X-rays.

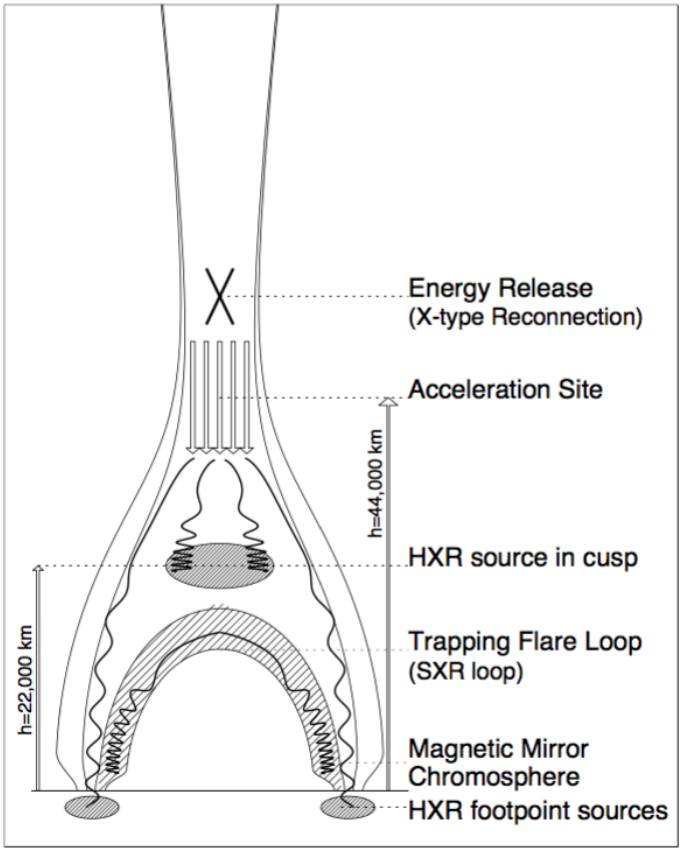

Figure 2.4: Cartoon for a possible scenario for a flare with an above the loop HXR source (Aschwanden et al. 1996).

The evolution of the spectrum as a function of time is the result of the evolution of the acceleration processes combined with the transport effects. This *soft-hard-soft* (SHS) evolution is a common pattern, but other scenarios have been observed. In addition, this behavior has been seen in coronal HXR sources which could indicate that the evolution is more reflective of the acceleration process than the transport of particles.

In most flares, the Soft X-Ray rise time is delayed in comparison to the HXR. The time integral of the non-thermal emissions tracks the time profile of the thermal emissions: the so-called *Neupert* effect, first discovered by him after observing a delay between the peaks of SXR and microwave emissions (Neupert 1968).

The underlying reason for this is that the non-thermal emission in HXR corresponds to a small fraction of the energy budget. Most energy of the initially high-energy particles is lost to Coulomb collisions, heating the chromosphere material and inducing an evaporation up-flow of very hot plasma in those loops.

Those loops can be seen in SXR during the flare or afterwards. Post-flare emission consists of super hot material ($\sim$ 1 MK) evaporating in the newly formed magnetic structure

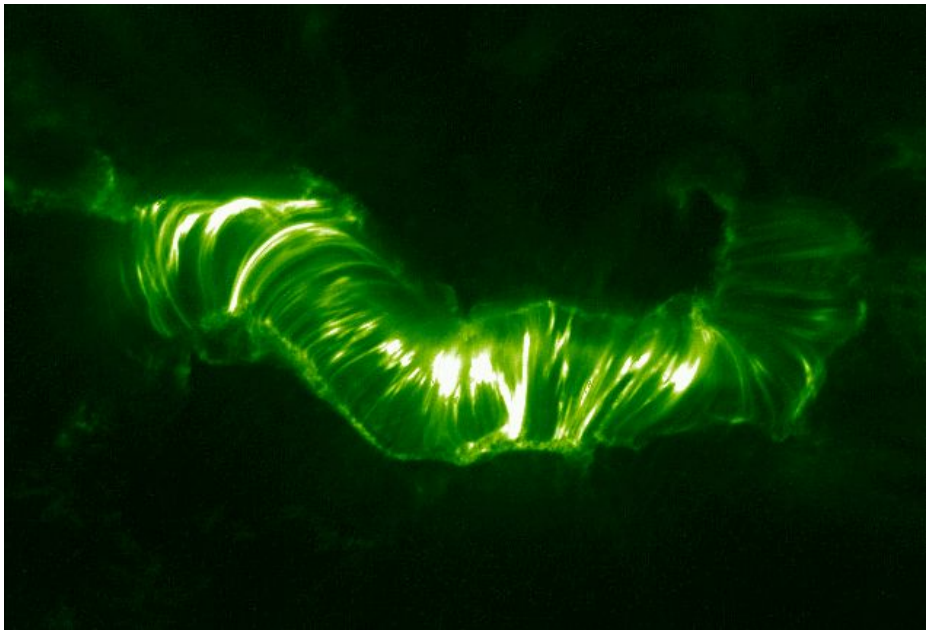

Figure 2.5: Following a very large flare on July 2000, million degrees material is seen filling a large magnetic loops structure by TRACE.

above the active region, as observed in Extreme UV by the Transition Region and Coronal Explorer(TRACE) observatory (Figure 2.5 illustrated by the Astronomical Picture of the Day on July 20, 2000[1]).

2.2.2 High-Energy Protons and Ions

High-energy protons and ions produce a wealth of gamma-ray emission when interacting with the target solar material. The density needs to be high enough to get effective gamma-ray production, so the radiation site is thought to be close to the chromosphere or lower corona. There is also evidence of neutron production.

In the 1-10 MeV range, gamma-ray nuclear line spectroscopy can provide valuable information on the spectrum of the accelerated ions population as well as its composition. The modeling of this complex spectrum also provides informations on the composition, densities and temperatures of the solar atmosphere they interact with (Murphy, 2007). The spectrum of the powerful 2002 July 23 flare is shown in Figure 2.6 with some new lines resolved for the first time by RHESSI (Lin et al. 2003).

Up until the launch of RHESSI, no localization had been precise enough to put constraints on the energetic proton and ion populations. But in the case of a very bright flare on October 28, 2003, RHESSI observations showed strong emission in the nuclear

[1] `http://apod.nasa.gov/apod/ap120315.html`

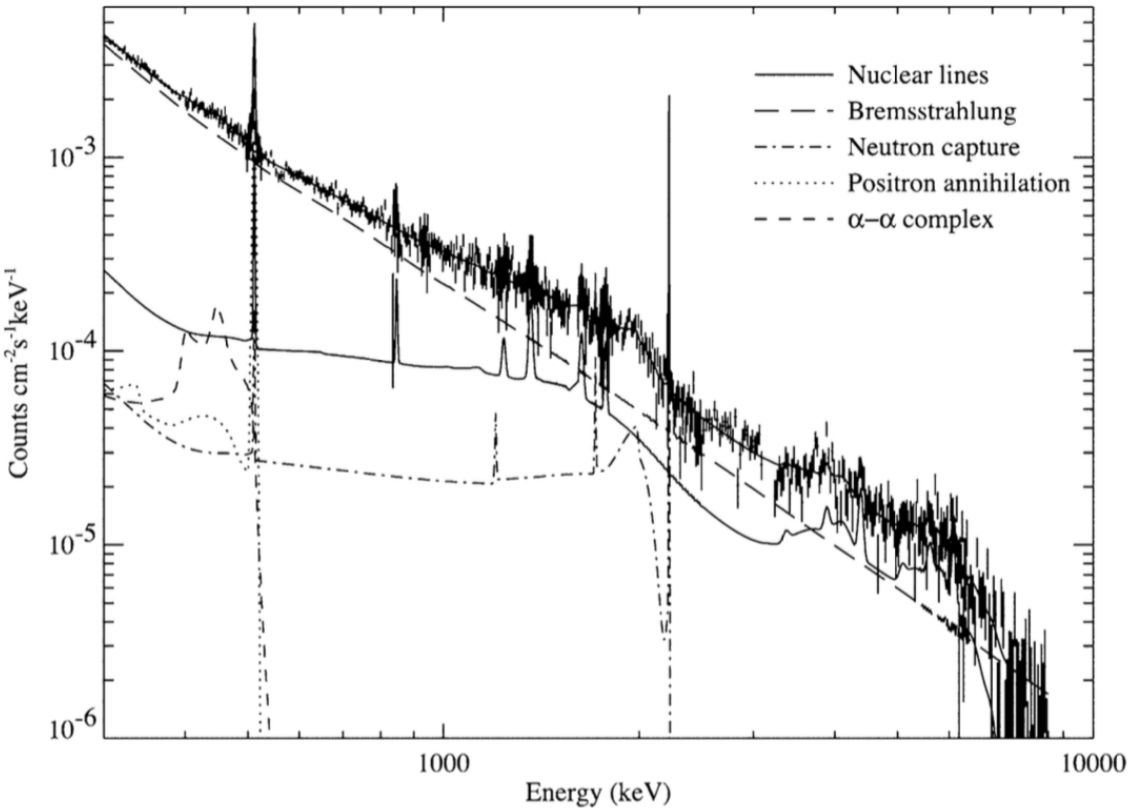

Figure 2.6: RHESSI gamma-ray count spectrum with the different high-energy components fitted and continuum for the 2002 July 23 flare from Lin et al. (2003).

gamma-ray lines, and precise imaging was able to pin the 2.218-2.228 MeV emission to two compact sources on each side of the flare loop. In addition, Hurford et al. (2006) found a significant shift in position from the two compact 200-300 keV sources from thick target bremsstrahlung (see Figure 2.7).

Those observations confirm the presence of high-energy protons and ions in the flare loop system, however, their slightly different positions could indicate differences in acceleration rate or site, or different transport to the solar atmosphere, which is yet to be understood.

Detection of gamma rays above 10 MeV and neutrons shows the presence of protons and ions with energies above 200 MeV/nucleon (Aschwanden 2005). This is also confirmed by the detection in-situ of high-energy protons and ions (> 100 MeV), as well as neutrons. Their time-of-arrival, spectrum and composition can show whether they could have been accelerated at the flare site during the impulsive phase of the flare or at the CME shock front (Raymond et al. 2012). It can be difficult to disentangle the two for large flares.

In the next section I will describe the datasets that are available to monitor solar activity.

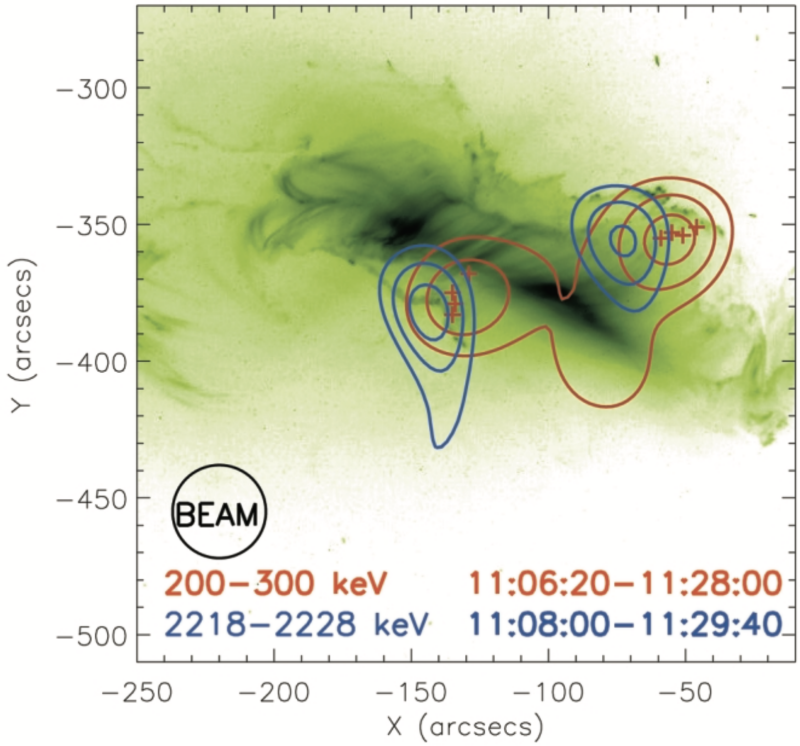

Figure 2.7: Hard X-ray and gamma-ray localization for the October 28, 2003 flare with two distinct compact 2.2 MeV line sources, superimposed on a TRACE 195 Å image (Hurford et al. 2006).

GOES Class	Peak Flux (1 – 8 Å) (W/m^{-2})	Frequency (events/year)
B	$\geqslant 10^{-7}$	240 – 1062
C	$\geqslant 10^{-6}$	170 – 1797
M	$\geqslant 10^{-5}$	16 – 205
X	$\geqslant 10^{-4}$	0 – 16

Table 2.2: Solar flare X-ray classification. Frequency in events/year (minimum and maximum reached between 2010 and 2016).

2.3 Multi Messenger Data

This section presents the description of the available solar data that is relevant to this work, in particular X-rays and particles detections which are important for the study of high-energy solar processes.

2.3.1 GOES observatory

A common measure of the magnitude of a solar flare is the peak of the associated soft X-ray (SXR) flux. Part of the Geostationary Operational Environmental Satellite (GOES)

mission has been dedicated to near-continuously monitor the solar activity for over three decades. 17 GOES satellites have succeeded each other from 1974 until the last launch of GOES-17 in March 2018. A selected number of satellites carry a high-energy proton detector and have a sun-pointed UV and Soft X-Ray sensors. Details on the satellites and instruments are available in the GOES Series Data Book[2]. A list of data products[3] and data access[4] are also provided. The main data used in this work consists of two 5-minutes averaged Soft X-ray channels with ranges 0.5 – 4 Å and 1 – 8 Å which correspond to 3 – 24 keV and 1.5 – 12keV respectively. It also monitors Solar Energetic Particles, in particular measuring protons fluxes in channels from 10 MeV up to 850 MeV.

Solar flare classification is entirely based on the observations of the soft X-ray in the 1 – 8 Å channel, using a logarithmic scale known as GOES class, with letters designating the order of magnitude in W/m^2 respectively (see Table). The brightest flare ever observed with a X 45 class occurred during the series of "Halloween flare" of October 2003. GOES defines the start of the flare with the following three conditions[5]: " a.) All 4 values are above the B1 threshold and b.) All 4 values are strictly increasing and c.) The last value is greater than 1.4 times the value which occurred 3 minutes earlier. The peak defines the class of the flare as the maximum reached by the GOES 1-8 $\mathring{A}$. The event ends when the current flux reading returns to 1/2 the peak (peak is the sum of the flux at maximum plus the flux value at the start of the event)." The peak flux in soft X-ray, i.e. the class of an event, is a good proxy for estimating the total energy of the accelerated particles in a solar flare (not including possible CMEs). The soft X-ray evolution corresponds roughly to the integral of the non-thermal component, and the consequent heating of the material as described by the Neupert effect (see section 2.2.1).

2.3.2 STEREO Telescopes

The Solar TErrestrial RElations Observatory (STEREO) mission, launched on 25 October 2006, provides a unique view of the Sun-Earth system. Two nearly identical observatories follow the Earth's orbit: STEREO A ahead of Earth and STEREO B trailing behind. They are able to produce the images of the Sun activity beyond the visible part of the Sun as seen from Earth, as well as the first stereoscopic images of CMEs. Their separation gradually increased so that after six years from their launch they were almost at equal distance from each other and the Earth (see Figure 2.8).

[2] Latest: `https://www.goes-r.gov/downloads/resources/documents/GOES-RSeriesDataBook.pdf`
[3] `https://www.ngdc.noaa.gov/stp/satellite/goes/datanotes.html`
[4] `https://www.ngdc.noaa.gov/stp/satellite/goes/dataaccess.html`
[5] `https://www.ngdc.noaa.gov/stp/solar/solarflares.html#xray`

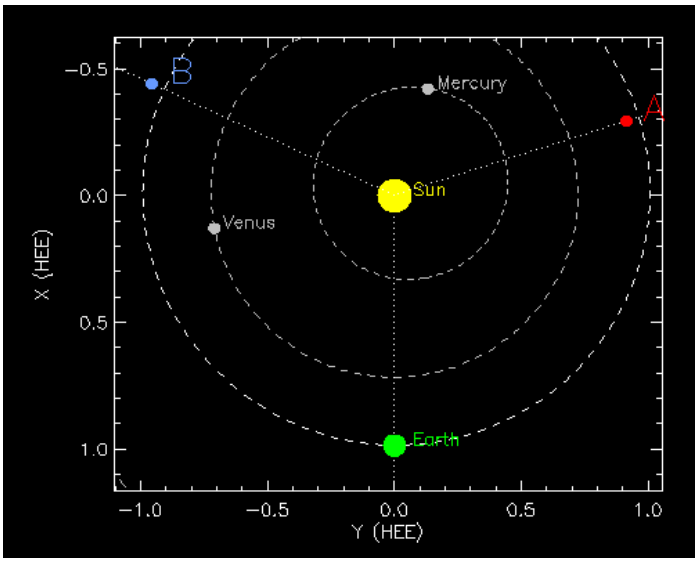

Figure 2.8: Positions of the two satellites STEREO A and B in January 2012.

2.3.3 Coronal Mass Ejections (CMEs)

CME properties have been cataloged from observations by the *Large Angle and Spectrometric Coronagraph* (LASCO) onboard the *Solar and Heliospheric Observatory* (SOHO). Data have been gathered in the Coordinated Data Analysis Workshops (CDAW) CME catalog[6] (see Brueckner et al. 1995).

CMEs are manually identified from scattered white light (H-alpha) observations from 2 to 32 solar radii. The data is obtained from tracking the progression of the ejection. the date and time indicated in the catalog corresponds to the first appearance in the LASCO/C2 field of view at 2 solar radii.

The speed of the CME might be obtained by a linear fit of the CME front height versus time data points. However, when the acceleration is significant, this linear speed is only representative of the average speed of the CME between 2 and 32 solar radii. To account for the acceleration or deceleration of the CME a quadratic fit is performed and the speed at 20 solar radii is estimated. It can give a rough estimate of the error on the CME speed. Similarly, the CME onset time is obtained by extrapolating back the time at 1 solar radius using the speed from linear fit (or quadratic fit to evaluate the uncertainty on the onset time). Each CME is also characterized by a mass and a kinetic energy, which are subject to numerous assumptions and large uncertainties. CMEs with an apparent width of 360°

[6] This CME catalog is generated and maintained at the CDAW Data Center by NASA and The Catholic University of America in cooperation with the Naval Research Laboratory. SOHO is a project of international cooperation between ESA and NASA. A full description of the LASCO CDAW catalog fields is available at `http://cdaw.gsfc.nasa.gov/CME_list/catalog_description.htm`

are called Halo CMEs.

2.3.4 Solar Energetic Particles (SEPs)

As part of the energy released in solar flares, particles accelerated to high energies are released in inter-planetary space: charged particles, neutrons, and energetic neutral atoms, referred to as SEPs. Thus we sometimes refer to observations of flares that include high-energy particle detections as "multi-messenger" observations. Some SEP events are of an impulsive nature: most likely directly related to the impulsive acceleration of particles immediately following the reconnection above the flare site; while some SEP events are gradual: related to CME shock accelerated particles. Gradual SEP events last much longer, from a few hours to days and are usually more intense than the impulsive phase related ones.

The observed flux of SEPs depends highly on the magnetic connectivity between the solar flare location and the observer. In space, the GOES satellites network as well as both STEREO satellites provide SEP observations at 1AU. A database of SEP major events[7] observed with GOES satellites is compiled for events when the particle intensity in the E $>$ 10 MeV proton channel exceeds 10 particles cm^{-2} s^{-1} sr^{-1}.

Another way to infer the acceleration of high-energy particles is through the network of neutron monitors around the world. Those are used mainly for cosmic ray observations, but in the case of large solar flares they measure both the neutrons produced in the solar chromosphere and the neutrons from atmospheric cascades from very high-energy protons and ions reaching the Earth (from a few hundreds MeVs to tens of GeVs). Such increase in radiation, detected by neutrons detectors at sea level, are termed Ground Level Enhancements (GLE)[8]. The neutron spectrum can be of great importance when trying to determine the spectrum of the accelerated protons at the highest energies (above hundreds of MeV).

The next section will go into the details of the high-energy gamma-ray observations of solar flares before the launch of the Fermi telescope.

2.4 Gamma-Ray Solar Flares

2.4.1 First Evidence of High-Energy Gamma-Ray Emission

The first reported observation of gamma rays with energies above 50 MeV was made with SMM spectrometer during a X2.5 class flare on 1980 June 21 (Chupp et al. 1982). The

[7] `https://cdaw.gsfc.nasa.gov/CME_list/sepe/`
[8] Catalog available at `http://gle.oulu.fi/`

observation of high-energy neutrons indicated that protons must have been quickly accelerated (in less than 60 seconds) to energies up to GeVs during the impulsive phase of the flare.

The first indication of gamma rays from pion production in a solar flare was observed by SMM on the 1982 June 3 flare from an X8.0 flare. The flare exhibited high-energy emission during the first intense impulsive phase, and a separate high-energy phase (about 2 min later), which accounted for the majority of the very high-energy emission. The gamma-ray emission then exponentially decayed with time (Dunphy & Chupp 1994). The hadronic nature of the gamma rays was confirmed by the observation of neutrons and the 0.511 MeV positron annihilation line from the decay of positively charged pions that showed a similar time profile (Share et al. 1983).

Although Murphy et al. (1987) speculated that the protons responsible for the time-extended phase are not the same as those responsible for the impulsive phase, the data are ambiguous and, as will be shown later, can be interpreted in several ways.

Since the era of those early measurements, improved spectrometers detected the presence of pion-decay emission in several more flares, and in two cases a gamma-ray emission up to at least 1 GeV was observed (Kanbach et al. 1993, Akimov et al. 1996, Vilmer et al. 2003, Kuznetsov et al. 2010). With the increased number of high-energy flares detected in the 1980s and 1990s, new behaviors came to view, in particular observations of gamma rays not directly temporally correlated with hard X-ray emission, leading to a new solar flare class known as Long Duration Gamma-Ray Solar Flares, or Delayed-emission Gamma-Ray Solar Flares (reviewed in Ryan 2000 and Chupp & Ryan 2009).

2.4.2 Long Duration Gamma-Ray Solar Flares

During solar cycle 22, the EGRET instrument detected gamma rays above 100 MeV for more than an hour after the impulsive phases of 3 flares (Ryan 2000). Among them, the 1991 June 11 flare is remarkable because the gamma-ray emission (> 50 MeV) lasted for 8 hours after the impulsive phase of a GOES X12.0 flare (Kanbach et al. 1993). The 2.223 MeV gamma-ray line emission was detected for 5 hours (Rank et al. 2001).

The measured gamma-ray spectrum throughout the duration of the emission was proposed to be from electron bremsstrahlung but was later interpreted to be due to pion-decay components (Ramaty et al. 1994). The gamma-ray flux showed a smooth exponential decay (Kanbach et al. 1993). The light curve and spectra are shown in Figure 2.9.

The designation “Long Duration Gamma-Ray Flares” was first introduced by Ryan (2000) to describe flares with gamma-ray emission (nuclear and high-energy gamma-ray emission) lasting longer than emission in other ranges like X-ray or radio. Ryan (2000)

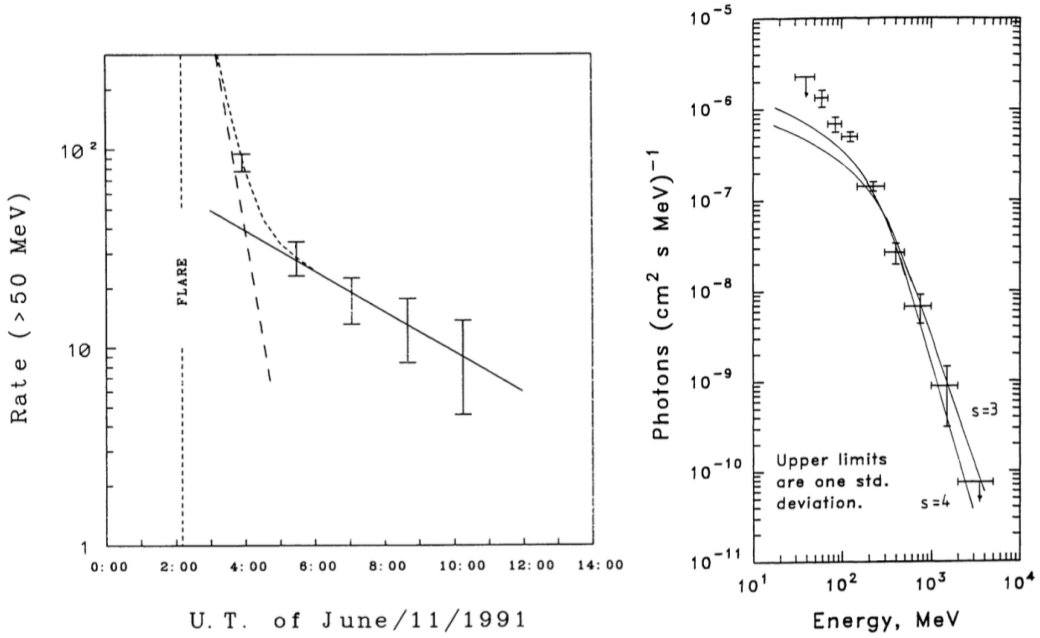

Figure 2.9: Left: time profile of the gamma-ray emission above 50 MeV. Right: Integrated spectrum over the first three hours. Pion models for power law of protons with indexes 3 and 4 attempt to fit the data (Kanbach et al. 1993).

and Chupp & Ryan (2009) reviewed the long duration gamma-ray solar flares and other examples of high-energy gamma-ray emission in flares (see Table 2.3). All those gamma-ray flares were very bright GOES X-ray flares, with classes between X1.4 and X15.

The first observations of Long Duration flares presented the interesting challenge of explaining the presence of high-energy protons or ions long after the standard flare model particle acceleration timescale.

2.4.3 Behind The Limb Solar Flares

So far in the standard model description, we always assumed that the gamma-rays originated from thick-target emission in the chromosphere at the footprints due to energetic protons and ions. This is why the first detection of gamma-rays in the MeV range from a flare with its footpoints occulted was so surprising. In the case of the 1989 September 29 flare, located 15° behind the limb, nuclear line continuum in the MeV range and 2.2 MeV neutron capture line were observed (Vestrand & Forrest 1993, Vestrand & Forrest 1994).

Two plausible scenarios have been proposed: one with the top of flare loop (anchored to the occulted footpoints) being high enough in the corona that it is visible beyond the limb and one with a larger magnetic structure which would reconnect to its footpoint on the front of the disk (see geometry in Figure 2.10). The column density required for effective line

Date	Duration	τ_1 (min)	τ_2 (min)	SXR	Flare pos	Instrument	Ref
1982-06-03	20 min	1.15	11.7	X8.0	S09E71	SMM	1
1984-04-25	15 min	3.23	$\geqslant$10	X13	S12E43	SMM	1
1988-12-16	10 min	3.34		X4.7	N27E33	SMM	1
1989-03-06	25 min	2.66		X15	N35E69	SMM	1
1989-09-29	10 min			X9.8	S26W105	SMM	2
1990-04-15	30 min			X1.4	N32E57	GRANAT	3
1990-05-24	8 min	0.35	22	X9.3	N36W76	GRANAT	3,4
1991-03-26	10 min			X4.7	S28W23	GAMMA-1	5
1991-06-04	2.8 hrs	7	27	X12	N30E70	EGRET	6,7
1991-06-06	17 min			X12	N30E70	EGRET	6,7
1991-06-09	15 min			X10	N34E04	EGRET	6,7
1991-06-11	8.3 hrs	9.4	220	X12	N31W17	EGRET	8,9
1991-06-15	1.4 hrs	12.6	180	X12	N33W69	GAMMA-1	9,10

Table 2.3: List of delayed gamma-ray flares seen above 10 MeV with the GRS, EGRET instruments and the GRANAT and GAMMA-1 satellites (adapted from Ryan 2000). Refs 1: Dunphy & Chupp (1994), 2: Vestrand et al. (1999), 3: Trottet (1994), 4: Chupp & Ryan (2009), 5: Akimov et al. (1994), 6: Schneid et al. (1996), 7: Murphy et al. (1997), 8: Kanbach et al. (1993), 9: Rank et al. (2001), 10: Akimov et al. (1996).

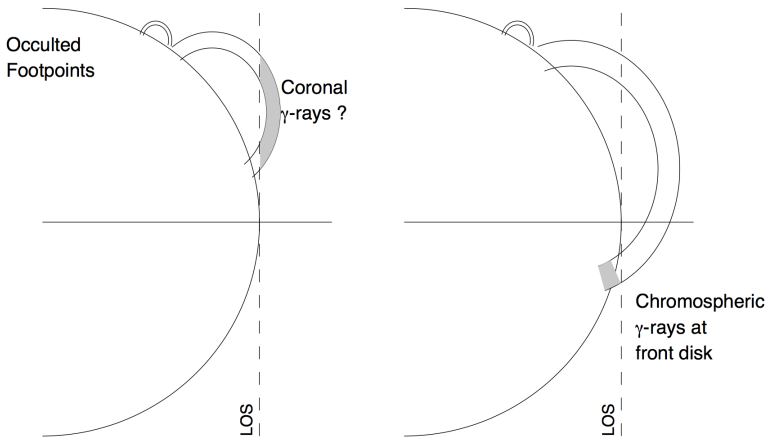

Figure 2.10: Geometry of two scenarios for gamma-ray emission associated with behind the limb solar flares (Aschwanden 2005).

emission can not be attained with the solar corona typical densities which points toward a gamma-ray source on the solar disk connected to the flare site by large loops.

Other cases of HXR emission coupled with nuclear line emission (but no 2.2 MeV line) might point more preferably to a looptop emission, where electrons and protons might be effectively trapped, although there is some tension with the required densities for line emission at the heights observable above the limb (Hudson 1978, Barat et al. 1994, Trottet et al. 1996).

HXR emission has been observed in the cases of very powerful solar flares happening behind the limb. Krucker et al. (2007) describes the case of a flare happening 40° behind the limb was associated with HXR emission seen by RHESSI up to 60 keV and associated with a very fast CME (about 2300 km/s). They would imply the presence of electrons with energy above 1 MeV. Whether this emission can only be from bremsstrahlung from electrons moving outward through a region with very low density is debatable, and a contribution from Inverse Compton emission has been proposed Chen & Bastian (2012).

2.5 Challenges

As presented in the previous section, a handful of solar flares were detected in the gamma-ray range during solar cycles 21 and 22. They presented clear signatures of proton acceleration through nuclear lines, neutron production and gamma ray spectrum above 50MeV specific to neutral pion decay.

The behaviors of the high-energy gamma-ray emission in solar flares can be classified into two categories:

- Gamma-ray emission coincident with HXRs, possibly with delays of few seconds, referred as the impulsive / PROMPT phase.
- Gamma-ray emission detected past the HXR emission, for up to an hour (or more in two cases), referred as the Long Duration/Delayed phase.

The general scenario for the impulsive phase of solar flares has been studied through numerous observations and the basis of a standard model for flares has been elaborated (Fletcher et al. 2011; Miller 2000). However this standard model still faces some challenges to provide a comprehensive view of solar flares especially at high energies, and more observations are still needed to explain particle acceleration to high energies in the solar environment.

Several processes have been suggested such as shock acceleration, direct current sheet, stochastic acceleration in presence of turbulence. (Ellison-Ramaty 1985; Petrosian et al.

1994; Park et al. 1997; Ryan 2000; Aschwanden 2004; Petrosian & Liu (2004); Chupp-Ryan 2009). Petrosian (2012) reviews the process of stochastic acceleration by turbulence and its application to solar flare models.

In terms of energetics, high-energy gamma-ray emission has been typically associated with intense Soft X-Ray flares recorded by GOES having peak powers exceeding $10^{-4} Wm^{-2}$ (X-class). Out of the 65 gamma-ray line flares observed by the gamma-ray spectrometer on SMM flares, only 3 had GOES classifications of M5.0 or less (Vestrand et al. 1999). Similarly, out of the 20 gamma-ray lines flares reported by RHESSI, only 3 were below the M5.0 class and the lowest class was characterized as C9.7 flare (Shih et al. 2009).

- Can less energetic solar flares have the capability of accelerating electrons to energies up to hundreds of MeVs and protons to energies >300 MeV?

Using RHESSI data, the same study showed a correlation between the intensities of the very hard X-ray electron bremsstrahlung (above 300 keV) and the gamma rays from neutron capture line detected in the prompt phase of the flares (see Figure 2 from Shih et al. 2009). This could indicate that the same processes are at play to accelerate very high-energy electrons, protons and ions. The same study showed that a large number of short and bright GOES X-ray flares do not show any signs of high-energy emission, in HXRs or gamma rays (Shih et al. 2009).

- Is this trend observed for gamma-ray emission of higher energy than the 2.2 MeV neutron line?

Only a few of the gamma-ray solar flares have signatures observed by SMM and EGRET lasting for more than an hour but they raise some significant questions that the standard model does not address.

- Is the acceleration only occurring during the impulsive phase, for which we have considerable evidence, with the high-energy particles being stored efficiently for the entire duration of the gamma-ray emission?

- Could a separate acceleration process be at play for a longer duration, decoupled from the impulsive phase, and not give any radiation signature except in the gamma-ray range?

To account for these observations, any model needs to characterize the efficiency of the acceleration process, its location and timescale, as well as the possible storage of particles and transport processes. Most proton acceleration models require a local low density with

the acceleration site located above the looptop (Ryan 2000). The radiation site is thought to be at the footpoints of the flare loop as gamma-ray production is most effective at high densities.

Two general class of models have been suggested:

- A scenario where the particles are accelerated during the impulsive phase of the flare and could remain trapped for the entire duration of the flare and precipitate gradually into the denser solar atmosphere to produce the gamma-rays.
- Alternatively, a continuous acceleration process with possible origin, either in the CME shock or in a turbulent closed magnetic loop (Rank et al. 2001).

The localization of the gamma-ray emission is also in question and is crucial in understanding the preferred scenario for both Behind The Limb (BTL) and Long Duration flares:

- Are the > 10 MeV gamma rays only produced at the footpoints for disk flares, as was observed by RHESSI with nuclear lines emission?
- Is there an emission component from the corona or alternative loops footpoints as suggested by the observation of the BTL flares?
- Does the localization of the gamma-ray emission change with time in the case of Long Duration flares?

Those questions remained standing after the high-energy gamma-ray observations by EGRET or other instruments up to the 1990s. Additional and more detailed flare observations were clearly necessary to shed some light on the acceleration mechanisms at work to produce the high-energy gamma rays.

2.6 Motivation for this Work

Throughout the solar cycle 24, the Fermi mission continuously observed the Sun. The greatly improved sensitivity of theFermi-LAT as well as its spatial resolution can give some answers to the challenges with the current solar flare models. Despite this solar cycle being much less prolific in flares and CMEs, the Fermi-LAT has detected high-energy emission from 45 flares, more than tripling the number of observations from past experiments.

In the next Chapters, I will describe the Fermi observatory and the LAT, its main instrument for high-energy gamma-ray observations; followed by the description of the data analysis methodology and the results of the first high-energy gamma-ray solar flare catalog.

Chapter 3

The Fermi Gamma-ray Space Telescope

The Fermi Gamma-ray Space Telescope (Fermi) is a major advance in the field of high-energy gamma-ray observations. Fermi brings together a large community in Astrophysics and Particle Physics and provides public data analyzed both by the instrument teams and the general community. The Fermi observatory supports two instruments: the Large Area Telescope (LAT) detecting high-energy gamma-rays from 20 MeV to more than 300 GeV (Atwood et al. 2009), and the Gamma-ray Burst Monitor (GBM), observing the sky from Hard X-rays to soft gamma-rays, from 8 keV to 40 MeV (Meegan et al. 2009) (see picture of the satellite before launch in Figure 3.1).

3.1 Fermi Mission

The Fermi Gamma-ray Space Telescope (Fermi) satellite was launched into a low-Earth orbit on 2008 June 11 (see Figure 3.1). The mean altitude of the orbit is 565 km, and the orbital plane is inclined by 25.6° relative to the equator. A single orbital period is $\sim$ 96 minutes, and the orbital pole precesses with a period of 53.4 days.

3.1.1 Observation Modes

The normal survey mode (about 95% of the time) for Fermi maximizes the coverage of the celestial sphere. In this mode the satellite rocks about the zenith, north for one orbit then south for the next. The rocking angle has varied from 35° to 52° over the mission timeline to accommodate thermal engineering constraints for the satellite, in particular for managing the temperature of the batteries. Operating in this scan mode keeps most of the Earth albedo out of the Field of View (FoV). In standard sky-survey mode, every region is viewed

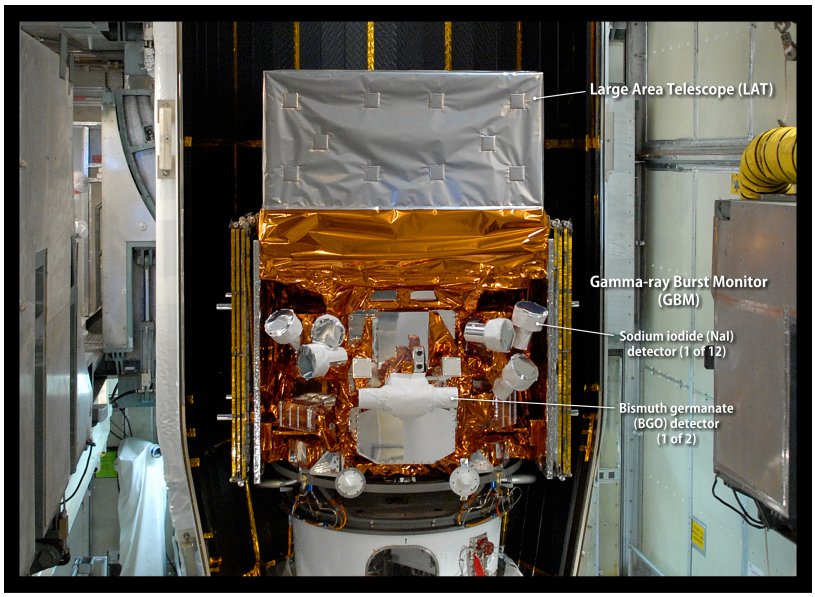

Figure 3.1: Fermi observatory before launch.

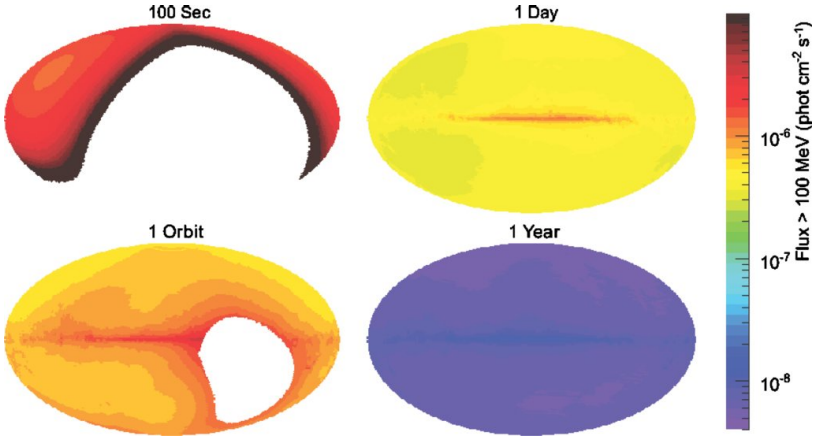

Figure 3.2: LAT source sensitivity for exposures on various timescales.

for about 30 contiguous minutes every 3 hr, with a nearly uniform exposure achieved every two orbits (see Figure 3.2).

The orbit of the satellite goes through the South Atlantic Anomaly, where the density of trapped charged particles is enhanced, due to the configuration of the Earth magnetic field. During that passage, no science data is collected while the voltage of PMTs that readout the Anti Coincidence Detector (ACD) is lowered. This constraint reduces the livetime by about 15%.

Other pointing strategies can be implemented, either autonomously by onboard decision or from the ground. Both the GBM and LAT can request an automatic repoint to follow a transient phenomenon with a fast time response and by default monitors it for 2.5 hours. The Fermi mission team can also implement specific pointing strategies to maximize exposure for a particular source of interest (target of opportunity), which can be proposed by any member of the community. The satellite can also be pointed at the Earth limb, a bright source of gamma rays generated by comic-ray interactions with the Earth's atmosphere, for scientific or calibration purposes; or pointed toward the Earth to study terrestrial gamma-ray flashes.

3.1.2 Gamma-ray Burst Monitor (GBM)

The GBM monitors the full unocculted sky and covers a energy range between 8 keV up to 40 MeV (Meegan et al. 2009). It consists of two types of detectors: an array of 12 sodium iodide scintillators (NaI) and two bismuth germanate scintillators (BGO). The NaI detectors cover the 8 keV to 1 MeV energy range and are used to determine the directions of bursts. The BGO detectors cover the 200 keV to 40 MeV, positioned on opposite sides of the spacecraft so that any burst is observable by one of them. Over the first 8 years of the mission the GBM generated a total of about 5,000 triggers with about 1,200 classified as solar flares[1].

3.2 The Large Area Telescope (LAT)

The Fermi-LAT is a wide field of view (FoV) imaging telescope for high-energy gamma rays, designed to cover an energy range from 20 MeV up to more than 300 GeV. It is the primary instrument on Fermi, with about 30 times more sensitivity that its predecessor EGRET.

The Fermi-LAT is a pair conversion gamma-ray telescope (Atwood et al. 2009). The strategy for detecting gamma rays rests on two stages: first a precision tracker determining the direction of the incoming photon, and then calorimeter to infer the energy of

[1] Catalog of Fermi-GBM triggers: `https://heasarc.gsfc.nasa.gov/W3Browse/fermi/fermigtrig.html`.

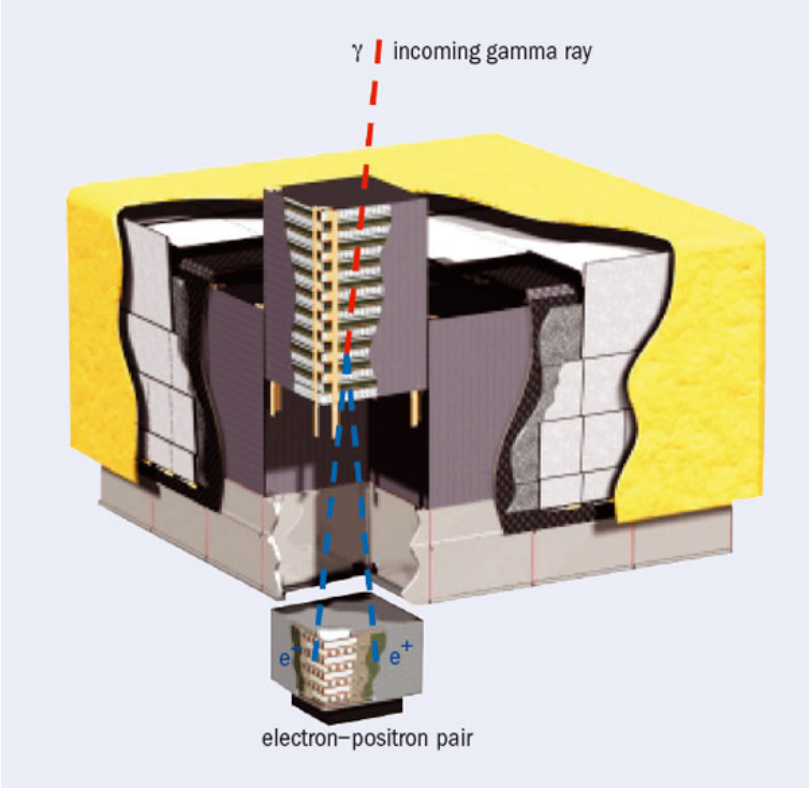

Figure 3.3: Schematic Structure of the Fermi-LAT.

the photon. It is the largest precision tracker ever launched in space, above a cesium-iodide imaging calorimeter. The instrument consists of a modular 4x4 array of tracker and calorimeter vertical modules (See Figure 3.3). All are enclosed in the plastic scintillators of the Anti-Coincidence Detector (ACD) that provides charged-particle tagging for background rejection. The LAT is 0.72 m deep and 1.8 m^2. Its total mass is 2789 kg and it uses 650 W of electric power.

3.2.1 Tracker

Each tracker module consists of 16 layers of conversion material and Silicon Strip Detectors (SSD) that deter the passage of a charged particle. The conversion layer is made of tungsten, a high-Z material maximizing the chance of conversion of a gamma ray into a pair electron-positron (Atwood et al. 2007). Layers of SSD then track the trajectories of the initial electron and positron and the subsequent particle shower. Figure 3.4 shows a single tracker module layer and a schematic diagram illustrating the conversion process. The detector layers alternate in orientation of the strips by 90° providing x and y positions for the electron and positron and the ensuing shower. The classification of events uses the tracker hits to reconstruct the initial direction of the incoming gamma ray. The accuracy of the

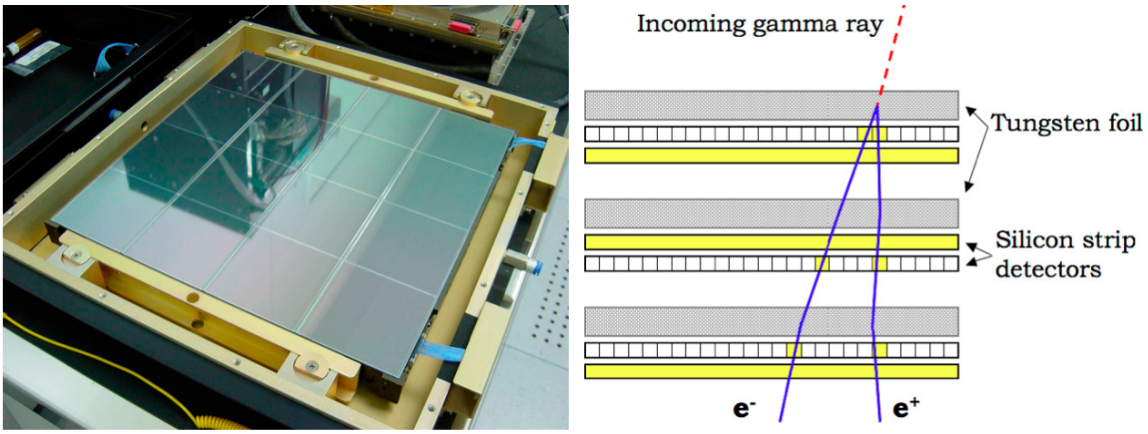

Figure 3.4: LAT Tracker. Left: a single tracker tray. Right: schematics of a conversion into e-/p pair with silicon detectors hits highlighted in yellow (not to scale).

incoming direction determination is limited by multiple scattering of the electron-position pair, especially at lower energies, as well as the intrinsic spatial resolution of the tracker, determined by the spacing of the silicon strips. The location of the initial conversion in the tracker also affects the reconstructing resolution for the gamma-ray event. Tungsten converters in the first 12 layers are each 3% radiation length thick (FRONT section), followed by 4 layers of 18% radiation length each (BACK section).

These sections have intrinsically different Point Spread Function (PSF) due to multiple scattering. On average the PSF for FRONT converting events is approximately a factor of two better than the PSF for BACK converting events.

3.2.2 Calorimeter

The particle shower then reaches the calorimeter made of Cesium Iodine (CsI) which is thick enough (total depth of 8.6 radiation lengths) to give a measurement of the total energy deposited by the entire shower (see Grove & Johnson 2010 for details). Each module consists of 96 CsI crystals in an eight-layer hodoscopic configuration, getting a longitudinal and lateral position of the energy deposition (see Figure 3.5). Photodiodes at each end of the crystal measure the intensity of the light proportional to the energy of the particles in the shower, as well as the asymmetry of the light produced within the crystal to get the third space coordinate of the energy deposit, which gives a 3D profile of the particle shower and is a useful background discriminator.

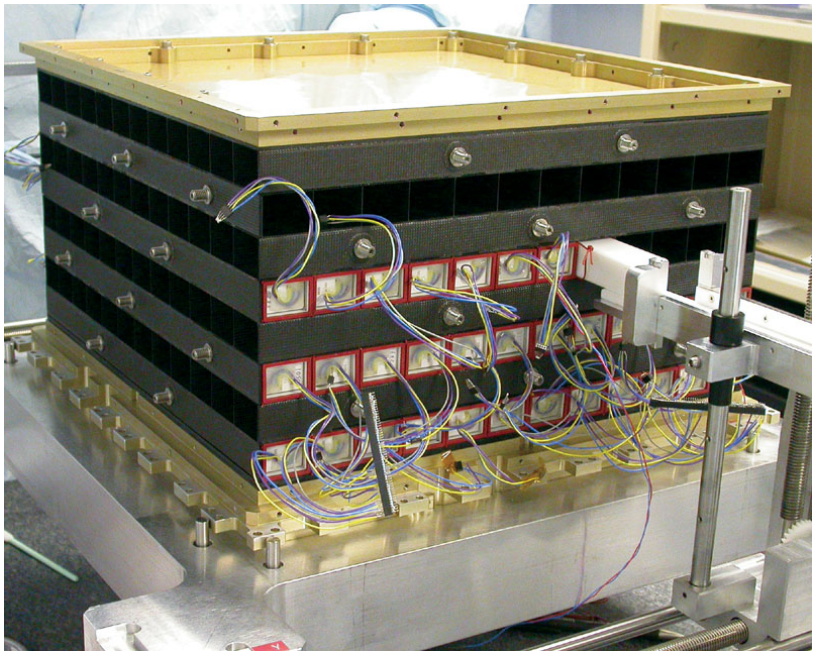

Figure 3.5: LAT Calorimeter.

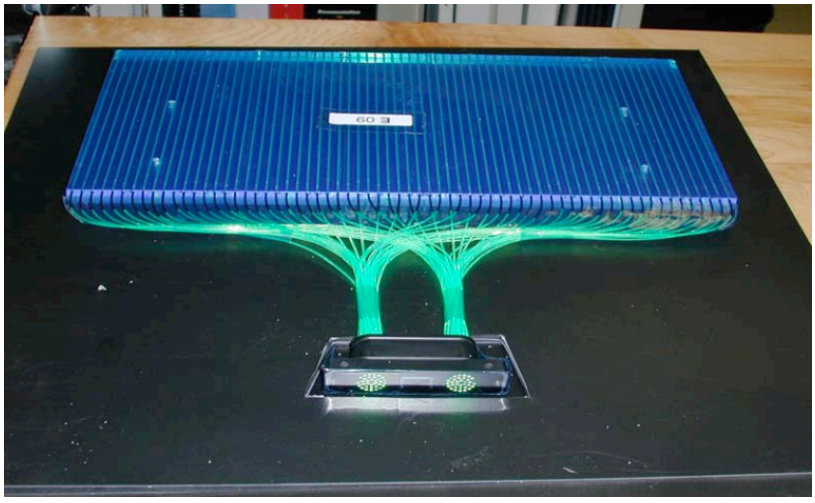

Figure 3.6: ACD Tile: Plastic scintillator with wavelength shifting (WLS) fibers and dual photomultiplier tube (PMT) readout.

3.2.3 Anti Coincidence Detector

The Anti-Coincidence Detector (ACD) is a segmented system of scintillators tiles covering the entire area around the tracker and the sides of the calorimeter. A charged particle incident on the LAT will interact with a scintillator tile and produce light (see Figure 3.6). Its purpose is to reject events detected by the LAT that not gamma rays but charged particles. This is particularly critical since the particle background is a factor 1,000 greater than the rate of gamma rays. Details can be found in Moiseev et al. (2007).

3.2.4 Data Acquisition System and Trigger

The Femi-LAT uses a programmable onboard self-trigger and Data Acquisition System (DAQ) which is a great advance compared to previous gamma-ray observatories (Atwood et al. 2009). The continuous monitoring of the Fermi-LAT tracker, calorimeter and ACD can lead to form a trigger as defined by the criteria chosen in the programmed onboard filters. The tracker is the source of most of the triggers (first level criteria defined by coincidence in three successive layers generally). Upon triggering, the DAQ reads out data from the three subsystems and utilizes the onboard event processing optimized to reduce most events likely triggered by cosmic-rays and maximize the number of events triggered by gamma rays. This first selection is described rather an onboard kill rate, to filer most noise since the average downlink available for the LAT is limited to about 1 Mbps.

3.3 The Fermi-LAT Performance

It is essential to understand the characteristics of the instrument (effective area, energy resolution, angular resolution, background rejection) to infer the temporal, spatial and spectral properties of the high-energy emission of astrophysical sources. The response of the Fermi-LAT in mapping photons to counts is determined by the hardware design, the onboard trigger efficiency, the event reconstruction and the level of background rejection required for the analysis. It is reviewed in details in Abdo et al. (2009) and Ackermann et al. (2012a). The Fermi-LAT performance is summarized by the Instrument Response Functions (IRFs) package, which are functions of photon energy, incidence angle, conversion point within the instrument, and the event quality [2]. A photon refers to the astrophysics radiation with properties independent of the detector (energy E and direction $\vec{v}$ in the Fermi-LAT frame). An event is the detection by the Fermi-LAT instrument of a photon, particle or noise. A count is an event classified by the different analysis filters to be corresponding to a photon. Not all counts are photons and not all photons results in counts.

[2] See `http://fermi.gsfc.nasa.gov/ssc/data/analysis/documentation/Cicerone/Cicerone_LAT_IRFs/IRF_overview.html` for more details

From the onboard trigger and acquisition system, the reading of the ACD, calorimeter and tracker subsystems and downloaded and the first stage of ground processing consists of reconstruction of the different tracks of the particles in the shower through the tracker, the pattern of the energy deposited in the calorimeter and the hits in ACD tiles. A classification algorithm assigns a probability that an event is a photon. This classification can use different sets of cuts, based on tradeoffs between the non-photon background, the effective area and the spatial and energy resolution.

The loosest selection criteria called TRANSIENT are designed for short duration events, such as gamma-ray bursts or the impulsive phase of solar flares, with benefit from increased photon statistics and can tolerate higher background. An intermediate photon selection called SOURCE is most favorable for analysis point sources on medium to long timescales, with a lower background contamination at the expense of a lower effective area than of TRANSIENT. Two cleaner nested event classes, CLEAN and ULTRACLEAN, provide 2 to 4 times lower background rate than the SOURCE event class. They are best suited for the study of the diffuse gamma-ray emission. The effective area for different classes is plotted in Figure 3.9.

3.3.1 Effective Area

The effective area depends on the true energy and direction of the photon as well as the selection criteria for events (see Figures 3.7, 3.8 and 3.9).

In addition, each photon is characterized by its azimuth angle, defined by reconstructed angle of incidence (ϕ) of the event with respect to the +X axis (the line normal to the sun-facing side of the spacecraft). Because of the square shape of the Fermi-LAT, the effective area has an azimuthal dependence with a 4-fold symmetry (see Figure 3.10). The effective area can differ from the azimuthal averaged by 5% typically and more than 10% below 100 MeV or far off axis (incidence angle $> 60^{\circ}$). It is important to account for this dependency for short time observations. The effect averages out for most analysis of sources, over time scales of days and longer. However on scales of minutes and hours, those relevant to solar flare analysis, the effective area values to use for the range of angle for an individual source is not well-represented by the azimuthal average. Moreover, the motion of the spacecraft is specific to the Sun's position: it is optimized for the solar panels to face the Sun as much as possible, and for the battery to be hidden from the Sun to avoid overheating. Thus, the Sun is more or less always observed at the same azimutal angle. Therefore the azimuthal (ϕ) dependence of the effective area of the Fermi-LAT is included when calculating the exposure for the likelihood analysis in order to characterize the spectral parameters of the source.

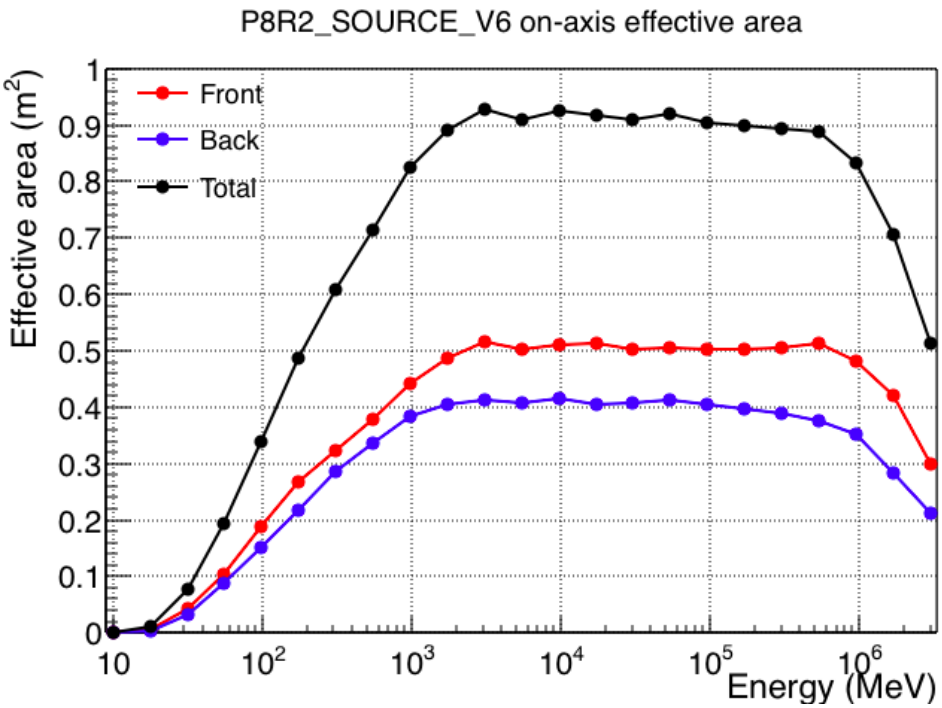

Figure 3.7: Effective Area of the Fermi-LAT as a function of energy for normal incidence photons ($\theta = 0$).

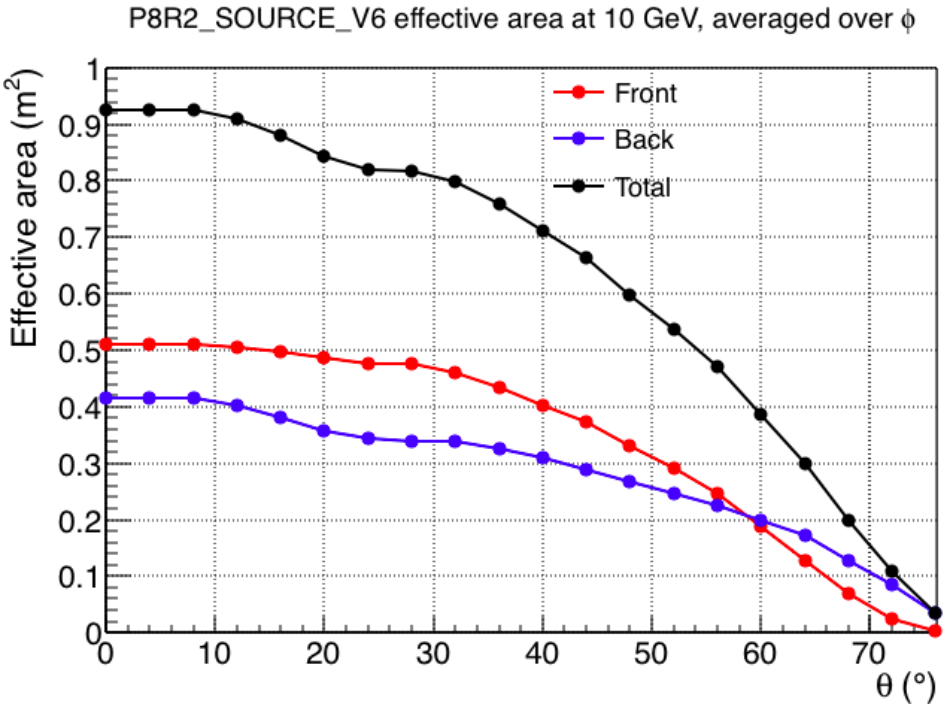

Figure 3.8: Effective Area of the Fermi-LAT as a function of incidence angle theta for 10 GeV photons.

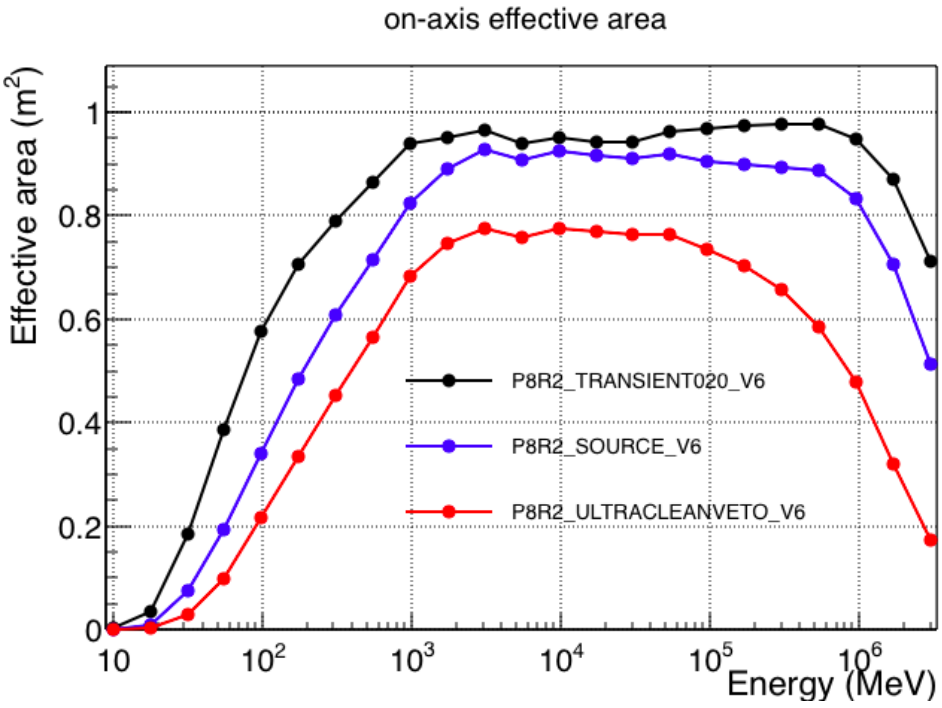

Figure 3.9: Comparison of the on-axis effective area ($\theta = 0$) for different Pass8 event classes (total effective area, combining Front and Back events as shown in Figure 3.7 for the SOURCE event class.

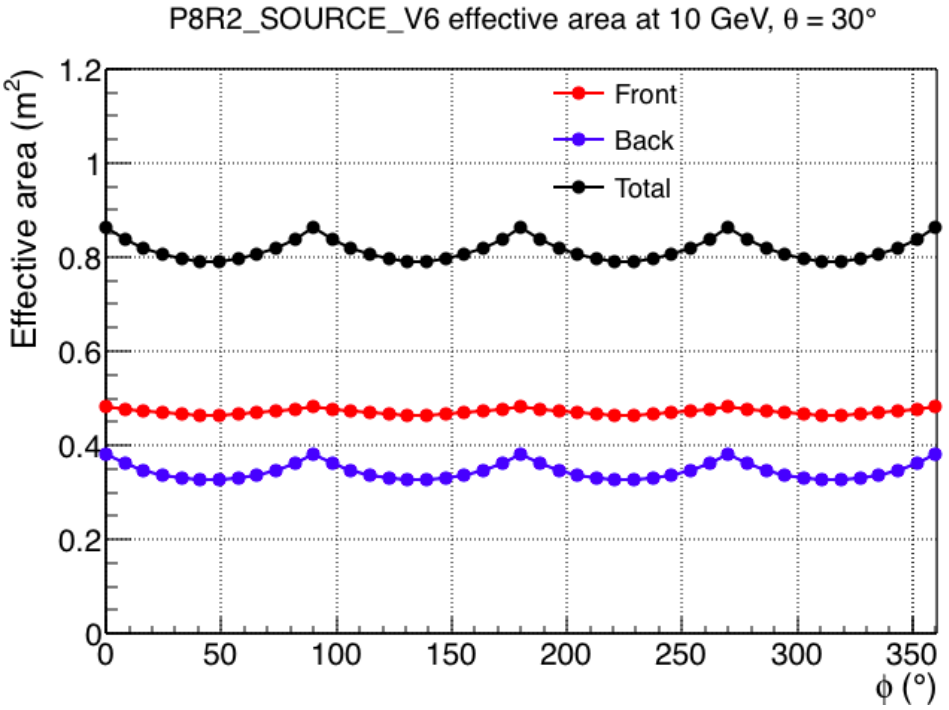

Figure 3.10: Effective Area of the Fermi-LAT as a function of the azimuthal angle ϕ.

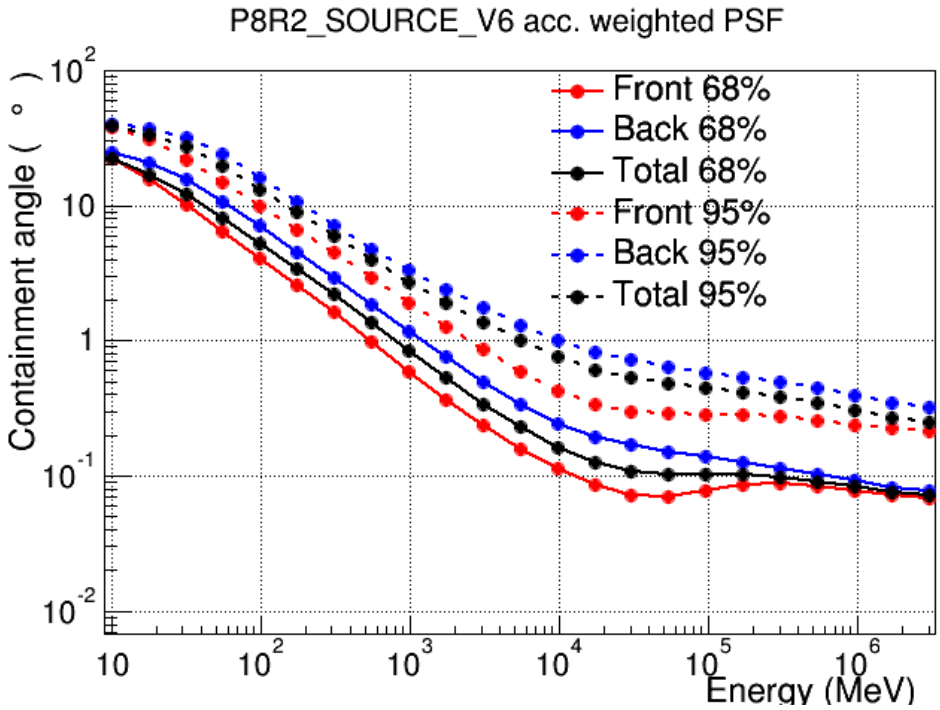

Figure 3.11: 68% and 95% containment angles of the acceptance weighted PSF for both front and back conversion event types.

3.3.2 Point Spread Function

The Point Spread Function (PSF) is derived entirely from MC simulations. Figure 3.11 presents the containment angle of a photon as a function of its energy (at a 68% and 95% confidence levels). The conversion type of the event in the Fermi-LAT tracker affects the PSF as mentioned in Section 3.2.1. The Front-conversion PSF (in red) can be twice as better as the Back-converstion PSF (in blue).

For energies below 300 MeV the angular resolution is limited by multiple scattering in the silicon strip tracking section of the detector and it is several degrees at 100 MeV. The total PSF improves with energy, approaching a 68% containment radius of about 0.1° at the highest energies (when averaged over the acceptance of the Fermi-LAT). It is then limited by the ratio of the strip pitch to the height of the tracker (Atwood et al. 2009). However, since most high-energy astrophysical sources have spectra that decrease rapidly with increasing energy, there are typically fewer higher energy photons with improved angular resolution. Therefore, sophisticated analysis techniques are required to maximize the localization accuracy of Fermi-LAT sources.

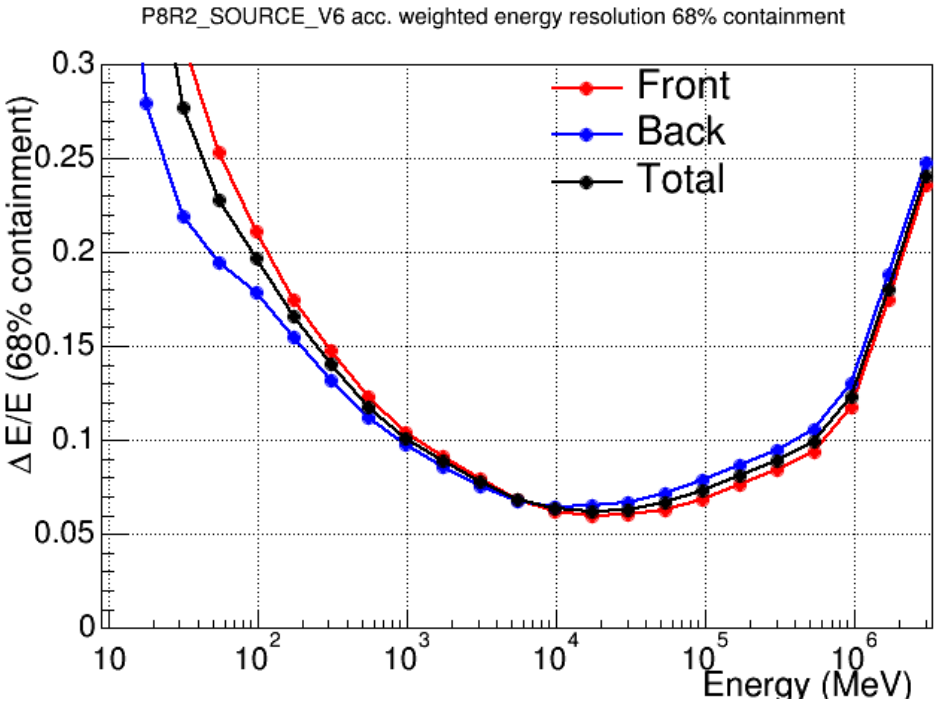

Figure 3.12: Energy resolution (i.e. 68% containment half width of the reconstructed incoming photon energy) as a function of energy.

3.3.3 Energy Dispersion

The energy dispersion of the Fermi-LAT is defined in terms of the fractional difference between the reconstructed energy (E') and the true energy (E) of the events. It depends on both true energy (E) and true incidence angle (θ) (see Figure 3.12). It contributes to the systematic error on the fit of spectral parameters.

Chapter 4

Fermi-LAT Data Analysis

The current framework in gamma-ray astronomy is the maximum likelihood approach first developed by Cash (1979) for astrophysical photon-counting experiments, answering the following questions: What is the probability of obtaining the observed data given a model? How to find the best fit model? How to compare models?

This chapter describes of the maximum likelihood statistical framework employed to search for and analyze gamma-ray sources and the specific aspects of solar flare observations.

4.1 Gamma-ray Source Detection

The process of analyzing gamma-ray astrophysical emission from a source starts with the classification of events as photons and the characterization of their properties by the instrument and processing, as described in the previous chapter. Background estimation from neighboring areas is particularly difficult given the non-isotropic nature of the background. Both because the diffuse component, especially close to the galactic plane, and because of the proximity of sources in the some area of the sky. This complexity require the use of statistical data analysis using the maximum likelihood strategy.

4.1.1 The Maximum Likelihood Method

The likelihood approach for gamma-ray astronomy was first applied to EGRET data by Mattox et al. (1996) and is the primary method to analyze Fermi-LAT data. It consists of evaluating the likelihood $\mathcal{L}$:

$$\mathcal{L}(\text{Parametrized model(x)}) = \text{Probability(data} \mid \text{if the model is true (x))}$$

The probability is usually estimated by binning the data and in each bin calculating the probability of the observed counts given the model. In high-energy gamma-ray astronomy

the data is usually binned in time, space or energy; and a Poisson statistic is needed to calculating the probability in each bin because of the low counts regime.

$$p_i = m_i^{n_i} \ \frac{exp(-m_i)}{n_i!} \tag{4.1}$$

where n_i are the counts observed and m_i are the counts predicted by the model in that bin. The likelihood $\mathcal{L}$ is the product of p_i for all i.

However, binning the data destroys some information and if the bins are chosen small enough, the function becomes more accurate. The number of photons in each bins would be either 0 or 1, and the likehood function results in an unbinned function where j accounts for each photon individually and N_{ph} is the expected number of photons. This approach is best when the number of photons is limited as in the case of solar flares, but becomes increasingly prohibitive for long observations. The logarithm of the likelihood is easier to handle computationally, and in effect the is the quantity maximized.

$$\mathcal{L}_{unbinned} = exp[-N_{ph}] \prod_j m_j \tag{4.2}$$

$$log\mathcal{L} = \sum_j log(m_j) - N_{ph} \tag{4.3}$$

When comparing two models, Model 1 and Model 2, we rely on the likelihood ratio test, or using the more convenient difference of logarithm of maximized likelihoods, which is defined as Test Statistic TS (Mattox et al. 1996):

$$\mathrm{TS} = 2 * \left[log\mathcal{L}(M_1) - log\mathcal{L}(M_2)\right] \tag{4.4}$$

In order to estimate the significance of the source, we use Model 1 with a diffuse and point sources background (called null hypothesis), and Model 2 with the same diffuse components and add the target source. The Wilks' theorem tells us that the probability distribution function of the TS will follow a χ^2_n distribution, where n is the number of fitted parameters used to describe the target source (Wilks 1938). In a typical point source detection analysis we use a threshold of TS=25 for a 5 σ detection.

The likelihood function we use needs to account for the complexity of the Fermi-LAT dataset: the energy-dependent effective area, PSF, energy diffusion, and the pointing history. Assuming a source model describing the gamma-ray sky, fitting the data consists of

maximizing the likelihood function for a given source model $S(E, \vec{v})$,where $\vec{v}$ refers to the celestial directions of the gamma rays. The response of the instrument can be factored in the following components:

1. $A_{eff}(E, \vec{v}, s)$: the effective area which is the product of the cross-sectional geometrical collection area, gamma-ray conversion probability, and the efficiency of a given event selection (denoted by s) for a gamma ray with energy E and direction $\vec{v}$ in the Fermi-LAT frame.

2. $PSF(\vec{v}'|E, \vec{v}, s)$: the PSF which is the probability density to reconstruct an incident direction $\vec{v}'$ for a gamma ray with $(E, \vec{v})$ in the event selection s.

3. $E_{disp} = (E'|E, \vec{v}, s)$: the energy dispersion which is the probability density to measure an event energy E' for a gamma ray with $(E, \vec{v})$ in the event selection s.

We can then compute the predicted photon distribution (using a given event class s) as:

$$M(E', \vec{v}^{\,'}) = \iiint S(E, \vec{v})\ A_{eff}(E, \vec{v})\ PSF(\vec{v}^{\,'}|E, \vec{v})\ E_{disp}(E'|E, \vec{v})\ dEd\vec{v}dt$$

We define the exposure as the integral of the effective area for the time of the observation, accounting for the distribution of observing time in the Fermi-LAT reference frame of any given direction in the sky:

$$\mathcal{E}(E, \vec{v}) = \int A_{eff}(E, \vec{v}) t_{obs}(\vec{v}, t) dt \tag{4.5}$$

4.1.2 Spectral Analysis

For the standard Fermi-LAT point source analysis the source model $S(E, \vec{v})$ is split between the spectral model component and the spatial component. For point source the spatial distribution is a delta function at the position of the point source. The diffuse emission models are described by a spatial template map for the galactic diffuse emission and a uniform distribution for the extragalactic emission.

We model the spectrum of the source dN/dE with different ad-hoc models.The units for the spectral models described below are $\mathrm{cm}^{-2}\ \mathrm{s}^{-1}\ \mathrm{MeV}^{-1}$.

- A Power Law model (PL) defined as:

$$\frac{dN}{dE}(E) = N_0\ E^{\gamma} \tag{4.6}$$

where the normalization N_0 and the index of the power law γ are left free.

- The other model tested is a Power Law with an Exponential Cutoff (EXP) defined as:

$$\frac{dN(E)}{dE} = N_0 \; E^{\gamma} \; exp(-E/E_c) \tag{4.7}$$

The normalization, spectral index and cutoff energy E_c are left free.

To initially test for gamma-ray solar emission from a flare, the Sun is assumed to be a point source with a gamma-ray spectrum described by a power law and we estimate the significance of the source: TS_{PL} as compared to the null hypothesis. In order to estimate whether the addition of the exponential cut-off is statistically significant, we also calculate the TS of the source with the exponential cutoff model : TS_{EXP}. We compare the likelihood ratio between the two model, which is equivalent to calculate $\Delta TS = TS_{EXP} - TS_{PL}$. The significance of the exponential cut-off, with an additional degree of freedom, can be approximated as $\sigma = \sqrt{\Delta TS}$. A threshold of $\Delta TS = 9$ is chosen to select the EXP model as preferred model.

To calculate the Spectral Energy Distribution (SED) the full energy range in split in 10 energy bins and a simple analysis is run in each bin, only fitting the flux of the source and leaving the background parameters fixed to their best values calculated in the source analysis over the entire energy range.

4.1.3 Systematic Errors

Uncertainties in the calibration of the Fermi-LAT introduce systematic errors on the measurements. Effective area uncertainty is dominant, and for the Pass 8 SOURCE event class it is estimated to be ∼10% at 100 MeV, decreasing to ∼5% at 560 MeV, and increasing to ∼10% at 10 GeV and above. For all the results in the following chapters, a 5% systematic error on the flux values should be added to the statistical errors.

4.1.4 Analysis Parameters

We will use the SOURCE class of the Pass 8 event classification which has been tuned to balance statistics with background for point source analysis. We use events between 60 MeV and 10 GeV. Most Fermi-LAT analysis start at 100 MeV, but the particularly soft spectrum of the gamma-ray emission of solar flares peaks at energies of about 100MeV or lower. We also need to cut events generated by Earth limb emission. The limb emission, which results from cosmic rays interacting with the Earth's atmosphere, contaminates the data. A cut is applied to select events only when the entire Region Of Interest (ROI) is contained in a zenith angle smaller than 100°. Other cuts are applied to select good quality

data and the proper Fermi-LAT configuration (as recommended by the Fermi-LAT team). Together they define the Good Time Intervals (GTIs).

The ROI is modeled with a target source and the background elements. We use two templates for the diffuse gamma-ray background emission: a Galactic component produced by the interaction of cosmic rays with the gas and interstellar radiation fields of the Milky Way, and an isotropic component that includes both the contribution of the extragalactic diffuse emission and the residual cosmic rays[1]. We also account for the point sources close to the Sun at a given time using the third Fermi-LAT source catalog (referred as 3FGL for third Fermi Gamma-ray LAT catalog, covering the first 4 years of the Fermi mission Acero et al. 2015).

We fix the normalization of the Galactic component and all the background point sources parameters, but leave the normalization of the isotropic background as a free parameter. We use the ScienceTools version *11-06-00* available on the Fermi Science Support Center web site `http://fermi.gsfc.nasa.gov/ssc/`)

A word on photometric approaches to analyze Fermi-LAT gamma-ray data: for detection of transients, it consists in photon counting during a given time window and dividing that count by the exposure in that window. An estimation of the background is usually calculated by using a separate window when the transient is thought not to be present. It is fast method to confirm the presence of bright gamma-ray emission. However, this method does not permit any optimization of parameters to fit both source and background. Without a comprehensive characterization of the background it hard to estimate the significance of a detection and it is impossible to compute upper limits on the flux of a source. In addition it does not use any information related to the direction of photons and it is impossible to localize a source in the sky. The next section describes in details how the localization study is done using the likelihood statistical approach.

4.2 Localization

The standard tool to study the localization of gamma-ray sources with an unbinned likelihood analysis is the `gtfindsrc` algorithm from the ScienceTools[2]. The standard likelihood analysis is based on sky models with background sources at fixed spatial positions and the best spectral fit for the source of interest. `gtfindsrc` uses a multidimensional minimization of the unbinned likelihood for a grid of positions around an initial guess until the convergence tolerance for a positional fit is reached.

[1] The models used for this analysis, `gal_2yearp7v6_v0.fits` and `iso_p7v6source.txt` , are available at `http://fermi.gsfc.nasa.gov/ssc/data/access/lat/BackgroundModels.html`

[2] Available at `http://fermi.gsfc.nasa.gov/ssc/data/analysis/software/`

However, the observation of solar flares happens over short timescales and can yield an inhomogeneous exposure across the FoV. A better approach in these cases is the use of TS map for localization. A TS map consists of a scan of pixels: within each pixel, the algorithm computes the TS of a test-source added to a given input background model. The values of background sources can be mostly fixed when the search is aimed to locate a new source, such as a flaring source. Or some parameters can be left free when trying to optimize the fit of a complex region with multiple sources close to one another. In this model comparison, a simple power-law model is used for the test-source. The best position is located at the position of the maximum TS. The uncertainty on the position corresponds to a TS drop by a value 2.30 corresponds to a 1 sigma statistical localization error, or a 68% containment radius (4.61 and 9.21 correspond to 2 and 3 sigma respectively).

Figure 4.1 presents the example of two TS maps, computed a solar flare at different time windows: one particularly bright case and the other just above the minimum significance. In these examples, the peak TS values of the maps are very different, but the same procedure is applied. The best position is marked by the black point, and the thin contours mark the different TS drops (2.3, 4.6, 9.2). Those are not always perfectly circular, but a circular error containment region (black circle) provides a good approximation. The extent of the localization error reflect the different significance of the gamma-ray emission: in the first time window the total number of events detected by the Fermi-LAT was 6473, whereas it was a mere 40 events in the second time window presented.

To verify the general quality of the fit, and the correct position of the source, we compute a residual TS map: the target source, here the Sun, is set in the background model to with the best fitted value fixed. Leaving the EG background normalization free, we repeat the TS map procedure with an extra test-source. If the model describes the data correctly there should not be any peak above a value of 9. Above this value, this would mean that the model for the ROI did not accurately describe the data: this can be a misfit of the spectral fit of the sources, or an additional gamma-ray emission component from a new source. Figure 4.2 presents the residual TS map for a single time window. There are no significant residuals, which indicates that the model for this flare accurately describes the data.

Once that position is set, the morphology of a source can be inferred from iterated `gtlike` analyses for different sizes or shapes. A measure of the extension, or upper limit can be inferred from the likelihood profile. However, this procedure is computationally intensive and does not account for a simultaneous fit of the position, extension, and spectrum of the source to find the best fit parameters and to maximize the statistical significance of the detection.

A second maximum likelihood fitting package called `pointlike` was developed in the

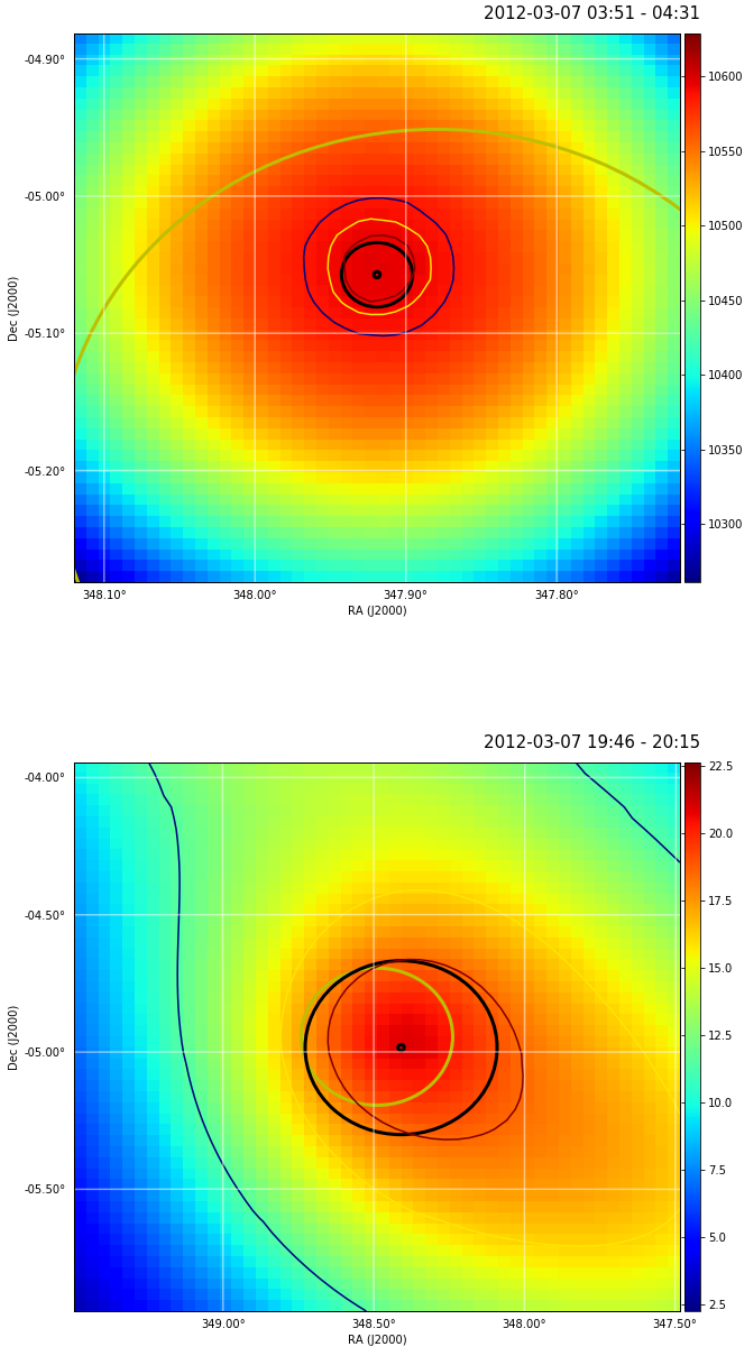

Figure 4.1: TS maps for observations of gamma-ray emission associated with the solar flare on March 7, 2012 (top: 03:51UT ; bottom 19:46UT). Solid yellow circle represents the solar disk. Solid black circle the 68% statistical error. The thin lines track the 1, 2 and 3 sigma contours on the TS map.

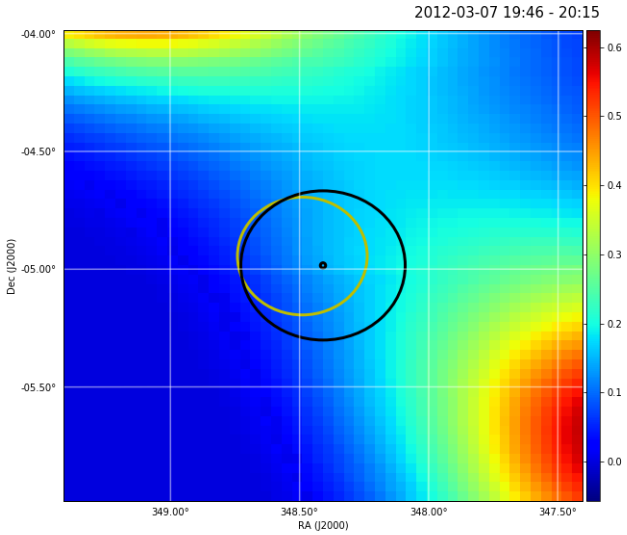

Figure 4.2: Residual TS map for one time window of the solar flare on March 7, 2012 (starting at 19:46UT). Yellow circle represents the solar disk and black circle the position of the gamma-ray source derived from the TS map.

Fermi-LAT Collaboration (Abdo et al. 2010d; Kerr 2011). It is optimized to handle larger numbers of sources efficiently and was used in the development of the Fermi-LAT source catalogs (Acero et al. 2015). It also allows for simultaneous fit of source extension together with the position and the spectral parameters. This approach was used extensivelly in the production of the extended source catalog presented in Lande et al. (2012). Two models are compared: a point source model to a disk model of radius r which is left as a free parameter. The significance of the extension is TS_{ext} is the difference of TS between the best fit extended model and the point model. The choice of a threshold TS_{ext} set to 16 (corresponding to a formal 4 significance) is usually reasonable.

This procedure was attempted to characterize the gamma-ray emission from solar flares, but unsuccessful even with a particularly bright flare. The spectrum of the gamma-ray emission from solar flares is extremely soft compared to other sources: it usually cuts off before 1 GeV, which is usually the minimum energy used the localization and morphology studies.

The Fermi-LAT localization capabilities are limited by some small systematics errors due to the instrument and the spacecraft alignment precision, which have been evaluated to multiplying by a 1.1 scale factor, and then adding 0.005° (18 arcmin) in quadrature to the 95% error radius (Nolan et al. 2012).

4.3 Specificities of Solar Flare Analysis

The study of solar flares with the Fermi-LAT poses some specific analysis challenges that I will describe in the next sections.

4.3.1 Bad Time Intervals

For bright solar flares an intense flux of X-rays during the impulsive phase of the flare can result in pulse pile-up in the ACD scintillators within the integration time of the ACD readout. A coincident gamma ray entering the Fermi-LAT within that integration time can be misidentified by the instrument's flight software or event-classification ground software as a charged particle and thereby mistakenly vetoed. During these periods, the nominal Fermi-LAT instrument response functions do not apply, and the data cannot be analyzed by standard software. These issues were addressed in detail in Ackermann et al. (2012b) for the 2010 June 12 solar flare. The Fermi-LAT instrument team closely monitors for this effect and tags such data as Bad Time Intervals (BTI) through redeliveries to the public data archive[3].

The instrument response functions (used for high-level analysis) does not account for this effect, and the value of the measured flux will not be correct during time intervals with high ACD pile-up, biased toward lower flux. We therefore remove such time intervals in the detailed analysis of standard Fermi-LAT data.

In June 2015, an overall improvement of the Fermi-LAT data was released as Pass 8 (Atwood et al. 2013). The collection of event classes was expanded, with a new transient class tailored to be used for data collected during bright solar flares with reduced pileup effects, named TRANSIENT015S, which will be referred as S15 thereafter[4]. Another strategy which increases acceptance at low energies is described below.

4.3.2 LAT Low Energy (LLE) Analysis

The LAT Low Energy (LLE) technique is an analysis method developed for the spectral analysis of bright transient phenomena, such as GRBs and solar flares in the low energy range of the Fermi-LAT (namely between 30 MeV and 1 GeV). It is presented in details in Pelassa et al. (2010) and the appendix of Ajello et al. (2014). The LLE approach relies on a relaxed event selection compared to the SOURCE data class used in the standard analysis, which is best suited for point sources. As explained in the previous section the Fermi-LAT event rate can be compromised by pileup effects in the ACD during the impulsive phase of

[3] `http://fermi.gsfc.nasa.gov/ssc/data/access/`

[4] In this case, the recommended isotropic diffuse template is tabulated in the `iso_P8R2_TRANSIENT015S_V6_v06.txt` file.

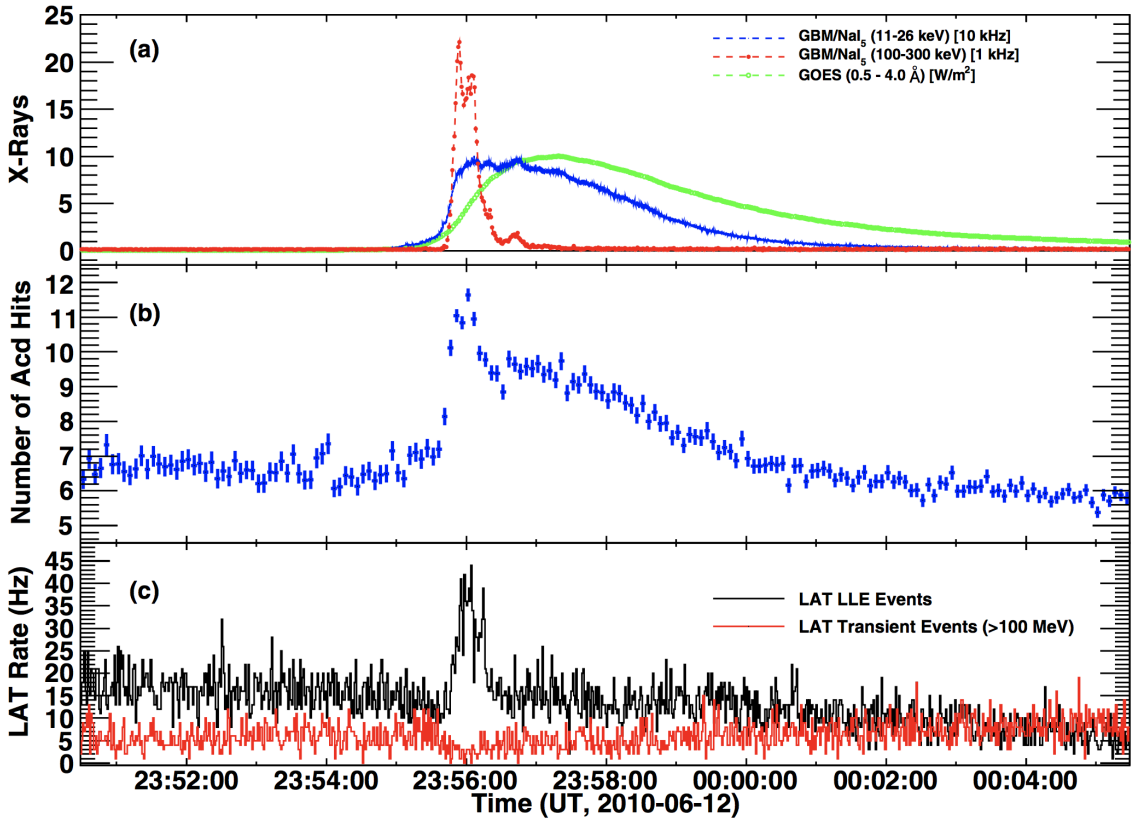

Figure 4.3: Time histories related to the 2010 June 12 solar flare. a) GOES 0.5 – 4 Å in green , and GBM NaI 11-26 keV and 100-300 keV relative rates; b) Fermi-LAT ACD hit rate above 100 keV containing contributions from background, >100 keV solar flare X rays (impulsive peak) and pulse pile up from 10's of keV solar X rays following the NaI 11-26 keV profile in 1a); and c) LLE and Fermi-LAT Transient Class event rates (Ackermann et al. 2012b).

a flare in X-rays. The LLE event selection does not rely on information from the ACD and therefore is not affected by the pileup. As seen in Figure 4.3b the rate of Fermi-LAT ACD hit increases in the same behavior as the X-ray > 100 keV light curve due to pileup. This results in a deficit of events in the transient event rate as plotted in Figure 4.3. Therefore, the LLE method or the analysis with the S15 event class are the only way to obtain reliable measures of the flux for the study of any flares associated with a BTI.

In addition, the LLE analysis achieves a larger effective area in the 30 MeV to 1 GeV band than standard analysis. This event class includes much more noise from the charged particle background, but for the detection of transients on short timescales it can have a better sensitivity than the analysis using S15. We will see in later Chapters that some flares with a very soft spectrum can only be detected using the LLE approach. The LLE approach was first used for solar flare analysis in the case of the M2.0 flare of 2010 June 12 which was exhibited an impulsive emission lasting less than a minute, consistent with the HXR

data seen with the GBM (see Ackermann et al. 2012b). It was also applied to the study of the prompt phase of the two flares on March 7, 2012 (Ajello et al. 2014).

4.3.3 Quiet Sun Emission

The Sun can be very bright in X-ray and gamma-rays during strong flares. However, other high-energy processes are at play, unrelated to any flare activity. Interactions of high-energy hadronic cosmic rays with the solar atmosphere and photosphere produce a quiescent disk emission in gamma-ray (first mentioned by Dolan & Fazio 1965). In addition, the inverse Compton scattering of cosmic ray high-energy electrons off solar photons produces a spatially extended gamma-ray component (Moskalenko et al. 2006). This component is brightest in the region within a few degrees of the Sun but extend up to 20° away from the Sun, where it can be comparable in intensity to the isotropic (presumably extragalactic) gamma-ray background. The flux for both gamma-ray components emission is expected to change over the solar activity. Emissions of matter and electromagnetic fields from the Sun increase during high solar activity, making it harder for cosmic rays to reach the solar system. Cosmic-ray intensity and the quiescent solar emission they cause is lower when solar activity is high.

When the Fermi observatory launched in 2008, it coincided with the minimum of solar activity between solar cycles 23 and 24. Until 2010 when the activity started to pickup, this minimum was the lowest in a century resulting in a high heliospheric flux of cosmic rays. Therefore, the cosmic-ray induced quiescent gamma-ray emission from the Sun is expected to be near its maximum. The analysis the first 18 months of the Fermi-LAT observations presented in Abdo et al. (2011) shows a significant detection and separation of the two components of solar gamma-ray emission. The observed integral flux (> 100 MeV) from the solar disk is $4.6 \pm 0.2^{stat} \pm^{1.0syst}_{0.8} \times 10^{-7}$ cm^{-2} s^{-1}. The observed integral flux of the extended emission from a region of 20° radius centered on the Sun, but excluding the disk itself, is $6.8 \pm 0.7^{stat} \pm 0.5^{syst} \times 10^{-7}$ cm^{-2} s^{-1}. The observed spectrum of the disk component can be well fitted by a single power law with a spectral index of 2.11 ± 0.73.

We need to account for these emissions in the analysis of gamma-ray solar flares. However, on the small time windows we use for flares, the background is relatively low, with sometimes just a few photons being identified to background. Therefor, we only include the disk component as a point source and let the isotropic background free to account for the additional inverse Compton effect.

These flux values for the quiet Sun emissions are computed during the solar minimum and are expected to be a slight overestimation of the actual flux when the solar activity increases. Further study would estimate this variation as a function of time and could be

included in the background models for the relevant flares. Preliminary results for the first seven years of observations with the Fermi-LAT presented in Rainó et al. (2017) show an evolution of the flux from the disk component, anti-correlated with the solar activity.

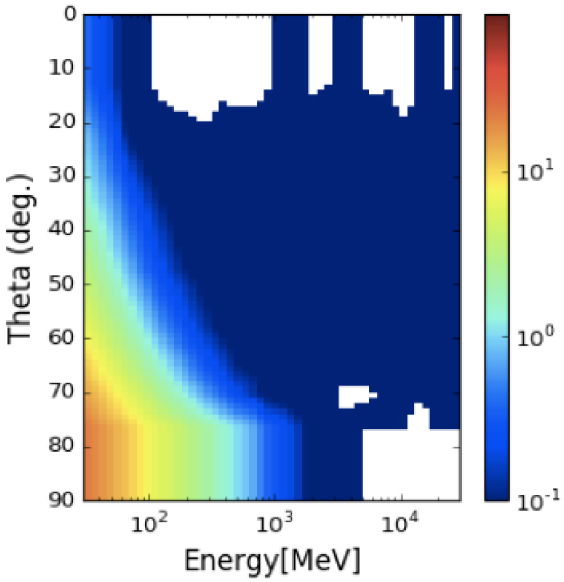

Figure 4.4: Fisheye correction simulations: color scale indicates the magnitude of the correction to apply to (in degrees), as a function of the true incidence angle of the photon (θ) and its true energy.

4.3.4 Localization and Fisheye Effect

The fisheye effect is a selection bias in the Fermi-LAT trigger and reconstruction algorithms. At low energies and high-incidence angles, particles that scatter toward the Fermi-LAT boresight (having a smaller apparent incidence angle) are reconstructed with higher efficiency than particles that scatter away from the Fermi-LAT boresight (having a larger apparent incidence angle). The reconstructed position of the source biased and appearing closer to the boresight axis than its true position. The fisheye effect is estimated using Monte-Carlo simulations. The correction depends both on the true incidence and the energy of the particle. Of course it varies from event to event in the simulation, but the mean correction is plotted in Figure 4.4. The correction becomes dramatic at energies below 100 MeV and incidence angle greater than 70°, reaching several degrees shift. This will prompt us to only consider the photons above 100 MeV when performing the localization study.

The correction of the fisheye effect is crucial particularly for bright flares, when the statistical error on the position becomes smaller than 0.1° and the uncertainty becomes dominated by systematics. We study the effect of the fisheye effect correction on two cases of bright emission from solar flares. We use different minimum energy threshold to quantify

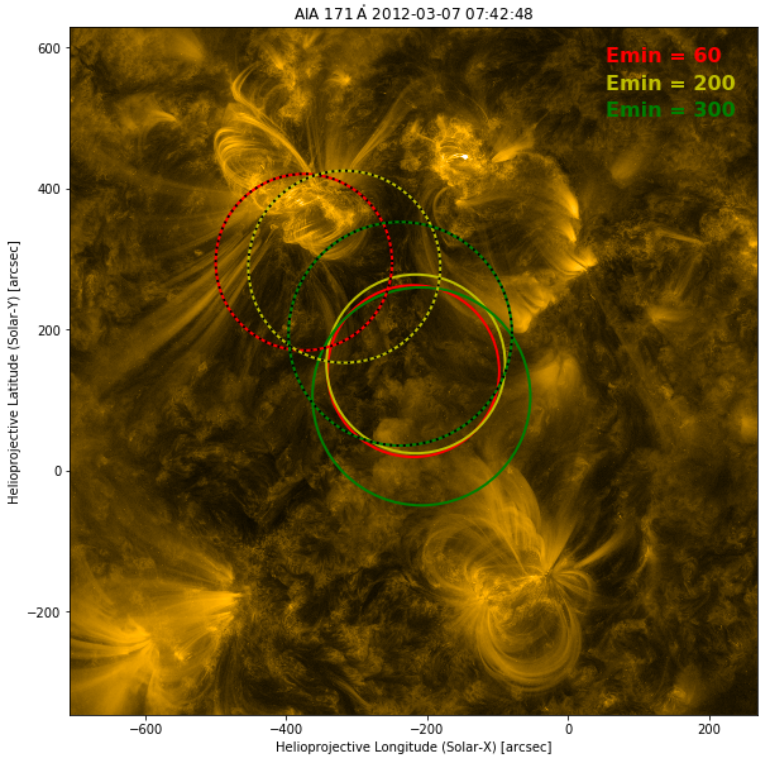

Figure 4.5: Comparison of the localization between fisheye corrected (solid line) and not corrected (dashed line) at different energy thresholds for a time window of a bright solar flare (2012-03-07).

the amplitude of the correction and the systematic error it induces. The amplitude of the fisheye correction decreases with energy. So we expect the distance between the corrected and uncorrected positions to decrease with energy. This is indeed what we observe on Figure 4.5: the correction is the largest above a 60 MeV minimum energy, and above 300 MeV the two positions are consistent.

For most other gamma-ray sources observed by Fermi (blazars, pulsars), the localization is best characterized when setting a minimum energy above 500 MeV or energy 1 GeV, where the PSF is about 0.1°. However in the case of most solar flares, the gamma-ray emission shows such a soft spectrum, turning over at energies just above 100 MeV, that the localization error (statistical) does not really improve as the threshold energy is increased, as can be seen in an example in Figure 4.5, where the statistical error on the localization above 300 MeV (green) is larger than the one above 60 MeV (red). In another example in Figure 4.6 shows a situation a bit more complex. If the gamma-ray emission is coming from a point source, the corrected positions should be consistent with any minimum energy threshold chosen. We observe that the 68% error circles corresponding to the $>$ 60MeV and $>$ 300MeV positions only overlap by half. They are still consistent, but this could indicate that the systematic error due to fisheye correction is as large as the distance between those

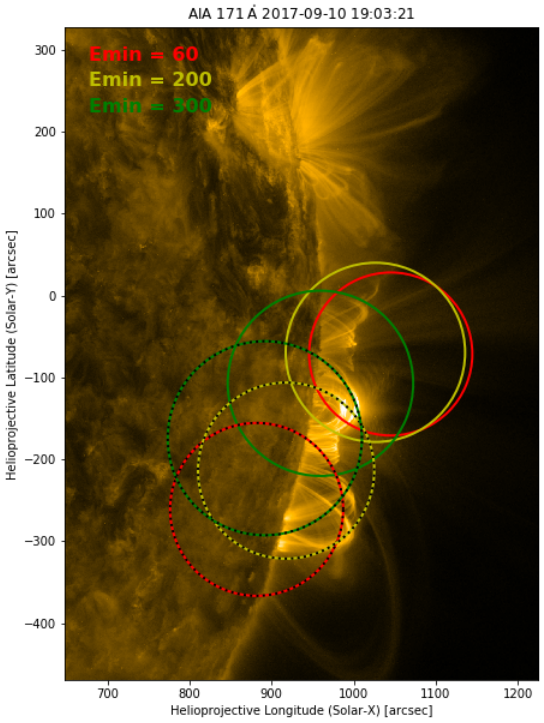

Figure 4.6: Comparison of the localization between fisheye corrected (solid line) and not corrected (dashed line) at different energy thresholds for a time window of the 2017-09-10 flare. Each circle marks the 68% statistical containment radius.

two points. If our assumption of a point source is wrong, these results could indicate that the source has a spectral dependent morphology, where the true position of the gamma-ray emission below 100 MeV is slightly different than the position of the $>$ 300MeV emission.

4.3.5 Solar Flares Spectral Analysis

The hadronic component of the gamma-ray emission observed by the Fermi-LAT above 60 MeV, or the nuclear components observed by the GBM can be represented by a template based on a detailed study of nuclear gamma-ray production from accelerated-particle interactions with elements found in the solar atmosphere (Murphy et al. 2007).

Such templates depend on the energy and pitch angle distributions and composition of the accelerated-particle population. It also depends on the assumed ambient composition which can be inferred from the ratio of the nuclear lines in the 4-12 MeV range. A detailed study of the nuclear lines is not covered by this work and we used a arbitrary templates based on earlier studies (updated from Murphy et al. 1987). The accelerated particles are

assumed to interact in a thick target with a coronal composition (Reames 1995), but with $He/H = 0.1$. They do not take into account transport effects but instead assume that the accelerated particles have a power-law differential spectrum ($dN_p/dE \propto E^{-\beta}$ with β as the proton index), coronal elemental abundance (with an accelerated α/p ratio of 0.2), and that the angular distribution of the radiation is isotropic. The templates library cover proton indexes from 2 to 6 in increments of 0.1.

The spectral analysis using templates for the pion emission from protons is a good way to characterize the proton distribution, with the following caveats. The proton spectrum is solely described with a power-law distribution. Secondary emission from charged pions decaying into electron and positrons producing bremsstrahlung could influence the spectrum in the lower part of the Fermi-LAT range. Below 10 MeV, the proton and ion spectrum is best evaluated by the relative intensities of the nuclear lines and the 2.223 MeV neutron capture line.

To evaluate whether these models provide a good fit to the data, a likelihood analysis is computed for each template of the entire set. However, the TS values of the template fits can not be directly compared to the TS a power law model, or an exponential cutoff model because the models are not nested (Wilks 1938). Since the exponential cutoff model approximates the curvature of the pion-decay spectra we expect that if the exponential model is preferred, the template model also provides a good fit. In Figure 4.7, the spectrum of a bright solar flare is shown, with the best fits for the different spectral models: Power Law, Power Law with an Exponential Cutoff, and the best fit pion template. In this case, the Exponential Cutoff model is clearly preferred, but we can observe that the pion template fits the data even better.

Following the likelihood statistical approach prescribed in Section 4.1.2, if the exponential cutoff model provides a significantly better fit than the power law ($\Delta\mathrm{TS} > 9$), we also fit the data with the templates models to determine the best proton spectral index following the same procedure described in Ajello et al. (2014). We constructs a log-likelihood profile for the range of proton spectral indices. In clear cases, the distribution marks a minimum for the preferred spectral index. We fit that resulting profile of the log-likelihood values with a parabola and determine its minimum ($\mathcal{L}_{\min}$) and the corresponding value s_0 as the maximum likelihood value of the proton index. The 68% confidence level is evaluated from the intersection of the profile with the horizontal line at $-2\,\Delta\log(\mathcal{L}_{\min}) + 1$. The insert of Figure 4.7 shows the likelihood profile built for the each pion template model, and the fit to this profile gives the preferred proton index value at 4.70 ± 0.07.

As mentioned in Section 4.2 on the localization, a good way to make sure the best

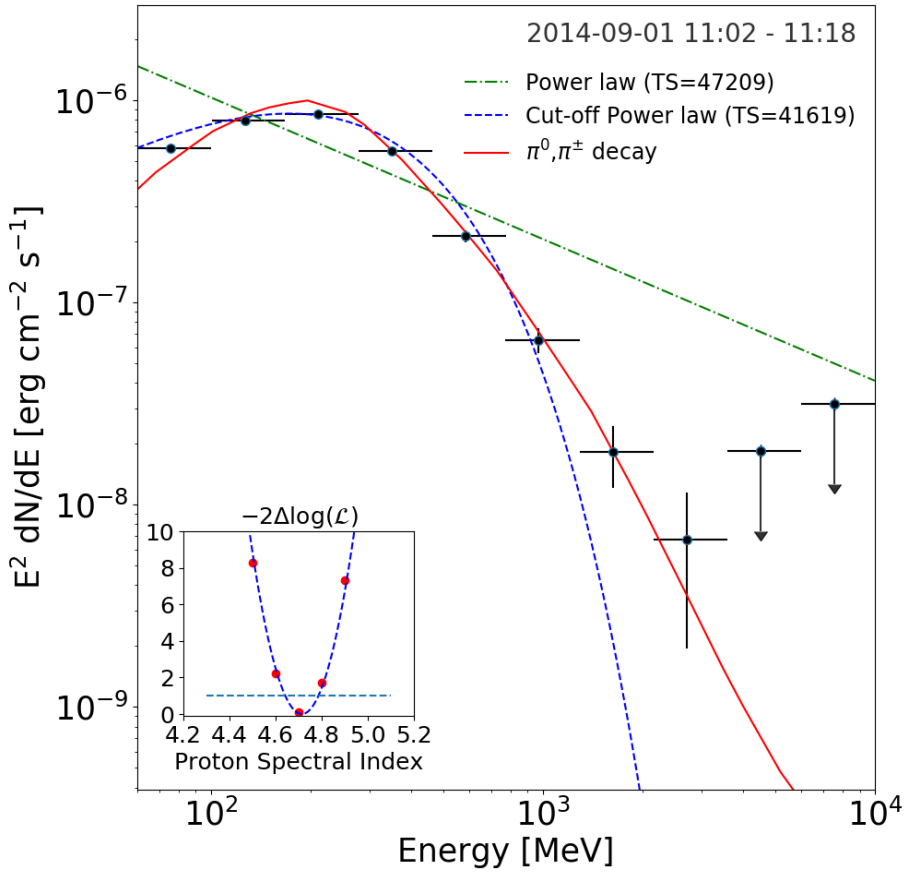

Figure 4.7: Spectral energy distribution for a bright flare (Sept 2014): the best fits for the spectral models (Power Law, Power Law with an Exponential Cutoff, best fit pion template) are shown (in green, blue and red respectively). The insert shows the likelihood difference between the likelihood value of the best fit template index and the likelihood values of each of the other template indexes. The likelihood profile is fitted with a parabola to estimate the best proton value and its statistical error: 4.70 ± 0.07 in this case.

fit model accurately describes the ROI is the making of residual TS maps. In the case of the bright flare presented in this section, the TS map showed a significant residual (in Figure 4.2), which is the indication of an issue of the modeling of the ROI. For this bright flare, the model chosen for to make the residual TS map was the best ExpCutOff fit (compared to PL). But this flare was so bright that the difference between the best ExpCutOff and the best pion template actually mattered.

In Figure 4.8, the residual TS maps for the ExpCutOff and template models are compared. When the best model for pion emission is used, there are no significant residual and the ROI is correctly fitted, confirming that the residual present was not associated with a new gamma-ray source in addition to the solar flare fitted with a point source.

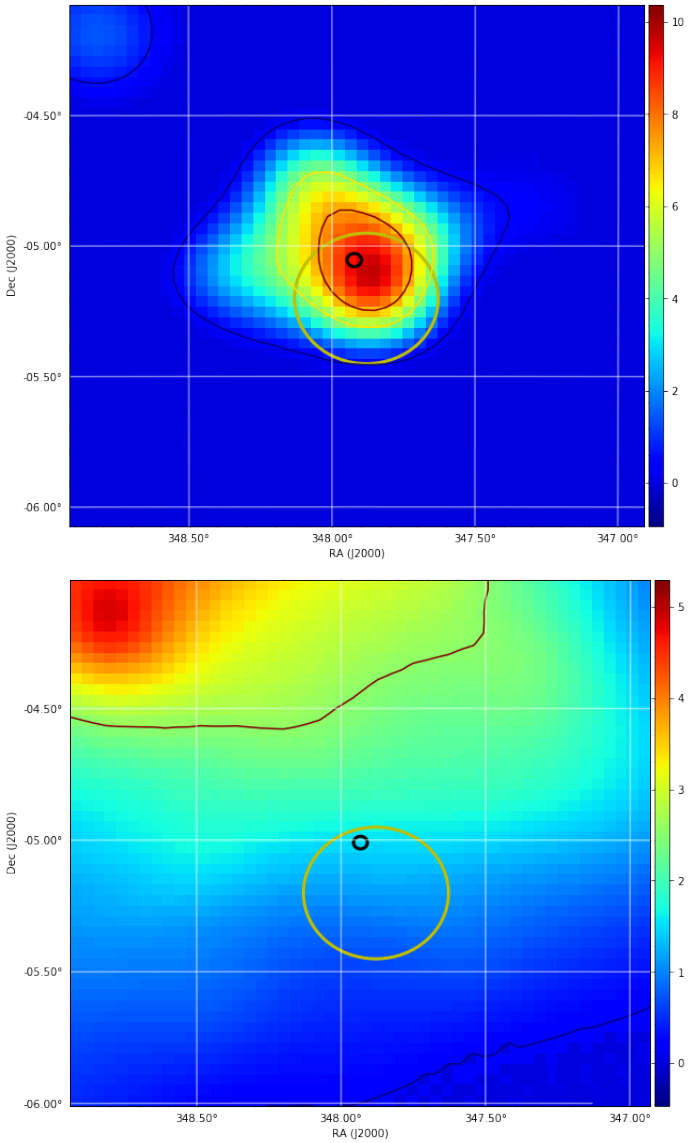

Figure 4.8: Residual TS maps for the same time window on March 7, 2012. Two different spectral models are chosen for the emission from the solar flare: Exponential with a cutoff (top panel); Pion template on the right (bottom panel). The position of the gamma-ray source is shown in black.

4.3.6 Intrinsic Motion of the Sun

The maximum deviation of the true position of the Sun during a 30 minutes time window due to its apparent motion is less than 2.5 arcmin. To compare, the 68% containment angle of the direction of a single photon at normal incidence at 1 GeV is 0.8° and at 100 MeV is 6°. As we will see in the next chapter, for a typical bright solar flare the localization uncertainty is of the order of 40% of the solar radius, so about 12 arcmin. It is therefore not necessary to apply a correction to account for the motion of the Sun from the center of the

ROI. However, for a solar flare detected in consecutive time windows, the time integrated analysis needs to account for that proper motion. A dedicated "Sun-centering" analysis tool for moving sources was developed. It transforms the directions of all the gamma-rays into ecliptic coordinates and then translate them into ecliptic longitude to keep the Sun at position (0,0) as time passes. The same operation is applied to the pointing history of the Fermi-LAT to keep an accurate account of the exposure. In Sun-centered coordinates the choice of background model used for the standard model can not be used. We approximate the background as an isotropic template. The galactic diffuse emission from cosmic rays interacting with the interstellar medium and radiation field is far from isotropic, but on short time scales it can not be spatially resolved. We do not include background point sources from the 3FGL catalog, which are rarely resolved during such short timescales (appart very few cases for which we will not apply this procedure). We confirmed that fitting a isotropic template to the data with a free normalization coefficient provides a good representation of the backgrounds.

Chapter 5

Notable Solar Flares

From the unprecedented number of gamma-ray solar flares observed by the Fermi-LAT throughout cycle 24, some stand out that are brighter or longer duration than ever detected before, or even exhibit new behaviors. This opens a new window in the field of high-energy solar physics that may provide new insights into the physics of solar flares.

Some flares have already been the object of independent publications by the Fermi-LAT collaboration. The first gamma-ray detection of the impulsive phase of a M2.0 flare on June 12, 2010 was presented by Ackermann et al. (2012b). A second publication followed with the analysis of the first two flares detected by the Fermi-LAT over more than 2 hours: the 2011-03-07 and 2011-06-07 flares are described in details in Ackermann et al. (2014) as well as a first attempt at a list of flares detected by the Fermi-LAT from August 2008 to August 2012. Two flares stood out

In this Chapter I will present details on two of the brightest and longest flares which happened on March 7, 2012 and on September 10, 2017. They were each the focus of dedicated articles: Ajello et al. (2014) and Omodei et al. (2018). I will also present the results of the analysis of the behind the limb flares detected by the Fermi-LAT, also studied by Pesce-Rollins et al. (2015) and Ackermann et al. (2017).

5.1 March 7, 2012 Flares

On March 7, 2012 the solar activity increased dramatically with two bright X-class flares associated with gamma-ray emission detected by the Fermi-LAT for more than 20 hours. For that day, the Sun dominated the gamma-ray sky, outshining the brightest gamma-ray source, the Vela pulsar, by nearly a factor of 100. This extraordinary detection was illustrated by the Astronomical Picture of the Day on March 15, 2012[1] (Figure 5.1).

[1] `http://apod.nasa.gov/apod/ap120315.html`

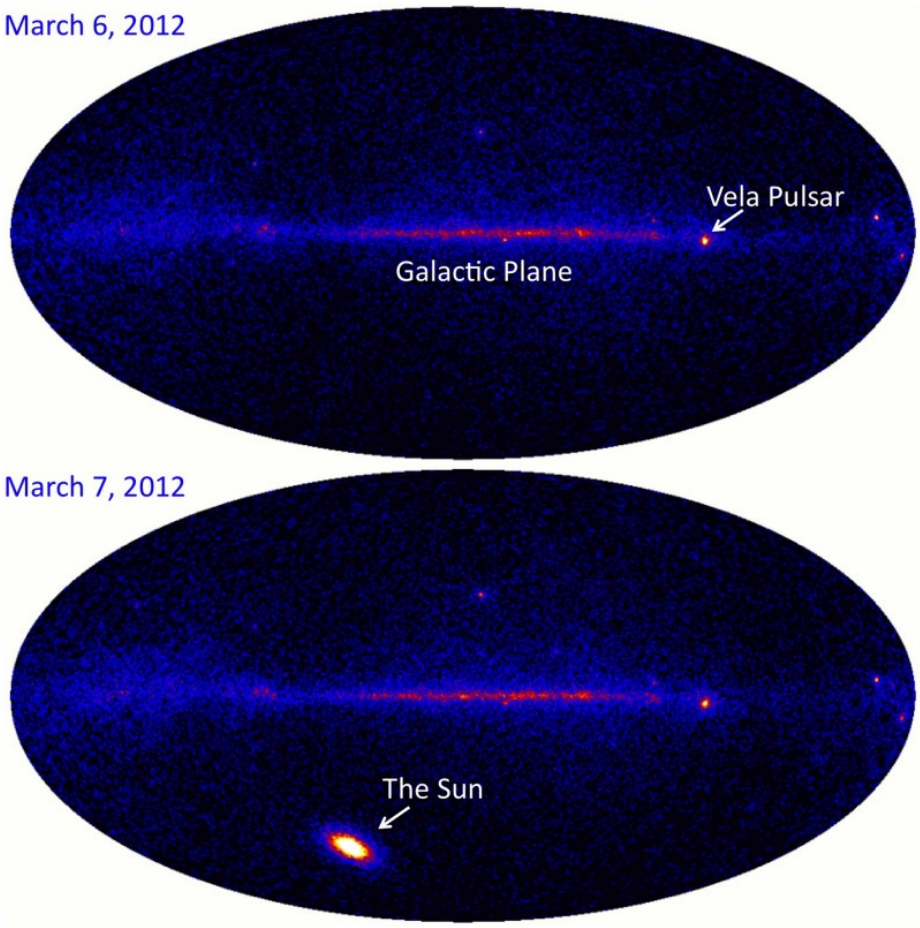

Figure 5.1: Comparison of the full gamma-ray sky on March 6 with March 7, 2012.

By its remarkable length and brightness, the observation of this flare enables the investigation of several aspects of high-energy processes happening in solar flares that were not previously accessible. In this section we present the details of the long-duration high-energy gamma-ray observations of the intense X-class solar flares of 2012 March 7 by the Fermi-LAT and other instruments dedicated to solar physics.

5.1.1 X-rays

On 2012 March 7, two bright X-class flares erupted from the very complex Active Region #11429, located at position near N18E31, or (-260",380"). This same active region was extremely prolific, producing solar flares that were also detected above 100 MeV by the Fermi-LAT on March 5, 9 and 10, 2012.

The two X-class flares peaked within an hour of each other, marking March 7, 2012 one of the most active days of Solar Cycle 24. The first flare, a X5.4 class, started at 00:02

UT and reached its maximum intensity at 00:24:00 UT while the second X1.3 class flare occurred at 01:05UT, reaching its maximum 9 minutes later. They will be considered as one gamma-ray event with recurrent activity. The evolution of the Soft X-rays is presented in Figure 5.2 in both the 0.5 – 4.0 Å and the 1.0 – 8.0 Å GOES bands.

Some intense HXR emission was observed by the Fermi-GBM during the impulsive phase although this phase was only partially observed by the Fermi-GBM. The orbital sunrise occurred less than six minutes after the peak of the first flare, triggering the GBM at 00:30UT. Non-thermal emission up to 300 keV was observed in the decaying phase of the first X5.4 flare. The second X1.3 flare was observed in its entirety and showed a sharp peak of non-thermal emission up to 300 keV and a possible detection in the BGO in the 1-10 MeV range. The first two panels of Figure 5.6 show GOES and GBM data during the impulsive phase. A full analysis of these HXR observations is beyond the scope of this work, but it is worth noting that this powerful flare was very efficient in accelerating electrons and yielded a potential nuclear signal in the MeV range. Unfortunately RHESSI was not observing the Sun during the impulsive phase of either of these two flares.

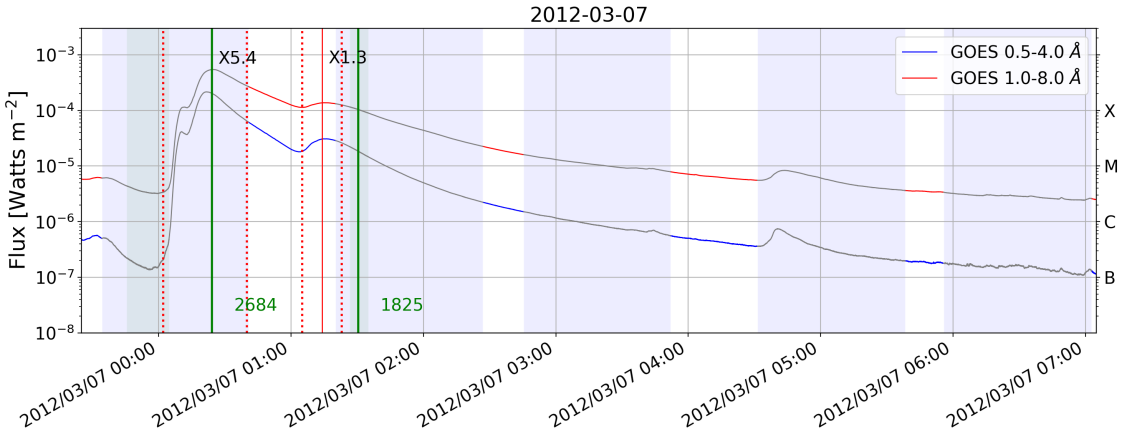

Figure 5.2: GOES light curve for the bright March 7, 2012 flares and the 7 hours following. The blue shaded regions indicate that the Sun was not observable by the Fermi-LAT at those times. The light green shaded regions indicate the time when Fermi is in the SAA. The red vertical lines indicate the peak of the GOES flare (solid red) and the start and end of the GOES flare (dashed red). The vertical green lines show the appearance time of the two very fast CMEs associated with those flares (at 2 solar radii).

5.1.2 SEP and CME

The combination of these two flares was associated with a very strong Solar Erupting Event. Two very fast CMEs started shortly after each flare with initial speeds of 2685 and 1850 km/s respectively (see LASCO catalog described in Section 2.3. The estimated onset time

place them around 00:17UT for the first one and between 00:56 and 01:04 for the second one (see vertical green lines in Fig 5.2). This first CME is the second fastest of the entire solar cycle 24. Very strong fluxes of Solar Energetic Particles, and in particular protons, were observed.

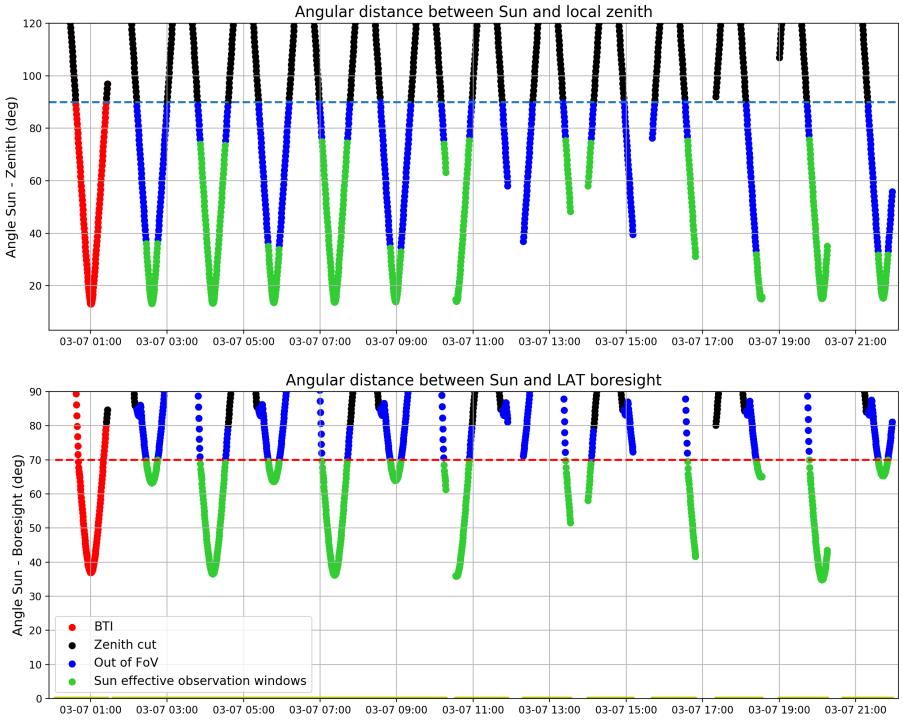

Figure 5.3: Observation profile of the Sun during the March 7 2012 solar flares, showing the position of the Sun throughout the entire observation of gamma-ray emission. The green intervals indicate the effective times of data collection for our analysis. The gaps in between reflect the motion of the Sun in and out of the FoV as well as the zenith and SAA cuts. The red interval shows the time range when data was collected but was affected pile up effect and classified as Bad Time Intervals. Top panel: angular distance between the Sun and the Earth's limb; Bottom panel: angular distance between the position of the Sun and the Fermi-LAT boresight direction.

5.1.3 Fermi-LAT Gamma-ray Data

Fermi had very good coverage of the flares after the impulsive phase. The entire observation profile for this flare is shown in Figure 5.3. This Figure shows the evolution of the position of the Sun with respect to the Earth's limb position as seen by the Fermi-LAT (upper panel) as well as the angle between the position of the Sun and the Fermi-LAT boresight direction (bottom panel). At normal incidence (small boresight angle) the effective area is maximum

	Time on 2012-03-07	Exposure (minutes)	Flux	TS	ΔTS	Photon Index	Proton Index	Average Boresight
a)	00:40 - 01:20	40	232.6 ± 8.23*	75611	-	-	3.87 ± 0.02	50
b)	02:26 - 02:45	18	75.05 ± 2.62	2377	117	-	3.77 ± 0.10	66
c)	03:51 - 04:31	40	95.09 ± 1.18	21100	1459	-	4.01 ± 0.05	50
d)	05:38 - 05:55	18	97.34 ± 3.24	2675	249	-	4.51 ± 0.13	66
e)	07:02 - 07:42	40	62.79 ± 0.98	12829	1210	-	4.71 ± 0.07	50
f)	08:49 - 09:06	17	49.76 ± 2.47	1181	123	-	5.17 ± 0.24	66
g)	10:14 - 10:54	25	26.75 ± 0.87	2803	344	-	5.28 ± 0.17	52
h)	13:24 - 14:04	13	8.58 ± 0.93	258	31	-	5.71 ± 0.60	62
i)	16:35 - 16:48	13	1.54 ± 0.32	49	10	-	>6	55
j)	18:23 - 18:32	9	2.20 ± 0.74	25	8	-2.91 ± 0.41	-	66
k)	19:46 - 20:15	29	0.26 ± 0.08	22	3	-2.37 ± 0.30	-	45

Table 5.1: Evolution of spectral parameters of the gamma-ray emission during the 2012-03-07. Columns: 1) Start and end time of each time window on 2012-03-07 (UT); 2) Exposure in minutes, defined as the effective duration of observation (accounting for time loss due to the SAA); 3) Flux averaged over the time window computed for the preferred spectral model (unit (10^{-5} $cm^{-2}s^{-1}$ between 100 MeV and 10 GeV); 4) TS value for the Power Law model; 5) Difference of TS between EXP and PL models, a value above 9 indicates the EXP is favored; 6 and 7) give the best fit photon index for a PL model or the best fit proton index from the pion fit if the EXP model is preferred; 8) Average angle between the Sun and the LAT boresight axis (* indicates that the Fermi-LAT response was affected by pile-up, and the S15 event class is used for the analysis).

and the PSF is minimized. As the Sun moves far off-axis, the sensitivity drops and the fisheye effect increases.

The color codes the different cuts applied to the data. The position of the Earth limb with respect to the Fermi-LAT greatly affects the background level, and a cut is set the source to be below a zenith angle of 90°. We also apply a 70° cut on the boresight angle. The effective time intervals that were considered for our analysis are highlighted in green. The Fermi-LAT data is not collected while the satellite is in the SAA resulting in some small gaps around 10:30UT and 13:30UT. In red we show the times when the Fermi-LAT was affected by pile-up during the impulsive phase of the flares, as explained in section 4.3.1. For these intervals the Fermi-LAT event class specific to solar flares is used.

During the entire duration of the gamma-ray emission the Sun came in and out of the FoV every orbit, with an asymmetrical profile. It was only visible at high-incidence angle for a relative short amount of time in every other time windows (such as the time window starting at 02:26UT, lasting only 18 minutes with an average boresight angle of 66°). Exposure and average boresight angle are given for each interval in table 5.1 in the second and last columns.

Gamma-ray emission was detected by the Fermi-LAT for almost 20 hours after the peak of the first X-ray flare in a total of 11 individual time windows. The gamma-ray intensity associated with these flares was so intense that we can analyze both the spectral and spatial characteristics of the gamma-ray emission as a function of time, for both the long duration

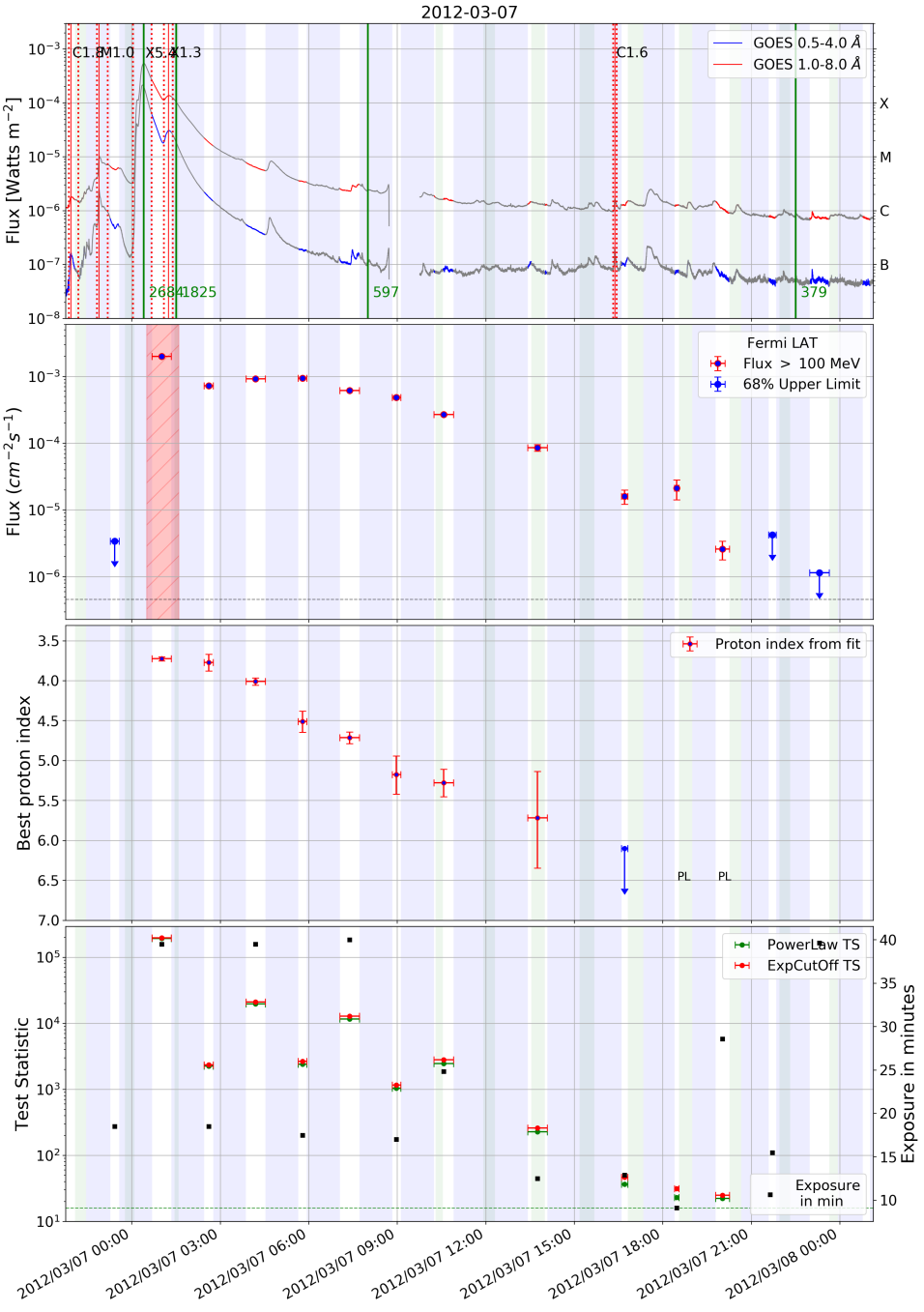

Figure 5.4: Composite lightcurve for the entire duration of the gamma-ray emission for the 2012-03-07 flare. Top panel: GOES lightcurve (full description of shaded areas and vertical markers in Figure 5.2). Second panel: Time evolution of the averaged gamma-ray flux in each time window (values in Table 5.1). The red shaded area indicates the time range when the Fermi-LAT was affected by pile-up, caused by the intense soft X-ray emission. The S15 event class is used for that first window. Third panel: best fitted proton distribution index (with 68% statistical error). Bottom panel: TS values of the gamma-ray source (red and green for the Power Law and Power Law with Exponential Cutoff models respectively); Exposure of each time window (black).

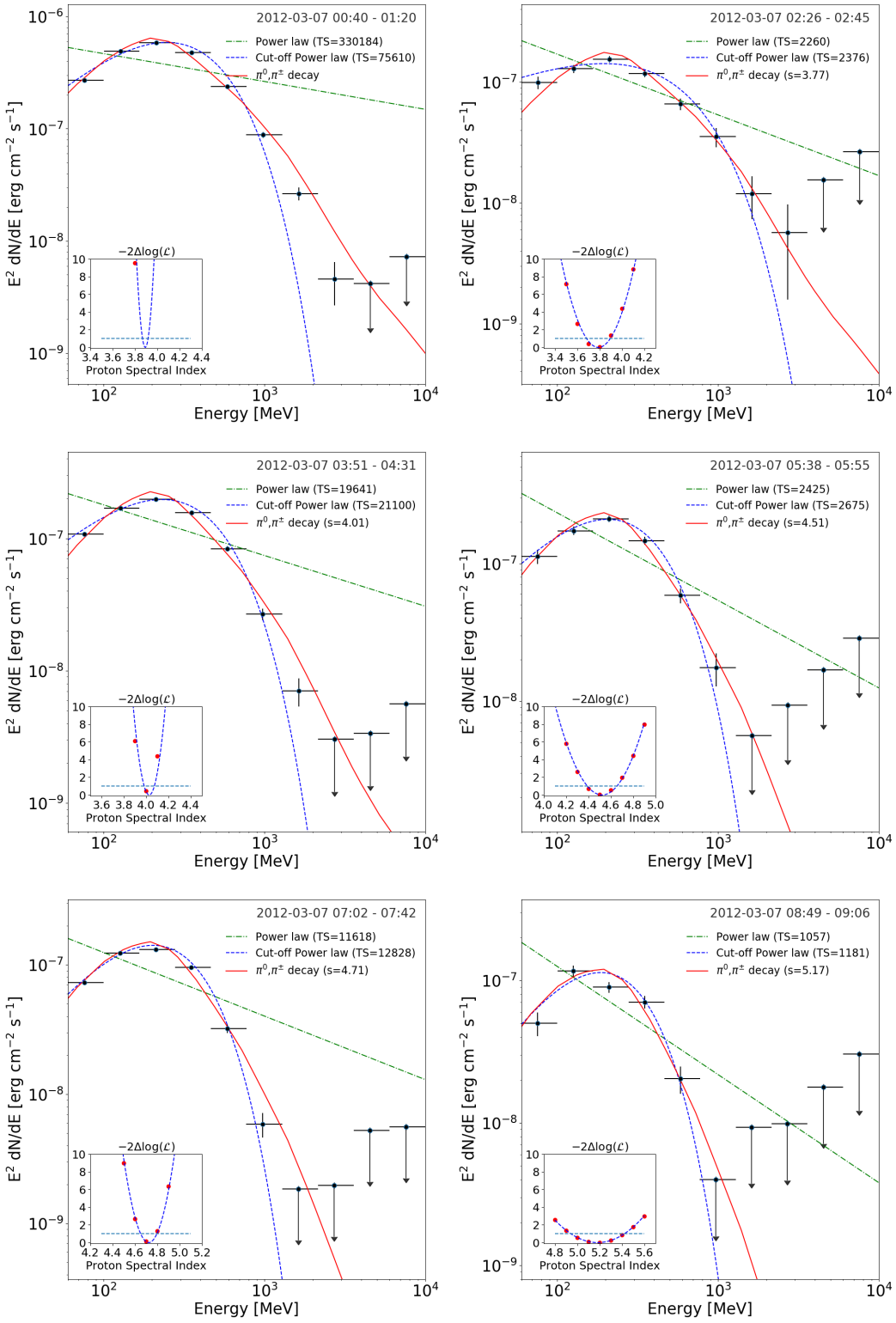

Figure 5.5: Spectral energy distribution for each of the first six time windows of the 2012-03-07 flare (see Figure 4.7 for full description). Best proton indexes vary from 3.8 ± 0.10 to 5.3 ± 0.17 (all values in Table 5.1).

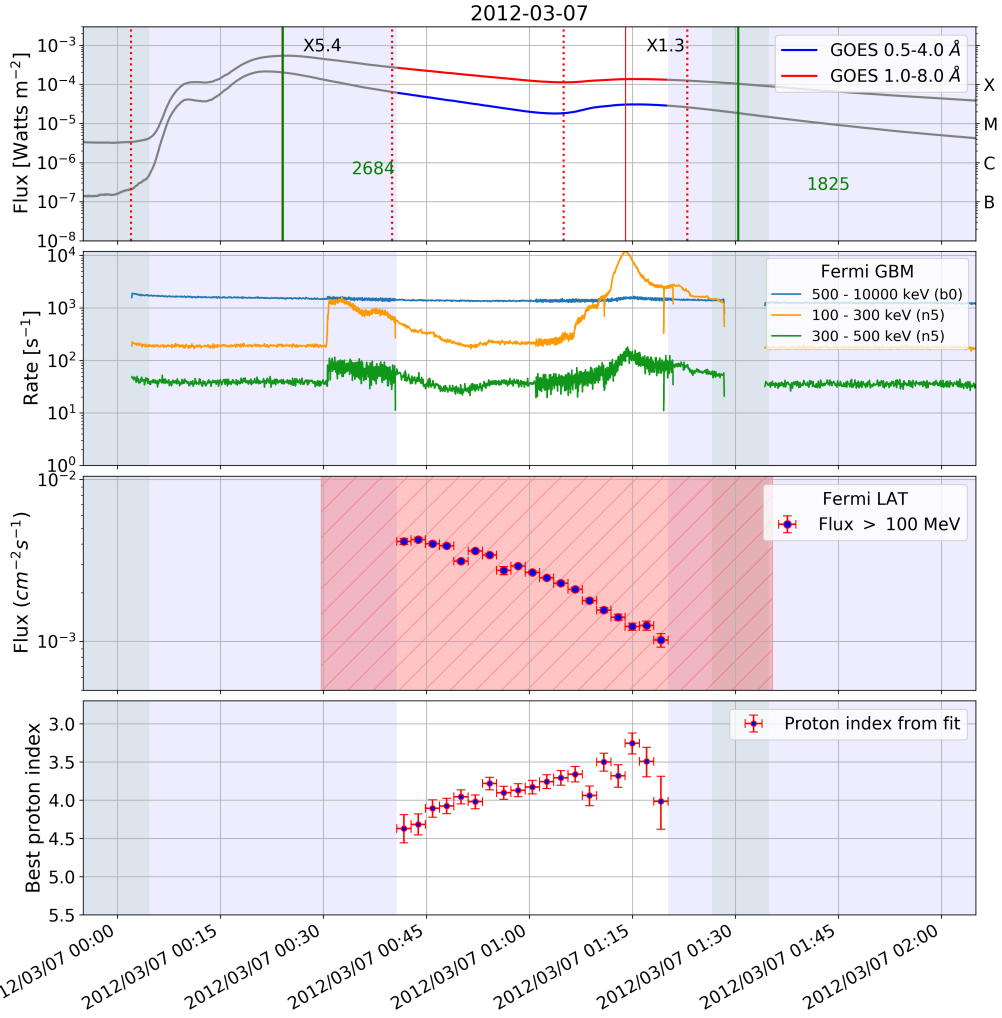

Figure 5.6: Composite lightcurve for the impulsive phase of the 2012-03-07 flare. From top to bottom: GOES; GBM NaI and BGO channels; Fermi-LAT flux; Best proton index. The last two quantities are computed using the S15 event class because of the BTI.

phase of the flare, but also within the remarkably bright impulsive phase. The gamma-ray emission initially peaks in the first time window coincident with the X-ray flares, but then the gamma-ray emission rises and then decays on timescales of a few hours. In each time interval, a spectral analysis is performed using spectral models described in Sections 4.1.2 and 4.3.5. If the observed spectrum clearly diverges from a pure power law spectrum and the exponential cutoff model provides a better fit (chosen if the ΔTS is greater than 9) we consider which pion template best fit the spectrum. Figure 5.4, shows the evolution of the flux and TS for the best spectral model as well as the best fit proton spectral index when applicable (values given in Table 5.1). The spectral evolution over the long duration phase shows a continuous softening of the emission, independent from the rise and fall pattern of the flux. Individual examples of spectral energy distributions are shown in Figure 5.5. In the case of the first 9 time windows, we can constrain the best index for the proton from values of 3 all the way to 6. In the last of those time intervals, starting at 16:35UT, the spectrum can be fitted to a curved model, but the proton index is not well constraint and is indicated as >6. In the very last two time windows, after 18:00UT, the gamma-ray emission is significant just below the 5σ level, but consistent with the emission coming from the Sun. However the spectrum is not well constrained and a power law is the simplest distribution that fits the observation.

Focusing on the Impulsive phase of the flare: the Sun entered the Fermi-LAT FoV at 00:40UT and was observable for about 40 minutes. For this entire time window, the X-rays produced by both flares were so intense that the Fermi-LAT suffered from pile-up and therefore the S15 event class that is immune to that effect was used. The impulsive phase was sliced into 2 minutes time intervals to study the evolution of the flux and spectral shape. In all time windows, the observed spectrum clearly diverges from a pure power law spectrum and the exponential cutoff model provides a better fit in all time intervals. The two bottom panels of Figure 5.6 show the temporal evolution of the flux and the best fit proton distribution index. A continuous decay of the emission is observed, but the spectrum is hardening with time (values given in Table 5.2).

5.1.4 Gamma-ray Localization

Localization of the gamma-ray emission can provide critical information about the origin of the high-energy particles and the processes operating in solar flares. The key questions are whether that emission is tightly constrained to the active region site, or displaced, or possibly spatially extended. We focus the localization study on the selected time intervals observed with exposures greater than 25 minutes and with average boresight angle lower than 55°. It corresponds to four time windows: starting at 00:40UT, 03:51UT, 07:02UT,

Time on 2012-03-07	Exposure (minutes)	Flux (10^{-5} cm^{-2}s^{-1})	TS	ΔTS	Photon Index	Proton Index
00:40:41 - 00:42:46	2	415.13 ± 18.39*	7458	114	-	4.37 ± 0.18
00:42:46 - 00:44:51	2	425.17 ± 13.94*	13830	281	-	4.32 ± 0.14
00:44:51 - 00:46:55	2	400.79 ± 11.12*	19132	274	-	4.11 ± 0.11
00:46:55 - 00:49:00	2	389.77 ± 9.54*	24756	369	-	4.07 ± 0.10
00:49:00 - 00:51:05	2	313.09 ± 7.33*	27410	-	-	3.96 ± 0.09
00:51:05 - 00:53:10	2	362.39 ± 7.89*	30947	445	-	4.02 ± 0.09
00:53:10 - 00:55:14	2	342.18 ± 7.39*	31215	431	-	3.78 ± 0.08
00:55:14 - 00:57:19	2	274.22 ± 15.72*	30451	-	-	3.90 ± 0.09
00:57:19 - 00:59:24	2	292.08 ± 6.45*	6712	528	-	3.87 ± 0.09
00:59:24 - 01:01:28	2	266.85 ± 6.15*	6213	476	-	3.83 ± 0.09
01:01:28 - 01:03:33	2	246.93 ± 6.04*	5174	394	-	3.76 ± 0.09
01:03:33 - 01:05:38	2	229.02 ± 5.99*	5210	352	-	3.71 ± 0.09
01:05:38 - 01:07:43	2	209.87 ± 5.94*	4309	286	-	3.66 ± 0.10
01:07:43 - 01:09:47	2	178.99 ± 5.86*	2977	221	-	3.94 ± 0.13
01:09:47 - 01:11:52	2	156.15 ± 5.71*	2557	192	-	3.50 ± 0.12
01:11:52 - 01:13:57	2	141.17 ± 5.97*	1736	118	-	3.68 ± 0.15
01:13:57 - 01:16:02	2	123.50 ± 6.37*	1183	64	-	3.26 ± 0.14
01:16:02 - 01:18:06	2	125.43 ± 8.21*	748	48	-	3.49 ± 0.19
01:18:06 - 01:20:11	2	101.97 ± 9.90*	300	21	-	4.02 ± 0.35

Table 5.2: Evolution of spectral parameters of the gamma-ray emission during the impulsive phase of the 2012-03-07 flare. Columns: 1) Start and end time of bin during the first time window on 2017-09-10 (UT); 2) Exposure in minutes; 3) Flux computed for the preferred spectral model (> 100 MeV); 4) TS value for the Power Law model; 5) Difference of TS between EXP and PL models, a value above 9 indicates the EXP is favored; 6 and 7) give the best fit photon index for a PL model or the best fit proton index from the pion fit if the EXP model is preferred (* indicates that the Fermi-LAT response was affected by pile-up, and the S15 event class is used for the analysis).

10:14UT (see last column of Table 5.1). This selection enables us to limit the statistical error and the systematic error due to the fisheye effect. Section 4.3.4 describes in details the localization procedure and the limitations due to the fisheye effect.

We have mentioned that the very first time interval observation suffered from pileup in the ACD, so we use the S15 event class instead of SOURCE. For localization purposes there is no reason to discard this time window, as there is no indication that the event class choice introduces any spatial systematic effect. If anything, we know that there are more photons, so the statistical error is smaller.

In Figure 5.7 the localizations of the gamma-ray source for each of the four different time intervals is shown with the 68% and the 95% localization contours (statistical errors). The localizations have been corrected for the fisheye effect. If not accounted for, the position of a source can shift to a distance greater than the statistical error itself. In Section 4.3.4, Figure 4.5 shows this comparison for one of the time windows studied here (interval starting at 07:02UT).

As time passes the gamma-ray emission becomes dimmer and the statistical uncertainty increases. With gamma-ray emission of this intensity and soft spectrum, it is impossible to quantify the morphology of the source and its possible extension and the localization study

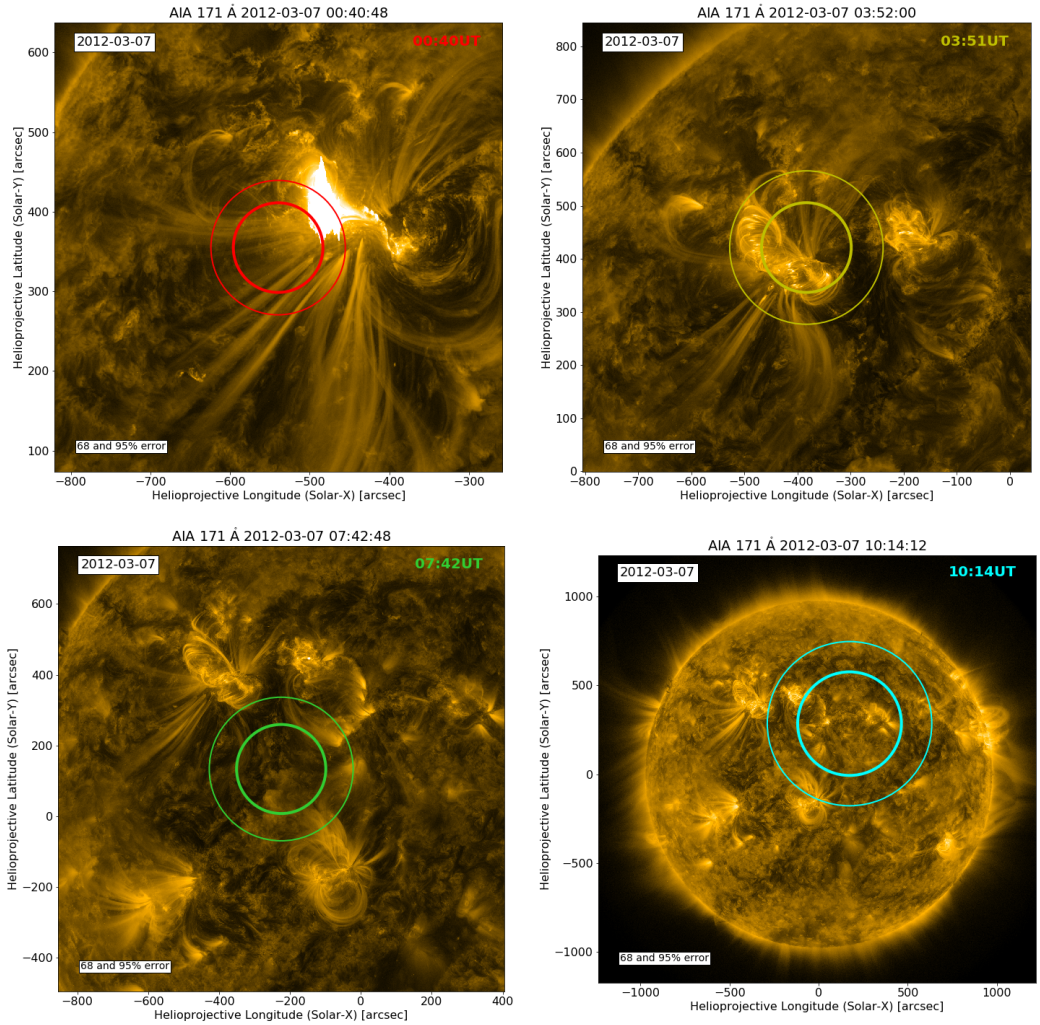

Figure 5.7: Localization of the gamma-ray source during different time windows following the 2012-03-07 flare, with 68% and 95% error circle. All SDO/AIA images are selected at the start of the time windows, except for the third time window when the image was not available.

assumes a point source. The extent of the localization error does not reflect a gamma-ray source extending to large portions of the Sun.

We can over plot the different positions on a single SDO AIA image, chosen as the time when the Sun first came in the FoV. We introduce a small error by plotting the position of the gamma-ray source at 10:34UT onto the background image of the Sun at 00:40UT, but that error is small compared to the uncertainty of that position. As shown on Figure 5.8, the gamma-ray source is progressively displaced away from the flare site as time passes.

Table A gives the exact position of the centroid of the Fermi-LAT source in different time windows and the 68 and 95% containment radii. The angular distance is calculated between the position of the AR and the Fermi-LAT source position. The relative distance

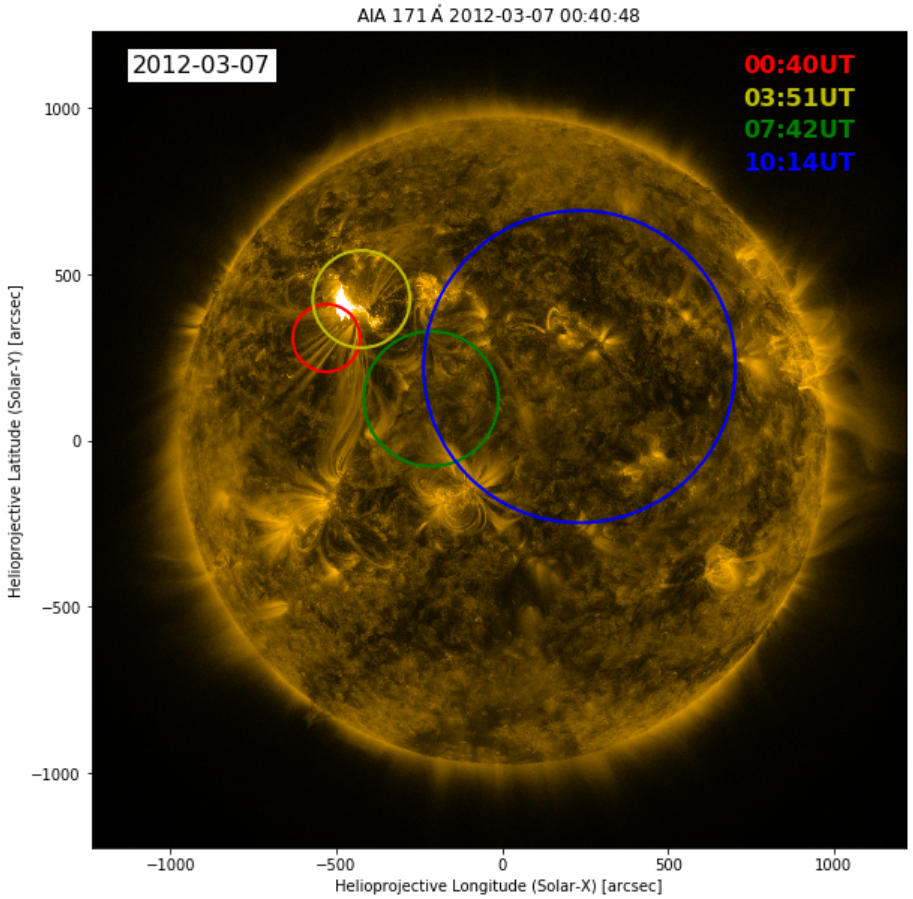

Figure 5.8: Localization evolution over the first 10 hours of delayed gamma-ray emission of the 2012-03-07 flare. From red to blue at respective times: 01:03, 04:11, 07:22 and 10:29 on March 7, 2012, over plotted on the AIA 171 Å of 00:40UT. Circles show the 95% uncertainty.

consists of the ratio of the angular distance relative to the 95% error radius. In the third and fourth time windows the source is localized 300 and 650 arcseconds away from the flare site which is more about 1.5 times the uncertainty on the localization of the gamma-ray source which shows a clear motion away from the flare site.

5.2 September 2017 Flares

Another example of a spectacular long duration gamma-ray flare occurred in September 2017. As the solar flare cycle was ramping down throughout 2016 and 2017, a large sunspot formed in September 2017 and became extremely prolific, producing 27 M-class and 4 X-class flares in the span of 7 days! AR 12673 was also the source of at least 10 CMEs in the same time range (between 2017-09-04 and 2017-09-10). The Fermi-LAT detected gamma-ray emission above 100 MeV for several hours from two flares on 2017-09-06 and 2017-09-10

	Start Date and Time	Helio X,Y	ERR 68%	ERR 95%	Angular Distance	Relative Distance (95)	Average Boresight (°)
a)	2012-03-07 00:40	-543,343	64.2	99.5	87.0	0.9	50
c)	2012-03-07 03:51	-397,428	90.8	142.2	83.8	0.6	50
e)	2012-03-07 07:02	-319,140	121.9	198.0	299.9	1.5	50
g)	2012-03-07 10:14	167,285	288.7	462.3	652.2	1.4	52

Table 5.3: Time resolved localization of the gamma-ray source during the first 10 hours of the 2012-03-07 flare. The positions are computed for each window with fisheye correction and reported in the helioprojective coordinate system in column 2. The 68 and 95% containment error computed with the TS maps contours are given in columns 3 and 4. The angular distance between the position of the AR and the position of the gamma-ray source is reported in column 5 in arcseconds. In column 6 we compare this value to the 95% containment radius to estimate the relative distance: a value greater than 1 indicates that the position of the gamma-ray source is incompatible with the AR. The average angle between the Sun and the Fermi-LAT boresight axis is given in column 7 to indicate the amplitude of the fisheye correction.

reported in ATel #10720 and #10735 (Longo et al. 2017, Longo & Pesce-Rollins 2017). The 2017-09-10 flare stands out as one of the brightest and longest of solar cycle 24 observed in high-energy gamma rays, along with the 2012-03-07 flares described above. The 2017-09-10 flare is already the object of many publications with Omodei et al. (2018) focusing on the Fermi-LAT gamma-ray data (see also Liu et al. 2018 in EUV, Gary et al. 2018 in microwave and HXR).

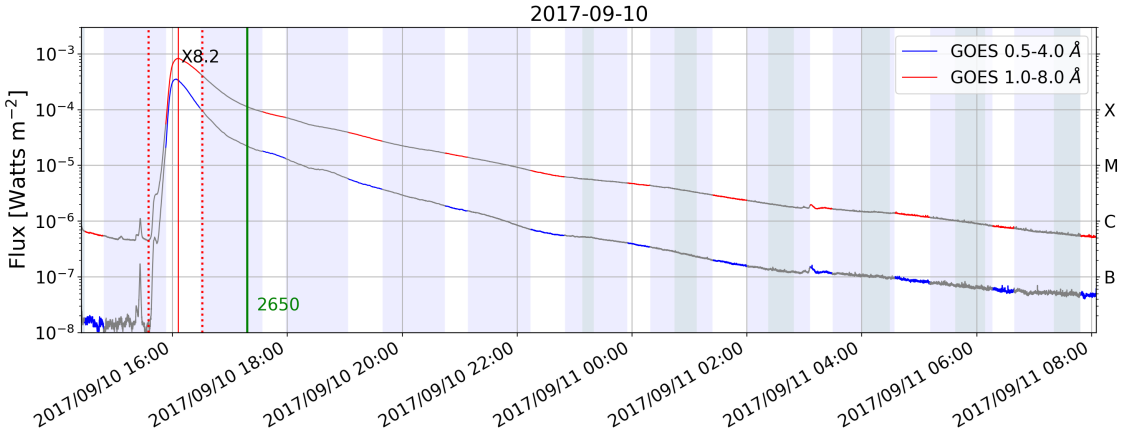

Figure 5.9: GOES light curve for the bright September 10, 2017. The vertical green line marks the time at 21.5 solar radii of the very fast CME associated with this flare.

5.2.1 X-rays, CME, SEP Observations

This active region produced the brightest GOES flare of cycle 24, the brightest in 12 years: a X9.3 flare starting on September 6 at 11:53UT, peaking at 12:02UT. It lasted 17 minutes

and was associated with a rather fast CME, with an estimated speed of 1571 km/s. On September 10, another remarkable flare followed: a X8.2 class flare starting at 15:35UT and peaking at 16:06UT. According to the GOES definition, it lasted 56 minutes, ending at 16:31 UT, but it shows a very long decay as show in Figure 5.9. A very fast CME was associated with this flare with an estimated speed of 3163 km/s, which makes it by far the fastest CME in solar cycle 24. This flare was associated with a very strong SEP event and Ground Level Enhancement #72, the second of cycle 24 (Augusto et al. 2018).

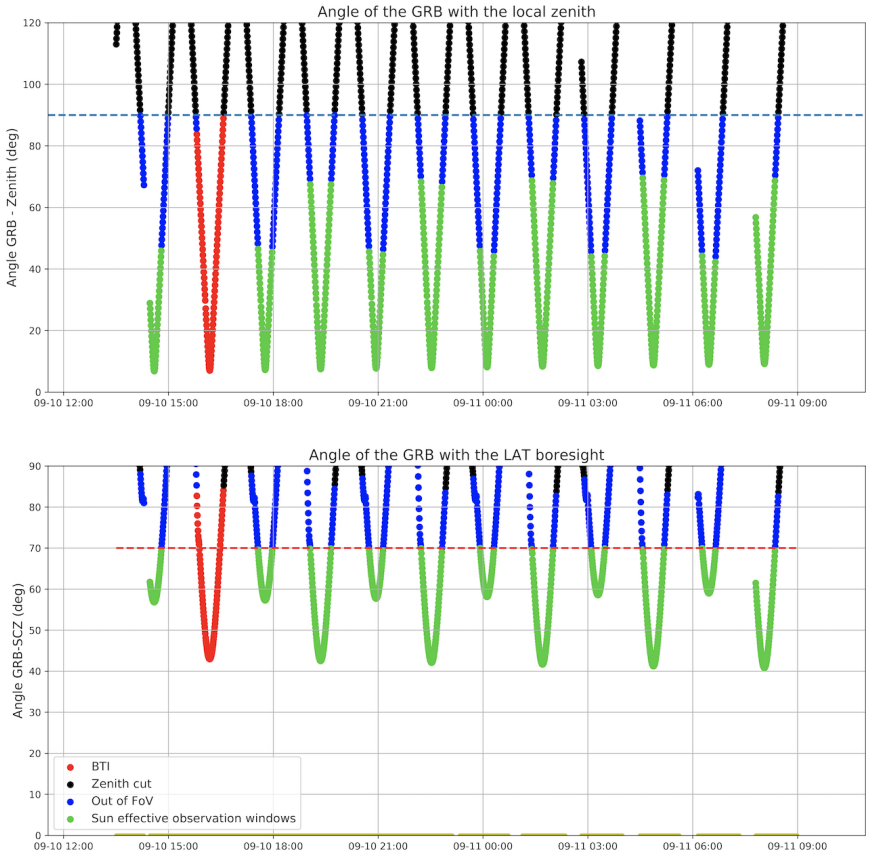

Figure 5.10: Observation profile of the Sun during the September 10, 2017 solar flare, tracking the position of the Sun. The green intervals indicate the effective times of data collection for our analysis. The gaps in between reflect the motion of the Sun in and out of the FoV as well as the zenith and SAA cuts. The red interval shows the time range when data was collected but was affected pile up effect and classified as Bad Time Intervals. Top panel: angular distance between the Sun and the Earth's limb; Bottom panel: angular distance between the position of the Sun and the Fermi-LAT boresight direction.

5.2.2 Fermi-LAT Observations

For both flares the coverage by Fermi was excellent, with a time window of observation lasting between 24 and 36 minutes every 1.5 hours. Because the flares were so bright in Soft X-rays, it caused a large pileup in the Fermi-LAT and analysis of the data collected during the BTI requires the use of the S15 event class. The entire observation profile for the bright 2017-09-10 flare is show in Figure 5.10. It is very similar to the observational profile of the 2012-03-07 flare: a BTI interval during the impulsive phase of the flare, followed by the Sun coming in and out of the FoV, visible every orbit but with an asymmetrical profile, only visible at higher incidence angles for shorter amounts of time in every other time window.

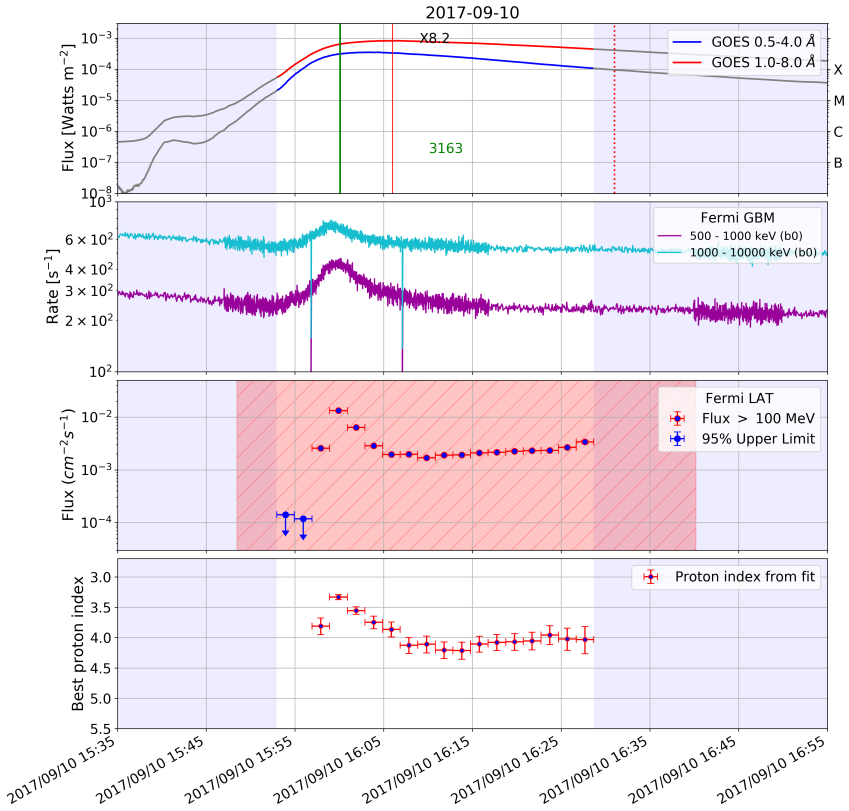

Figure 5.11: Multi-wavelength light curve for the impulsive phase of the Sept 10, 2017 flare. The RHESSI data is not corrected for background or use of the different attenuators during the flare. The GBM data is not corrected for background.

During the impulsive phase the HXR component, RHESSI observed indications of emission above 300 keV. The second panel in Figure 5.11 shows the uncorrected photon counts. The high resolution imaging by RHESSI showed a single HXR footpoint source (with the other one occulted) and a looptop source above the solar limb (Omodei et al. 2018; Gary et al. 2018).

The Fermi GBM had good coverage of the impulsive phase of the flare and recorded a count increase above 500 keV with its BGO instrument occurring between the start and the peak of the GOES flare.

Time on 2017-09-10	Exposure (minutes)	Flux (10^{-5} cm^{-2}s^{-1})	TS	ΔTS	Photon Index	Proton Index
15:56:55 - 15:57:55	1	24.78 ± 4.40*	117	15	-	3.89 ± 0.64
15:57:55 - 15:58:54	1	463.89 ± 18.41*	9601	2030	-	3.77 ± 0.14
15:58:54 - 15:59:54	1	1306.98 ± 27.74*	38514	498	-	3.21 ± 0.06
15:59:54 - 16:00:54	1	1319.45 ± 26.78*	42028	472	-	3.46 ± 0.06
16:00:54 - 16:01:53	1	807.59 ± 19.87*	26938	327	-	3.50 ± 0.08
16:01:53 - 16:02:53	1	414.54 ± 12.85*	16129	-	-	3.64 ± 0.10
16:02:53 - 16:04:52	2	286.20 ± 8.20*	3897	267	-	3.75 ± 0.10
16:04:52 - 16:06:51	2	194.82 ± 6.16*	3225	213	-	3.87 ± 0.12
16:06:51 - 16:08:50	2	197.63 ± 6.13*	3436	269	-	4.13 ± 0.13
16:08:50 - 16:10:49	2	169.78 ± 5.53*	2865	241	-	4.11 ± 0.14
16:10:49 - 16:12:48	2	189.90 ± 5.90*	3368	310	-	4.21 ± 0.14
16:12:48 - 16:14:47	2	191.58 ± 6.04*	3136	231	-	4.21 ± 0.14
16:14:47 - 16:16:46	2	210.85 ± 6.49*	3386	284	-	4.11 ± 0.13
16:16:46 - 16:18:45	2	215.19 ± 6.88*	3091	283	-	4.08 ± 0.13
16:18:45 - 16:20:44	2	226.26 ± 7.57*	2685	198	-	4.07 ± 0.14
16:20:44 - 16:22:43	2	231.36 ± 8.54*	2224	218	-	4.06 ± 0.15
16:22:43 - 16:24:42	2	232.81 ± 9.77*	1754	154	-	3.96 ± 0.16
16:24:42 - 16:26:41	2	266.22 ± 13.28*	1254	95	-	4.02 ± 0.18
16:26:41 - 16:28:40	2	338.21 ± 21.44*	871	58	-	4.03 ± 0.22

Table 5.4: Evolution of spectral parameters of the gamma-ray emission during the impulsive phase of the 2017-09-10 flare. Columns: 1) Start and end time of bin during the first time window on 2017-09-10 (UT); 2) Exposure in minutes; 3) Flux computed for the preferred spectral model (> 100 MeV); 4) TS value for the Power Law model; 5) Difference of TS between EXP and PL models, a value above 9 indicates the EXP is favored; 6 and 7) give the best fit photon index for a PL model or the best fit proton index from the pion fit if the EXP model is preferred (* indicates that the Fermi-LAT response was affected by pile-up, and the S15 event class is used for the analysis).

The Fermi-LAT observed intense gamma-ray emission, starting about 4 minutes after the Sun came into the field of view (see third panel of Figure 5.11). The flux increased at a roughly similar rate as the SGR seen by the GBM, or the second burst of HXR seen by RHESSI, with a possible small time delay. Gamma-ray emission peaked around 16:00UT and decreased for 6 minutes, followed by a slightly rising plateaus for more than 22 minutes, until the Sun got out of the FoV (see Table 5.4). The proton index follows a time evolution roughly similar to the flux, becoming harder for high fluxes followed by a plateau with an average value of 4.1±0.1.

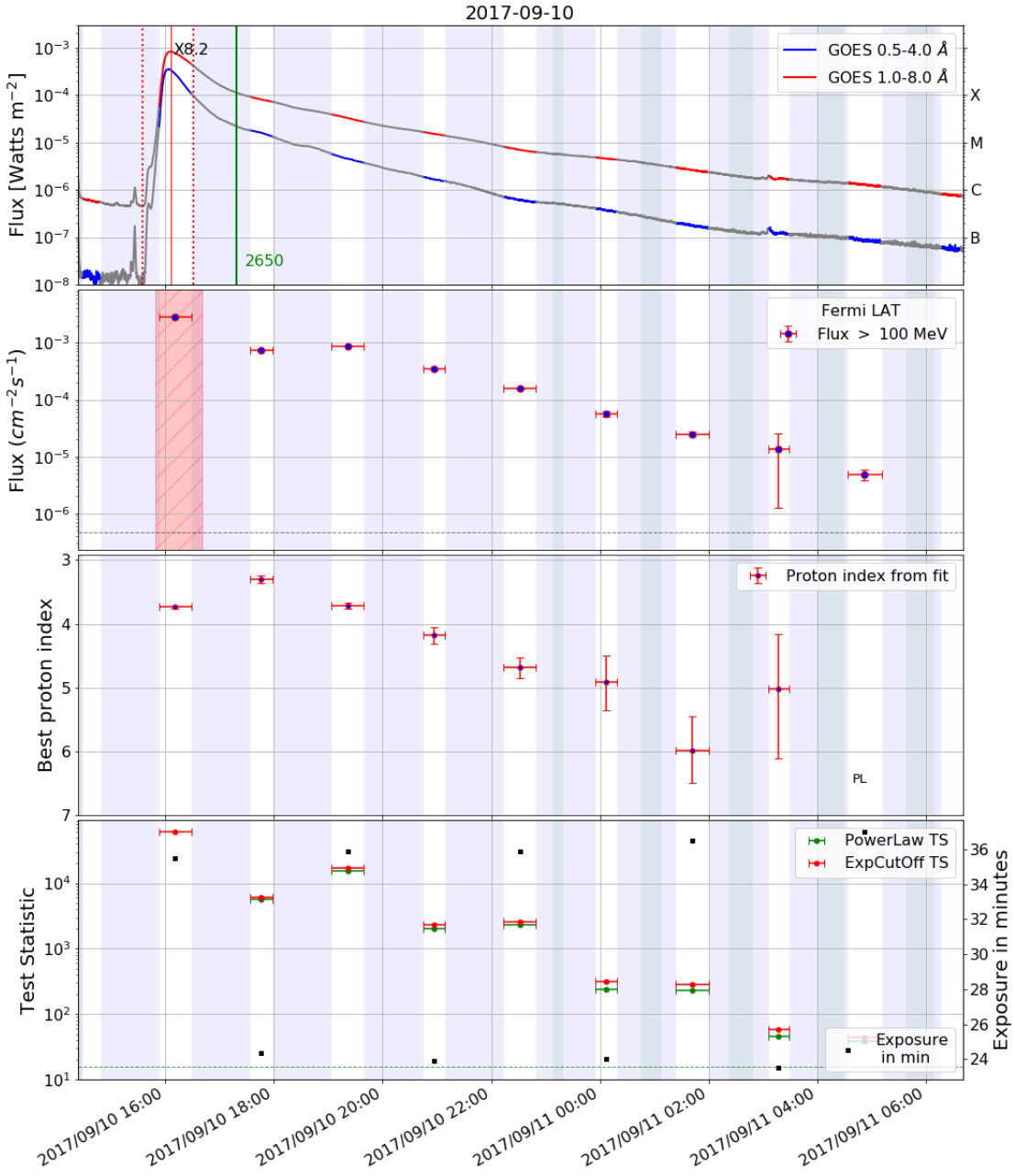

Figure 5.12: Composite lightcurve for the entire duration of the gamma-ray emission for the 2017-09-10 flare. Top panel: GOES lightcurve (full description of shaded areas and vertical markers in Figure 5.2). Second panel: Time evolution of the averaged gamma-ray flux in each time window (values in Table 5.1). The red shaded area indicates the time range when the Fermi-LAT was affected by pile-up, caused by the intense soft X-ray emission. The S15 event class is used for that first window. Third panel: best fitted proton distribution index (with 68% statistical error). Bottom panel: TS values of the gamma-ray source (red and green for the Power Law and Power Law with Exponential Cutoff models respectively); Exposure of each time window (black).

	Time on 2017-09-10	Exposure (minutes)	Flux	TS	ΔTS	Photon Index	Proton Index	Average Boresight
a)	15:52 - 16:28	35	290.96 ± 2.10*	61725	4429	-	3.74 ± 0.03	54
b)	17:33 - 17:58	24	76.44 ± 1.87	6112	469	-	3.30 ± 0.06	62
c)	19:03 - 19:39	36	88.31 ± 1.30	16954	1819	-	3.70 ± 0.05	53
d)	20:44 - 21:08	24	35.81 ± 1.34	2311	276	-	4.18 ± 0.14	62
e)	22:13 - 22:49	36	15.01 ± 0.53	2559	315	-	4.67 ± 0.16	53
f)	23:54 - 00:18	24	5.60 ± 0.54	310	68	-	4.92 ± 0.43	63
g)	01:23 - 02:00	36	2.38 ± 0.22	284	55	-	5.97 ± 0.54	53
h)	03:05 - 03:29	24	1.39 ± 0.28	59	12	-	5.02 ± 0.97	63
i)	04:34 - 05:11	37	0.49 ± 0.11	43	2	-2.65 ± 0.24	-	53

Table 5.5: Evolution of spectral parameters of the gamma-ray emission during the 2017-09-10 flare. Columns: 1) Start and end time of each time window on 2017-09-10 and 2017-09-11 (UT); 2) Exposure in minutes, defined as the effective duration of observation (accounting for time loss due to the SAA); 3) Flux averaged over the time window computed for the preferred spectral model (unit (10^{-5} cm^{-2}s^{-1} between 100 MeV and 10 GeV); 4) TS value for the Power Law model; 5) Difference of TS between EXP and PL models, a value above 9 indicates the EXP is favored; 6 and 7) give the best fit photon index for a PL model or the best fit proton index from the pion fit if the EXP model is preferred; 8) Average angle between the Sun and the LAT boresight axis (* indicates that the Fermi-LAT response was affected by pile-up, and the S15 event class is used for the analysis).

Following the impulsive phase, this flare was observed over a total span of 13 hours after the start of the X-ray flare. The entire light curve is presented on Figure 5.12 along with the values of the spectral parameters in Table 5.5. Three phases are clearly observed in the Fermi-LAT light curve: a first very bright peak coincident with the impulsive phase, and a second phase described as long duration emission, unrelated to the HXR and soft gamma-ray emission.

After the peak in the impulsive phase, the Sun next entered the FoV at 17:33UT, and at that same time the HXR had already died down, although this flare was particularly long in soft X-rays. The gamma-ray flux nevertheless increased for almost 2 hours and but then follows a smooth decay for about 9 hours and a half. In all time bins from 17:33UT to 02:00UT on 2017-09-11, the gamma-ray emission is strong and consistent with pion emission. It shows a continuous softening of the proton distribution. Significant emission is detected in the last two bins, and its spectrum is best fitted by a power law.

Although this flare was detected for 13 hours in gamma rays, it exhibits behaviors similar to the bright 2012-03-07 flare which lasted more than 20 hours. In particular in the long duration phase when the high-energy gamma-ray emission follows a rise-and-fall pattern. This behavior has never been observed in previous gamma-ray detection of solar flares. In addition, the spectrum is consistent with pion decay emission from a softening proton distribution. However the impulsive phase is different: the flux plateaus for 20 minutes in this flare, beyond the duration of the HXR and soft gamma rays as seen in Figure 5.11.

For the 2012-03-07 event, the high-energy gamma-ray emission showed a steep decrease

	Start Date and Time	Helio X,Y	ERR 68%	ERR 95%	Angular Distance	Relative Distance (95)	Average Boresight (°)
a)	2017-09-10 15:52	1027,205	95.3	153.3	99.7	0.7	54
c)	2017-09-10 19:03	1045,-71	99.5	167.5	108.8	0.6	53
e)	2017-09-10 22:13	1104,141	270.2	442.7	312.8	0.7	53

Table 5.6: Time resolved localization of the gamma-ray source during the 2017-09-10 flare. The positions are computed for each window with fisheye correction and reported in the helioprojective coordinate system in column 2. The 68 and 95% containment error computed with the TS maps contours are given in columns 3 and 4. The angular distance between the position of the AR and the position of the gamma-ray source is reported in column 5 in arcseconds. In column 6 we compare this value to the 95% containment radius to estimate the relative distance: a value greater than 1 indicates that the position of the gamma-ray source is incompatible with the AR. The average angle between the Sun and the Fermi-LAT boresight axis is given in column 7 to indicate the amplitude of the fisheye correction.

for 40 minutes but no plateau, and the spectrum was continuously hardening. One fact to remember when comparing the two flares is the fact that the March 2012 event is a combination of two flares and the Fermi-LAT did not observe the peak of the first X5.1 flare but only its end, and then the impulsive phase of the second X1.3 as seen in Figure 5.6.

5.2.3 Gamma-ray Localization

This flare is bright enough to do a time resolved localization study. Similar to the situation of the 2012-03-07 flare, we face the same difficulties with the fisheye correction: the asymmetric observational profile induces fisheye errors that change the apparent position of the gamma-ray source in each time window, but in a different direction from one orbit to the next. We focus the localization study on the selected time intervals observed with exposures greater than 20 minutes and with average boresight angle lower than 55°.

We limit our localization study to the time intervals that fit the same criteria for the localization study of the 2012-03-07 gamma-ray flare: exposure longer than 25 minutes and average boresight angle smaller than 55 ° (see Table 5.5). We select the time windows a), c) and e) starting at 15:52UT, 19:03UT and 22:13UT respectively. For the first time window we compute the position using the S15 event class immune to the pile-up effect and maximize the number of photons collected.

Table 5.6 gives the positions for the chosen time windows and the 68% and 95% statistical errors. In the table we also give the relative distance between the position of the AR (estimated to [957,-135] arcseconds) and the best position for the gamma-ray source, relative to the 95% containment radius. The gamma-ray emission is consistent with the AR throughout the duration of the flare, although it is interesting to note that the centroid is not on the solar disk but in the corona.

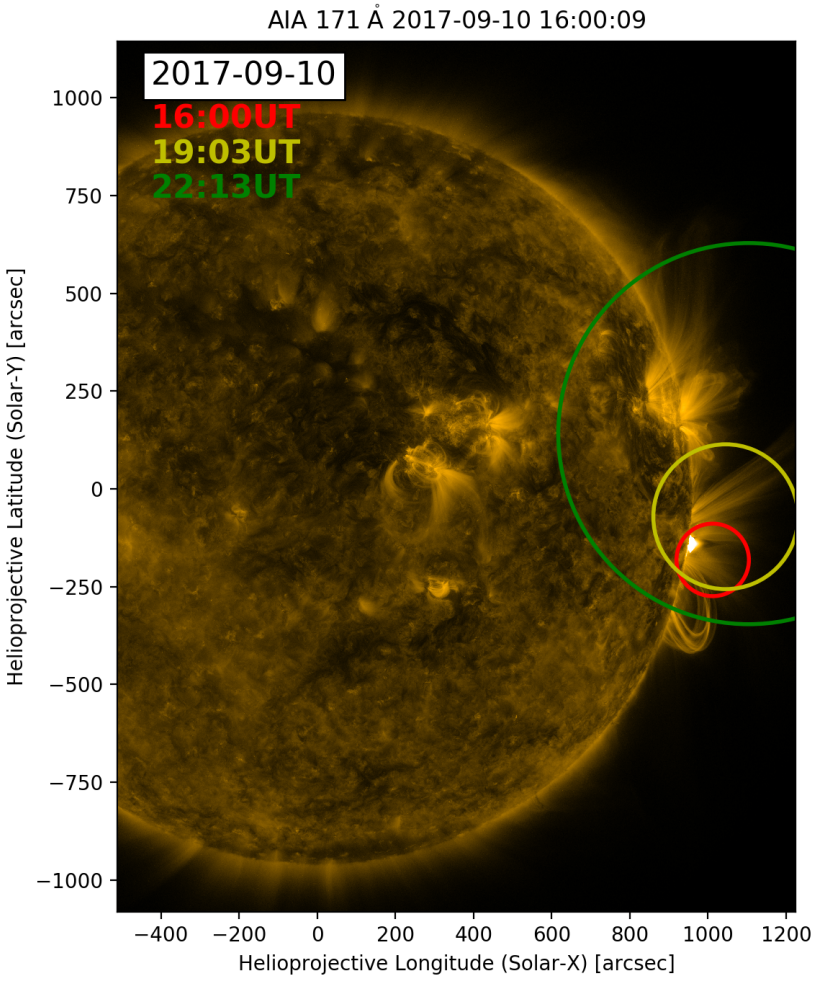

Figure 5.13: Localization evolution: from red to green at times 16:00UT, 19:03UT and 22:13UT on Sept 10, overlay on the SDO AIA 171 image of the Sun at 16:00UT.

5.3 Behind The Limb Flares

High-energy emission for flares that occurred from flare sites behind the limb has been observed in the past, but still poses serious challenges to most standard models for solar flares. The Fermi-LAT observed three of those flares, one of which occurred on September 1st, 2014 and turned out to be the one of the brightest flares observed in gamma rays by the Fermi-LAT. This section goes into the detailed analysis of this flare.

On September 1st, 2014 a flare occurred on the occulted part of the Sun. GOES did not observe any X-ray emission, but STEREO-Behind detected strong Extreme UltraViolet

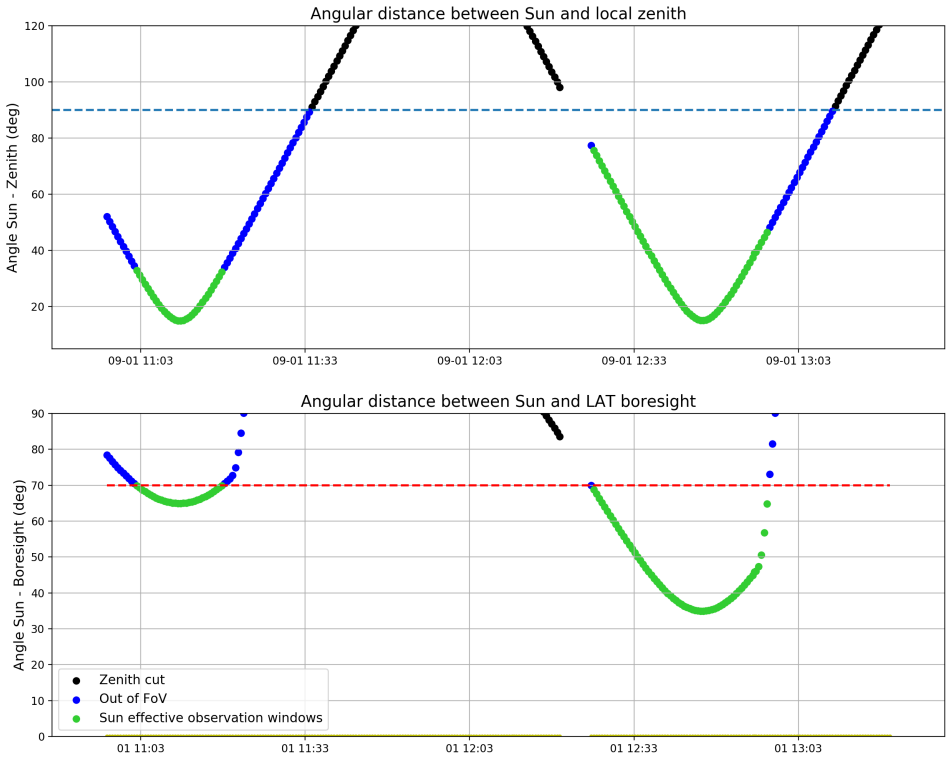

Figure 5.14: Observation profile of the Sun during the September 1^{st} 2014 behind the limb solar flare, showing the position of the Sun. The green intervals indicate the effective times of data collection for our analysis. The gaps in between reflect the motion of the Sun in and out of the FoV as well as the zenith and SAA cuts. The red interval shows the time range when data was collected but was affected pile up effect and classified as Bad Time Intervals. Top panel: angular distance between the Sun and the Earth's limb; Bottom panel: angular distance between the position of the Sun and the Fermi-LAT boresight direction.

emission. The 5-minutes cadence imaging indicates the flare start time between 10:55:56 and 11:00:56 UT and places the active region at position N14E126, which is 36° behind the limb (Ackermann et al. 2017). From the peak flux observed in EUV of 1.7×10^7 photons s^{-1} in the 195 Å channel, the equivalent GOES class of the flare can be evaluated to a X2.4 class flare, from the prescription for bright flares presented in Nitta et al. (2013). This solar flare was associated with a strong Solar Eruptive Event, with a fast CME and SEP fluxes. The CME was first detected at 2 solar radii at 11:12UT with an initial speed of 1901 km/s (the estimated onset time is 10:55UT $\pm$ 5 minutes and the initial speed from the second order fit is above 2500 km/s). Additional observations in radio and HXR are presented in Grechnev et al. (2018).

In gamma rays, the Sun was visible by the Fermi-LAT right after the onset of the flare, but unfortunately at a large incidence angle (see Figure 5.14): it entered the Fermi-LAT FoV at 11:02UT and was visible for 16 minutes, then re-entered the FoV at 12:25UT and was visible for 32 minutes. During the impulsive phase, although no signal was detected by GOES, the GBM detected emission up to a few MeV in temporal coincidence with the Fermi-LAT emission in both the BGO and NaI detectors.

The gamma-ray emission in the first time window of observation is bright enough to do a variability study and the light curve in Figure 5.15 shows a rise in the emission reaching a peak between 11:10 and 11:15UT. In this first time window, the peak emission in high-energy gamma-ray is the only second to the brightest peak of the 2017-09-10 flare. This is remarkable, considering that the AR and its footpoints, where we expect strong gamma-ray emission, were hidden. Which brings us to wonder whether the gamma-ray emission would have been much brighter if this AR had been on the visible part of the solar disk...

Despite the emission being very bright, the localization study is complicated by the fact that the Sun was on the edge of the FoV during the first time window. The average boresight angle over the 16 minutes of this first window was 67°. This creates a large uncertainty on the position due to the fisheye effect (see Section 4.3.4). To quantify this effect for this flare, a localization analysis was run with five different energy thresholds. Figure 5.17 shows the large effect of the correction. The corrected localization contours are all centered on a position roughly consistent with the different minimum energies thresholds (solid). However, the uncorrected localization contours change drastically with the minimum energy, moving toward the corrected localization (dashed). The magnitude of the correction is the greatest at low energies, as expected, and then decreases as the minimum energy increases.

This position is in tension with the position published in Ackermann et al. (2017), but this might have been caused by the use of the distributed gtfindsrc tool which has been associated with some systematic errors in the case of observations of solar flares.

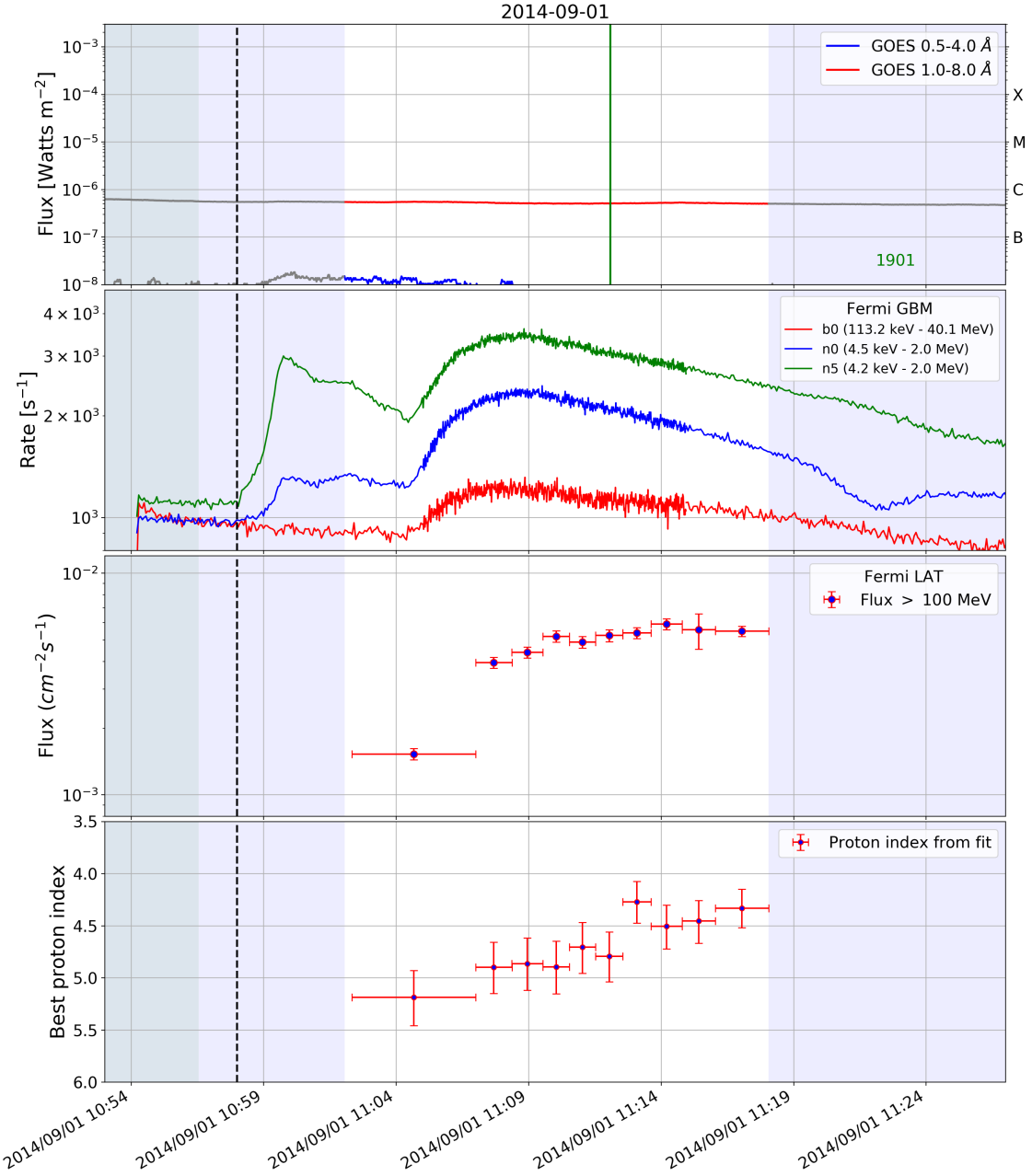

Figure 5.15: GOES, GBM and LAT light curve for the September 1st 2014 flare.The vertical dashed line represents the estimated starting time of the flare, 10:58:00 UT based on STEREO-B emission.

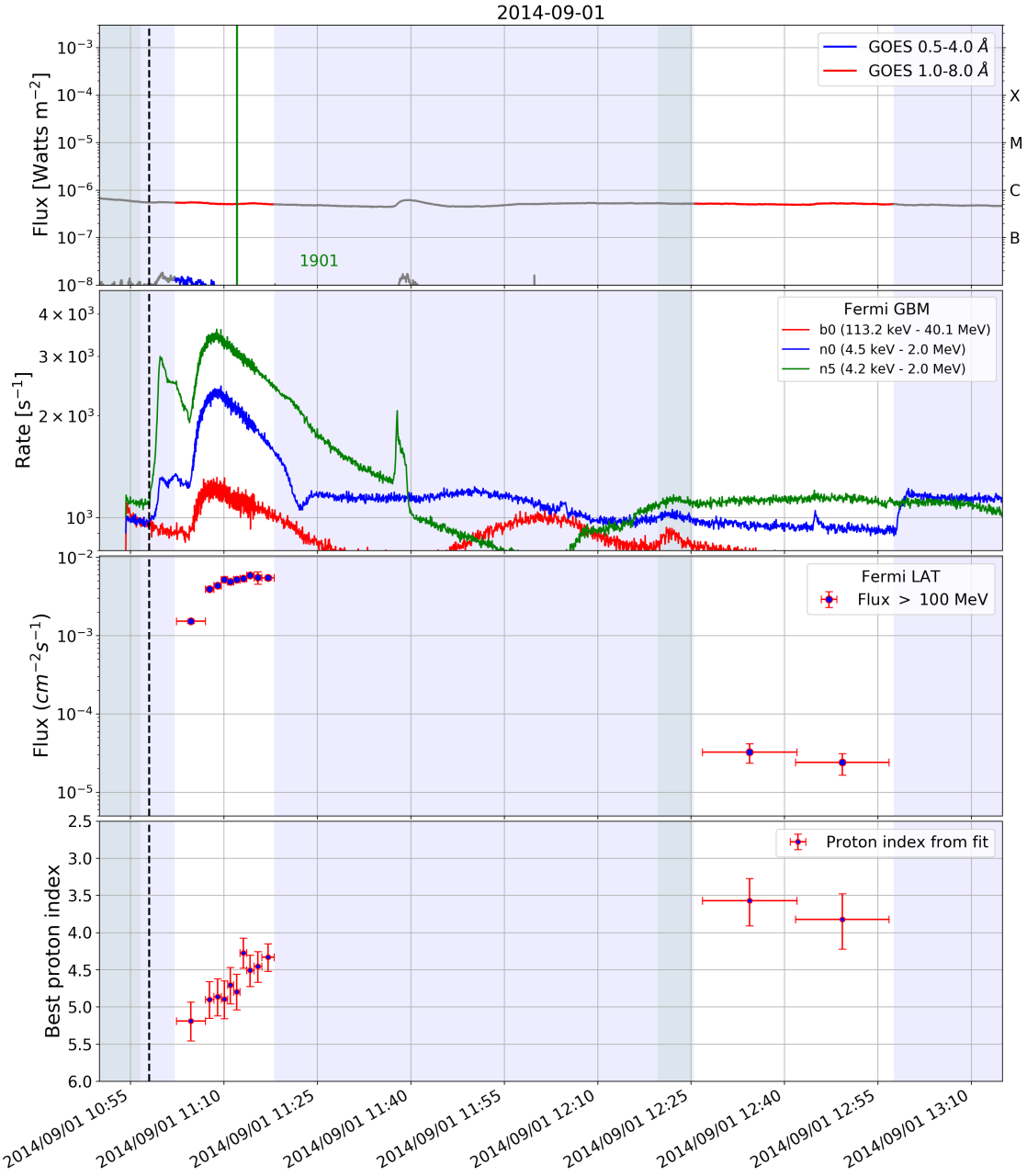

Figure 5.16: GOES, GBM and LAT light curve for the September 1st 2014 flare.The vertical dashed line represents the estimated starting time of the flare, 10:58:00 UT based on STEREO-B emission. The increase in rate seen in the Fermi-GBM at 11:38 UT is due to an unrelated small on-disk flare.

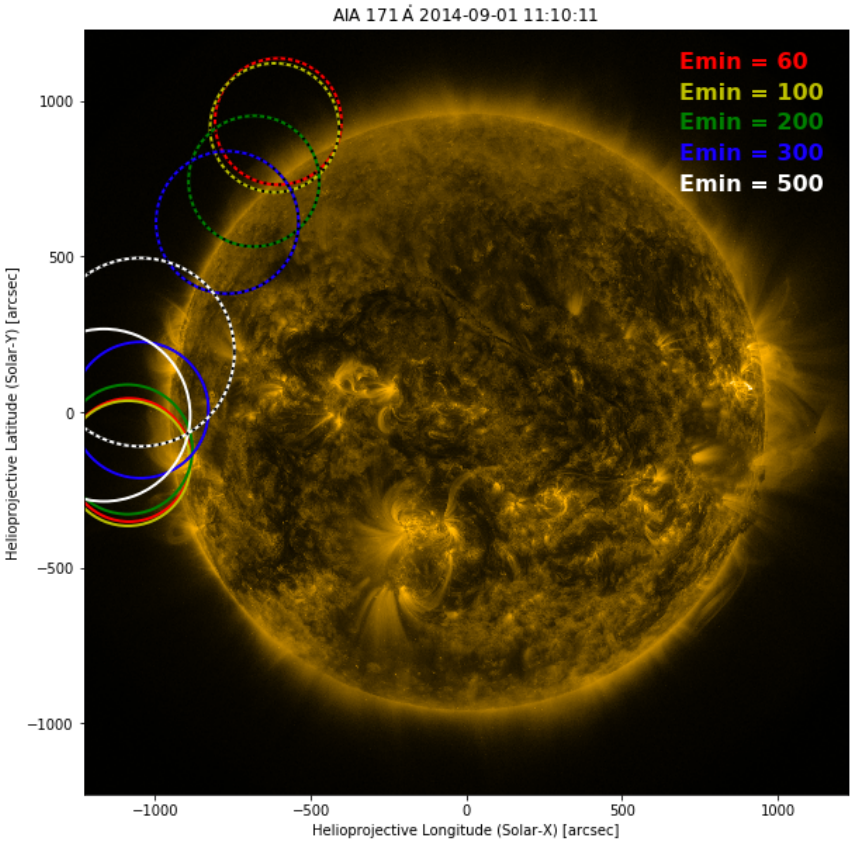

Figure 5.17: Localization for different minimum energies threshold from 60 up to 500 MeV. Solid is fisheye corrected, dashed is not. Circles mark the 68% error circle.

Chapter 6

Fermi-LAT Solar Flare Catalog

Throughout solar cycle 24, the Fermi-LAT instrument continuously monitored the Sun as part of the scanning strategy of the Fermi satellite. Despite this solar cycle being much less prolific in solar flares and CMEs, the Fermi-LAT detected high-energy gamma-ray emission from a total of 45 flares, more than tripling the number of observations of solar flares in the high-energy gamma-ray range from past experiments. Figure 6.1 shows the flares detected in the past solar cycles and the new detections by the Fermi-LAT.

This chapter will describe the first comprehensive catalog of solar flares for a full solar cycle from January 2010 to the end of October 2017: the Fermi-LAT Solar Flare catalog (FLSF). I will present the results of the systematic study of the entire Fermi-LAT solar flare sample and the general conclusions we can draw from them.

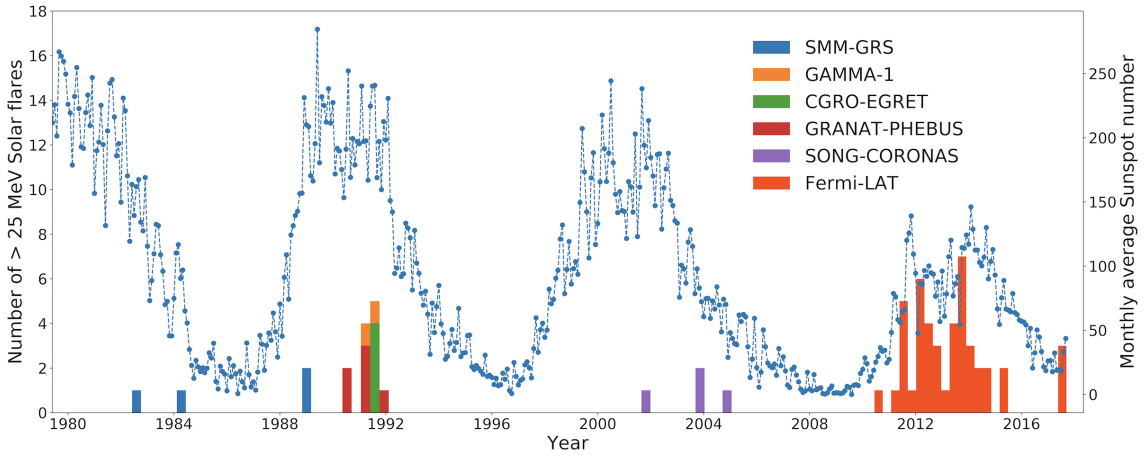

Figure 6.1: Gamma-ray solar flares detections above 30 MeV throughout solar cycles 21 to 24 with available observatories. The averaged numbers of sunspots track the solar activity, and Solar Cycle 24 is one of the weakest in 100 years (Hathaway 2015).

6.1 Solar Flare Catalog Framework

The Fermi-LAT instrument continuously scans the sky with a uniform all-sky exposure completed every 2 orbits of the Fermi Observatory (about 180 minutes, as seen in Figure 3.2). The Sun generally enters the field of view about 40 minutes every three hours, depending on the orbital cycle and the observation mode. To systematically catalog all flares detected by the Fermi-LAT two approaches have been used:

- The first, referred as the `SunMonitor`, systematically analyses each time interval when the Sun is in the field of view. It compiles the significance of detection of the Sun, regardless of the solar activity.
- A second approach consists of following up on any solar flares detected by the Fermi-GBM using the LAT Low Energy (LLE) event class first developed for GRB analysis (see Section 4.3.2).

Fermi has spent more than 95% of its mission to date in survey mode, in which the spacecraft rocks every orbit to put the center of the Fermi-LAT boresight axis 50° north and 50° south of the orbital equator on alternate orbits.In this way the Fermi-LAT monitors the entire sky every two orbits, or about every three hours, and observes the Sun for about 20 to 40 contiguous minutes in that time. An automated data analysis pipeline called the Fermi-LAT `SunMonitor` was created to monitor the high-energy gamma-ray emission from the Sun throughout the Fermi mission[1].

The systematic analysis is run over time windows defined by the Sun being within 70° from the telescope boresight axis. Although the field of view of the Fermi-LAT is usually defined as 60°, gamma rays can be detected with higher incidence angle. However the effective area drops dramatically beyond 60°, so only very bright transients would be detectable past that threshold. This is the case for the 2014-09-01 flare first time window, when the Sun was located at an incidence angle greater than 60° for the entire time of the observation. By choosing 70°, each interval corresponds to the maximum time with continuous Sun exposure, and the duration of these intervals varies as the Earth advances along the ecliptic and as the orbit of Fermi precesses.

From January 2010 to the end of October 2017, the `SunMonitor` pipeline analysis was applied to 33511 intervals of duration longer than 5 minutes. In cases when the duration is less than 5 minutes, the ROI is mostly grazing the maximum zenith angle, or cut short by a passage of the satellite into the SAA. These are generally not long enough to yield a reliable point source likelihood detection and constrain the background. Overall the Sun

[1] The `SunMonitor` data was made available to the public with the solar data browser: `http://sprg.ssl.berkeley.edu/~tohban/browser/` in the Fermi-LAT panel.

was observable for an average duty cycle of 28% for the entire timespan of the FLSF catalog. The distribution of the duration of the time windows of the `SunMonitor` pipeline reflects the combination of orbital variations and position of the Sun throughout the year (see Figure 6.2). Some time windows turn out to be of durations longer than 60 minutes due to combinations of the orbital path, Sun position in the sky and SAA location. In the `SunMonitor` analysis pipeline, an unbinned maximum likelihood calculation is performed in each time window, assuming an exponential cutoff spectral model for the Sun and a background modeled with the diffuse backgrounds used in standard Fermi-LAT analysis (see Section 4.1.2). During time windows when pile-up compromised the Fermi-LAT response, we performed a follow up analysis with the S15 event class.

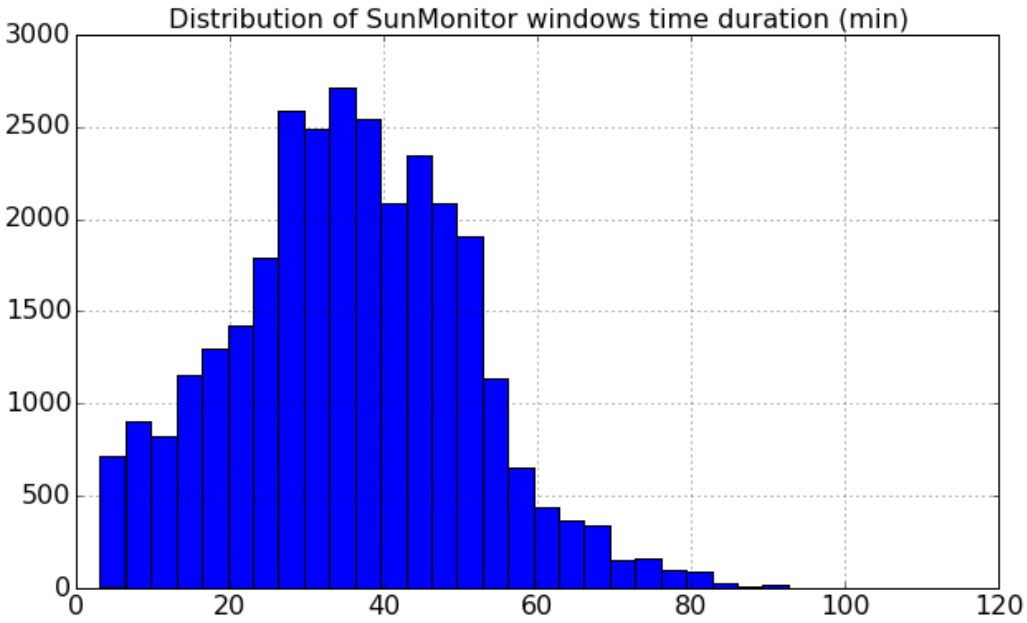

Figure 6.2: Duration of `SunMonitor` time windows determined by the Sun in the Field of View defined as (70°).

To understand the statistical significance of a gamma-ray source detected in the `SunMonitor` with a particular value of TS, we need to account for the trial factor. Indeed with a pipeline testing for detection in so many time windows (33511), we suffer from a "we-are-looking-everywhere" effect. Assuming independent trials a TS of 20, which would otherwise guarantee a result with a confidence of about 4.5 sigma, corresponds to 1.38 sigma post trial. If we want at least 3 sigma detection post-trial: we restrain ourselves to cut on the TS with a minimum of 30. This corresponds to a selection of 133 time windows, some of them consecutive in time for solar flares lasting more than an hour.

From this `SunMonitor` systematic sweep, a follow up detailed analysis is performed

on those seed windows with a TS above 30. The detailed analysis include all aspects presented in Chapter 4 for the overall methodology, and illustrated on the study of the flares described in Chapter 5. This yielded significant detections in 92 time windows. In addition to the selected significant `SunMonitor` time windows, we compute a similar likelihood analysis with the power law spectral model for the time windows right before and after the gamma-ray detection to characterize the upper limits on the transient gamma-ray activity of solar flares. This is a cross check to test for emission that might extend past the selected `SunMonitor` points and characterize the maximum duration of a gamma-ray flare, which can help constrain the model for emission.

To complement the results of the `SunMonitor` another starting point for the Fermi-LAT gamma-ray solar flare catalog is the Fermi-GBM solar flare search. The Fermi-GBM automatically triggers on gamma-ray transients, designed for detecting Gamma-Ray Bursts but performing also for solar flares (about 1200 triggers classified as solar flares). We followed up on all GBM triggers associated with solar flares and performed an analysis using the LLE event class.

The two approaches are complementary: the LLE method suffers from a large background contamination but is very sensitive to short transients. In addition, the effective area associated with this event class is much larger than the SOURCE event class, and is even more sensitive at high incidence angles. Indeed, the 2010-06-12 flare was detected with the LLE approach when the Sun was more than 75° off-axis (Ackermann et al. 2012b).

6.2 Fermi-LAT Catalog Results

Continuous monitoring of the Sun has led to the high-confidence detections of 45 Fermi-LAT solar flares with gamma-ray emission above 60 MeV. Gamma-ray emission was significant in 92 `SunMonitor` time windows, which corresponds to 39 solar flares. A total of 14 flares were detected through the LLE approach: 8 of them correspond to flares also detected through the `SunMonitor` approach and 6 are only detected with LLE, such as the very first detected by the Fermi-LAT on June 12, 2010.

6.2.1 `SunMonitor` Results

The characteristics of the gamma-ray emission for each `SunMonitor` time window are listed in Table 6.1. The windows are described by the start and end times as well as the effective exposure (accounting for time loss due to the SAA). The significance of the source is evaluated by the TS value for the PL model, and the best spectral model chosen by the difference of TS between EXP and PL models (value above 9 indicates the EXP is favored). The flux and spectral parameters are evaluated from the best fit model.

In the cases of flares detected in more than one time window the results are listed together by solar flares. More than half of the solar flares detected by the Fermi-LAT are only detected in a single time window, whereas 16 are detected in more than one window. From the analysis of the gamma-ray data within each time window, we can piece together the evolution of the gamma-ray emission as a function of time.

The Fermi-LAT observed gamma-ray fluxes from solar flares spanning 4 orders of magnitude. The distribution of flux values in each of the 92 time windows is shown in Figure 6.3 upper panel. Fluxes are calculated from 100 MeV to 10 GeV. The distribution peaks in the lower fluxes range, but the tail toward higher fluxes is due solely to the 4 brightest flares: 2012-03-07, 2014-02-25, 2014-09-01 and 2017-09-10, which are all detected over several time windows. The rest of the gamma-ray solar flares in the catalog have peak fluxes distributed around 2×10^{-5} cm^{-2}s^{-1}. The 2017-09-10 flare shows the largest variation from a peak flux of 10^{-2} cm^{-2}s^{-1} in the prompt phase all the way to a minimum value of 4.8×10^{-6} cm^{-2}s^{-1} over a time range of 11 hours.

Almost all the `SunMonitor` time windows with a TS larger than 100 are best fit with a spectrum consistent with an exponential cutoff model. It does not mean that all fainter gamma-ray flares are only consistent with a power law model, but rather that the lower statistics make it difficult to distinguish between the two spectral models. This points to the very common feature of the gamma-ray emission originating from hadronic collision processes and the decay of neutral pions.

Date and Time	Exposure (minutes)	Flux (10^{-5} cm^{-2}s^{-1})	TS	ΔTS	Model	Photon Index	Cutoff Energy	Proton Index
2011-03-07 20:10 - 20:39	29	2.06 ± 0.19	317	27	Exp	-0.76 ± 0.45	171.6 ± 55.1	4.29 ± 0.40
2011-03-07 23:21 - 00:05	44	3.04 ± 0.20	710	70	Exp	-0.31 ± 0.36	137.6 ± 27.4	4.13 ± 0.26
2011-03-08 02:33 - 03:16	43	3.23 ± 0.22	621	66	Exp	-0.15 ± 0.41	109.6 ± 21.6	4.70 ± 0.32
2011-03-08 05:44 - 06:27	44	1.40 ± 0.15	219	32	Exp	0.67 ± 0.99	63.4 ± 21.5	>6
2011-03-08 09:13 - 09:39	26	0.48 ± 0.11	46	0	PL	-2.55 ± 0.25	-	-
2011-06-07 07:47 - 08:23	36	3.18 ± 0.20	740	76	Exp	-0.13 ± 0.37	103.8 ± 18.5	4.97 ± 0.33
2011-06-07 11:16 - 11:34	19	0.32 ± 0.10	19	5	PL	-2.70 ± 0.35	-	-
2011-08-04 04:55 - 05:37	42	2.30 ± 0.18	413	49	Exp	-0.09 ± 0.50	94.7 ± 21.2	5.39 ± 0.44
2011-08-09 07:37 - 08:09	32	2.29 ± 0.23*	186	26	Exp	-0.04 ± 0.87	91.5 ± 36.7	5.39 ± 0.61
2011-09-06 22:11 - 22:47	36	22.77 ± 0.43*	8197	437	Exp	-0.89 ± 0.09	161.1 ± 11.3	4.89 ± 0.11
2011-09-07 23:35 - 00:23	48	0.77 ± 0.08	270	30	Exp	-0.10 ± 0.69	114.0 ± 39.8	4.40 ± 0.45
2011-09-24 09:18 - 09:47	30	0.50 ± 0.10*	50	5	PL	-2.51 ± 0.22	-	-
2012-01-23 04:06 - 04:46	40	1.12 ± 0.11	258	26	Exp	0.12 ± 1.09	80.9 ± 39.9	5.46 ± 0.60
2012-01-23 05:33 - 06:21	48	1.99 ± 0.12	796	92	Exp	0.25 ± 0.41	80.2 ± 13.4	5.57 ± 0.36
2012-01-23 07:20 - 07:47	27	1.97 ± 0.31	93	12	Exp	-0.25 ± 1.05	100.0 ± 48.9	5.50 ± 0.91
2012-01-23 08:58 - 09:26	28	1.63 ± 0.23	116	27	Exp	1.81 ± 1.41	51.4 ± 17.9	5.57 ± 0.79
2012-01-27 19:37 - 19:55	18	3.32 ± 0.49	102	14	Exp	0.31 ± 1.43	64.7 ± 33.1	>6
2012-01-27 21:08 - 21:36	28	0.72 ± 0.14	66	8	PL	-2.53 ± 0.20	-	-
2012-01-28 00:19 - 00:55	36	0.25 ± 0.09	19	1	PL	-2.60 ± 0.39	-	-
2012-03-05 04:07 - 04:49	42	0.58 ± 0.09	100	11	Exp	0.34 ± 1.33	63.2 ± 31.4	>6
2012-03-05 05:36 - 06:24	48	0.63 ± 0.07	175	16	Exp	-0.20 ± 0.85	79.2 ± 30.7	>6
2012-03-05 07:18 - 07:54	36	0.55 ± 0.11	53	6	PL	-2.52 ± 0.21	-	-
2012-03-07 00:40 - 01:20	40	232.56 ± 8.23*	75611	-	Exp	-0.65 ± 0.03	182.2 ± 3.7	3.87 ± 0.02
2012-03-07 02:26 - 02:45	18	75.05 ± 2.62	2377	117	Exp	-1.45 ± 0.13	354.9 ± 47.4	3.77 ± 0.10

Continued on next page

Date and Time	Exposure (minutes)	Flux (10^{-5} cm^{-2}s^{-1})	TS	ΔTS	Model	Photon Index	Cutoff Energy	Proton Index
2012-03-07 03:51 - 04:31	40	95.09 ± 1.18	21100	1459	Exp	-0.84 ± 0.05	198.5 ± 7.8	4.01 ± 0.05
2012-03-07 05:38 - 05:55	18	97.34 ± 3.24	2675	249	Exp	-0.59 ± 0.17	146.5 ± 13.6	4.51 ± 0.13
2012-03-07 07:02 - 07:42	40	62.79 ± 0.98	12829	1210	Exp	-0.30 ± 0.08	119.6 ± 5.2	4.71 ± 0.07
2012-03-07 08:49 - 09:06	17	49.76 ± 2.47	1181	123	Exp	-0.17 ± 0.32	101.8 ± 14.2	5.17 ± 0.24
2012-03-07 10:14 - 10:54	25	26.75 ± 0.87	2803	344	Exp	0.27 ± 0.21	84.0 ± 6.9	5.28 ± 0.17
2012-03-07 13:24 - 14:04	13	8.58 ± 0.93	258	31	Exp	0.30 ± 0.75	77.6 ± 21.5	5.71 ± 0.60
2012-03-07 16:35 - 16:48	13	1.54 ± 0.32	49	10	Exp	1.41 ± 1.91	46.2 ± 23.2	>6
2012-03-07 18:23 - 18:32	9	2.20 ± 0.74	25	8	PL	-2.91 ± 0.41	-	-
2012-03-07 19:46 - 20:15	29	0.26 ± 0.08	22	3	PL	-2.37 ± 0.30	-	-
2012-03-09 05:12 - 05:55	43	0.27 ± 0.08	32	0	PL	-2.24 ± 0.25	-	-
2012-03-09 06:47 - 07:30	43	0.96 ± 0.12	139	20	Exp	0.09 ± 0.92	86.9 ± 33.6	5.49 ± 0.74
2012-03-09 08:22 - 09:05	43	0.89 ± 0.12	140	28	Exp	1.78 ± 1.21	50.0 ± 15.4	5.61 ± 0.78
2012-03-09 09:58 - 10:41	22	0.43 ± 0.13	25	0.3	PL	-2.51 ± 0.32	-	-
2012-03-10 21:00 - 21:34	34	0.23 ± 0.06	25	2	PL	-2.50 ± 0.30	-	-
2012-03-10 22:35 - 23:15	40	0.19 ± 0.06	18	3	PL	-3.04 ± 0.40	-	-
2012-05-17 02:12 - 02:44	32	1.19 ± 0.19	100	10	Exp	-0.72 ± 0.77	207.2 ± 116.5	3.69 ± 0.49
2012-05-17 03:49 - 04:18	30	0.44 ± 0.13	29	7	PL	-2.30 ± 0.28	-	-
2012-06-03 17:38 - 18:02	24	3.06 ± 0.25	395	39	Exp	-0.19 ± 0.63	103.9 ± 33.9	4.96 ± 0.42
2012-07-06 23:20 - 00:08	48	3.06 ± 0.15	1173	143	Exp	0.40 ± 0.35	73.5 ± 9.7	5.75 ± 0.29
2012-10-23 04:13 - 04:43	30	0.73 ± 0.18	39	9	PL	-2.73 ± 0.27	-	-
2012-11-13 01:34 - 02:14	40	0.46 ± 0.09*	60	7	PL	-2.61 ± 0.21	-	-
2012-11-27 15:48 - 16:34	46	0.27 ± 0.07	44	2	PL	-2.22 ± 0.21	-	-
2013-04-11 07:00 - 07:39	39	5.71 ± 0.24*	1422	120	Exp	-0.43 ± 0.27	105.1 ± 15.2	5.67 ± 0.27
2013-05-13 04:31 - 05:14	43	0.96 ± 0.11	188	36	Exp	3.00 ± 0.14	31.0 ± 2.0	>6
2013-05-13 17:15 - 17:58	30	2.41 ± 0.21	371	43	Exp	-0.24 ± 0.48	141.7 ± 37.6	3.91 ± 0.31

Continued on next page

Date and Time	Exposure (minutes)	Flux (10^{-5} cm^{-2}s^{-1})	TS	ΔTS	Model	Photon Index	Cutoff Energy	Proton Index
2013-05-13 20:26 - 21:09	43	1.72 ± 0.14	371	43	Exp	0.21 ± 0.73	79.7 ± 24.8	5.55 ± 0.51
2013-05-14 01:08 - 01:55	47	1.02 ± 0.09*	292	46	Exp	0.55 ± 0.67	65.2 ± 15.5	>6
2013-05-14 02:43 - 03:31	47	3.30 ± 0.15	1518	193	Exp	0.62 ± 0.32	77.0 ± 9.1	4.95 ± 0.24
2013-05-14 04:19 - 05:06	47	2.32 ± 0.16	546	87	Exp	1.26 ± 0.61	53.8 ± 9.4	5.91 ± 0.43
2013-05-14 05:59 - 06:42	42	0.59 ± 0.09	105	19	Exp	1.05 ± 1.43	54.3 ± 24.1	>6
2013-05-15 04:12 - 04:58	46	0.36 ± 0.07	51	9	PL	-2.62 ± 0.22	-	-
2013-10-11 06:56 - 07:39	42	12.55 ± 0.36	3949	317	Exp	-0.34 ± 0.16	130.8 ± 11.5	4.33 ± 0.12
2013-10-25 08:15 - 08:57	42	1.15 ± 0.12*	211	21	Exp	0.07 ± 0.88	79.2 ± 29.9	6.00 ± 3.61
2013-10-28 15:45 - 16:05	21	0.81 ± 0.12	120	8	PL	-2.32 ± 0.15	-	-
2014-01-06 07:55 - 08:30	34	0.42 ± 0.09	52	13	Exp	1.84 ± 2.16	48.8 ± 26.1	5.77 ± 1.94
2014-01-07 18:41 - 19:29	48	0.29 ± 0.07	32	5	PL	-2.68 ± 0.27	-	-
2014-02-25 01:09 - 01:29	20	169.60 ± 1.97*	24030	2121	Exp	-0.33 ± 0.06	154.4 ± 5.2	3.78 ± 0.04
2014-02-25 04:20 - 04:40	20	28.34 ± 0.91	2707	370	Exp	1.17 ± 0.28	46.9 ± 3.7	>6
2014-02-25 07:30 - 07:51	21	0.87 ± 0.17	74	11	Exp	2.39 ± 2.53	28.8 ± 14.4	>6
2014-06-10 14:00 - 14:26	25	1.17 ± 0.26	49	5	PL	-2.47 ± 0.22	-	-
2014-06-11 09:06 - 09:30	24	0.99 ± 0.26*	30	3	PL	-2.77 ± 0.30	-	-
2014-09-01 11:02 - 11:18	16	378.66 ± 6.63	41620	-	Exp	-1.03 ± 0.09	177.5 ± 10.3	4.70 ± 0.07
2014-09-01 12:25 - 12:57	32	2.98 ± 0.22	545	31	Exp	-1.16 ± 0.29	289.6 ± 81.8	3.72 ± 0.24
2014-09-10 17:35 - 17:53	18	7.44 ± 0.51*	559	66	Exp	0.35 ± 0.54	86.5 ± 20.2	4.66 ± 0.34
2015-06-21 02:09 - 02:42	33	0.25 ± 0.08	23	5	PL	-3.05 ± 0.39	-	-
2015-06-21 05:19 - 05:53	33	1.26 ± 0.15	162	16	Exp	-0.18 ± 0.74	117.8 ± 43.7	4.29 ± 0.56
2015-06-21 08:30 - 09:03	33	0.81 ± 0.13	101	12	Exp	0.03 ± 1.14	109.8 ± 56.9	4.24 ± 0.67
2015-06-21 11:40 - 12:14	33	0.38 ± 0.10	31	10	Exp	2.05 ± 2.61	48.8 ± 28.8	>6

Continued on next page

Date and Time	Exposure (minutes)	Flux (10^{-5} cm^{-2}s^{-1})	TS	ΔTS	Model	Photon Index	Cutoff Energy	Proton Index
2015-06-25 09:24 - 10:09	45	0.40 ± 0.08	48	6	PL	-2.72 ± 0.22	-	-
2017-09-06 08:51 - 09:19	28	1.31 ± 0.16*	130	21	Exp	0.59 ± 1.05	59.7 ± 22.0	>6
2017-09-06 12:10 - 12:35	25	0.96 ± 0.11*	156	17	Exp	0.05 ± 1.06	58.1 ± 22.8	>6
2017-09-06 13:23 - 14:10	26	2.63 ± 0.17*	604	66	Exp	0.39 ± 0.55	60.1 ± 12.1	>6
2017-09-06 15:03 - 15:40	18	2.93 ± 0.41	137	24	Exp	1.20 ± 1.29	58.8 ± 22.5	5.61 ± 0.79
2017-09-06 16:45 - 17:09	19	3.56 ± 0.52	130	24	Exp	1.24 ± 1.24	64.4 ± 22.0	5.16 ± 0.69
2017-09-06 18:14 - 18:50	36	2.73 ± 0.24	337	49	Exp	0.67 ± 0.68	70.9 ± 16.8	5.36 ± 0.48
2017-09-06 19:55 - 20:20	25	2.27 ± 0.35	96	17	Exp	0.74 ± 1.33	65.2 ± 27.1	>6
2017-09-06 21:25 - 22:00	35	2.56 ± 0.24	318	36	Exp	0.11 ± 0.67	84.2 ± 23.5	5.51 ± 0.54
2017-09-06 23:05 - 23:31	26	0.96 ± 0.22	43	4	PL	-3.06 ± 0.30	-	-
2017-09-07 00:36 - 01:11	35	0.62 ± 0.13	52	4	PL	-2.63 ± 0.22	-	-
2017-09-10 15:52 - 16:28	35	290.96 ± 2.10*	61725	4429	Exp	-0.67 ± 0.03	195.4 ± 4.5	3.74 ± 0.03
2017-09-10 17:33 - 17:58	24	76.44 ± 1.87	6112	469	Exp	-0.70 ± 0.30	248.4 ± 49.4	3.30 ± 0.06
2017-09-10 19:03 - 19:39	36	88.31 ± 1.30	16954	1819	Exp	-0.02 ± 0.07	139.5 ± 5.1	3.70 ± 0.05
2017-09-10 20:44 - 21:08	24	35.81 ± 1.34	2311	276	Exp	0.07 ± 0.22	117.5 ± 11.2	4.18 ± 0.14
2017-09-10 22:13 - 22:49	36	15.01 ± 0.53	2559	315	Exp	0.35 ± 0.22	90.8 ± 7.9	4.67 ± 0.16
2017-09-10 23:54 - 00:18	24	5.60 ± 0.54	310	68	Exp	2.03 ± 0.84	54.7 ± 11.0	4.92 ± 0.43
2017-09-11 01:23 - 02:00	36	2.38 ± 0.22	284	55	Exp	1.69 ± 0.83	47.6 ± 10.2	5.97 ± 0.54
2017-09-11 03:05 - 03:29	24	1.39 ± 0.28	59	12	Exp	1.00 ± 1.58	69.8 ± 34.0	5.02 ± 0.97
2017-09-11 04:34 - 05:11	37	0.49 ± 0.11	43	2	PL	-2.65 ± 0.24	-	-

Table 6.1: Gamma-ray spectral parameters for each `SunMonitor` time window associated with solar flares detected by the Fermi-LAT. Columns: 1) Start and End Date indicates the time (UT) when the Sun is into the FoV; 2) Exposure in minutes, defined as the effective duration of observation (accounting for time loss due to the SAA); 3) Flux averaged over the time window computed for the preferred spectral model; 4) TS value for the Power Law model; 5) Difference of TS between EXP and PL models, a value above 9 indicates the EXP is favored; 6) Best spectral model; 7) Photon Index from the PL or the PLEXP models; 8) Cutoff energy when the PLEXP is preferred; 9) Best fit proton distribution index (* Fermi-LAT response affected by pile-up, data from S15 event class).

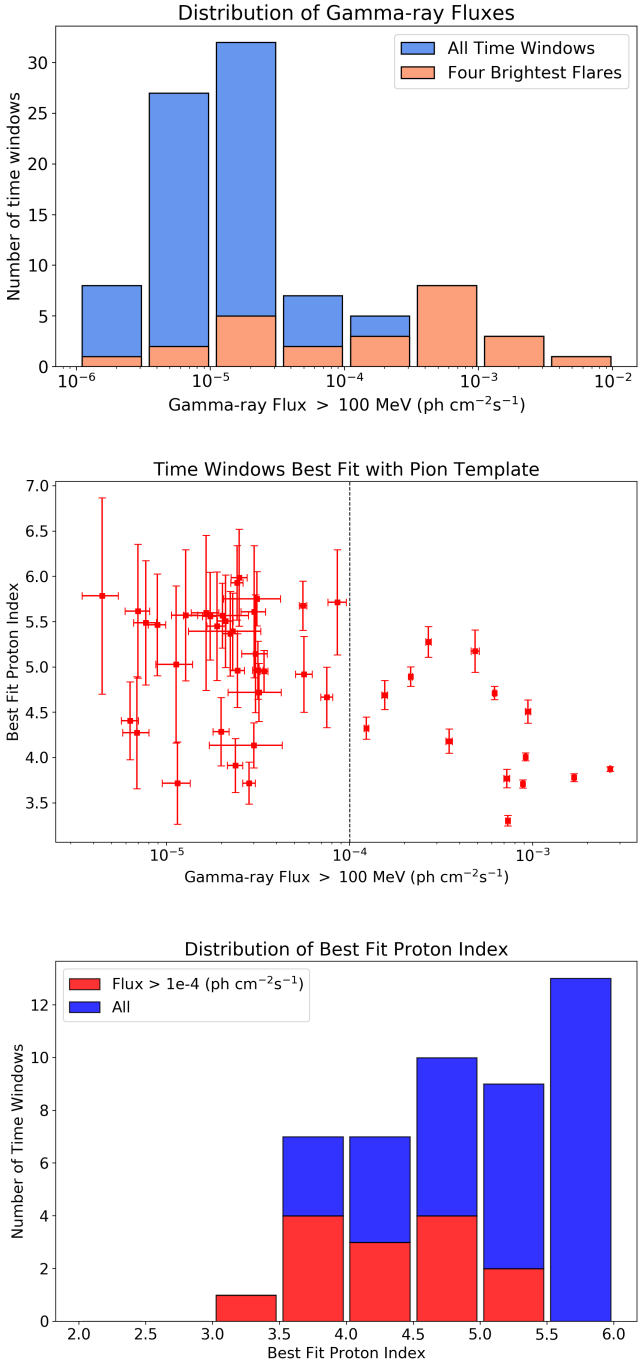

Figure 6.3: Characteristics of the gamma-ray emission in each `SunMonitor` time window (92 in total). Upper panel: Distribution of the fluxes measured in all windows. Middle panel: Best fit proton index as a function of the flux, only for windows when the pion template is preferred (47 time windows). Lower panel: Distribution of the best fit proton index in those windows.

For the time windows in which the pion template model is preferred (47 out of the 92),

Figure 6.3 middle panel presents the relation between the flux and the inferred best fit proton index. It appears that very bright flares (flux greater than 10^{-4} cm^{-2} s^{-1}) tend to be associated with slightly harder indexes (as can be seen in the proton index distribution (see Figure 6.3 lower panel). However the values of the best fit proton spectral index can vary largely from flare to flare. It can also vary with time during a long lived flare, although that is not always the case. For example during the 2017-09-06 flare the best fit index is constant at a value of about 5.5 for a duration of 9 hours. However, during the 2017-09-10 flare, the gamma-ray spectra show a continuous softening of the inferred proton power law distribution from 3.3 to 6.1 over more than 9 hours (see Figure 5.12 in the previous Chapter 5).

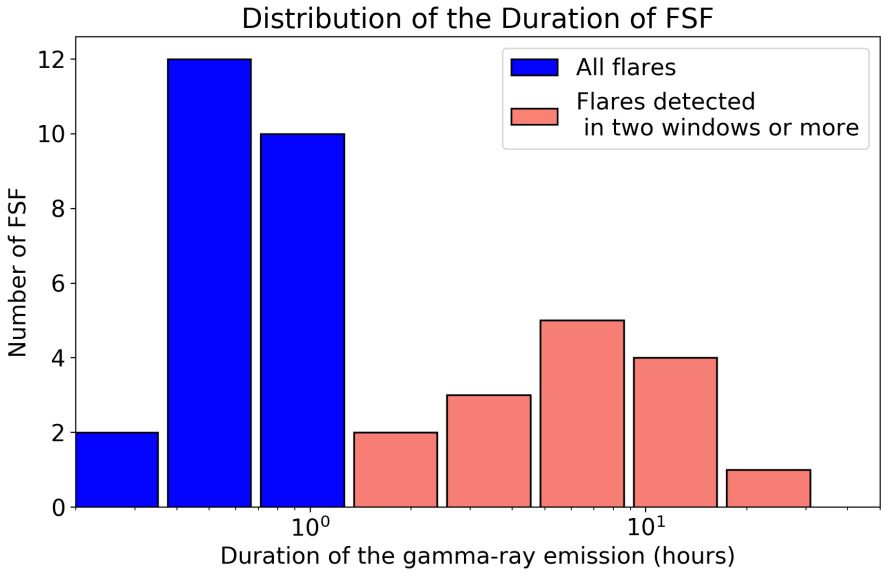

Figure 6.4: Durations of the gamma-ray emission for each Fermi-LAT Solar Flare in the catalog (excluding the LLE-only flares).

With the Sun being observable for 20 to 40 minutes time window every 1.5 to 3 hours, it is challenging to estimate the true duration of the gamma-ray emission. If the duration of a flare is defined as the time between the start of the gamma-ray detection until the end of the last time window, then the duration of flares ranges from minutes up to 20 hours as in the case of the 2012-03-07 flare. The distribution of duration of FLSF is shown in Figure 6.4. The duration of all flares detected in only one time window is only the duration of the window itself, mostly smaller than 1 hour. The duration of the flares detected in two windows or more is distributed around 6 hours. We will see in the next section that there are other ways to define the duration of the gamma-ray emission with respect to the X-ray activity.

Start Time	Duration (sec)	$Flux_{30}$	$Flux_{100}$	TS	SunMon detected	Out of FoV
2010-06-12 00:55:49	30	446.01 ± 35.18	190.60± 11.76	215		X
2011-08-09 08:01:51	250	31.20 ± 0.24	13.02± 0.22	124	X	
2011-09-06 22:18:07	100	53.97 ± 1.45	16.55± 1.10	125	X	
2011-09-24 09:35:53	100	65.23 ± 1.67	0.43± 0.07	8	X	
2012-06-03 17:53:20	20	110.54 ± 5.28	49.66± 4.54	120	X	
2012-08-06 04:36:01	30	204.73 ± 4.73	1.79± 0.12	0		
2012-10-23 03:15:33	20	3078.96 ± 272.89	105.04± 20.24	4	X	X
2013-10-25 20:56:52	10	38.90 ± 0.97	1.13± 0.09	0		
2013-10-28 01:59:15	70	0.45 ± 0.03	0.00± 0.00	5		
2013-10-28 04:37:48	50	25.93 ± 1.27	0.00± 0.00	3		
2013-10-28 20:54:47	50	9.82 ± 0.55	0.33± 0.05	7		
2014-02-25 00:44:47	400	1406.93 ± 24.95	631.28± 26.22	2652	X	X
2014-06-10 12:47:18	25	6.73 ± 1.26	2.86± 1.06	18	X	
2017-09-10 15:57:47	325	1059.78 ± 8.84	600.62± 6.59	13338	X	

Table 6.2: LLE Spectral results for all LLE flares. $Flux_{30}$ and $Flux_{100}$ indicate the flux computed from 30 MeV to 10 GeV and from 100 MeV to 10 GeV respectively (in units of 10^{-5} $cm^{-2}s^{-1}$).

6.2.2 LLE Results

The follow up of all Fermi-GBM triggers yielded the detection of prompt emission for 14 solar flares: 8 are associated with gamma-ray emission also detected with the `SunMonitor` approach and 6 are detected with the LLE method only. The results of the LLE analysis are listed in Table 6.2: the start time and duration of the flare identified from the LLE lightcurve, the flux averaged over the duration of the flare in two energy bands (from 30 MeV to 10 GeV and from 100 MeV to 10 GeV). The TS reports the significance of the of the gamma-ray emission above 60 MeV with a pion template spectral model. A value below 9 means that the emission above 60 MeV is not significant, even if the flare is detected above 30 MeV. This is caused by the very soft spectrum of some flares. The table also lists whether the gamma-ray flare is detected by the `SunMonitor` approach and whether the LLE detection was within a `SunMonitor` time window, which can be relevant when trying to understand the evolution of the gamma-ray emission flux and spectrum.

The duration is estimated from the photon count variation and ranges from 10 seconds to 6.7 minutes. The flux values are computed averaged over the entire duration of the LLE flare. Eleven of the LLE flares happened while the Sun was in the FoV, but for 3 of them it was not the case. This is because the effective area associated with the LLE event selection is much larger than the SOURCE event class at larger incidence angles. Two of those flares were followed by gamma-ray emission detected in the `SunMonitor` analysis. For 11 flares in the FoV, 5 are not detected above 60 MeV by the `SunMonitor` approach and an upper limit was obtained for the time window when the flare happened. For the 6 flares detected with both approaches in the same time window, the fluxes above 100 MeV reported in the `SunMonitor` results Table 6.1 are the averaged value over the entire time window.

A full characterization of the LLE analysis of those flares will be presented in a follow-up publication.

A full description of the FLSF catalog is presented in Appendix A with the temporal, spectral and spatial characteristics of the gamma-ray emission with the LLE and/or `SunMonitor` approaches.

From the gamma-ray emission detected by the Fermi-LAT, we compare the events to the solar activity in Hard X-rays detected by the GOES, STEREO and RHESSI missions, the Fermi-GBM, as well as protons detected by the GOES and STEREO.

6.3 Associations and Classifications of FLSF

We associate each significant detection of gamma-ray emission due to solar flares with solar events as seen by other instruments.

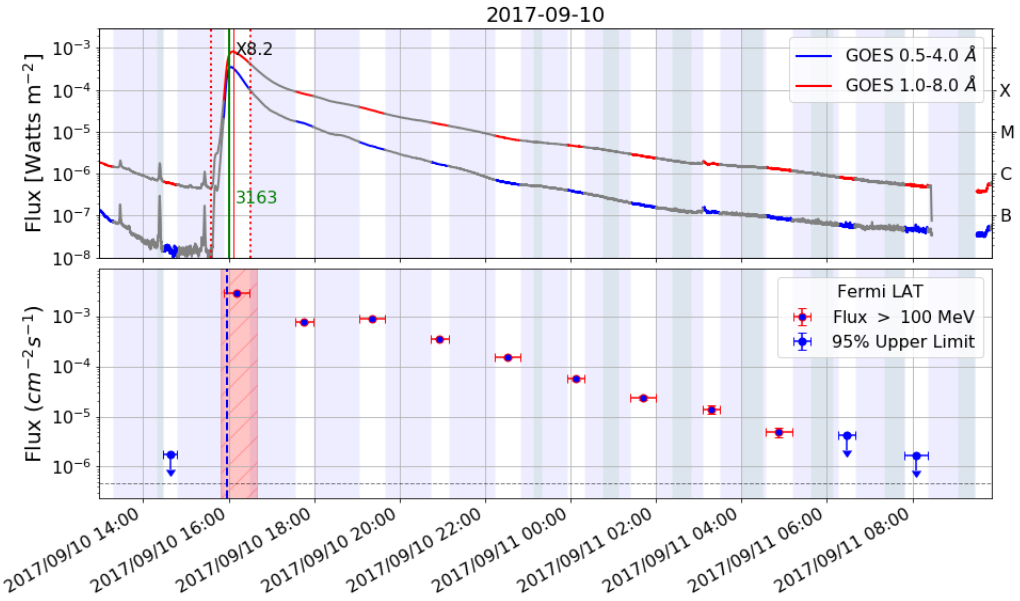

Figure 6.5: Time evolution of the GOES X-rays and Fermi-LAT gamma rays. The blue shaded regions indicate that the Sun is not observable by the Fermi-LAT at those times. The light green shaded regions indicate the time when Fermi is in the SAA. The red hashed band corresponds to a BTI and all coincident Fermi-LAT flux points are computed with the S15 event class. In the top panel for the GOES X-ray lightcurve, the vertical red lines mark the GOES X-ray flare (solid for peak time, dashed for start and end of the flare). The vertical green line show the detection time of the very fast CME associated with this flares (at 2 solar radii). In the bottom panel, the flux points correspond to the average flux computed within the time window shown. The vertical blue line indicates the time of a LLE flare detected.

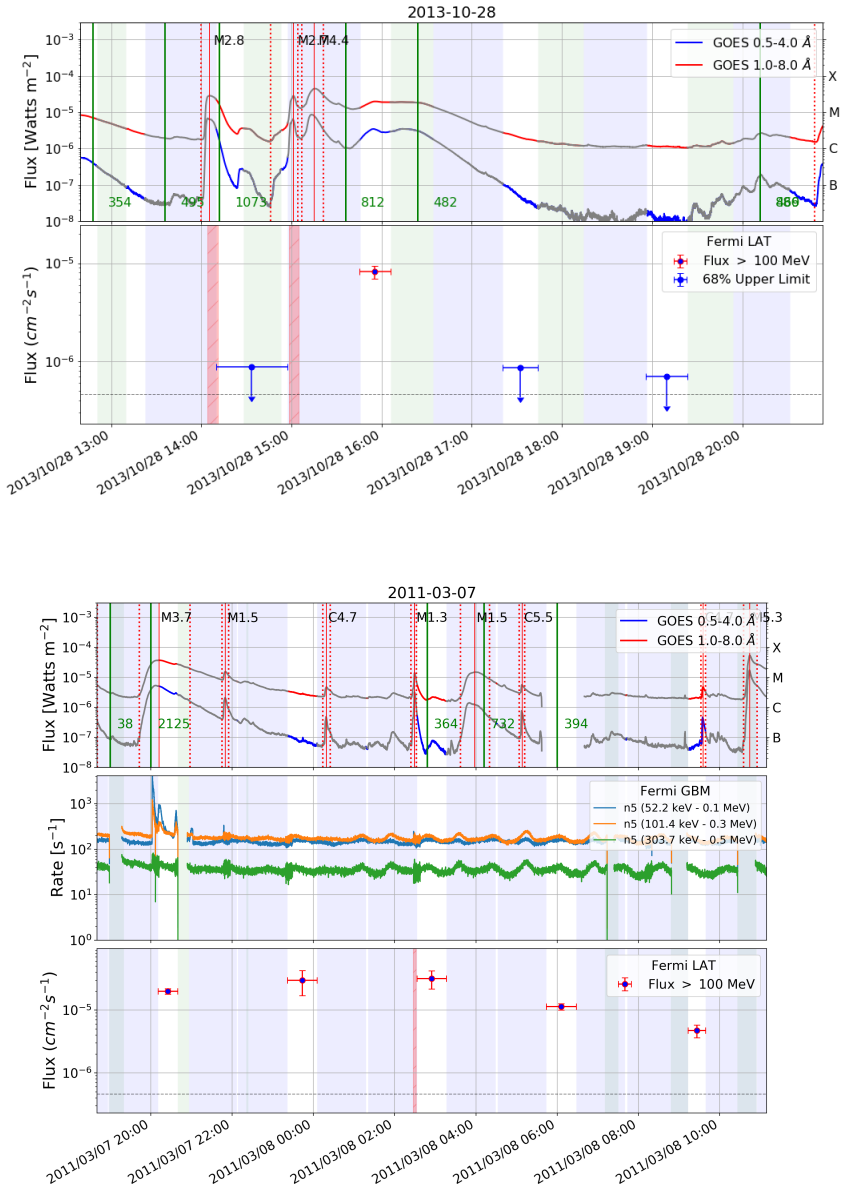

Figure 6.6: Examples of the 2013-10-28 flare (upper panel) with multiple flaring activity prior to the start of the gamma rays. The M2.7 and M4.4 and 812 km/s CME all from the same AR are likely associated with the gamma-ray emission, although it is possible that the activity from another AR (M2.8 flare and 1073 km/s CME) may contribute to the gamma-rays. The 2011-03-07 illustrates the case of prolonged solar activity throughout the duration of the gamma-ray emission (lower panel).

For most cases the association of the gamma-ray emission to a specific GOES flare or CME is straightforward: a FLSF can be linked to a single flare or CME within an hour of the start of the gamma rays, as we saw with the case of the 2017-09-10 flare in the previous Chapter (see summary lightcurve in Figure 6.5). In some cases however, the association with a single GOES flare or a single CME is not evident when several events happen within a short timeframe. An individual look for each of these events in the catalog leads to a likely association. For example in the case of the 2013-10-28 flare in Figure 6.6: a series of three M-class flares occurred, accompanied by two CMEs, all prior to the gamma-ray detection. In this case the gamma-ray emission is likely associated with the pair of flares M2.7 and M4.4 from the same AR and the associated CME with speed 812 km/s. We take note of those cases as potentially unclear associations due to multiple solar activities prior to the start of the gamma rays.

Another source of uncertainty for FLSF associations is due to periods of heightened solar activity with multiple GOES flares and CMEs occurring over the entire duration of the gamma-ray emission. It raises the question of which solar flare(s) is actually contributing to the gamma-ray emission, and whether multiple flares contributing to the gamma-rays lengthen the duration of the FLSF. The occurrence of multiple flares during the gamma-ray emission happened for the 2011-03-07 flare with a total of 4 M-class and two C-class flares over the 13.5 hours of gamma-ray emission (see lower panel in Figure 6.6). This is also the case for two other flares: 2015-06-21 and 2017-09-06 lasting 10 and 13 hours respectively. We aim to understand the characteristics of the long duration sustained and it is important to understand whether multiple solar flares contribute to the gamma rays during the same time range. In a comparison work, these cases will need to be set aside since we can not trace the origin to a single AR or flare.

In the cases of the Behind-The-Limb flares the Soft X-ray emission detected by GOES is either absent or biased toward lower flux than for a disk flare. For those, the STEREO satellites provides the direct EUV observation of the flare, and the estimated equivalent peak X-ray flux is used when comparing the characteristics of the flares (see the details of the procedure explained in Nitta et al. 2013 and Ackermann et al. 2017).

Table 6.3 lists the main results of the Fermi-LAT detections and the characteristics of the solar flares and CMEs they are likely to be associated with:

- Name of the flare chosen by the date of the start of the gamma-rays, with an added a, b, c for multiple flares in one day.
- Duration of the gamma-ray emission (in hours), calculated from the start of the GOES X-ray flare to the end of the gamma-ray emission.
- Type of gamma-ray emission Prompt, Delayed and or BTL as defined below.

Name	Duration (hrs)	Flare Type	GOES Class	CME Speed (km.s^{-1})	SEP (MeV)	HXR (keV)
2010-06-12 (A.1)	0.4	Prompt	M2.0	486	10	1000
2011-03-07 (A.2)	13.9	Delayed	M3.7*	2125 (H)	50	>100
2011-06-07 (A.3)	5.3	Delayed	M2.5	1255 (H)	100	100
2011-08-04 (A.4)	1.9	Delayed	M9.3	1315 (H)	100	300
2011-08-09 (A.5)	0.4	Prompt Delayed	X6.9	1610 (H)	100	300
2011-09-06 (A.6)	0.6	Prompt Delayed	X2.1	575 (H)	100	1000
2011-09-07 (A.7)	1.9	Delayed	X1.8	792	50‡	500
2011-09-24 (A.8)	0.4	Prompt Delayed	X1.9	1936	50‡	1000
2012-01-23 (A.9)	5.8	Delayed	M8.7	2175 (H)	100	>100
2012-01-27 (A.10)	7.3	Delayed	X1.7	2508 (H)	605	>100
2012-03-05 (A.11)	5.4	Delayed	X1.1	1531 (H)	40‡	>100
2012-03-07 (A.12)	20.2	Delayed	X5.4*	2684* (H)	605	1000
2012-03-09 (A.13)	7.3	Delayed only	M6.3	950 (H)	100‡	>100
2012-03-10 (A.14)	6.0	Delayed	M8.4	1296 (H)	100‡	>50
2012-05-17 (A.15)	2.9	Delayed	M5.1	1582 (H)	605	>100
2012-06-03 (A.16)	0.2	Prompt Delayed	M3.3	605	-	100
2012-07-06 (A.17)	1.1	Delayed	X1.1	1828 (H)	100	-
2012-08-06 (A.18)	0.1	Prompt	M1.6	198	-	100
2012-10-23 (A.19)	1.1	Prompt Delayed	X1.8	-	-	1000
2012-11-13 (A.20)	0.1	Prompt	M6.0	851	-	100
2012-11-27 (A.21)	0.2	Prompt Delayed	M1.6	-	-	500
2013-04-11 (A.22)	0.6	Delayed only	M6.5	861 (H)	100	100
2013-05-13a (A.23)	3.4	Delayed	X1.7	1270 (H)	60	>300
2013-05-13b (A.24)	5.4	Delayed	X2.8	1850 (H)	60	800
2013-05-14 (A.25)	6.7	Delayed only	X3.2	2625 (H)	60	500
2013-05-15 (A.26)	3.6	Delayed only	X1.2	1366 (H)	50	100
2013-10-11 (A.27)	0.6	BTL Delayed	M4.9†	1200 (H)	60	>10
2013-10-25a (A.28)	1.1	Delayed	X1.7	587 (H)	60	300
2013-10-25b (A.29)	0.1	Prompt	M1.9	-	60‡	100
2013-10-28a (A.30)	0.3	Prompt	X1.0	695 (H)	-	1000
2013-10-28b (A.31)	0.1	Prompt	M5.1	1201	-	1000
2013-10-28c (A.32)	1.3	Delayed	M2.7*	812 (H)	60	50
2013-10-28d (A.33)	0.1	Prompt	M1.5	771	100‡	100
2014-01-06 (A.34)	0.5	BTL Delayed	X3.5†	1402 (H)	605	>6
2014-01-07 (A.35)	1.4	Delayed	X1.2	1830 (H)	100	>20
2014-02-25 (A.36)	7.2	Prompt Delayed	X4.9	2147 (H)	100	7000
2014-06-10 (A.37)	1.8	Prompt Delayed	X1.5	1469 (H)	60	1000
2014-06-11 (A.38)	0.5	Delayed	X1.0	829	-	1000
2014-09-01 (A.39)	2.0	BTL Delayed	X2.4†	1901 (H)	100	>100
2014-09-10 (A.40)	0.5	Delayed	X1.6	1071*	100	100
2015-06-21 (A.41)	10.2	Prompt Delayed	M2.7*	1366 (H)	10	>50
2015-06-25 (A.42)	2.1	Delayed	M7.9	1627 (H)	10	1000
2017-09-06a (A.43)	0.3	Prompt	X2.2	391	-	300
2017-09-06b (A.44)	13.3	Delayed	X9.3*	1571 (H)	100	>300
2017-09-10 (A.45)	13.6	Prompt Delayed	X8.2	3163 (H)	605	3000

Table 6.3: Catalog of Fermi-LAT Solar Flares and their likely associations. See reference listed in the first column for the relevant Section in Appendix A. (*) in cases of possible associations with two GOES flares or two CMEs; † indicates the estimated X-ray flux for the BTL flares; the CME speed noted with (H) for Halo CMEs, which corresponds to a width of 360°).

- The X-ray GOES class (estimated for BTL flares).
- The speed of the CMEs and width are listed if the FLSF is associated with a CME (3 FLSF are not associated with a CME).
- Maximum SEP energy detected by GOES or STEREO in their different channels.
- Maximum HXR energy detected by RHESSI or Fermi-GBM in their different channels.

The analysis of the links between the gamma-ray flares and the characteristics of the solar activity will be detailed in the next Chapter.

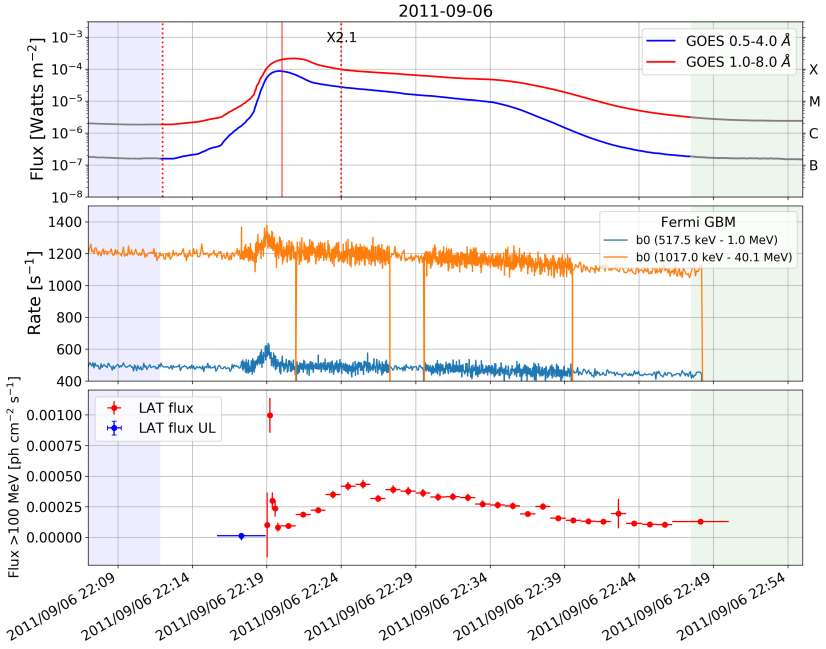

Figure 6.7: Example of the 2011-09-06 flare with a Prompt component coincident with the bright HXR peak followed by a gamma-ray delayed emission.

Different patterns emerge from the comparison of the timing of the gamma-ray emission and the evolution of the solar activity and we describe here a classification of the FLSF. In particular, the Hard X-ray emission traces the high-energy electron population accelerated during the flare energy release. Gamma-ray signatures of protons accelerated by the same processes and on the same time-scales have been observed in the past by SMM and EGRET. Gamma-ray emission evolution synchronous to the HXR evolution is therefore referred to

Prompt emission. A large number of solar flares observed by the Fermi-LAT do not fall in that category: gamma-ray emission is detected beyond the end of the HXR emission and even the end of the SXR seen by GOES. We refer to that general category as **Delayed** emission. The classification or type of behavior is listed in the column "Flare Type" of Table 6.3. For each FLSF from the catalog pipeline with a time window coincident with the prompt phase of a solar flare, we compare the HXR evolution observed by the two instruments of the Fermi-GBM to a finely time-resolved gamma-ray lightcurve.

A flare is **Prompt** only if the gamma-ray emission does not extend beyond the HXR duration. All flares detected through the LLE method are associated with Prompt emission, but some exhibit delayed emission as well. This is the case of the 2011-09-06 flare in Figure 6.7. A Prompt component coincident with the bright HXR peak appears in gamma rays and is immediately followed by a second phase lasting for more than 20 minutes after the start of the flare. This phase consists of a second less bright peak with a longer rise and fall timescales, but there is no sign of such behavior in the HXRs. The Sun passed in the FoV two hours later and no gamma rays were detected.

Because of the observing strategy of the Fermi-LAT, for more than half of the FLSF the prompt phase of the flare in X-rays is out of the FoV, so we do not have information whether they had a prompt component. But nevertheless, gamma-ray emission was detected in the minutes to hours following, making them Delayed flares (see Figure 6.8). In some cases the detection consists of a single time window and for others in multiple time windows with gamma rays lasting up to 20 hours. But all those cases show the common evidence of high-energy protons in the solar environment, well beyond the signatures in HXR of the high-energy electrons.

Sixteen FLSFs belong to the **Delayed** category and are detected in multiple time windows: 5 of those are detected in 2 time windows, and 11 flares are detected in at least 3 up to 11 time windows (over almost 20 hours). Out of the 11 flares detected in 3 or more time windows: 7 of those show a pattern of rise and decay phases, delayed from the X-ray activity and 2 show a decay phase only. All flares detected in 2 time windows show a decay between the two points, but it is impossible to know if the true evolution is a decay only or a reaches a peak in between the two time windows, so this decay rate can not be properly understood.

The catalog contains 18 flares with a Prompt component, some through the LLE technique, some through the `SunMonitor` approach. In total, the LLE approach found 14 flares, 8 of which were also detected with the catalog pipeline.

Another behavior seen in a few flares can be described as Delayed-only: no significant gamma rays are detected during the prompt phase of the flare in X-rays, but gamma-ray emission seen rising and falling later on. This is the case of the 2012-03-09 gamma-ray flare,

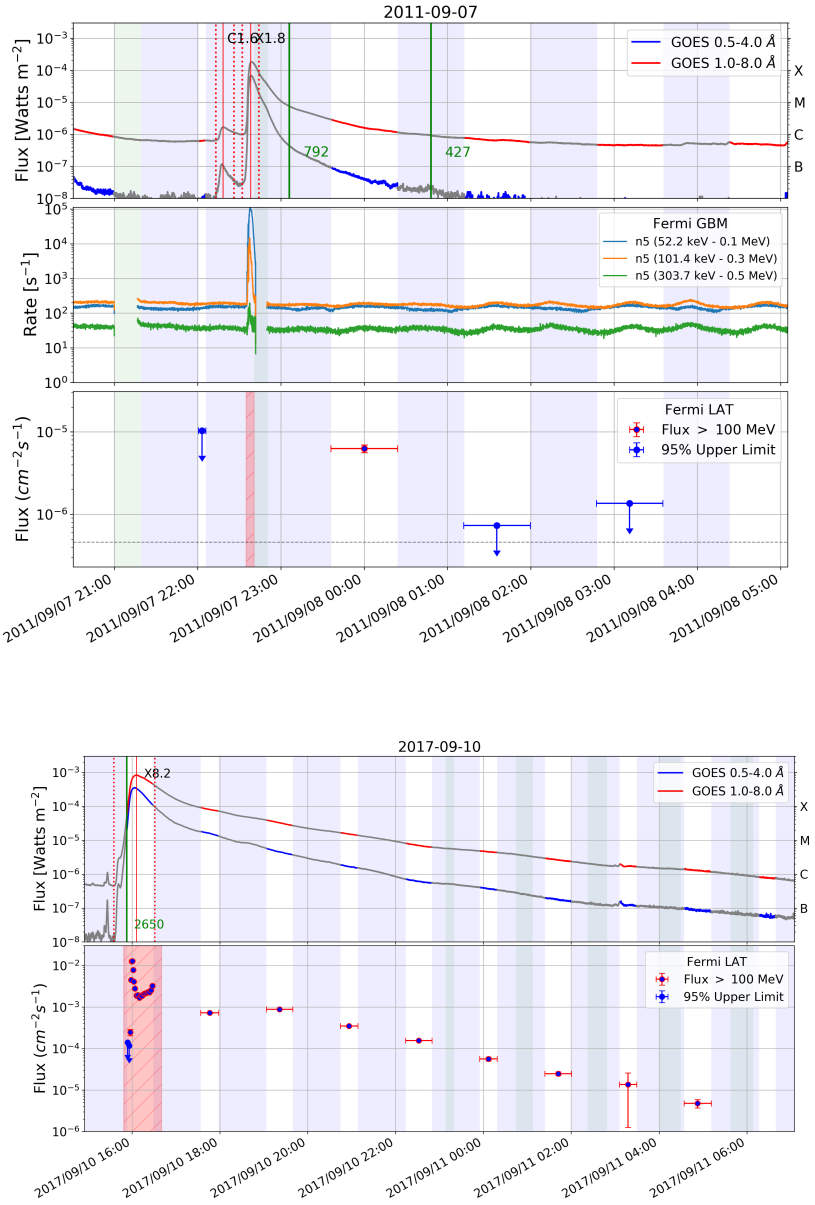

Figure 6.8: Example of two flares classified as Delayed: the 2011-09-07 flare with a single time window detection 50 minutes after then end of the GOES flare (upper panel); and the 2017-09-10 flare which extend over several hour, both Prompt and Delayed (lower panel).

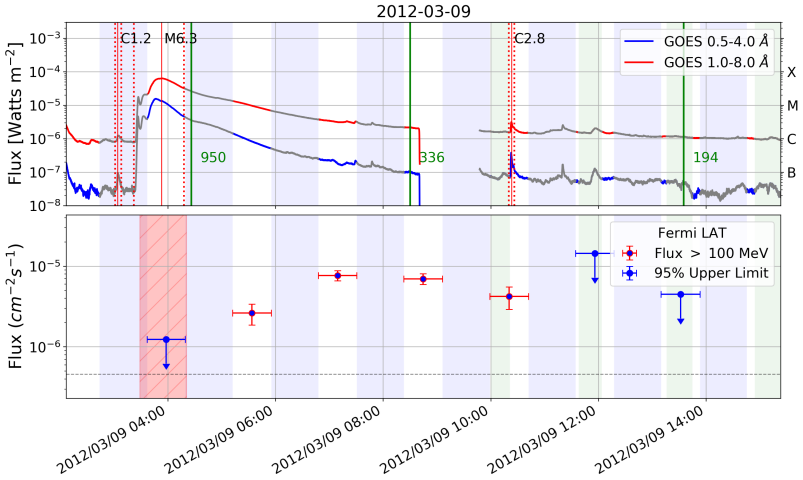

Figure 6.9: The 2012-03-09 flare lasting more than 6 hours but with no detectable high-energy gamma-ray emission in the impulsive phase, classified as *Delayed-only*.

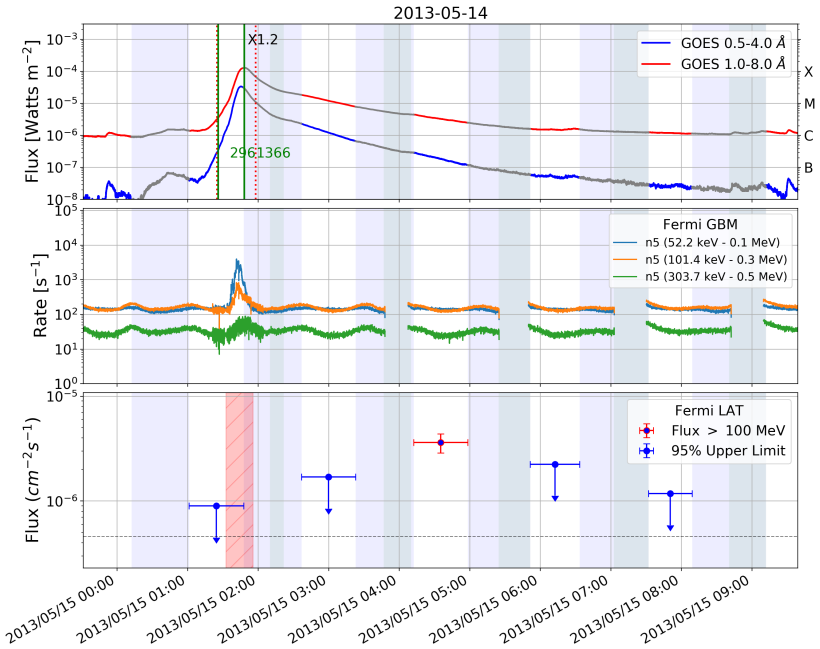

Figure 6.10: The *Delayed-only* 2013-05-15 flare with no detectable high-energy gamma-ray emission in the impulsive phase, or the following time window.

which is associated with a GOES M6.3 flare with HXR extending up to the NaI 100-300 keV channel. Most of the prompt phase was observable by the Fermi-LAT and the bright SXR affected the instrument response (BTI in red in Figure 6.9). No gamma-ray emission was detected during the peak of impulsive phase using the S15 event class or the LLE analysis method. Yet, gamma-ray emission was detected when the Sun came back in the FoV almost 2 hours after the start of the flare in X-rays and lasted for 4 orbits. It followed a rise and fall pattern reaching its peak 4 hours after the start of the flare in X-rays and ending 7 hours after the start of the flare in X-rays.

Similarly, the Fermi-LAT observed the 2013-05-15 flare with no significant emission detected during either the impulsive phase or in the first time window following the flare, but significant emission detected in the following time window (Figure 6.10). In itself, it might not a brand new type of behavior, as it can be seen as a rise-and-fall pattern with the starting flux being just below the Fermi-LAT sensitivity but the peak flux being high enough to be detected.

These behaviors highlight the possibility that high-energy emission above 100 MeV can arise at later times, even if the impulsive phase itself did not show a strong non thermal component (almost no HXR above 300 keV and no gamma rays below 30 MeV). Although these cases are rare, they are particularly interesting in understanding whether the acceleration of high-energy particles is solely due to the prompt phase of solar flares or the presence of a CME.

- Gamma-ray Duration

We saw that we can estimate the duration of the FLSF using only the gamma-ray data information: from the start of the first time window to the end of the last window, or from the start to end of the high-resolution time analysis, or from the LLE analysis. That will define the gamma-ray duration: Duration_{gamma}. But this approach fails to account for the X-ray data timing information which indicates when the release of energy and non-thermal processes started. Different start times can be used: time at the start of GOES flare, start of the HXR as seen by RHESSI or the GBM, estimated onset time of the CME. Since some flares are not associated with CMEs, and not all flares have coverage of the HXR phase, we use the start of the GOES flare as the reference time for the start of the flare, which is available for all flares (or using STEREO data for BTL flares). This will define what we refer to as Duration.

- Other publications on Fermi-LAT observations of solar flares

  Share et al. (2017) presented a list gamma-ray detections above 100 MeV seen by the Fermi-LAT with the characteristic of having a distinct component from the associated

solar flare. Compiled between 2008 and 2016, 30 gamma-ray events are listed, detected using a photometric analysis method to detected transients called 'light bucket' approach presented in the paper. All 30 detections are included in the FLSF catalog, but we want to highlight the additional gamma-ray flares:

- The 6 FLSFs detected through the LLE approach only. Indeed the work of Share et al. (2017) focused on gamma-ray emission distinct from the impulsive phase of the flare, which is the case here. They are: 2010-06-12, 2012-08-06, 2013-10-25b, 2013-10-28a, 2013-10-28b and 2013-10-28d.
- A total of 7 FLSFs were not present in that list, probably not detectable with the photometric approach chosen. They are: 2012-11-13, 2014-01-06, 2014-01-07, 2014-06-10, 2014-06-11, 2014-09-10 and 2015-06-25.
- The 3 FLSFs of year 2017

The case of a flare on June 2nd, 2011 was set aside for this work as a borderline detection. A further study of this flares is needed to establish it in the FLSF catalog and will be addressed in a later publication.

In the next Chapter I will put in context the FLSF catalog by comparing the gamma-ray data to other available catalogs tracking the solar activity.

Chapter 7

Multi-Wavelength Comparisons

Going beyond the study of single flares, a catalog of gamma-ray solar flares can help to understand the general processes at play at the highest energies and identify patterns. In the following sections we examine the possibility of trends or correlations between the characteristics of the gamma-ray emission with other solar multi-messenger data.

The results of the Fermi-LAT gamma-ray Solar Flare (FLSF) catalog is compared to other available datasets and catalogs (see Section 2.3):

- The LASCO catalog of Coronal Mass Ejections (CMEs).
- The GOES solar flare catalog.
- Solar Energetic Particles (SEP) Event and Ground Level Event (GLE) catalog.

7.1 CME Catalog

From a quick glance at the FLSF association list in Table 6.3 the large fraction of flares associated with CMEs is apparent. In this section we attempt to evaluate the link between CMEs and gamma-ray flares to make any conclusions about the role of the acceleration processes linked to CMEs and their capabilities of accelerating protons. CMEs are primarily characterized by their speed, inferred from the LASCO observations of the white-light emission at the edge of CMEs. The mass of the ejected material and the total kinetic energy can be estimated for bright CMEs, but generally involve many assumptions and are associated with large uncertainties, so they will not be considered in the population comparisons.

The LASCO catalog identifies 15841 CMEs for the entire time period covered in the FLSF catalog (Jan 2010 - Oct 2017). The average speed is 342 km/s and the maximum speed measured is a 3163 km/s CME associated the bright 2017-09-10 gamma-ray flare. The distribution of their speed is shown in Figure 7.1.

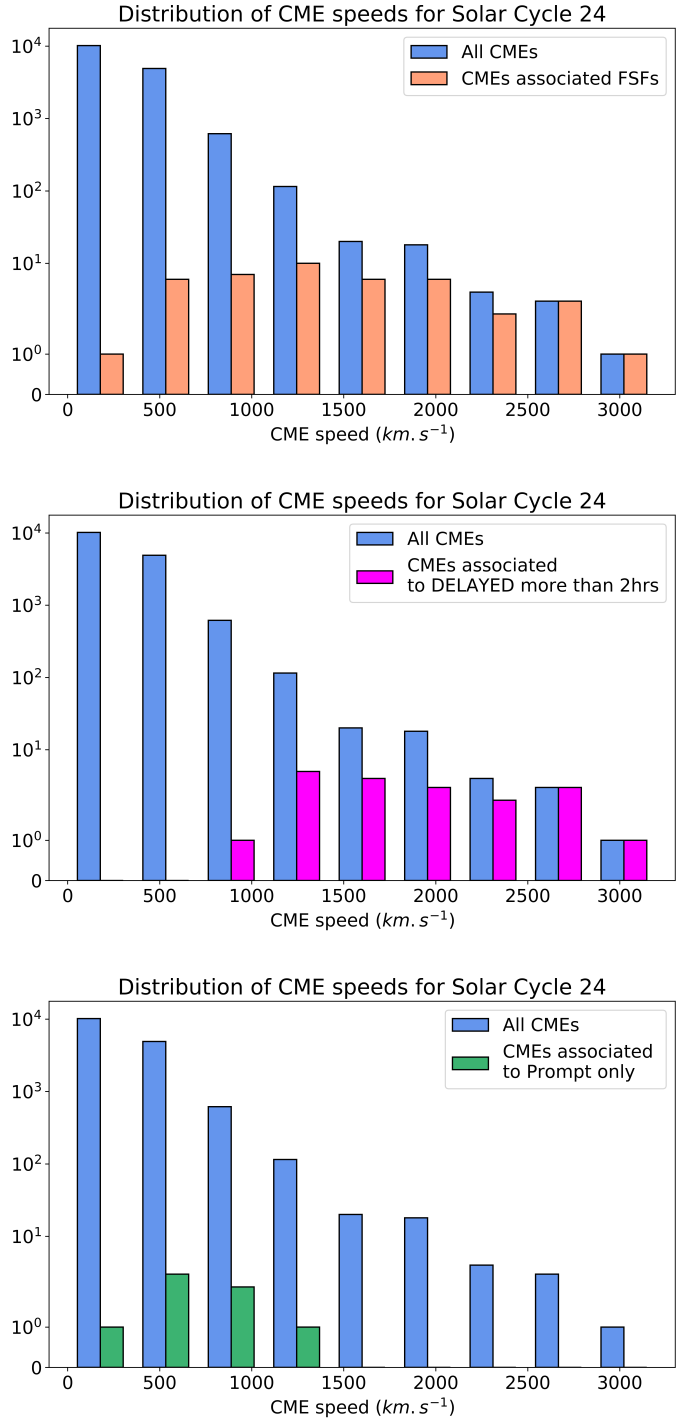

Figure 7.1: Distribution of CME speeds, in blue for the entire LASCO catalog. Top panel: distribution of the speeds of the CMEs associated with a FLSF (orange); Middle panel: distribution associated with FLSFs lasting longer than 2 hours (magenta); Bottom panel: distribution associated with Prompt-only FLSFs (green).

All FLSF but 3 flares are associated with CMEs, in most part with fast Halo CMEs. In some cases, the gamma-ray emission is coincident with the prompt phase of the flare as seen in X-rays by GOES or RHESSI, but precedes the appearance at C2 of the CME, or even the estimated onset time of the CME. The distribution of the speeds of the CMEs associated with FLSF spans the entire range of speeds, from 198 km/s to the fastest at speed 3163 km/s. The proportion of CMEs associated with FLSF gets larger with higher CME speeds, and almost half of the fastest CMEs (speed greater than 1500 km/s) are associated with FLSF (17 out of 39). However, when we break down the FLSF in categories, there is a clear distinction in the respective distributions. The category of FLSFs with a Delayed component can be split in two with a condition on the total gamma-ray duration smaller or greater than 2 hours (from start of the GOES flare to the end of the gamma rays). FLSFs that exhibit emission lasting longer than 2 hours are associated with faster CMEs, with a mean speed of 1841 km/s (shown in magenta in middle panel of Figure 7.1). We also study the category of FLSFs with a Prompt component only which tend to be associated with CMEs with lower speeds, with the mean speed at 656 km/s (shown in green in bottom panel of Figure 7.1).

The rest of the flares, associated with delayed emission of duration less than 2 hours, span the gap between those two opposite categories (not plotted).

Out of the three FLSFs that are not associated with any CME, all had a Prompt gamma-ray component detected[1]: 2013-10-25 20:56 is a LLE detection with no significant emission detected above 60 MeV ; 2012-11-27 is a Prompt flare with a short delayed component lasting less than 10 minutes. The third FLSF not being associated with any CME is 2012-10-23 and stands out as having a delayed component lasting more than an hour (gamma-rays are detected in the Prompt phase of the flare with the LLE analysis and then in the following time window).

Two FLSFs are associated with two CMEs concomitant with the start of the gamma-rays: 2012-03-07 associated with two very fast Halo CMEs ; 2014-09-10 with two CMEs from the same AR.

In Table 6.3 we also see that for a large number of flares associated with a CME, the CME is a Halo CME. Does this mean that a CME has to be a Halo CME to warrant gamma-ray emission? Or that may be an inherent characteristic of fast CMEs to be Halos. To study this link, we examine whether all fast CMEs are Halo CMEs. Figure 7.2 shows that CMEs with speed greater than 1000 km/s, have a 50% chance of being Halos CMEs with the fraction of Halo CMEs increasing with speed, and about 75% for speeds greater than 1500 km/s (see bottom panel of Figure 7.2 for the fraction of Halo CMEs in each bin).

[1] A forth event is the 2012-08-06 Prompt flare with the lowest CME speed detected, and described by the LASCO catalog as a poor detection.

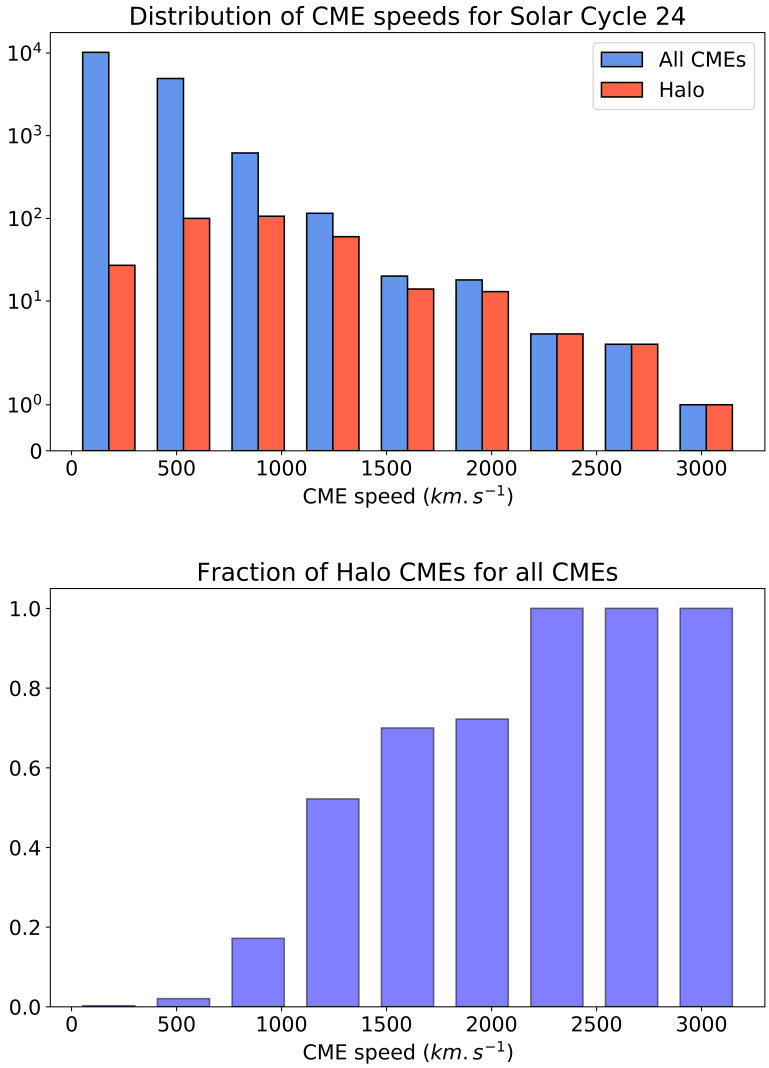

Figure 7.2: Top: Distribution of all CME speeds and Halo CMEs. Bottom: Fraction of Halo CMEs ordered by speed.

Now restricting the sample to CMEs associated with Fermi-LAT gamma-ray flares: Figure 7.3 shows that they are much more likely to be Halo CMEs with 90% chance of being a Halo CMEs if the speed is greater than 1000 km/s. Only 11 CMEs associated with FLSF are not full Halos, but 7 are partial Halos and the remaining 4 are very slow CMEs and associated with Prompt-only FLSFs.

From this comparisons we can draw the following general conclusions: 1- There is a trend for delayed to be associated with faster CMEs, but there does not seem to be any requirements on CME speed for impulsive (or even presence of a CME). 2- For almost all FLSF, the CMEs are halos, and for the one that aren't are all prompt events. 3- For a

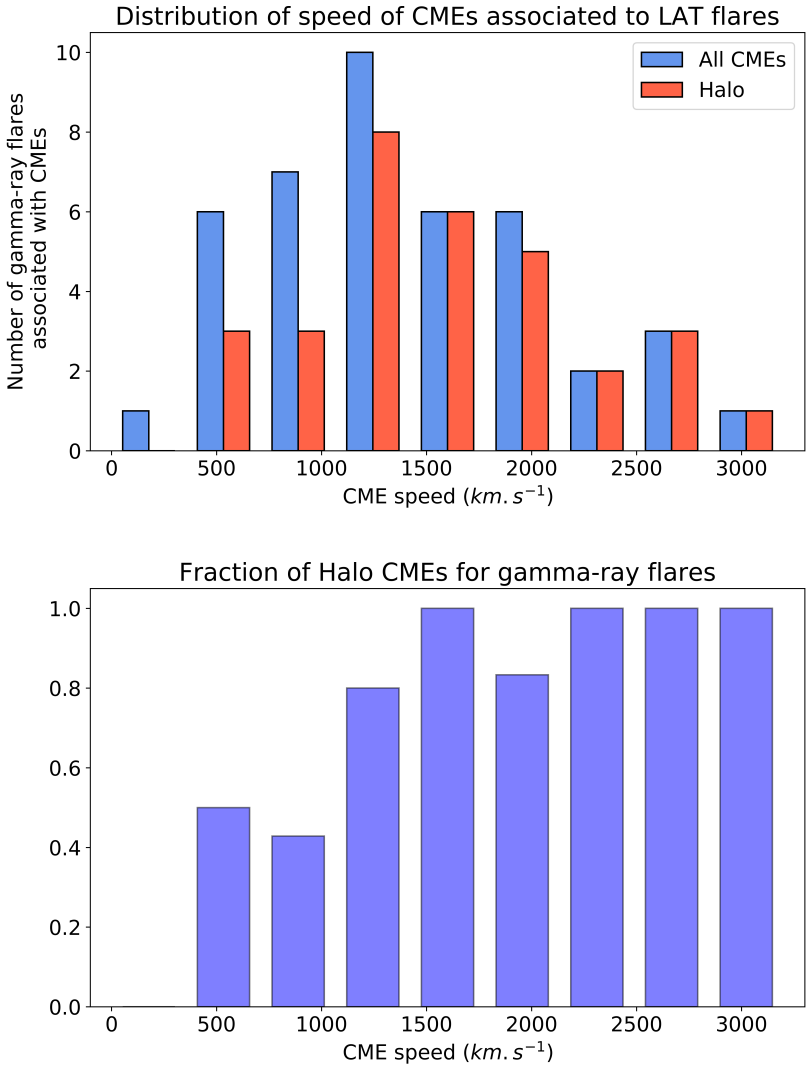

Figure 7.3: Top: Distribution of FLSF associated CME speeds and Halo CMEs. Bottom: Fraction of Halo CMEs ordered by speed.

FLSF to show a delayed component (long-lived?), it seem to requires a Halo CME of speed at least 1000 km/s.

There is one interesting counter example: the 2012-10-23 gamma-ray flare is not associated with any CME. A detailed study of this X1.8 GOES flare flare shows that an eruptive event was observed just above the AR but did not lead to the full development of a CME higher in the corona probably due to the large scale magnetic configuration before the start of the flare (priv. communication Ivan N. Sharykin). This eruptive event manifested itself with the second most powerful sunquake of solar cycle 24, leading to shock waves moving outward away from the flare site.

7.2 GOES X-ray Flares

The total of X-ray GOES solar flares during the time range of the Fermi-LAT solar flare catalog is 13431 (from January 2010 to the end of October 2017). Figure 7.4 shows the distribution of the peak flux in the 1 – 8 Å channel which is the main standard in solar flare physics defining their class. It roughly follows a power law (in blue). All FLSF are associated with GOES X-ray flares, detected by GOES for all the disk flares and by STEREO for the BTL flares. The distribution of the peak fluxes of GOES flares that are associated with any type of gamma-ray flares seen by the Fermi-LAT is plotted in Figure 7.4 (upper pannel). About half are associated with GOES M-class flares and half with X-class flares. As seen in the previous Chapter, the FLSF can be gathered in two populations, in particular flares that are have a Delayed component extending to a duration greater than 2 hours and those with a Prompt component only. The center and bottom panel in Figure 7.4 show the distributions of those categories in green and red respectively. The mean GOES peak flux for Prompt only flares and for 2-hours or more delay flares are 2.4e-04 W/m2 and 6.3e-05 W/m2 respectively. Out of the 19 flares with a 2-hour delay or greater, 11 are associated with X-class flares and 8 to M-class flares, which shows that the duration of the gamma-rays does not just scale with the peak intensity in soft X-rays.

The FLSF population can also be compared to the duration of the X-ray flares in SXR observed by GOES. All GOES flares are characterized by their fluxes and durations, computed for all GOES flares with the definition in Section 2.3.1. Figure 7.5 shows the distribution of duration of all GOES flares and the subset of flares associated with FLSF. Their distribution is rather uniform ranging from 8 minutes to 2.2 hours. However Long Delayed flares are significantly associated with longer GOES flares compared to the sample of Prompt only flares: average durations are 45 minutes and 18 minutes respectively.

7.3 SEP and GLE Catalogs

A first approach is to compare the FLSF catalog to the Major SEP events list seen by GOES (see description in Section 2.3).This catalog consists of 42 events from Jan 2010 to Jan 2016 (no full coverage of 2016 and 2017, but only 3 FLSFs occurred after 2016). Out of the 45 FLSFs in the catalog, 17 are associated with a major SEP event of that list. In addition, we examine the different SEP channels lightcurves of GOES and STEREO satellites and determine the presence or not of SEP and the maximum energy detected. This approach only provides a crude estimation of the characteristics of the SEPs since we know that the location of the flare site on the solar surface strongly affects the magnetic connectivity to the observatories and in consequence the observed flux of energetic particles.

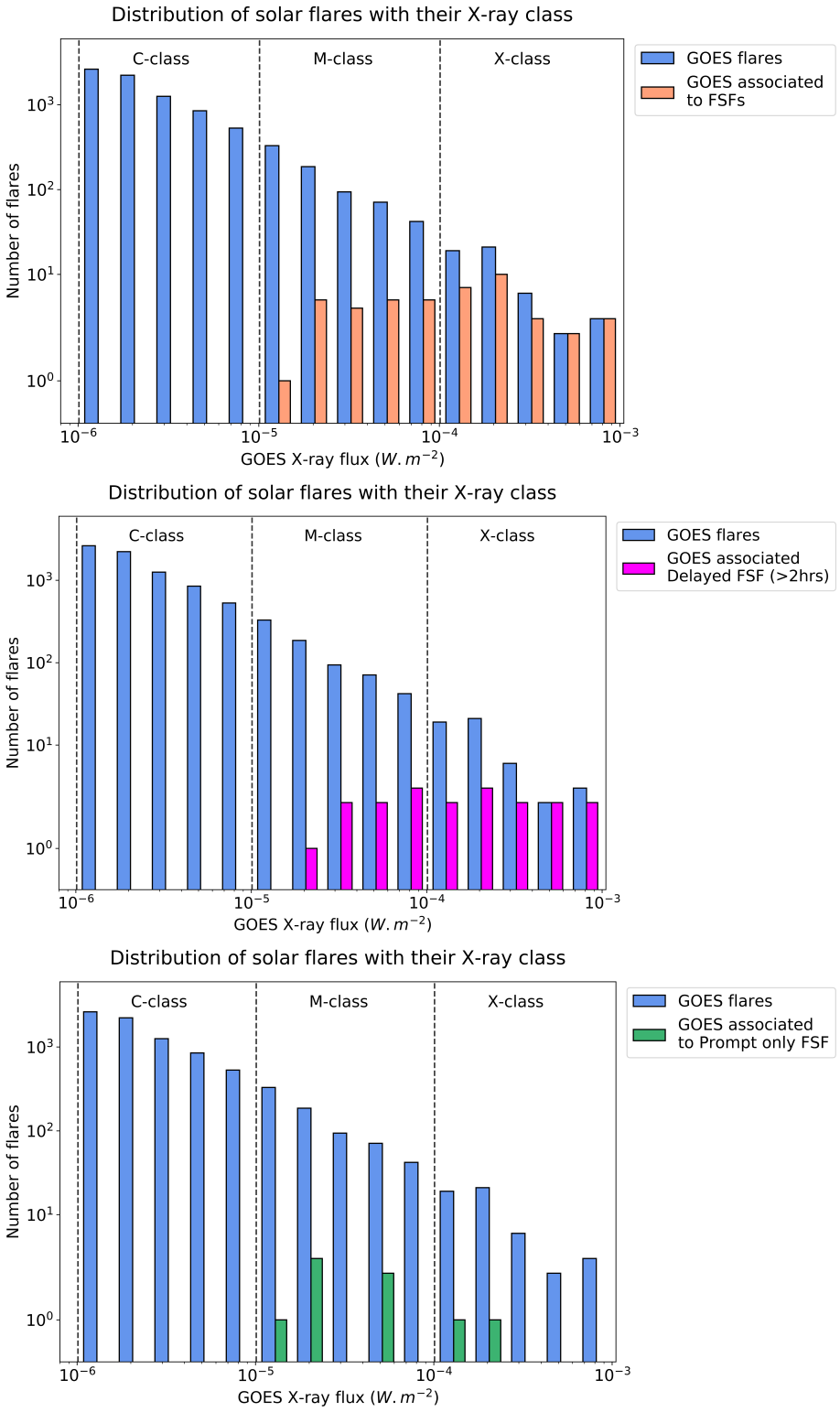

Figure 7.4: Distribution of GOES fluxes for flares associated with FLSFs, broken down by category of FLSFs.

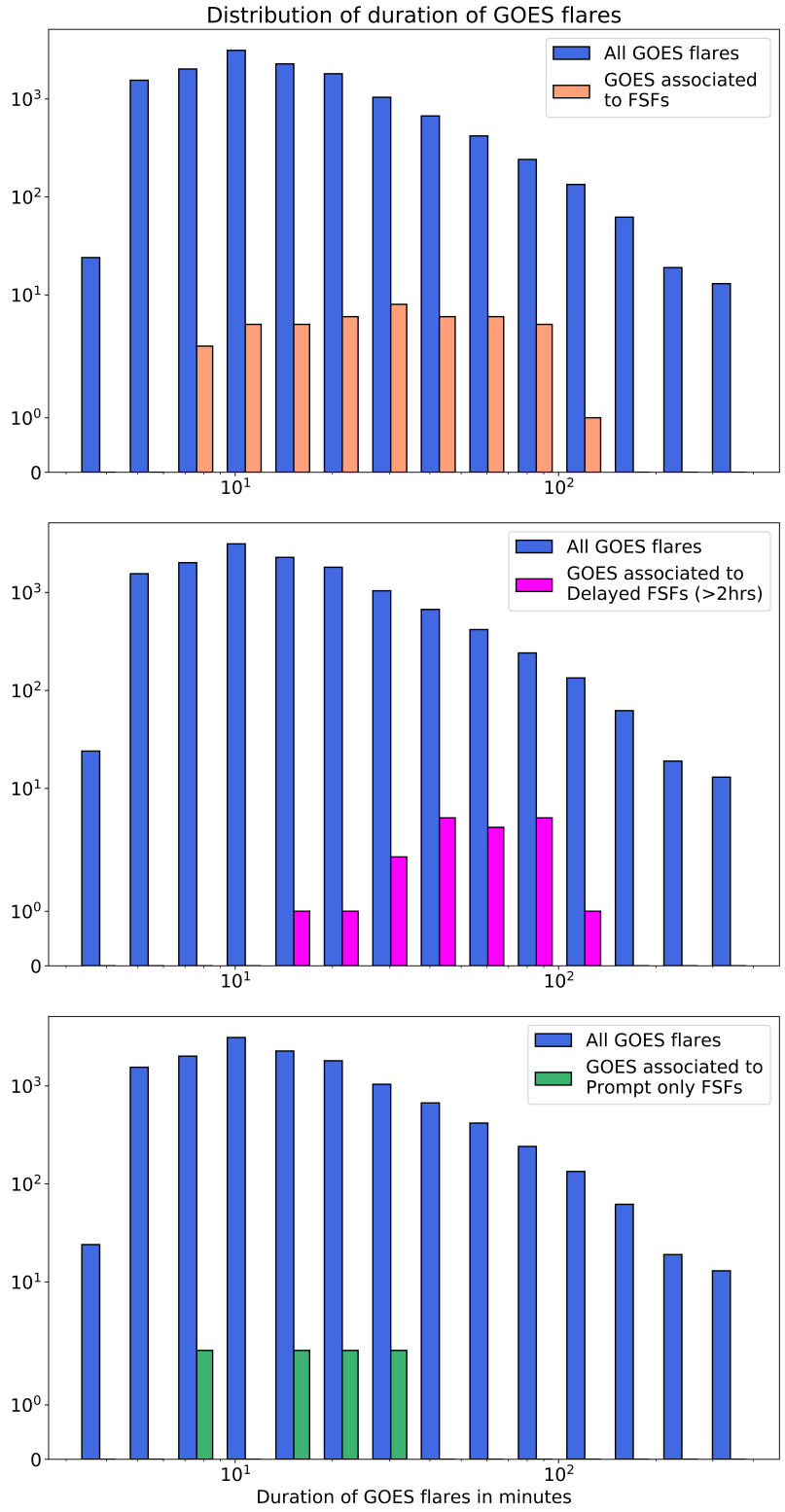

Figure 7.5: Distribution of durations of GOES flares associated with FLSFs, broken down by category of FLSFs.

For 7 FLSFs that occurred on the Eastern side of the Sun (for which we do not expect GOES to detected SEPs), SEPs were detected by STEREO instrument channels above 40 or 60 MeV. An additional 5 FLSFs are associated with significant SEP event seen by GOES, but are not listed in the catalog (among them two flares on Sept 2017), which puts the total of FLSF associated with SEP events to 29.

The rest of the the flares split in two categories: 1. the solar flare does not seem to be itself the source of an SEP event, but SEPs were present in the interplanetary space and it is unclear whether the flare contributed to the ongoing event (7 cases); 2. No SEPs were detected before or at the time of the flare (9 cases).

In this study, we do not try to evaluate the flux of SEPs, which requires a complicated analysis of the available background subtracted data and the estimation of correction factors to account for the SEP propagation in the interplanetary space and the magnetic connectivity between the position of the solar flare region and the chosen observatory. Share et al. (2017) describes a procedure applied to 14 gamma-ray solar flares and conclude that only a small fraction of the energetic protons detected as SEPs is needed to explain the flux detected with the Fermi-LAT.

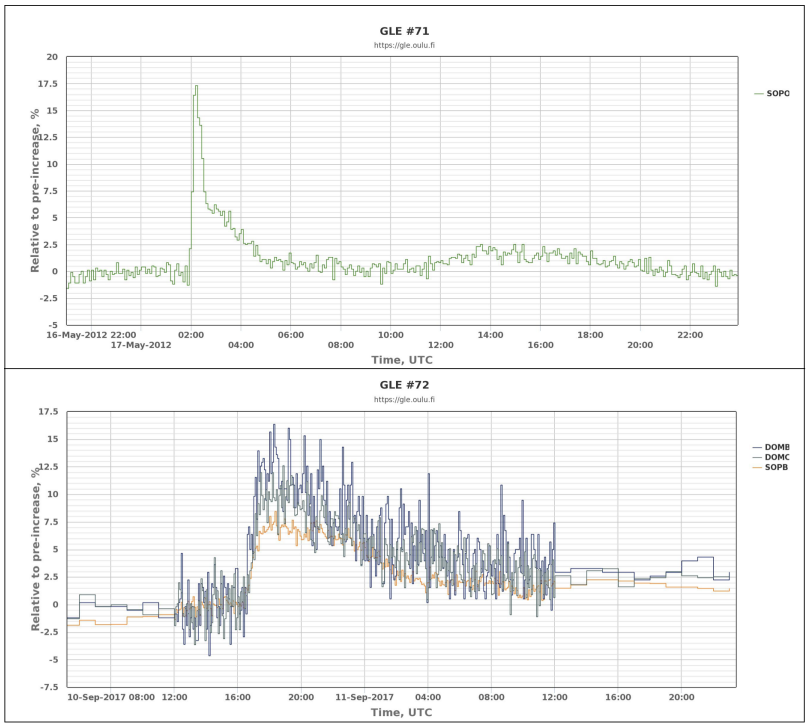

Figure 7.6: Neutron Monitor relative count rates. Top: 2012-05-17; Bottom: 2017-09-10 (see Section 2.3.4 and GLE catalog for more details).

GLE

Solar cycle 24 has been particularly poor in GLE events[2] and only two has been firmly identified GLE #71 and #72 which occurred on 2012-05-17 and 2017-09-10 (see Figure 7.6). GLE events are defined by multiple detections of neutrons in the sea-level detectors around the world. They indicate the presence of protons in space with energies higher up to 10 GeV and maybe more. Both events were detected with the Fermi-LAT. In addition to GLEs, five sub-GLE events have been identified. Sub-GLE events are detections from high-elevation neutron monitors only and correspond to less energetic events, extending to a few hundreds MeV (Poluianov et al. 2017). They occurred on 2012-01-27, 2012-03-07, 2014-01-06, 2015-06-07, 2015-10-29 at levels of relative increase of 5%, 5%, 4%, 8% and 7%, respectively (smaller than the relative increase of 17% for GLE#71). The first three correspond to flares in the FLSF catalog, but no emission was detected associated with the last two.

7.4 Others

Solar activity exhibits a large number of phenomena characterized through multi-messenger observations. In particular, we mentioned HXR as an important was way to track high-energy electrons during the prompt phase of the flare. A full joint analysis of the HXR and soft gamma-ray data from 12 keV to 10 MeV is beyond the scope of this work. We can roughly estimate the highest energy range reached by examining the HXR emission of the prompt phase of the flares associated with gamma-ray emission (seen by RHESSI or the Fermi-GBM when available). This is indicated for each flare in the Appendix A.

Another field not mentioned so far is radio observations of the Sun, which are linked to a wide range of phenomena such as emission from the quiet Sun, flares, CMEs, and interplanetary particles. Several high-energy processes related to flares emit radio waves, mostly tracking non-thermal electrons (see review by Benz 2008 and references therein). In particular, Type II radio bursts are associated with shock-accelerated electrons which indicates the capability of the shock to accelerate protons as well. A catalog of events is compiled with the description of the Type II bursts and the associated flare and CME from 1997 to 2016[3]. The full study of the association of the FLSFs with the Type II radio bursts is beyond the scope of this work, but is described by Share et al. (2017) for a subset of the FLSF catalog. Their findings indicate that all of their sample but one are associated with a Type II burst. A study of selected Fermi-LAT solar flares lasting more than 5 hours was performed by Gopalswamy et al. (2018): they find a relation between the duration of the gamma rays and both the end frequency of the radio burst and the duration of the burst.

[2] Catalog available at `http://gle.oulu.fi/`

[3] Type II bursts observed by theRadio and Plasma Wave (WAVES) experiment on board the Wind spacecraftat `https://cdaw.gsfc.nasa.gov/CME_list/radio/waves_type2.html`

7.5 Active Regions Positions Distribution

For each FLSF, the position of the AR associated with the flare on the solar surface is plotted in the top panel of Figure 7.7. The double peak structure of the FLSF latitude distribution is expected, following the overall distribution of ARs that is concentrated in two latitude bands on either side of the equator. However there is a North/South asymmetry, with twice as many FLSFs occurring in the northern hemisphere rather than the southern one. An asymmetry in the distribution of ARs has been observed during the solar cycle with one hemisphere dominating at a given time, although this is not a process well understood. We compare this distribution to the positions of all M and X-class flares over the period of 2010 to October 2017. Their latitude distribution shown in the bottom panel of Figure 7.7 peaks in the Southern hemisphere, opposite to that of the FLSF.

To understand whether the evolution of those trends changed with time, the latitude of active regions with M and X-class flares is plotted with time in Figure 7.8. They roughly follow the well known pattern of the butterfly effect, for which active regions tend to form at higher latitudes at the start of the solar cycle, and progressively form closer to the equator at the end of the cycle (Illarionov et al. 2011). From the overlaid positions of the FLSF in red, we notice that a larger fraction of FLSF happened earlier in the cycle (2011-2013), and independently a large number of X-ray flares happened in the southern hemisphere after 2013.

To quantify such an effect, we compare the distribution in time of the M and X-class flares, the fast CMEs and the FLSFL. Figure 7.9 shows the cumulative distribution in time of those three populations. The evolution of the FLSF follows much more closely the evolution of the fast CMEs, rather than the GOES M and X-class flares evolution. Using the K-S statistical test we evaluate the hypothesis that the FLSF distribution is drawn from the each distribution. The FLSF distribution is compatible with the fast CME distribution (p-value = 0.47). The FLSF distribution is incompatible with the M and X-class X-ray flares distribution, and can be excluded at the 3 sigma confidence level (p-value = 0.001).

The spatial distribution along the longitude does not show an East/West difference with the same number of flares in positive and negative longitudes between -90 and $+90^{\circ}$, and with three flares beyond the limb (their position was inferred from STEREO images).

An interesting feature is the disk center minimum in the longitude distribution of the FLSFs, whereas X-ray flares are uniformly distributed in longitude. This could be explained by an observational bias due to the directionality of gamma-ray emission. For simplicity, we have assumed so far that the production of gamma-rays from proton interactions is isotropic, when it is more likely to be beamed downward toward the photosphere.

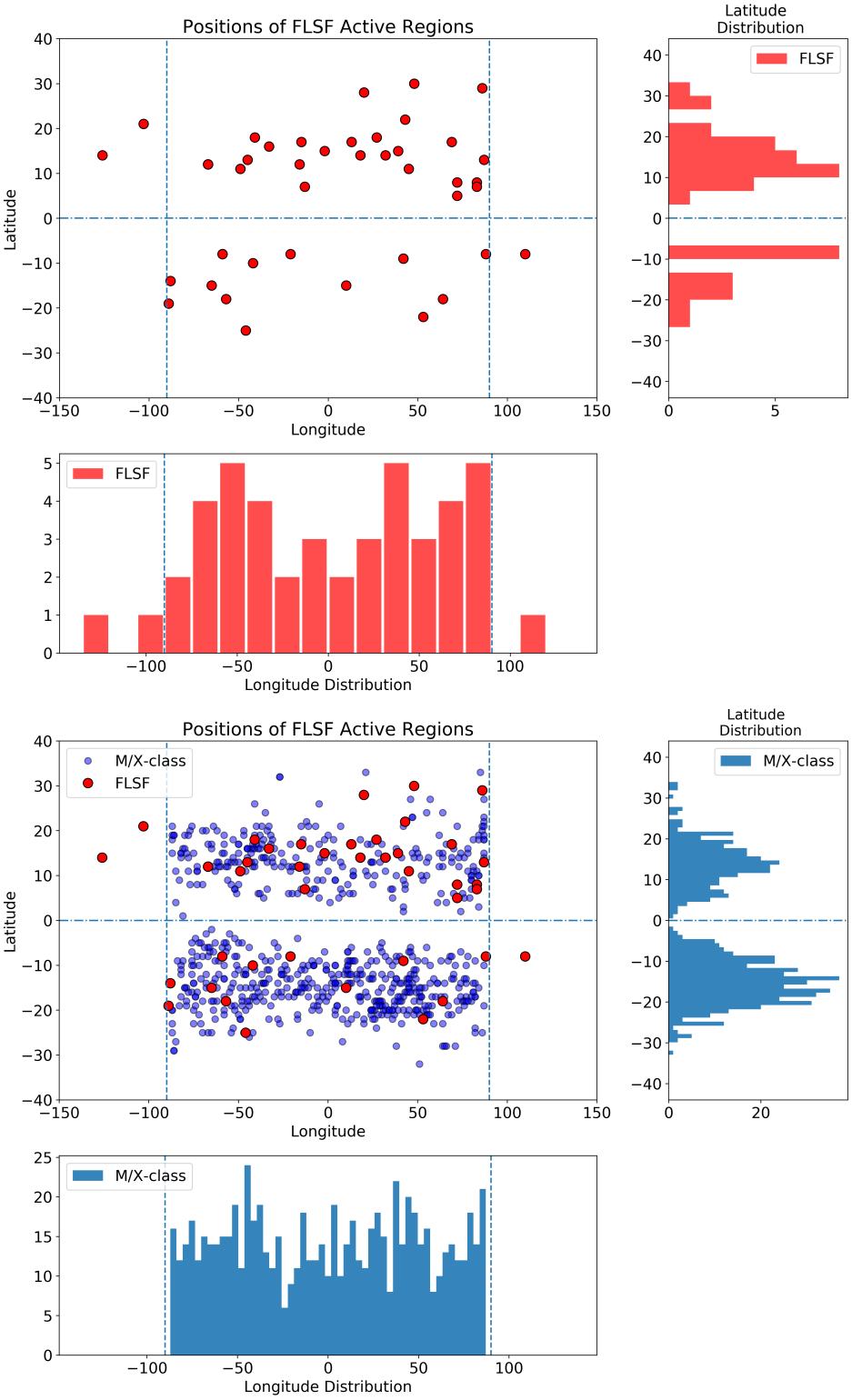

Figure 7.7: Distributions of the positions of the ARs associated with flares on the solar surface. Top panel: Positions of ARs associated with FLSFs (red). Longitudes beyond -90 and +90° correspond to BTL flares. Bottom panel: Positions of ARs associated with all GOES M and X-class (blue) over the same time period (2010-Oct. 2017). Longitudes selected between -88 and +88° to remove the limb events.

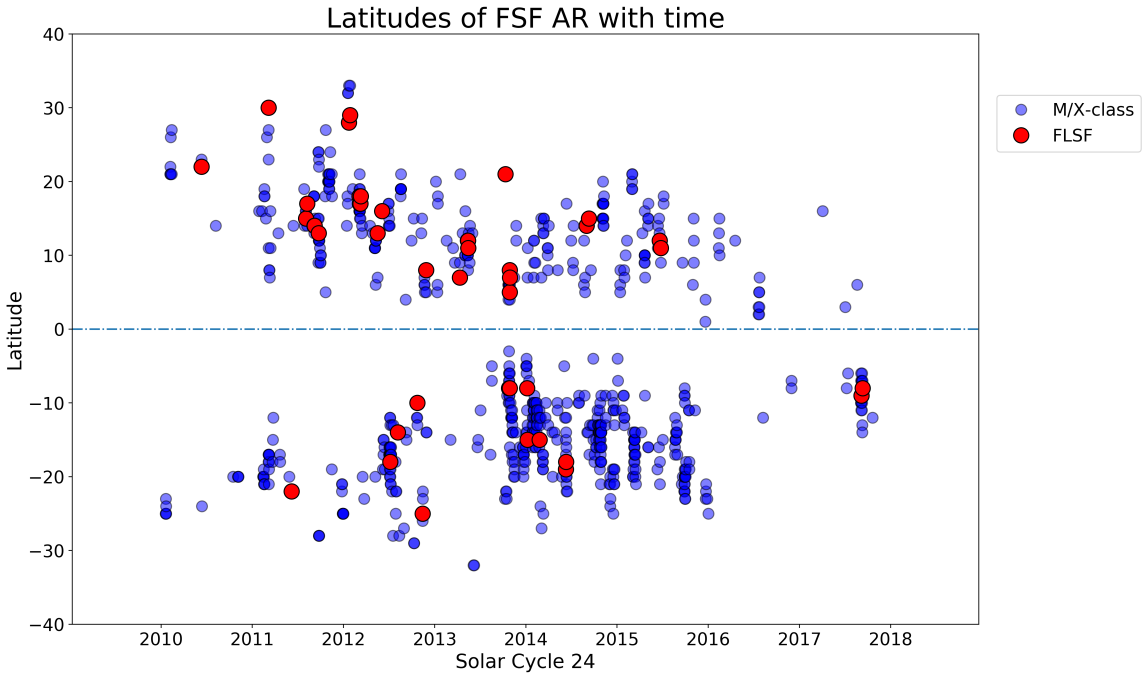

Figure 7.8: Latitudes of Active Regions associated with FLSF (red) and all M and X-class GOES flares (blue).

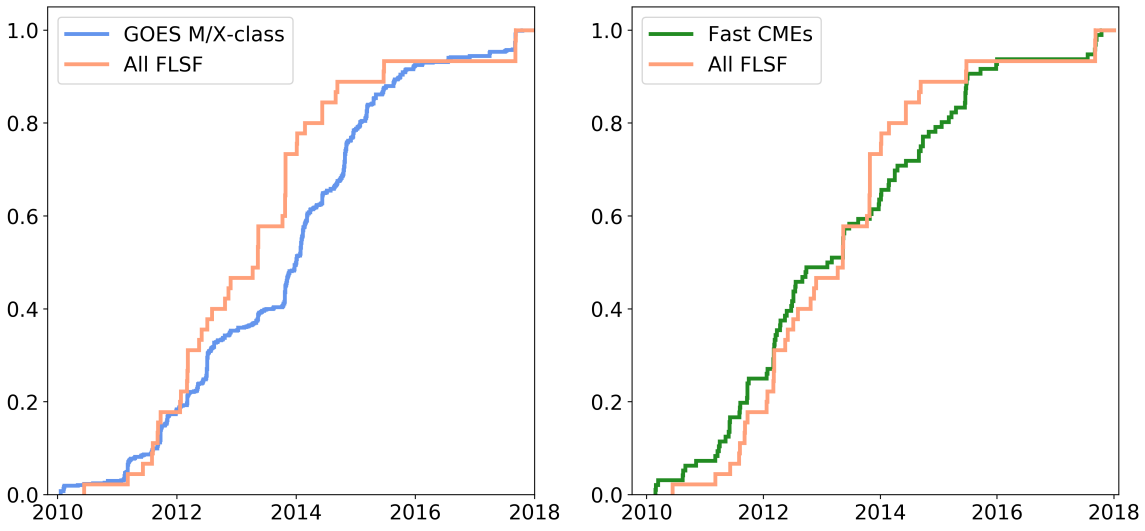

Figure 7.9: Cumulative distribution of solar events with time: FLSF in orange, M and X-class GOES X-ray flares in blue, fast CMEs (>1200km/s) in green. The KS test p-values are 0.001 and 0.47 respectively.

7.6 Flare Series

A noticeable feature of the FLSF population is the presence of several series of flares that happened over 1 or more days originating from the same AR (see Table 7.1). More than

half of the FLSF are part of a series of flares (25 out of 45). It is common for an AR to be the source of several flares, but the high ratio of such flare series in the FLSF catalog might indicate that some AR have more potential to gather the right conditions for gamma-ray emission. The most notable series happened from March 5 to 10, 2012 and from May 13 to 15, 2013 with each 4 FLSFs. All of those flares were associated with fast CMEs and both series contributed to strong and long lasting SEP events. They all yielded Delayed FLSF gamma-ray emission lasting more than 3 hours. In addition 3 of those 8 flares have been identified as having no gamma-ray detection of the Prompt phase, but detected Delayed emission only (only one additional FLSF behaves this way). This could indicate that the presence of previous SEP events and multiple fast CMEs is more important in those cases to produce long lasting gamma-ray emission than an energetic flare in HXR (maximum energy in HXR is in the 100-300 keV channel).

Name	Flare Type	Duration (hrs)	CME Speed (km s^{-1})	Width	GOES Class	SEP Emax (MeV)	HXR Emax (keV)	AR	Flare pos
2011-09-06 22:12	Prompt Delayed	0.6	575	H	X2.1	100	1000	11283	N14W18
2011-09-07 22:32	Delayed	1.9	792	290	X1.8	50‡	500	11283	N14W32
2012-01-23 03:38	Delayed	5.8	2175	H	M8.7	100	>100	11402	N28W20
2012-01-27 17:37	Delayed	7.3	2508	H	X1.7	605	>100	11402	N29W86
2012-03-05 02:30	Delayed	5.4	1531	H	X1.1	40‡	>100	11429	N18E41
2012-03-07 00:02	Delayed	20.2	2684*	H	X5.4*	605	1000	11429	N17E15
2012-03-09 03:22	Delayed only	7.3	950	H	M6.3	100‡	>100	11429	N17W13
2012-03-10 17:15	Delayed	6.0	1296	H	M8.4	100‡	>50	11429	N18W27
2013-05-13 01:53	Delayed	3.4	1270	H	X1.7	60	>300	11748	N12E67
2013-05-13 15:48	Delayed	5.4	1850	H	X2.8	60	800	11748	N12E67
2013-05-14 00:00	Delayed only	6.7	2625	H	X3.2	60	500	11748	N12E67
2013-05-15 01:25	Delayed only	3.6	1366	H	X1.2	50	100	11748	N11E49
2013-10-25 07:53	Delayed	1.1	587	H	X1.7	60	300	11882	S08E59
2013-10-25 20:54	Prompt	0.1	-		M1.9	60‡	100	11882	S08E59
2013-10-28 14:46	Delayed	1.3	812	H	M2.7*	60	50	11882	S08E21
2013-10-28 01:41	Prompt	0.3	695	H	X1.0	0	1000	11875	N05W72
2013-10-28 04:32	Prompt	0.1	1201	315	M5.1	0	1000	11875	N08W72
2013-10-28 20:48	Prompt	0.1	771	284	M1.5	100‡	100	11875	N07W83
2014-06-10 12:36	Prompt Delayed	1.8	1469	H	X1.5	60	1000	12087	S19E89
2014-06-11 08:59	Delayed	0.5	829	130	X1.0	0	1000	12087	S18E57
2015-06-21 02:04	Prompt Delayed	10.2	1366	H	M2.7*	10	>50	12371	N12E16
2015-06-25 08:02	Delayed	2.1	1627	H	M7.9	10	1000	12371	N11W45
2017-09-06 08:57	Prompt	0.3	391	245	X2.2	0	300	12673	S09W42
2017-09-06 11:53	Delayed	13.3	1571	H	X9.3*	100	>300	12673	S09W42
2017-09-10 15:35	Prompt Delayed	13.6	3163	H	X8.2	605	3000	12673	S08W88

Table 7.1: List of FLSF from similar Active Regions (* indicates several X-ray classes or CMEs during the duration of the gamma-ray emission. ‡ indicates the previous presence of SEPs, without this event being an SEP event).

7.7 Comparisons

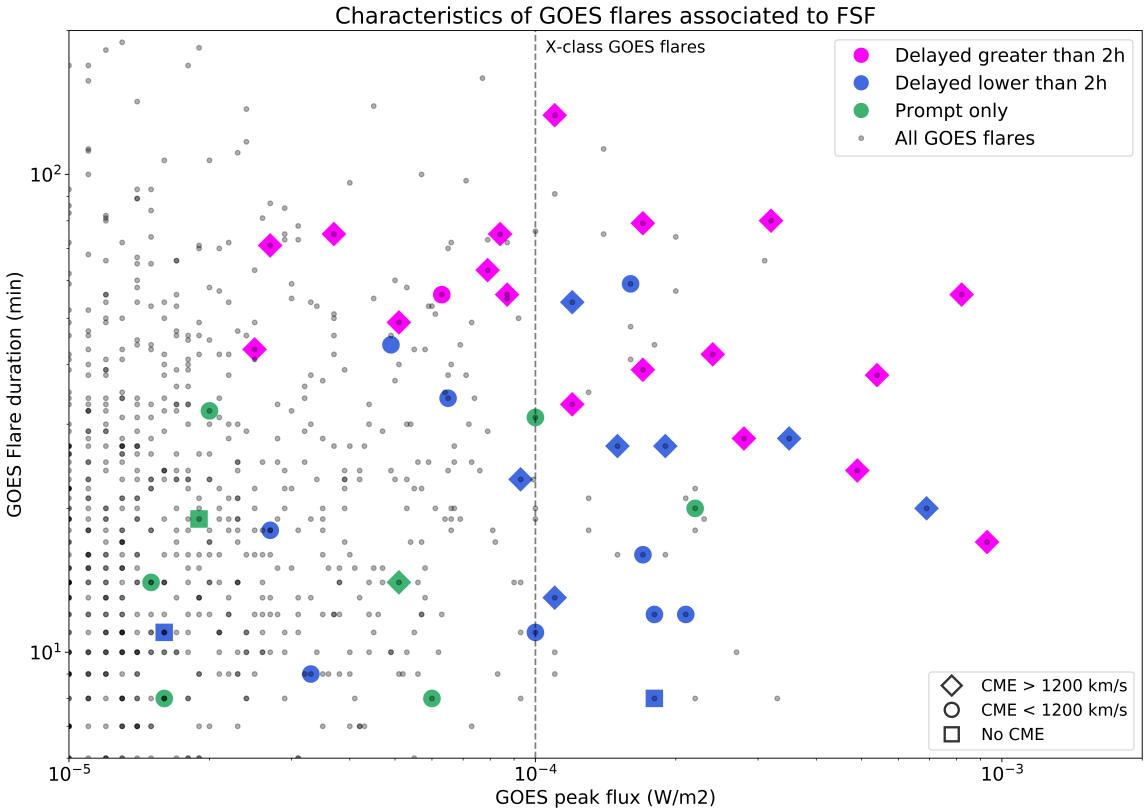

Figure 7.10: Distribution of peak fluxes with duration for all GOES flares (grey dots). The characteristics of the GOES flares associated with FLSF, are over-plotted, broken down by category (green for *prompt*, blue for *delayed* flares with a duration less than 2 hours and magenta for more than 2 hours). Diamond or circle indicates the presence of a CME (faster than 1200 km/s or not) and square notes that no CME was found. (The grid-like pattern visible for low fluxes or short durations is an artifact due to values in the catalog all given with a one digit precision).

Putting together the information gathered in the three previous sections on X-ray flares, CMEs and SEP events, we can try to compare those associations and understand their relationships. Two figures are presented, examining the GOES peak flux with GOES duration and GOES peak flux with CME speed. On Figure 7.10 the FLSFs with delays greater than 2 hours align with longer durations but are not necessarily constrained to only bright intensity flares. The FLSFs with a sole *prompt* component are clustered toward small duration and low intensity flares. In addition, the presence of a CME and indication of fast or slow CME is noted with the different markers in Figure 7.10 (diamonds or circles indicate the presence of a CME (faster than 1200 km/s or not) and square notes that no CME was found.). It confirms that the presence of a fast CME is very common for *delayed* flares.

Figure 7.11 shows the distribution of the CME speed for each FLSF category with respect

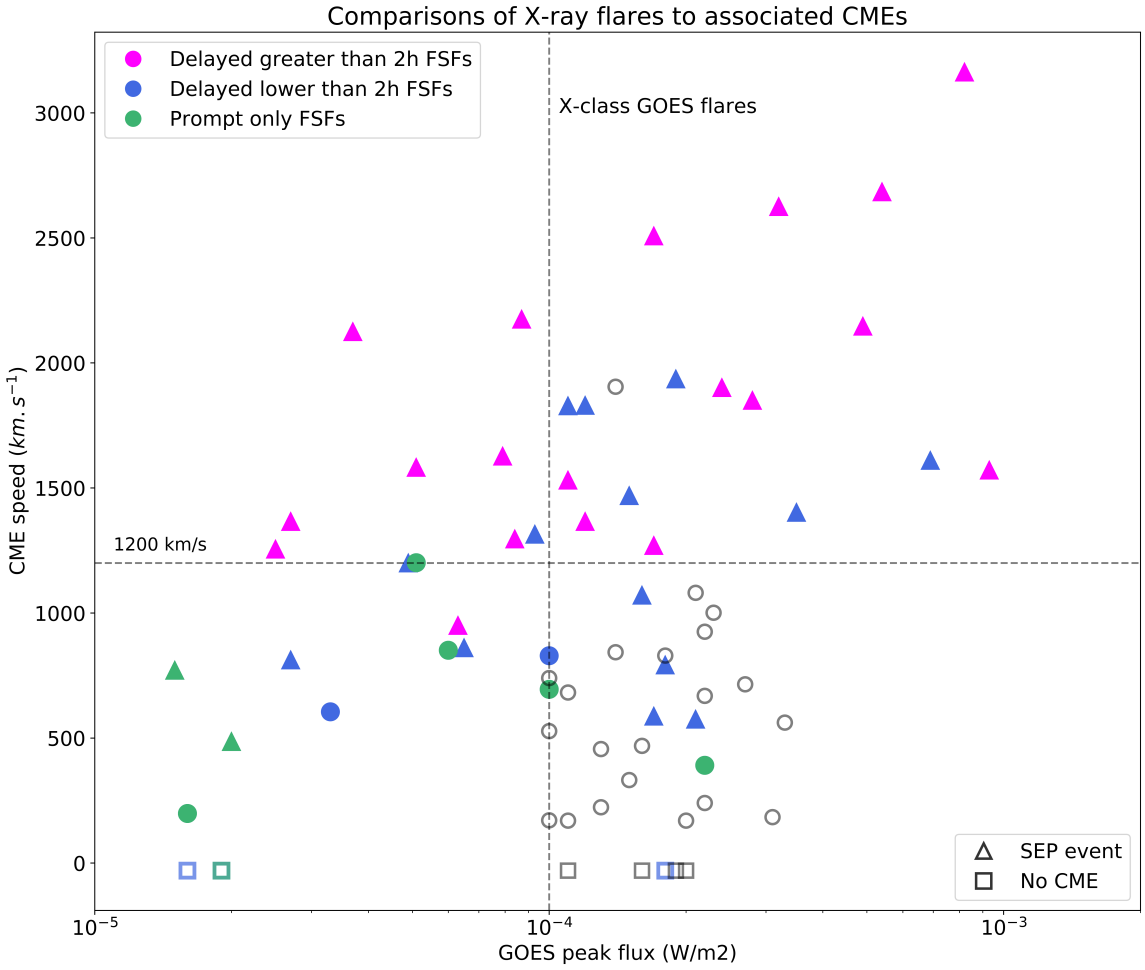

Figure 7.11: Distribution of the FLSF-associated GOES peak fluxes with respect their associated CME speed, broken down by category (green for *prompt*, blue for *delayed* flares with a duration less than 2 hours and magenta for more than 2 hours). Grey points correspond to X-class flare not detected by Fermi-LAT. Flares not associated with any CME are represented by a square, artificially set at speed 0. Triangle indicate an associated SEP event or the presence of SEPs in the environment.

to their associated GOES peak flux. 18 out of the 19 FLSFs with a delayed component lasting longer than 2 hours rank with a CME of speed greater than 1200 km/s and all flares with a Prompt only component rank below that limit. There is a wider range of behavior in the FLSFs with a delayed emission component shorter than 2 hours and we will try to illustrate those differences later, when considering the actual duration of gamma-ray emission. An added feature of Figure 7.11 is the flare association with an SEP event. It confirms that most events, especially at higher CME speeds, are associated with SEPs.

GOES Start-Stop	GOES Class	CME Appear time	CME Speed ($km.s^{-1}$)	CME Width (°)	LAT Observable	SEP event
2011-02-15 01:44 - 02:06	X2.2	2011-02-15 02:24	669	Halo	X	
2011-03-09 23:13 - 23:29	X1.5	2011-03-09 23:05	332	155	X	
2011-09-22 10:29 - 11:44	X1.4	2011-09-22 10:48	1905	Halo		SEP
2011-11-03 20:16 - 20:32	X1.9	-				
2012-07-12 15:37 - 17:30	X1.4	2012-07-12 16:24	843	76	X	SEP
2013-10-25 14:51 - 15:12	X2.1	2013-10-25 15:12	1081	Halo		
2013-10-29 21:42 - 22:01	X2.3	2013-10-29 22:00	1001	Halo		
2013-11-05 22:07 - 22:15	X3.3	2013-11-05 22:36	562	195		
2013-11-08 04:20 - 04:29	X1.1	-				
2013-11-10 05:08 - 05:18	X1.1	2013-11-10 05:36	682	262		
2013-11-19 10:14 - 10:34	X1.0	2013-11-19 10:36	740	Halo		
2014-03-29 17:35 - 17:54	X1.0	2014-03-29 18:12	528	Halo		
2014-04-25 00:17 - 00:38	X1.3	2014-04-25 00:48	456	296	X	
2014-06-10 11:36 - 11:44	X2.2	2014-06-10 11:48	925	111		
2014-10-19 04:17 - 05:48	X1.1	2014-10-19 06:12	170	43		
2014-10-22 14:02 - 14:50	X1.6	-			X	
2014-10-24 21:07 - 22:13	X3.1	2014-10-24 21:48	184	35		
2014-10-25 16:55 - 18:11	X1.0	2014-10-25 17:36	171	49		
2014-10-26 10:04 - 11:18	X2.0	-			X	
2014-10-27 14:12 - 15:09	X2.0	2014-10-27 15:12	170	55		
2014-11-07 16:53 - 17:34	X1.6	2014-11-07 17:12	469	87		
2014-12-20 00:11 - 00:55	X1.8	2014-12-20 01:25	830	257	X	
2015-03-11 16:11 - 16:29	X2.2	2015-03-11 17:00	240	74		
2015-05-05 22:05 - 22:15	X2.7	2015-05-05 22:24	715	Halo		
2017-09-07 14:20 - 14:55	X1.3	2017-03-09 12:36	223	7		

Table 7.2: X-class GOES flares not associated with any gamma-ray emission above 30MeV. The Fermi-LAT observable column indicates whether the prompt phase of the X-ray flare occurred within a `SunMonitor` time window. The SEP event column indicates the presence of this flare in the Major SEP Event list (see Section 7.3).

- Non-detections

As we attempt to characterize the solar flares associated with gamma-ray detections, we can also examine the population of solar flares not detected by the Fermi-LAT above 30 MeV. The durations and peak fluxes of the 773 M and X-class X-ray flares are plotted in grey on Figure 7.10 and unfortunately it is impossible to do a follow up on each of the non-detected flares. We can restrain our follow-up sample to the X-class flares (SXR peak flux greater or equal to $10^{-4}W/m^2$). During solar cycle 24, there were 49 X-class flares and 24 of those are associated with FLSFs[4]. Table 7.2 lists the X-class flares not associated with a gamma-ray detection and their possible associations to CMEs and SEP events. The characteristics of those non-detections are plotted in grey in Figure 7.11. All of the non-detected X-class flares but one are associated with slow CMEs, and 4 are not associated with any CME. This provides a strong case for the need of a fast CME to produce long lasting delayed emission rather than an intense GOES flare.

With the observational strategy of the Fermi-LAT, out of the 25 non-detected X-class GOES flares 7 happened while the Sun was in the Fermi-LAT FoV and 18 occurred when the Sun is out of the FoV. For the GOES flares occurring at times when the Sun is out of the FoV, an upper limit on the gamma-ray emission can be computed. For the others it is impossible to know whether there was prompt gamma-ray emission. But if that flare had a delayed gamma-ray emission component, it would have been detected in the time window following the flare. This can help us put an upper limit on the duration of the gamma-ray emission, if there had been any.

7.8 Correlations

The previous sections explored the trends of the associations of the Fermi-LAT solar flares with GOES flares, CMEs and SEP events. The flare catalog were separated in three categories based on the timing of the gamma rays compared to the X-rays: either a prompt component only or a delayed component smaller or greater than 2 hours. To go beyond in understanding the characteristics of the FLSF catalog, three quantities can be used to describe the general behavior of the gamma rays: the peak flux, the fluence and the duration of the gamma-ray emission.

Because of the gaps in the Fermi-LAT coverage of the Sun, estimating the peak flux and the fluence are particularly difficult, unless the gamma-ray detection consists of many

[4] Technically only 23 are associated with single FLSF, but we also include the case of 2012-03-07 which has two X-class flares back-to-back for which we are not exactly sure which one it is associated with. We will just not consider it when studying the non-detections; Also 2 of the 3 BTL flares have an estimated GOES class of X3.5 and X2.4, but are not considered in this comparison as we do not have a catalog of X-class flares happening behind the limb

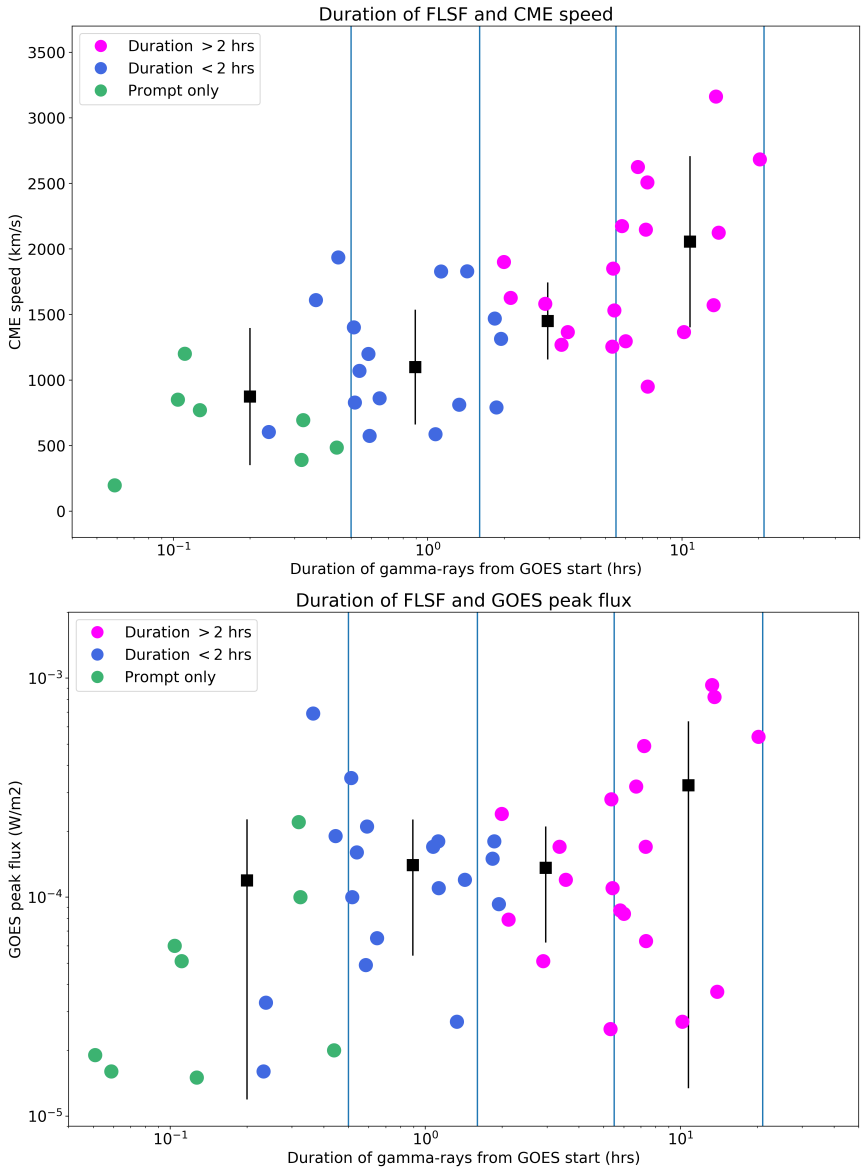

Figure 7.12: Top: CME speed as a function of the duration of gamma-rays (defined from the start of the GOES flare). Bottom: GOES peak flux vs the duration of gamma-rays . Vertical lines bins the catalog in 4 equal groups: in each bin the average (speed or peak flux) and standard deviation are plotted in black (FLSF points: green for *prompt*, blue for *delayed* flares with a duration less than 2 hours and magenta for more than 2 hours).

points, like the evolution of the 2012-03-07 flare described in Chapter 5. The duration of the gamma-rays is a quantity that is easier to compute, whether defined by the start of the gamma-rays or the start of the GOES flare. The relation between duration and CME speed or peak GOES flux is shown in Figure 7.12. There is a correlation between gamma-ray duration and CME speed with a Pearson coefficient of 0.7. The correlation with GOES peak flux is weaker, with a Pearson coefficient of 0.4.

Chapter 8

Summary

This dissertation presents the analysis of gamma-ray observations of solar flares by the Fermi-LAT during most of solar cycle 24 (from 2010 to October 2017). The properties of bright flares as well as the development of the first Fermi-LAT high-energy gamma-ray solar flare catalog have been presented.

The Fermi-LAT Solar Flare catalog lists 45 flares detected above 30 MeV. Contrary to past gamma-ray observations of solar flares which were exclusively very energetic X-ray flares (minimum flare was X1.4, Ryan 2000), about half of the Fermi-LAT detections are associated with more modest, M-class GOES flares. This suggests that acceleration of particles up to several GeV energies is a more common occurrence in more modest M-class flares than previously thought as was already hinted in Ackermann et al. (2014).

Below are a summary of key observations:

- Prompt phase observations with gamma-ray emission synchronous with HXR and nuclear lines emission confirm the acceleration of both electrons and protons immediately following reconnection. This behavior confirms observations by SMM, EGRET and RHESSI (at lower energies).
- The majority of solar flares detected by the Fermi-LAT exhibit a temporal extension of the gamma-ray emission, beyond the end of the non-thermal processes seen in HXR. A wide range of delays is observed from a few minutes to more than 20 hours. Different patterns emerge:
  - Exponential decay of the gamma-rays after the peak HXR, which is consistent with the past observations of long duration gamma-ray solar flares;
  - Rising gamma-ray flux starting only minutes after the initial prompt phase followed by a fast decay;
  - Rising and decay of gamma-ray emission on timescales of hours.

The last two behaviors could only be observed by the Fermi-LAT thanks to its much higher sensitivity.

- Spectral analysis confirms that high energy gamma rays originate from accelerated protons, with lines or pion bump signatures. All strong detections are compatible with a spectrum above 60 MeV due to proton collisions. The two brightest and longest flares show a progressing softening of the proton energy distribution.

- Our localization studies confirm the source of the gamma rays from the Sun to be generally consistent with the flare active region position. The common scenario places the gamma-ray production at the footpoints of the active region, which has been confirmed by RHESSI observation of line emission (with a very small shift in some cases). However, two types of observations challenge this view. During the bright 2012-03-07 flare, the centroid of the emission progressively moved away from the active region over 9 hours and the final position is incompatible with the position of the active region. During any of the behind the limb flares, in particular the 2014-09-01 flare, the gamma-ray emission started only 4 minutes after the start of the GOES flare, despite having the flare active region located 40° behind the limb.

  Both observations are incompatible with a scenario of initial proton acceleration and trapping in loops above the active region. Acceleration at the shock front of a CME seems to better fit these two observations. The 2012-03-07 flare observation suggests particles accelerated at the shock front moving downstream back to the solar disk can come back to areas away from the flare site. It could actually come onto a larger area and create spatially extended gamma-ray emission. However the Fermi-LAT can not measure extension at relatively low energies thus preventing us from drawing a definitive conclusion. In the case of the 2014-09-01 flare, the fast development of the Halo CME moving outward can accelerate particles along the front which can then follow open field lines tracing back to the visible part of the disk.

- The systematic analysis of all solar flares observed by the Fermi-LAT yielded 45 solar flares detected, all associated with X-ray flares and all but 3 associated with CMEs. For the first time, a correlation was found between the duration of the gamma-rays and the speed of the associated CMEs, likely to be Halos. No gamma-ray detection was associated with a CME only, showing that the mechanism of a flare and an associated CME are required for efficient particle acceleration leading to gamma-rays emission with delayed emission.

- It was found that throughout solar cycle 24, the spatial distribution of all GOES X-ray flares was not symmetric: the North dominated the first half of the cycle and after

the end of 2013 while the South dominated the second half which also happened to be overall more prolific in flares. Therefore the overall distribution of X-ray flares shows an asymmetric distribution toward the South. This distribution does not match the spatial distribution of the flares associated with the FLSF population, for which the majority of flares were in the northern hemisphere. This North dominance of the FLSF can be explained by two effects: first is that a large fraction of the FLSFs happened in the first half of the cycle when the North was dominating the solar activity; second is that the majority of CMEs also happened in the first half of the cycle. This reinforces the link between gamma-ray flares and CMEs.

I hope my work and future publications by the Fermi-LAT team will be used as a reference in the community for studying high-energy gamma-ray flares during Solar Cycle 24. There is still a great deal of solar observations to be compared to the gamma rays that I did not cover, in particular the spectral study of soft gamma rays for nuclear lines, microwave and radio observations for synchrotron emission and Type II bursts tracking high-energy electrons during flares and CMEs, sunquake observations and their possible link to protons acceleration, among others.
With the large sample of Fermi-LAT solar flares covering a range of different behaviors, more models can now be tested leading to a better understanding of the high-energy processes at play in solar flares.

The Fermi mission will continue observing the Sun in gamma rays and hopefully cover the entire Cycle 25.

Appendix A

Fermi-LAT Solar Flare Catalog

This appendix is compiling the results of the FLSF catalog for each flare. It includes the temporal and spectral characteristics of the gamma-ray emission whether detected with the LLE, `SunMonitor` approach or both, as well as spatial features when available.

- First we list the classification of the FLSF as either Prompt if the gamma-ray emission timing is consistent with the HXR timing or Delayed if the gamma-ray emission extends beyond the peak of the non-thermal activity (see Section 6.3 for more details). The FLSFs fall in one or both category with different timescales. The lightcurves presented give the best view of the timing of the gamma-ray emission with respect to the solar activity (details of the color coding in the different panels are described in Figure 5.2. Each section describes the association of the FLSFs with X-ray flares (all are associated with GOES or STEREO flares) and CMEs (for all but 3 FLSF). When available, HXR and SEP information are also listed. Some flares have only a partial HXR coverage, and the maximum energy observed before or after the flare is listed (i.e. $>$ 100 keV). About 28 FLSFs as associated with an SEP event, but in some cases a different SEP event happened hours or days before and particles are still detected by GOES or STEREO. It is then hard to determine whether the FLSF is indeed associated with a new SEP event or not. In addition, the presence of energetic particles in the interplanetary space may play a role in the delayed emission of gamma rays, so those cases are listed with the maximum energy observed followed by "present". For the few cases with potential confusion on the association, additional details are provided.

- For flares with a detected LLE component the following characteristics are listed in a Table. Start time and duration of the flare are identified from the LLE lightcurve; Flux averaged over this duration is given in two energy bands (from 30 MeV to 10

GeV and from 100 MeV to 10 GeV). The TS reports the significance of the of the gamma-ray emission above 60 MeV with a pion template spectral model. A value below 9 means that the emission above 60 MeV is not significant, even if the flare is detected above 30 MeV. It also indicates whether the gamma-ray flare is detected by the `SunMonitor` approach and whether the LLE detection was within a `SunMonitor` time window, which can be valuable when trying to understand the evolution of the gamma-ray emission during the flare. See Section 4.3.2 for a description of the LLE analysis and Section 6.2.2 for summary of the results for all LLE flares in the catalog.

For LLE flares GOES, GBM and LAT LLE are plotted together, with Fermi-LAT standard analysis if detected above 60 MeV by the `SunMonitor` .

- For flares with the `SunMonitor` approach, a Table summarizes the following characteristics: 1) Start Date is the time (UT) when the Sun came into the FoV; 2) Exposure in minutes, defined as the effective duration of observation (accounting for time loss due to the SAA); 3) Flux averaged over the time window computed for the preferred spectral model (computed between 100 MeV and 10 GeV); 4) TS value for the Power Law model; 5) Difference of TS between EXP and PL models, a value above 9 indicates the EXP is favored; 6 and 7) Best fit photon index for a PL model or the best fit proton index from the pion fit if the EXP model is preferred (* indicates that the Fermi-LAT response was affected by pile-up, and the S15 event class is used for the analysis).

- The results of the localization analysis is given for the `SunMonitor` time windows when the 68% containment radius is less than 0.15°: the locations are computed with fisheye correction above 60 MeV (see Section 4.2 for the details on the methodology and Section 4.3.4 for a description of the fisheye effect). For each flare, a Table reports the following quantities: 1) Start and End times; 2) Best fit position of the gamma-ray source in the helioprojective coordinate system; 3 and 4) 68 and 95% containment error computed with the TS maps contours; 5) Angular distance between the position of the X-ray flare and the position of the gamma-ray source, in arcseconds; 6) Comparison of distance to the 95% containment radius to estimate the relative distance: a value greater than 1 indicates that the position of the gamma-ray source is incompatible with the AR; 7) Average angle between the Sun and the Fermi-LAT boresight axis, a proxi to indicate the amplitude of the fisheye correction. The position of the X-ray flare is set to the best estimated position of the associated Active Region at the time of the GOES flare, given in the caption of each Table.

A.1 2010-06-12

Type of Gamma-ray Flare: **Prompt**.

Associated with a M2.0 GOES flare which started on 2010-06-12 00:30 and a CME with speed 486 km/s.

Fermi-LAT detected gamma-ray emission with the LLE approach only. Emission started on 2010-06-12 at 00:55:49 and ended at 00:56:20 with a total duration of 30 seconds.

Comments: Flare occurred when the Sun was more than 70 degrees from LAT boresight and thus was only detectable through the LLE approach (Ackermann et al. 2012b).

Start Time	Duration (sec)	$Flux_{30}$	$Flux_{100}$	TS	SunMon detected	Out of FoV
2010-06-12 00:55:49	30	446.01 $\pm$ 35.18	190.60$\pm$ 11.76	215		X

Table A.1.1: LLE Spectral results for flare 2010-06-12. $Flux_{30}$ and $Flux_{100}$ indicate the flux computed from 30 MeV to 10 GeV and from 100 MeV to 10 GeV respectively (in units of 10^{-5} $cm^{-2}s^{-1}$).

GOES	Class M2.0	Start 2010-06-12 00:30	Peak 2010-06-12 00:57	Stop 2010-06-12 01:02	Dur. (min) 32	AR position N22W43
CME	Speed 486 km/s	Width 289	C2 time 2010-06-12 01:31			
SEP	Instrument GOES	Emax 10 MeV				
HXR	Instrument BGO	Emax 1000 kev				

Table A.1.2: Properties of the events associated with 2010-06-12: GOES X-ray flare, CME, SEPs, HXRs .

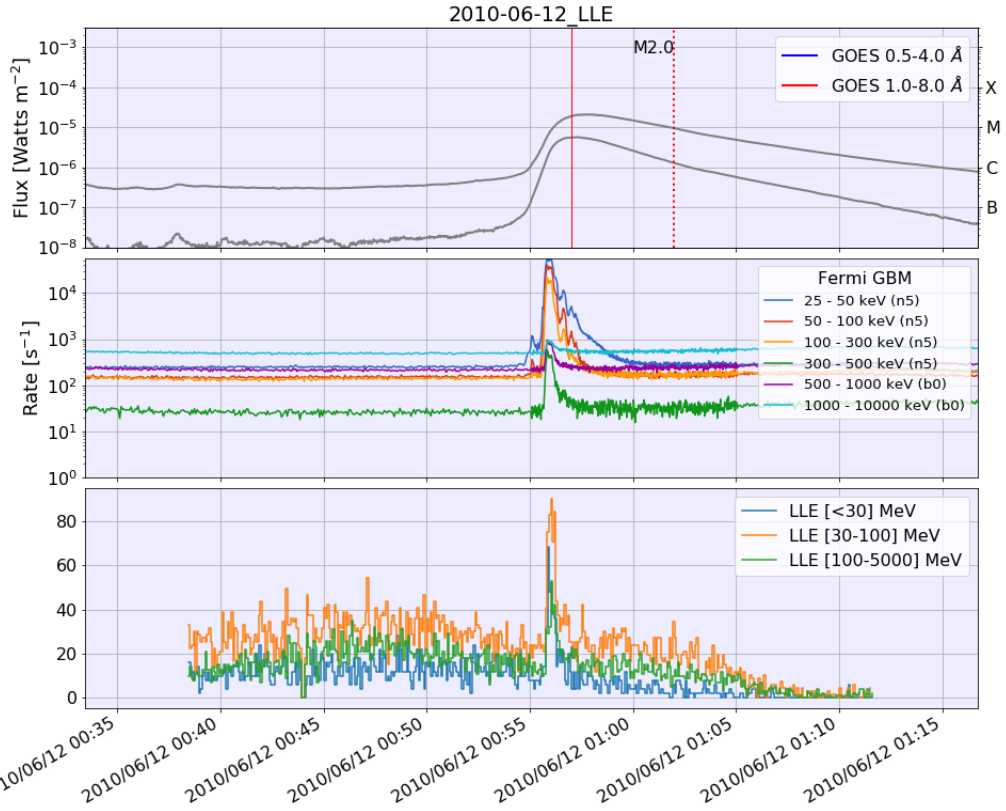

Figure A.1.1: Light curve for FLSF 2010-06-12. Panels from top to bottom: GOES X-rays; Fermi-GBM; Fermi-LAT LLE.

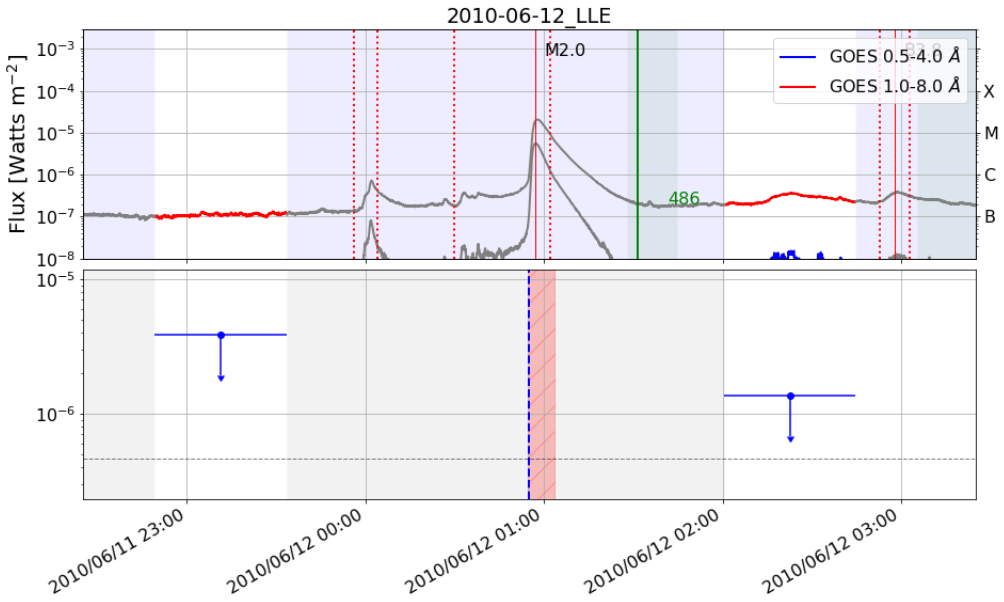

Figure A.1.2: Light curve for 2010-06-12. Top panel: GOES X-rays, bottom panel: Fermi-LAT flux > 100 MeV. Vertical blue line marks the start time of the LLE flare.

A.2 2011-03-07

Type of Gamma-ray Flare: **Delayed**.
Associated with a M3.7 GOES flare which started on 2011-03-07 19:43 and a CME with speed 2125 km/s.
Fermi-LAT detected gamma-ray emission above 60 MeV starting on 2011-03-07 20:10 and ending on 2011-03-08 09:39, lasting 13.5 hours.
Comments: Most of the non-thermal activity associated with the M3.7 flare happened before the first time window: the gamma-rays are delayed compared to the HXR. Additional solar flares occured during the 13.5 hours duration which could contribute the overall gamma-ray emission, making it appear longer. But no emission above 100 keV was observed with RHESSI or GBM, which leads us to only consider only the first M3.7 GOES flare and first CME (see Ackermann et al. 2014 for more details on this flare and analysis performed with Pass7 data).

Date and Time	Exposure (minutes)	Flux (10^{-5} cm^{-2}s^{-1})	TS	ΔTS	Photon Index	Proton Index
2011-03-07 20:10 - 20:39	29	2.06 ± 0.19	317	27	-0.76 ± 0.45	4.29 ± 0.40
2011-03-07 23:21 - 00:05	44	3.04 ± 0.20	710	70	-0.31 ± 0.36	4.13 ± 0.26
2011-03-08 02:33 - 03:16	43	3.23 ± 0.22	621	66	-0.15 ± 0.41	4.70 ± 0.32
2011-03-08 05:44 - 06:27	44	1.40 ± 0.15	219	32	0.67 ± 0.99	>6
2011-03-08 09:13 - 09:39	26	0.48 ± 0.11	46	-0.1	-2.55 ± 0.25	-

Table A.2.1: `SunMonitor` maximum likelihood results for 2011-03-07 (see Appendix A for description).

GOES	Class M3.7	Start 2011-03-07 19:43	Peak 2011-03-07 20:12	Stop 2011-03-07 20:58	Dur. (min) 75	AR position N30W48
CME	Speed 2125 km/s	Width Halo	C2 time 2011-03-07 20:00			
SEP	Instrument GOES	Emax 50 MeV				
HXR	Instrument BGO	Emax > 100 kev				

Table A.2.2: Properties of the events associated with 2011-03-07: GOES X-ray flare, CME, SEPs, HXRs (HXR coverage incomplete).

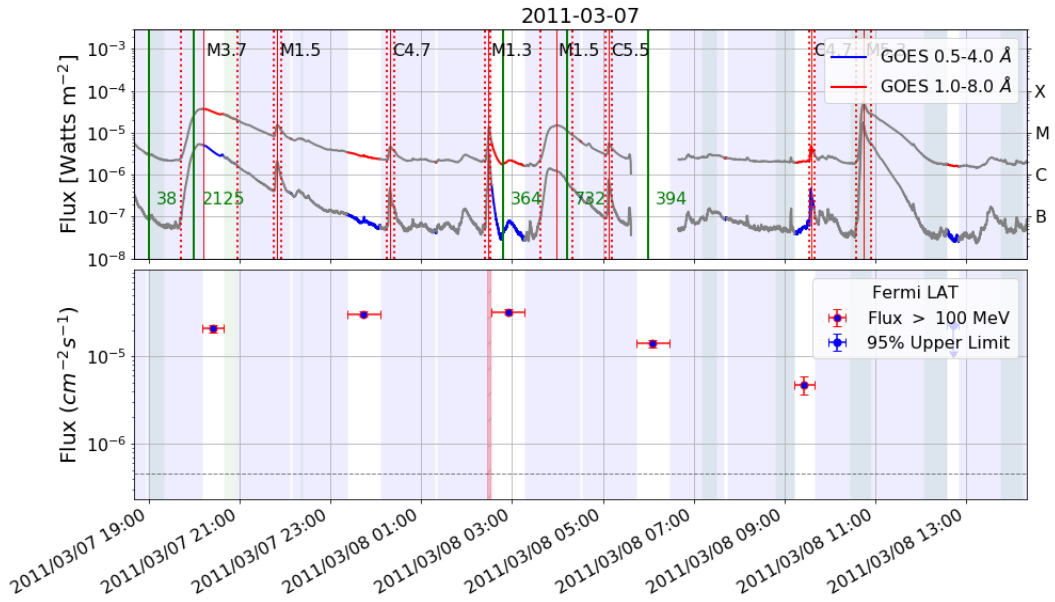

Figure A.2.1: Light curve for 2011-03-07. Top panel: GOES X-rays, bottom panel: Fermi-LAT flux > 100 MeV.

Date and Time	Helio X,Y	ERR 68%	ERR 95%	Angular Distance	Relative Distance (95)	Average Boresight (°)
2011-03-07 23:21 - 00:05	902,70	460	736	556	0.8	47
2011-03-08 02:33 - 03:16	584,92	481	758	461	0.6	46

Table A.2.3: The GOES X-ray flare associated with the FLSF originated from AR 1116 whose position at the time of the GOES flare was N30W48 (see Appendix A for description).

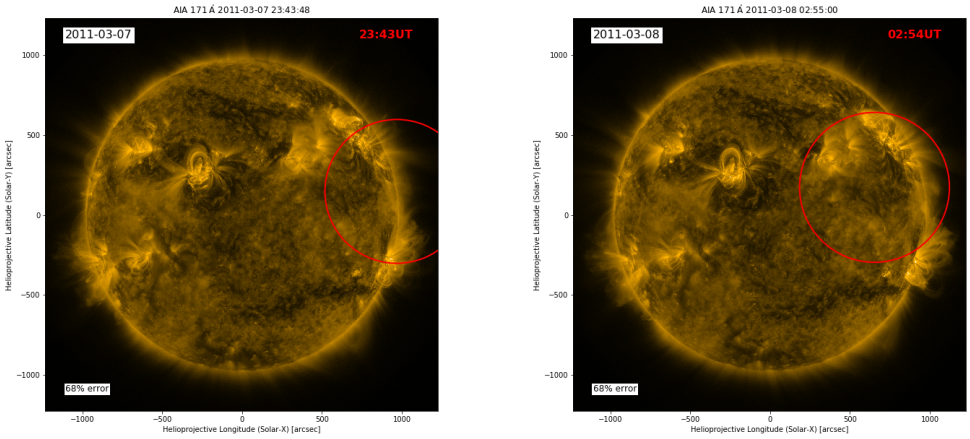

Figure A.2.2: Time resolved localization of the > 60 MeV emission from the 2011-03-07 flare. The mean time of each window is annotated in the upper right hand corner of each panel. The circles are the 68% source location uncertainty regions (results in Table A.2.3).

A.3 2011-06-07

Type of Gamma-ray Flare: **Delayed**.

Associated with a M2.5 GOES flare which started on 2011-06-07 06:16 and a CME with speed 1255 km/s.

Fermi-LAT detected gamma-ray emission above 60 MeV starting on 2011-06-07 07:47 and ending on 2011-06-07 11:34, lasting 3.8 hours.

Comments: Prompt phase not observable (see Ackermann et al. 2014 for more details on this flare and analysis performed with Pass7 data).

Date and Time	Exposure (minutes)	Flux (10^{-5} cm^{-2}s^{-1})	TS	ΔTS	Photon Index	Proton Index
2011-06-07 07:47 - 08:23	36	3.18 ± 0.20	740	76	-0.13 ± 0.37	4.97 ± 0.33
2011-06-07 11:16 - 11:34	19	0.32 ± 0.10	19	5	-2.70 ± 0.35	-

Table A.3.1: `SunMonitor` maximum likelihood results for 2011-06-07 (see Appendix A for description).

GOES	Class M2.5	Start 2011-06-07 06:16	Peak 2011-06-07 06:41	Stop 2011-06-07 06:59	Dur. (min) 43	AR position S22W53
CME	Speed 1255 km/s	Width Halo	C2 time 2011-06-07 06:49			
SEP	Instrument GOES	Emax 100 MeV				
HXR	Instrument NaI5	Emax 100 kev				

Table A.3.2: Properties of the events associated with 2011-06-07: GOES X-ray flare, CME, SEPs, HXRs .

Date and Time	Helio X,Y	ERR 68%	ERR 95%	Angular Distance	Relative Distance (95)	Average Boresight (°)
2011-06-07 07:47 - 08:23	649,-440	430	708	99	0.1	29

Table A.3.3: The GOES X-ray flare associated with the FLSF originated from AR 11226 whose position at the time of the GOES flare was S22W53 (see Appendix A for description).

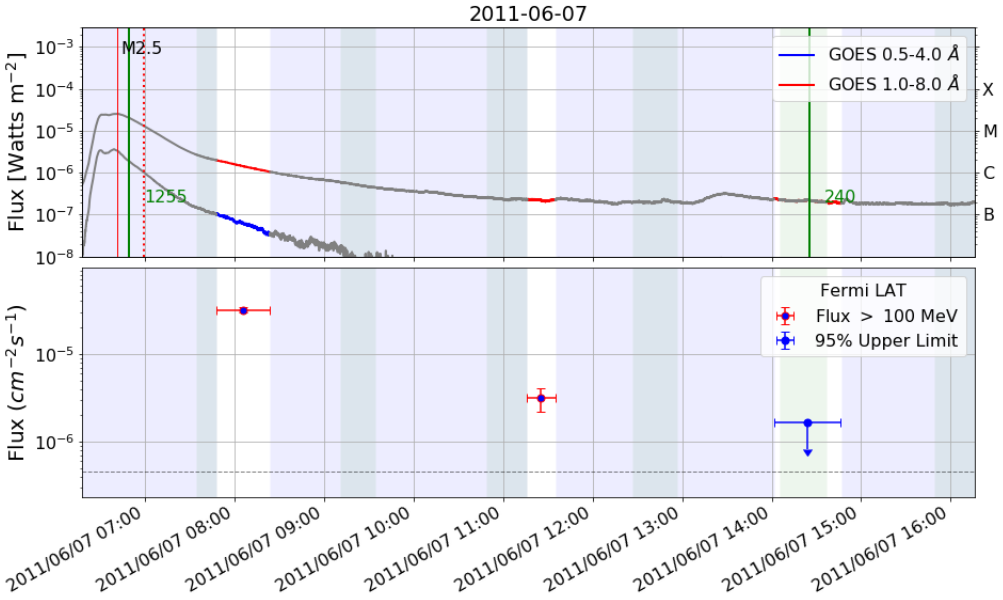

Figure A.3.1: Light curve for 2011-06-07. Top panel: GOES X-rays, bottom panel: Fermi-LAT flux > 100 MeV.

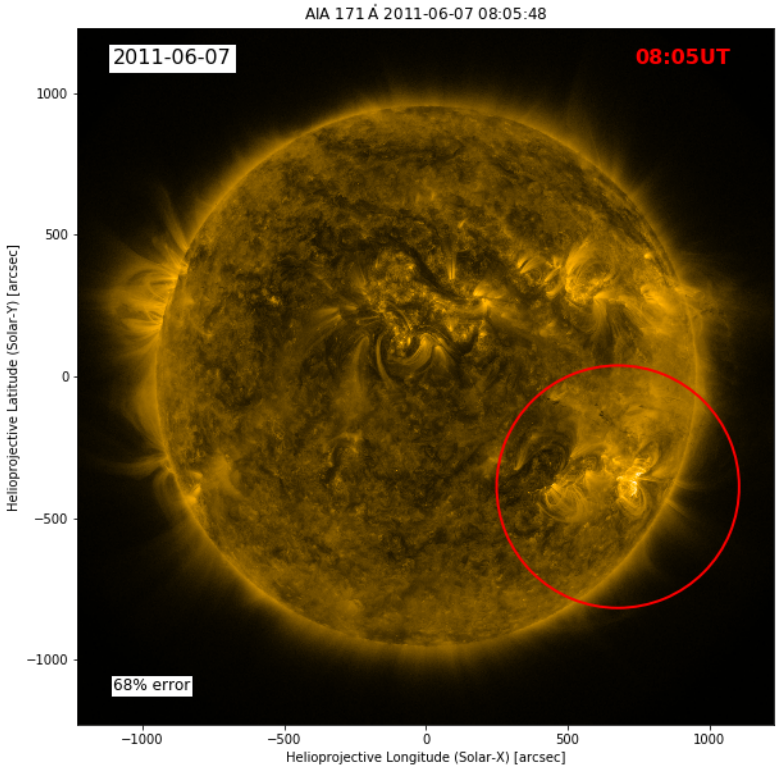

Figure A.3.2: Time resolved localization of the > 60 MeV emission from the 2011-06-07 flare. The mean time of each window is annotated in the upper right hand corner of each panel. The circles are the 68% source location uncertainty regions (results in Table A.3.3).

A.4 2011-08-04

Type of Gamma-ray Flare: **Delayed**.

Associated with a M9.3 GOES flare which started on 2011-08-04 03:41 and a CME with speed 1315 km/s.

Fermi-LAT detected gamma-ray emission above 60 MeV starting on 2011-08-04 04:55 and ending on 2011-08-04 05:37, lasting 42 minutes.

Comments: Prompt emission observed in HXR up to 300 keV with the Fermi-GBM, but the Sun was out of the Fermi-LAT FoV.

Date and Time	Exposure (minutes)	Flux (10^{-5} cm^{-2}s^{-1})	TS	ΔTS	Photon Index	Proton Index
2011-08-04 04:55 - 05:37	42	2.30 $\pm$ 0.18	413	49	-0.09 $\pm$ 0.50	5.39 $\pm$ 0.44

Table A.4.1: `SunMonitor` maximum likelihood results for 2011-08-04 (see Appendix A for description).

GOES	Class M9.3	Start 2011-08-04 03:41	Peak 2011-08-04 03:57	Stop 2011-08-04 04:04	Dur. (min) 23	AR position N15W39
CME	Speed 1315 km/s	Width Halo	C2 time 2011-08-04 04:12			
SEP	Instrument GOES	Emax 100 MeV				
HXR	Instrument NaI5	Emax 300 kev				

Table A.4.2: Properties of the events associated with 2011-08-04: GOES X-ray flare, CME, SEPs, HXRs .

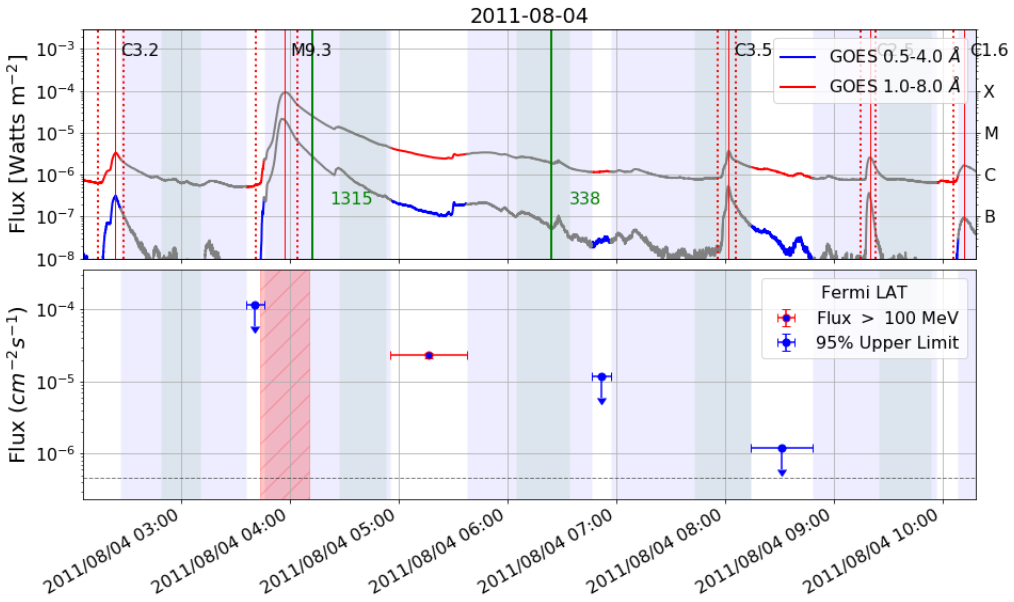

Figure A.4.1: Light curve for 2011-08-04. Top panel: GOES X-rays, bottom panel: Fermi-LAT flux > 100 MeV.

A.5 2011-08-09

Type of Gamma-ray Flare: **Prompt Delayed**.

Associated with a X6.9 GOES flare which started on 2011-08-09 07:48 and a CME with speed 1610 km/s.

Fermi-LAT detected gamma-ray emission above 60 MeV starting on 2011-08-09 08:01 and ending on 2011-08-09 08:09, lasting 8 minutes. The prompt phase of 2011-08-09 is also associated with a LLE detection. The emission detected by the LLE approach started on 2011-08-09 at 08:01:51 and ended at 08:06:01 with a total duration of 250 seconds.

Comments: Well seen in LLE synchronous with HXR peaks seen with the Fermi-BGO (the NaI instrument saturated during the peak of the GOES flare). Emission > 60 MeV detected with a delay and extending beyond HXR.

Start Time	Duration (sec)	$Flux_{30}$	$Flux_{100}$	TS	`SunMon` detected	Out of FoV
2011-08-09 08:01:51	250	31.20 ± 0.24	13.02± 0.22	124	X	

Table A.5.1: LLE Spectral results for flare 2011-08-09. $Flux_{30}$ and $Flux_{100}$ indicate the flux computed from 30 MeV to 10 GeV and from 100 MeV to 10 GeV respectively (in units of 10^{-5} $cm^{-2}s^{-1}$).

Date and Time	Exposure (minutes)	Flux (10^{-5} $cm^{-2}s^{-1}$)	TS	ΔTS	Photon Index	Proton Index
2011-08-09 07:37 - 08:09	32	2.29 ± 0.23*	186	26	-0.04 ± 0.87	5.39 ± 0.61

Table A.5.2: `SunMonitor` maximum likelihood results for 2011-08-09 (see Appendix A for description).

GOES	Class X6.9	Start 2011-08-09 07:48	Peak 2011-08-09 08:05	Stop 2011-08-09 08:08	Dur. (min) 20	AR position N17W69
CME	Speed 1610 km/s	Width Halo	C2 time 2011-08-09 08:12			
SEP	Instrument GOES	Emax 100 MeV				
HXR	Instrument NaI5	Emax 300 kev				

Table A.5.3: Properties of the events associated with 2011-08-09: GOES X-ray flare, CME, SEPs, HXRs .

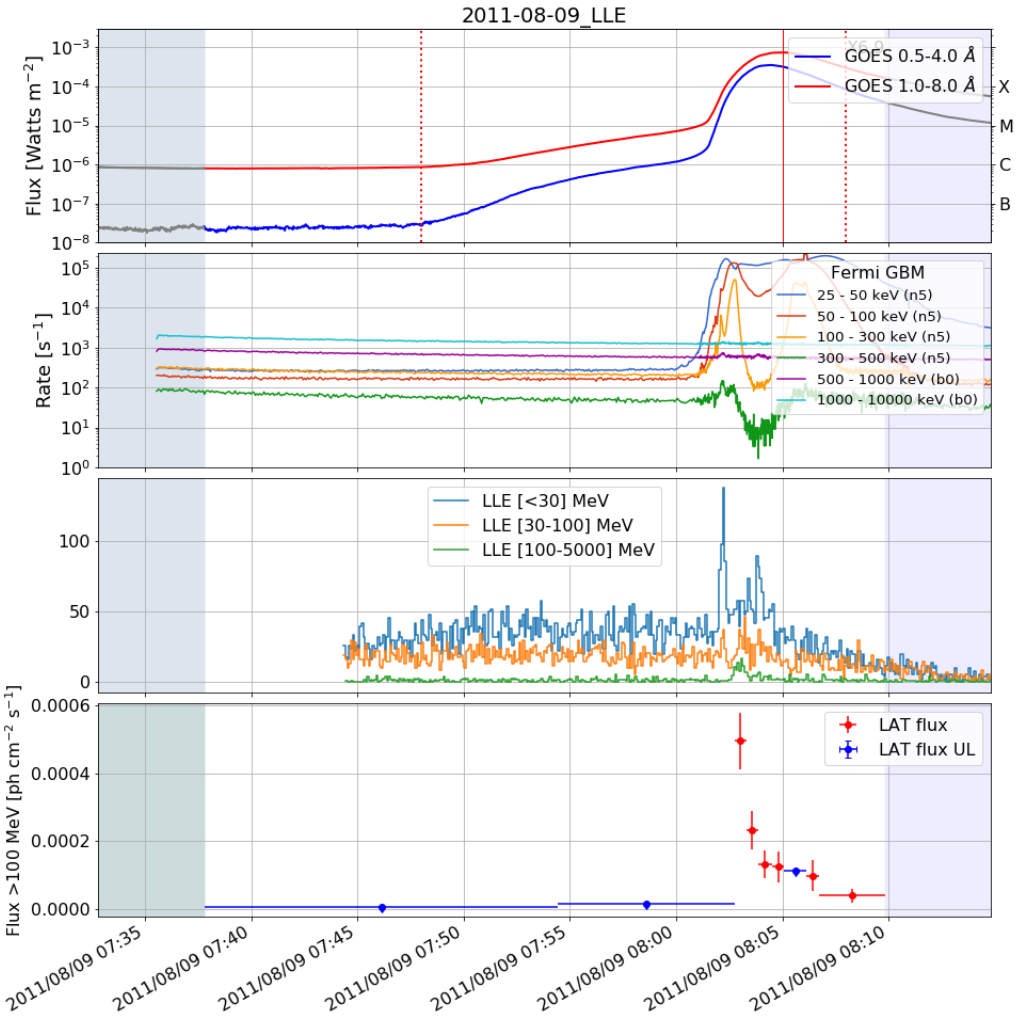

Figure A.5.1: Light curve for FLSF 2011-08-09. Panels from top to bottom: GOES X-rays; Fermi-GBM; Fermi-LAT LLE; Binned Fermi-LAT flux > 100 MeV.

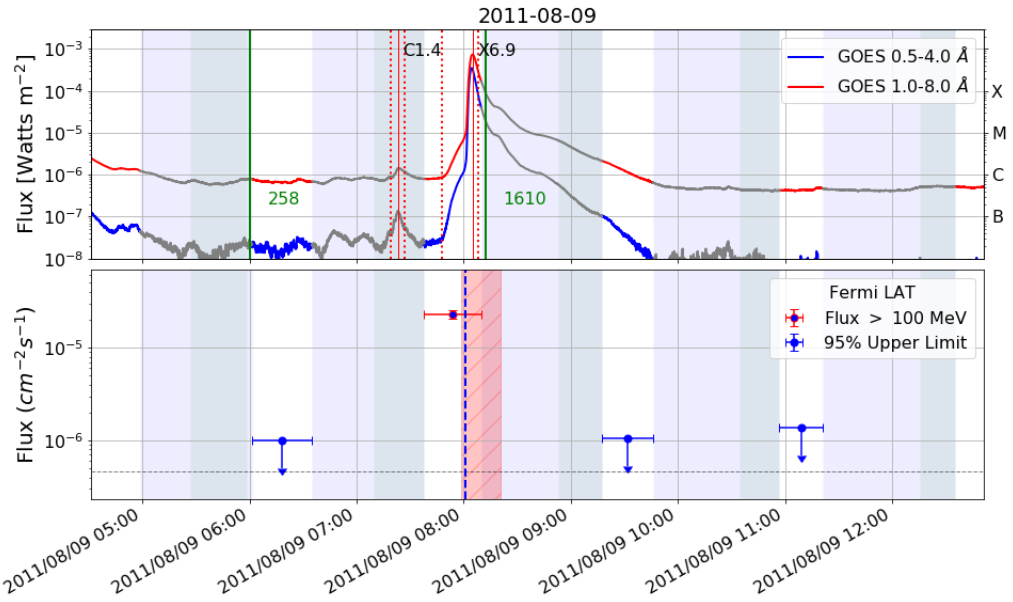

Figure A.5.2: Light curve for 2011-08-09. Top panel: GOES X-rays, bottom panel: Fermi-LAT flux > 100 MeV. Vertical blue line marks the start time of the LLE flare.

A.6 2011-09-06

Type of Gamma-ray Flare: **Prompt Delayed**.
Associated with a X2.1 GOES flare which started on 2011-09-06 22:12 and a CME with speed 575 km/s.
Fermi-LAT detected gamma-ray emission above 60 MeV starting on 2011-09-06 22:18 and ending on 2011-09-06 22:47, lasting 29 minutes. The prompt phase of 2011-09-06 is also associated with a LLE detection. The emission detected by the LLE approach started on 2011-09-06 at 22:18:07 and ended at 22:19:47 with a total duration of 100 seconds.
Comments: Gamma-ray detection with two components: one peaked synchronous with the HXRs and soft gamma rays; then a second short-term delayed component. Behavior may be similar to the first gamma-ray solar flares observed with a delayed component in the June 3, 1982 flare (see Ryan 2000 for a summary description). Associated with a slow CME and a minor SEP event.

Start Time	Duration (sec)	$Flux_{30}$	$Flux_{100}$	TS	`SunMon` detected	Out of FoV
2011-09-06 22:18:07	100	53.97 ± 1.45	16.55± 1.10	125	X	

Table A.6.1: LLE Spectral results for flare 2011-09-06. $Flux_{30}$ and $Flux_{100}$ indicate the flux computed from 30 MeV to 10 GeV and from 100 MeV to 10 GeV respectively (in units of 10^{-5} $cm^{-2}s^{-1}$).

Date and Time	Exposure (minutes)	Flux (10^{-5} $cm^{-2}s^{-1}$)	TS	ΔTS	Photon Index	Proton Index
2011-09-06 22:11 - 22:47	36	22.77 ± 0.43*	8197	437	-0.89 ± 0.09	4.89 ± 0.11

Table A.6.2: `SunMonitor` maximum likelihood results for 2011-09-06 (see Appendix A for description).

GOES	Class X2.1	Start 2011-09-06 22:12	Peak 2011-09-06 22:20	Stop 2011-09-06 22:24	Dur. (min) 12	AR position N14W18
CME	Speed 575 km/s	Width Halo	C2 time 2011-09-06 23:05			
SEP	Instrument GOES	Emax 100 MeV				
HXR	Instrument BGO	Emax 1000 kev				

Table A.6.3: Properties of the events associated with 2011-09-06: GOES X-ray flare, CME, SEPs, HXRs .

Date and Time	Helio X,Y	ERR 68%	ERR 95%	Angular Distance	Relative Distance (95)	Average Boresight (°)
2011-09-06 22:11 - 22:47	219,533	141	215	420	2	34

Table A.6.4: The GOES X-ray flare associated with the FLSF originated from AR 11283 whose position at the time of the GOES flare was N14W18 (see Appendix A for description).

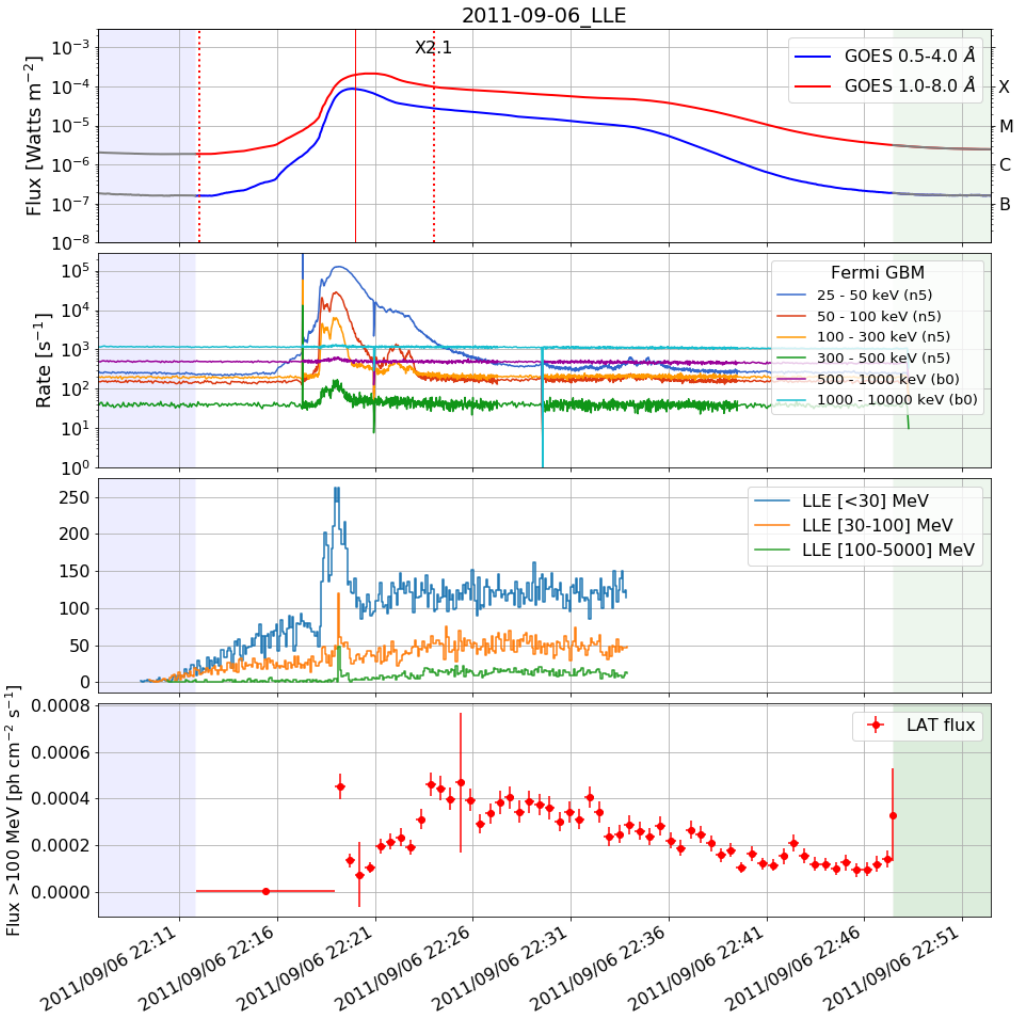

Figure A.6.1: Light curve for FLSF 2011-09-06. Panels from top to bottom: GOES X-rays; Fermi-GBM; Fermi-LAT LLE; Binned Fermi-LAT flux > 100 MeV.

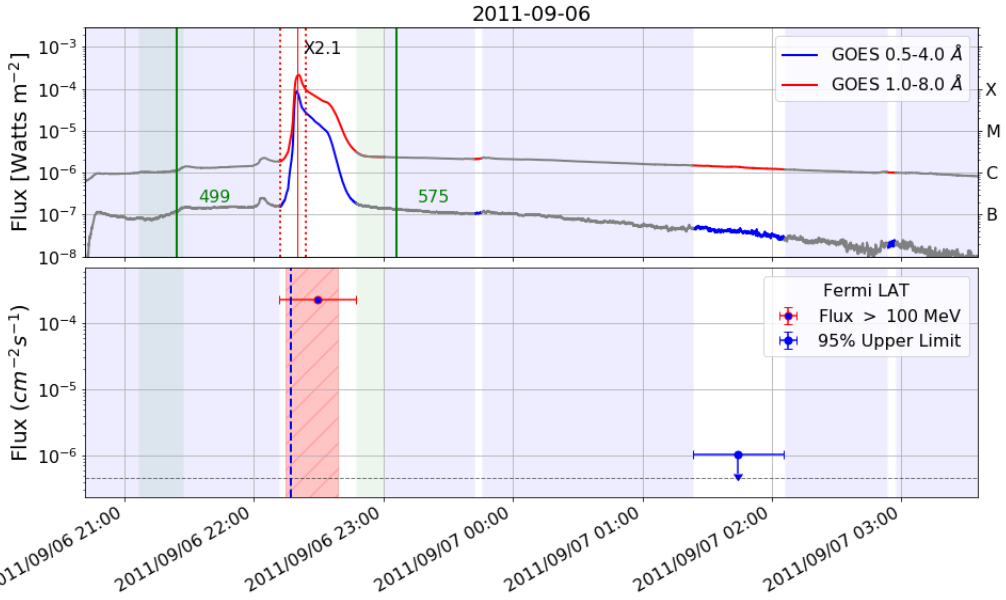

Figure A.6.2: Light curve for 2011-09-06. Top panel: GOES X-rays, bottom panel: Fermi-LAT flux > 100 MeV. Vertical blue line marks the start time of the LLE flare.

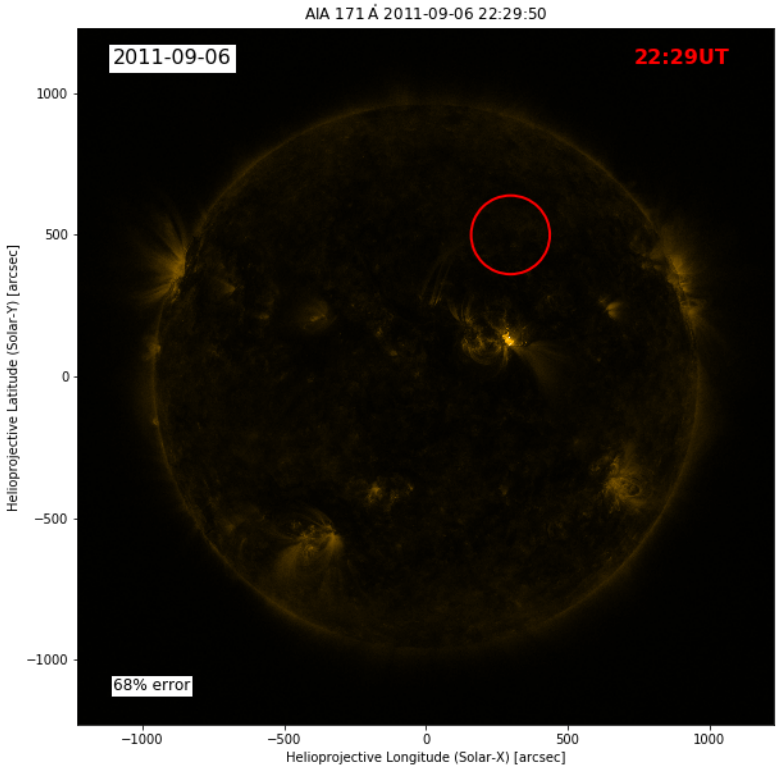

Figure A.6.3: Time resolved localization of the > 60 MeV emission from the 2011-09-06 flare. The mean time of each window is annotated in the upper right hand corner of each panel. The circles are the 68% source location uncertainty regions (results in Table A.6.4).

A.7 2011-09-07

Type of Gamma-ray Flare: **Delayed**.

Associated with a X1.8 GOES flare which started on 2011-09-07 22:32 and a CME with speed 792 km/s.

Fermi-LAT detected gamma-ray emission above 60 MeV starting on 2011-09-07 23:35 and ending on 2011-09-08 00:23, lasting 48 minutes.

Comments: A binned analysis shows decay.

Date and Time	Exposure (minutes)	Flux (10^{-5} cm^{-2}s^{-1})	TS	ΔTS	Photon Index	Proton Index
2011-09-07 23:35 - 00:23	48	0.77 $\pm$ 0.08	270	30	-0.10 $\pm$ 0.69	4.40 $\pm$ 0.45

Table A.7.1: `SunMonitor` maximum likelihood results for 2011-09-07 (see Appendix A for description).

GOES	Class X1.8	Start 2011-09-07 22:32	Peak 2011-09-07 22:38	Stop 2011-09-07 22:44	Dur. (min) 12	AR position N14W32
CME	Speed 792 km/s	Width 290	C2 time 2011-09-07 23:05			
SEP	Instrument GOES	Emax 50 MeV present				
HXR	Instrument BGO	Emax 500 kev				

Table A.7.2: Properties of the events associated with 2011-09-07: GOES X-ray flare, CME, SEPs, HXRs .

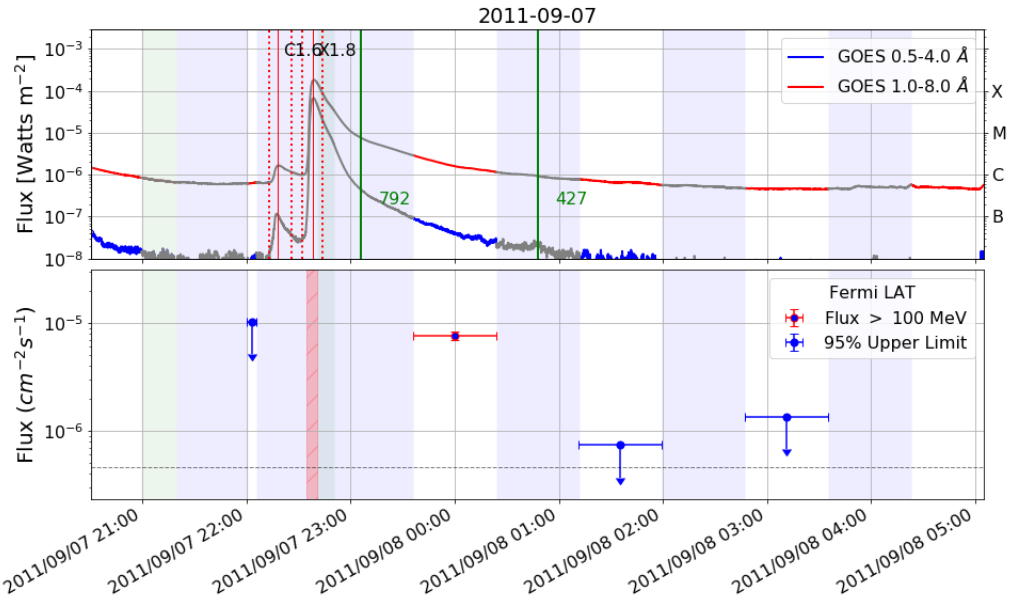

Figure A.7.1: Light curve for 2011-09-07. Top panel: GOES X-rays, bottom panel: Fermi-LAT flux > 100 MeV.

A.8 2011-09-24

Type of Gamma-ray Flare: **Prompt Delayed**.

Associated with a X1.9 GOES flare which started on 2011-09-24 09:21 and a CME with speed 1936 km/s.

Fermi-LAT detected gamma-ray emission above 60 MeV starting on 2011-09-24 09:35 and ending on 2011-09-24 09:47, lasting 12 minutes. The prompt phase of 2011-09-24 is also associated with a LLE detection. The emission detected by the LLE approach started on 2011-09-24 at 09:35:53 and ended at 09:37:33 with a total duration of 100 seconds.

Comments: LLE flare in the 30 - 100 MeV energy band coincident with HXR, but no greater than 100 MeV emission at that time. However short-term Delayed emission above 60 MeV is detected, peaking 5 minutes after.

Start Time	Duration (sec)	$Flux_{30}$	$Flux_{100}$	TS	`SunMon` detected	Out of FoV
2011-09-24 09:35:53	100	65.23 ± 1.67	0.43± 0.07	8	X	

Table A.8.1: LLE Spectral results for flare 2011-09-24. $Flux_{30}$ and $Flux_{100}$ indicate the flux computed from 30 MeV to 10 GeV and from 100 MeV to 10 GeV respectively (in units of 10^{-5} $cm^{-2}s^{-1}$).

Date and Time	Exposure (minutes)	Flux (10^{-5} $cm^{-2}s^{-1}$)	TS	ΔTS	Photon Index	Proton Index
2011-09-24 09:18 - 09:47	30	0.50 ± 0.10*	50	5	-2.51 ± 0.22	-

Table A.8.2: `SunMonitor` maximum likelihood results for 2011-09-24 (see Appendix A for description).

GOES	Class X1.9	Start 2011-09-24 09:21	Peak 2011-09-24 09:40	Stop 2011-09-24 09:48	Dur. (min) 27	AR position N13E45
CME	Speed 1936 km/s	Width 92	C2 time 2011-09-24 09:48			
SEP	Instrument GOES	Emax 50 MeV present				
HXR	Instrument BGO	Emax 1000 kev				

Table A.8.3: Properties of the events associated with 2011-09-24: GOES X-ray flare, CME, SEPs, HXRs .

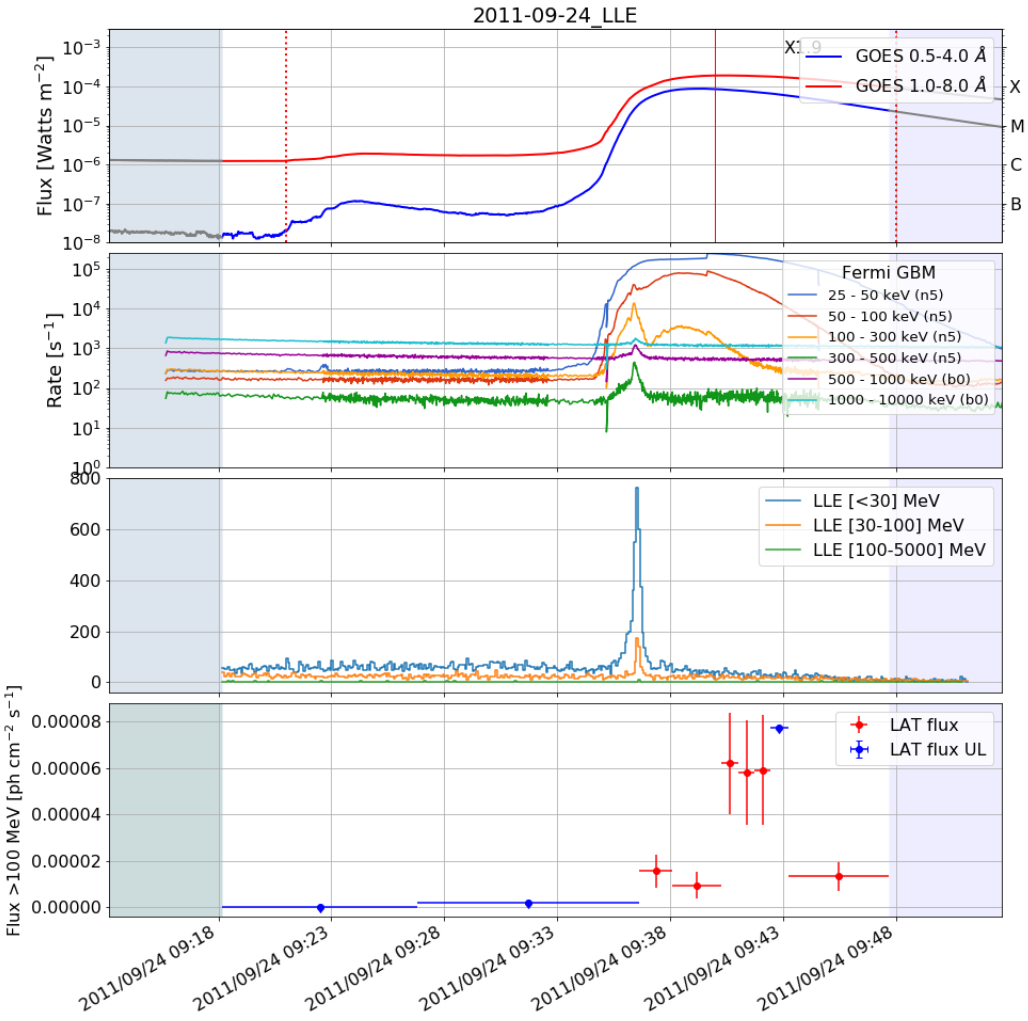

Figure A.8.1: Light curve for FLSF 2011-09-24. Panels from top to bottom: GOES X-rays; Fermi-GBM; Fermi-LAT LLE; Binned Fermi-LAT flux > 100 MeV.

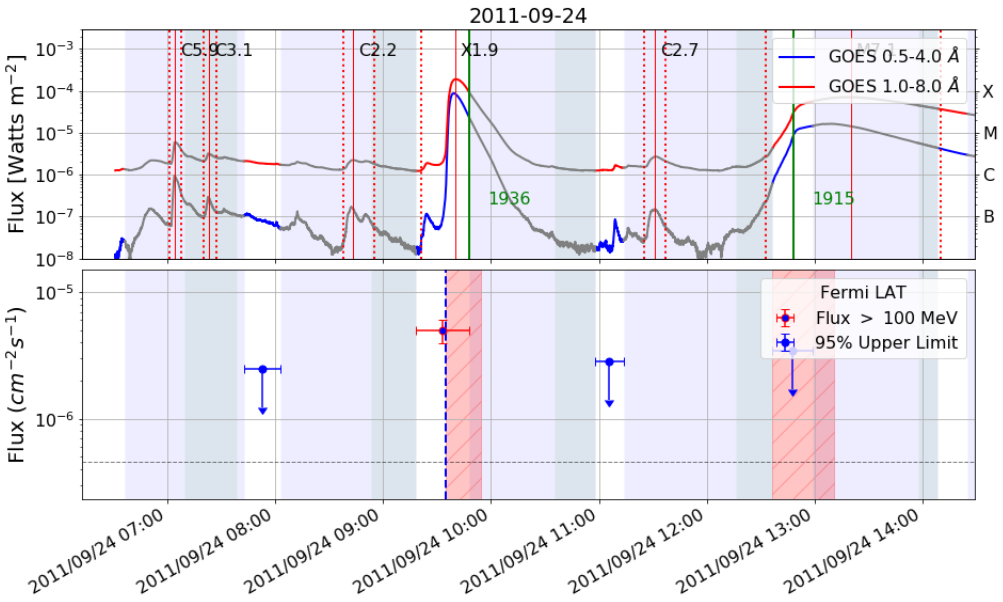

Figure A.8.2: Light curve for 2011-09-24. Top panel: GOES X-rays, bottom panel: Fermi-LAT flux > 100 MeV. Vertical blue line marks the start time of the LLE flare.

A.9 2012-01-23

Type of Gamma-ray Flare: **Delayed**.

Associated with a M8.7 GOES flare which started on 2012-01-23 03:38 and a CME with speed 2175 km/s.

Fermi-LAT detected gamma-ray emission above 60 MeV starting on 2012-01-23 04:06 and ending on 2012-01-23 09:26, lasting 5.3 hours.

Comments: Almost all HXR activity ended before the first time window start time: the gamma-ray emission is delayed component.

Date and Time	Exposure (minutes)	Flux (10^{-5} cm^{-2}s^{-1})	TS	ΔTS	Photon Index	Proton Index
2012-01-23 04:06 - 04:46	40	1.12 ± 0.11	258	26	0.12 ± 1.09	5.46 ± 0.60
2012-01-23 05:33 - 06:21	48	1.99 ± 0.12	796	92	0.25 ± 0.41	5.57 ± 0.36
2012-01-23 07:20 - 07:47	27	1.97 ± 0.31	93	12	-0.25 ± 1.05	5.50 ± 0.91
2012-01-23 08:58 - 09:26	28	1.63 ± 0.23	116	27	1.81 ± 1.41	5.57 ± 0.79

Table A.9.1: `SunMonitor` maximum likelihood results for 2012-01-23 (see Appendix A for description).

GOES	Class M8.7	Start 2012-01-23 03:38	Peak 2012-01-23 03:59	Stop 2012-01-23 04:34	Dur. (min) 56	AR position N28W20
CME	Speed 2175 km/s	Width Halo	C2 time 2012-01-23 04:00			
SEP	Instrument GOES	Emax 100 MeV				
HXR	Instrument NaI5	Emax > 100 kev				

Table A.9.2: Properties of the events associated with 2012-01-23: GOES X-ray flare, CME, SEPs, HXRs (HXR coverage incomplete).

Date and Time	Helio X,Y	ERR 68%	ERR 95%	Angular Distance	Relative Distance (95)	Average Boresight (°)
2012-01-23 05:33 - 06:21	-104,713	460	736	439	0.6	15

Table A.9.3: The GOES X-ray flare associated with the FLSF originated from AR 11402 whose position at the time of the GOES flare was N28W20 (see Appendix A for description).

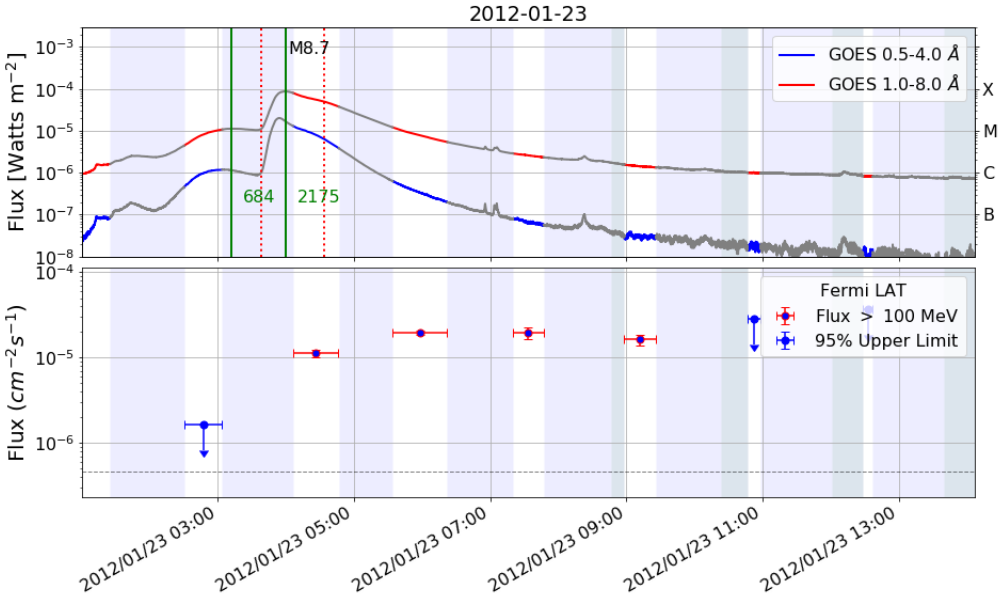

Figure A.9.1: Light curve for 2012-01-23. Top panel: GOES X-rays, bottom panel: Fermi-LAT flux > 100 MeV.

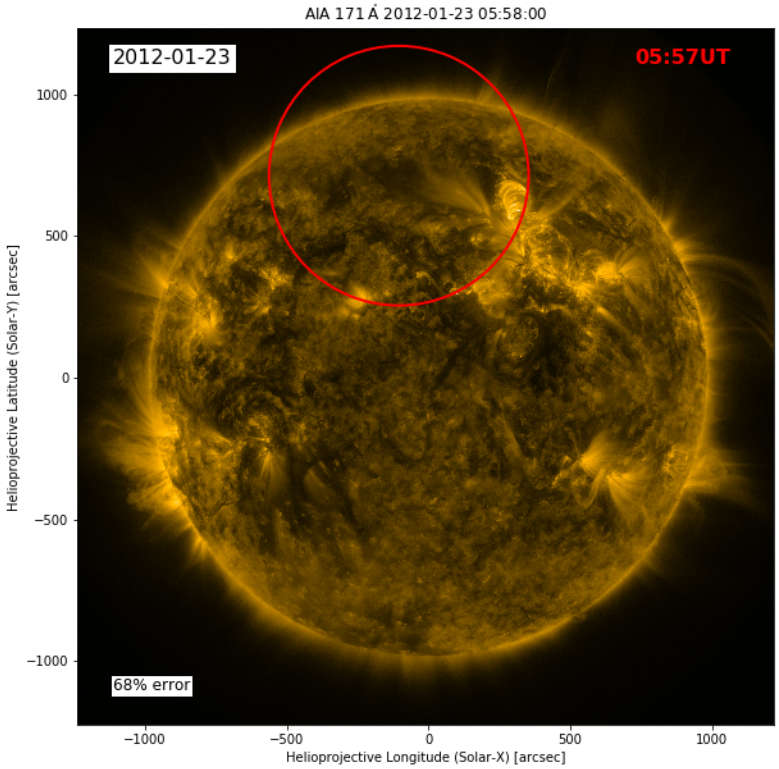

Figure A.9.2: Time resolved localization of the > 60 MeV emission from the 2012-01-23 flare. The mean time of each window is annotated in the upper right hand corner of each panel. The circles are the 68% source location uncertainty regions (results in Table A.9.3).

A.10 2012-01-27

Type of Gamma-ray Flare: **Delayed**.

Associated with a X1.7 GOES flare which started on 2012-01-27 17:37 and a CME with speed 2508 km/s.

Fermi-LAT detected gamma-ray emission above 60 MeV starting on 2012-01-27 19:37 and ending on 2012-01-28 00:55, lasting 5.3 hours.

Comments: Detection over 3 time windows, with a gap between the last two. A binned analysis shows a rise within the first time window, followed by a decay between the second and 3rd windows. The upper limit is consistent with the decaying phase. Associated with a strong energetic SEP event.

Date and Time	Exposure (minutes)	Flux (10^{-5} cm^{-2}s^{-1})	TS	ΔTS	Photon Index	Proton Index
2012-01-27 19:37 - 19:55	18	3.32 $\pm$ 0.49	102	14	0.31 $\pm$ 1.43	>6
2012-01-27 21:08 - 21:36	28	0.72 $\pm$ 0.14	66	8	-2.53 $\pm$ 0.20	-
2012-01-28 00:19 - 00:55	36	0.25 $\pm$ 0.09	19	1	-2.60 $\pm$ 0.39	-

Table A.10.1: `SunMonitor` maximum likelihood results for 2012-01-27 (see Appendix A for description).

GOES	Class X1.7	Start 2012-01-27 17:37	Peak 2012-01-27 18:37	Stop 2012-01-27 18:56	Dur. (min) 79	AR position N29W86
CME	Speed 2508 km/s	Width Halo	C2 time 2012-01-27 18:27			
SEP	Instrument GOES	Emax 605 MeV				
HXR	Instrument NaI5	Emax > 100 kev				

Table A.10.2: Properties of the events associated with 2012-01-27: GOES X-ray flare, CME, SEPs, HXRs (HXR coverage incomplete).

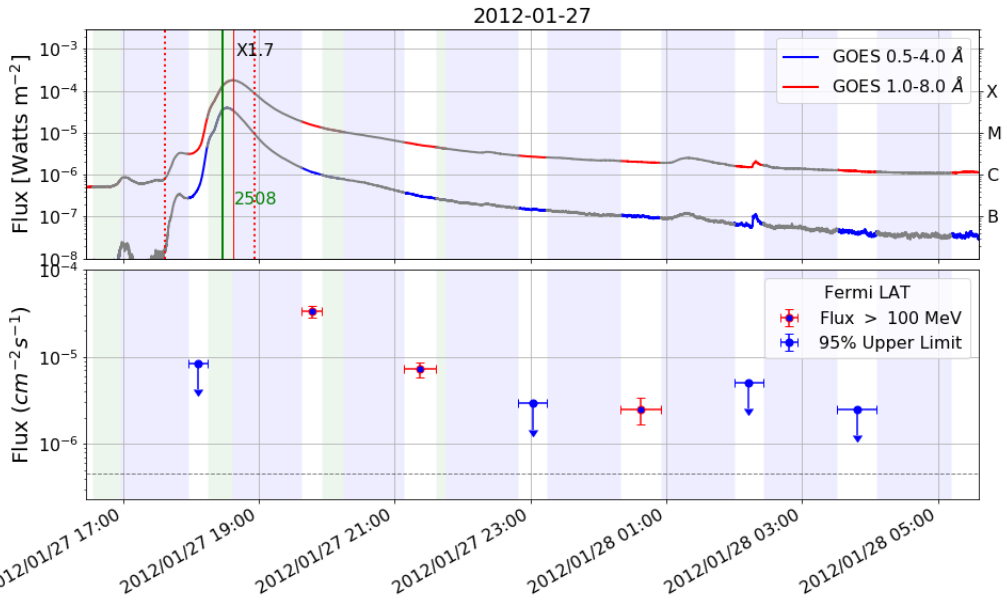

Figure A.10.1: Light curve for 2012-01-27. Top panel: GOES X-rays, bottom panel: Fermi-LAT flux > 100 MeV.

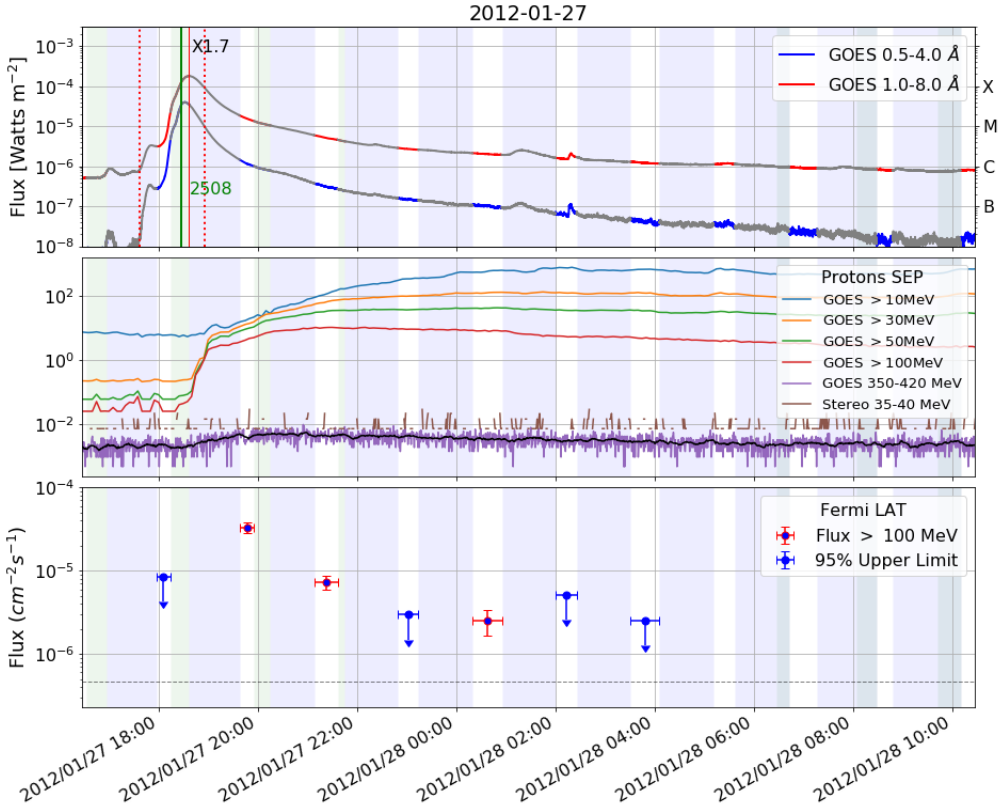

Figure A.10.2: Composite light curve for SEP event associated with 2012-01-27. Panels from top to bottom: GOES X-rays, GOES SEP count rate (ACE and STEREO data when available), Fermi-LAT >100 MeV flux.

A.11 2012-03-05

Type of Gamma-ray Flare: **Delayed**.

Associated with a X1.1 GOES flare which started on 2012-03-05 02:30 and a CME with speed 1531 km/s.

Fermi-LAT detected gamma-ray emission above 60 MeV starting on 2012-03-05 04:25 and ending on 2012-03-05 07:54, lasting 3.5 hours.

Comments: Delayed emission over 3 time windows. Most of the non-thermal activity subsided at the start of the first window, so no indication of the gamma-ray emission during the Prompt phase of the flare.

Date and Time	Exposure (minutes)	Flux (10^{-5} cm^{-2}s^{-1})	TS	ΔTS	Photon Index	Proton Index
2012-03-05 04:07 - 04:49	42	0.58 $\pm$ 0.09	100	11	0.34 $\pm$ 1.33	>6
2012-03-05 05:36 - 06:24	48	0.63 $\pm$ 0.07	175	16	-0.20 $\pm$ 0.85	>6
2012-03-05 07:18 - 07:54	36	0.55 $\pm$ 0.11	53	6	-2.52 $\pm$ 0.21	-

Table A.11.1: `SunMonitor` maximum likelihood results for 2012-03-05 (see Appendix A for description).

GOES	Class X1.1	Start 2012-03-05 02:30	Peak 2012-03-05 04:09	Stop 2012-03-05 04:43	Dur. (min) 133	AR position N18E41
CME	Speed 1531 km/s	Width Halo	C2 time 2012-03-05 04:00			
SEP	Instrument STEREO	Emax 40 MeV present				
HXR	Instrument NaI5	Emax > 100 kev				

Table A.11.2: Properties of the events associated with 2012-03-05: GOES X-ray flare, CME, SEPs, HXRs (HXR coverage incomplete).

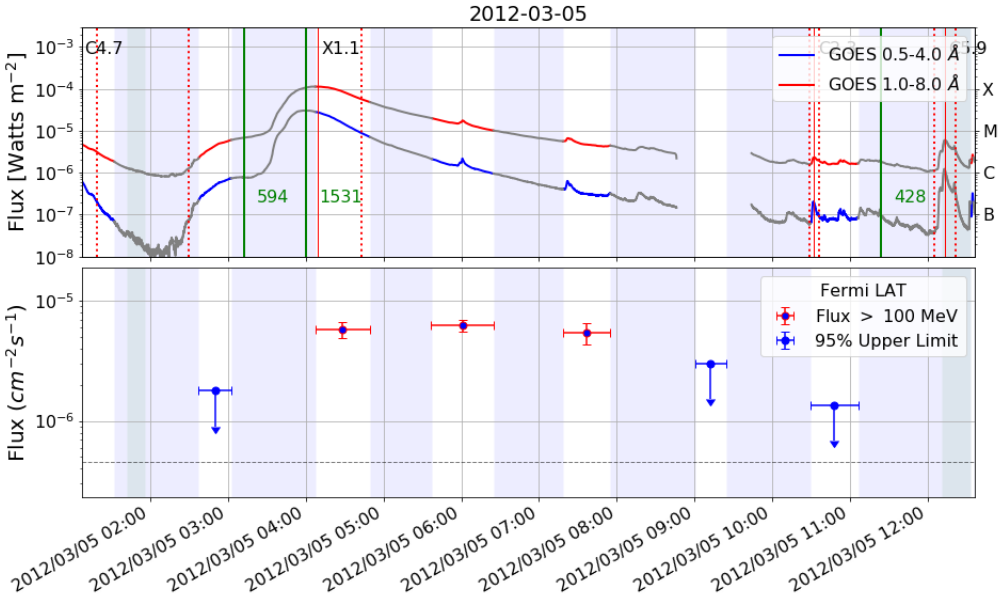

Figure A.11.1: Light curve for 2012-03-05. Top panel: GOES X-rays, bottom panel: Fermi-LAT flux > 100 MeV.

A.12 2012-03-07

Type of Gamma-ray Flare: **Delayed**.

Associated with a X5.4 GOES flare which started on 2012-03-07 00:02 and a CME with speed 2684 km/s.

Fermi-LAT detected gamma-ray emission above 60 MeV starting on 2012-03-07 00:40 and ending on 2012-03-07 20:15, lasting 19.6 hours.

Comments: Two GOES flares X5.4 and X1.3 and two CMEs with speeds 2684.0 and 1825km/s. See Section 5.1 for results of dedicated analysis.

Date and Time	Exposure (minutes)	Flux (10^{-5} cm^{-2}s^{-1})	TS	ΔTS	Photon Index	Proton Index
2012-03-07 00:40 - 01:20	40	232.56 ± 8.23*	75611	-254574	-0.65 ± 0.03	3.87 ± 0.02
2012-03-07 02:26 - 02:45	18	75.05 ± 2.62	2377	117	-1.45 ± 0.13	3.77 ± 0.10
2012-03-07 03:51 - 04:31	40	95.09 ± 1.18	21100	1459	-0.84 ± 0.05	4.01 ± 0.05
2012-03-07 05:38 - 05:55	18	97.34 ± 3.24	2675	249	-0.59 ± 0.17	4.51 ± 0.13
2012-03-07 07:02 - 07:42	40	62.79 ± 0.98	12829	1210	-0.30 ± 0.08	4.71 ± 0.07
2012-03-07 08:49 - 09:06	17	49.76 ± 2.47	1181	123	-0.17 ± 0.32	5.17 ± 0.24
2012-03-07 10:14 - 10:54	25	26.75 ± 0.87	2803	344	0.27 ± 0.21	5.28 ± 0.17
2012-03-07 13:24 - 14:04	13	8.58 ± 0.93	258	31	0.30 ± 0.75	5.71 ± 0.60
2012-03-07 16:35 - 16:48	13	1.54 ± 0.32	49	10	1.41 ± 1.91	>6
2012-03-07 18:23 - 18:32	9	2.20 ± 0.74	25	8	-2.91 ± 0.41	-
2012-03-07 19:46 - 20:15	29	0.26 ± 0.08	22	3	-2.37 ± 0.30	-

Table A.12.1: `SunMonitor` maximum likelihood results for 2012-03-07 (see Appendix A for description).

GOES	Class X5.4	Start 2012-03-07 00:02	Peak 2012-03-07 00:24	Stop 2012-03-07 00:40	Dur. (min) 38	AR position N17E27
CME	Speed 2684 km/s	Width Halo	C2 time 2012-03-07 00:24			
SEP	Instrument GOES	Emax 605 MeV				
HXR	Instrument BGO	Emax 1000 kev				

Table A.12.2: Properties of the events associated with 2012-03-07: GOES X-ray flare, CME, SEPs, HXRs .

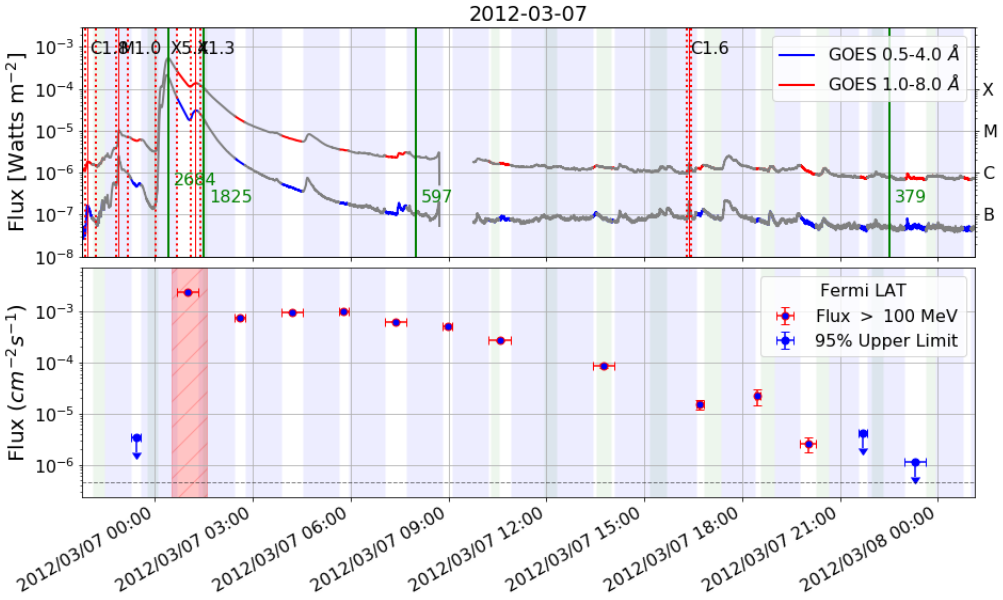

Figure A.12.1: Light curve for 2012-03-07. Top panel: GOES X-rays, bottom panel: Fermi-LAT flux > 100 MeV.

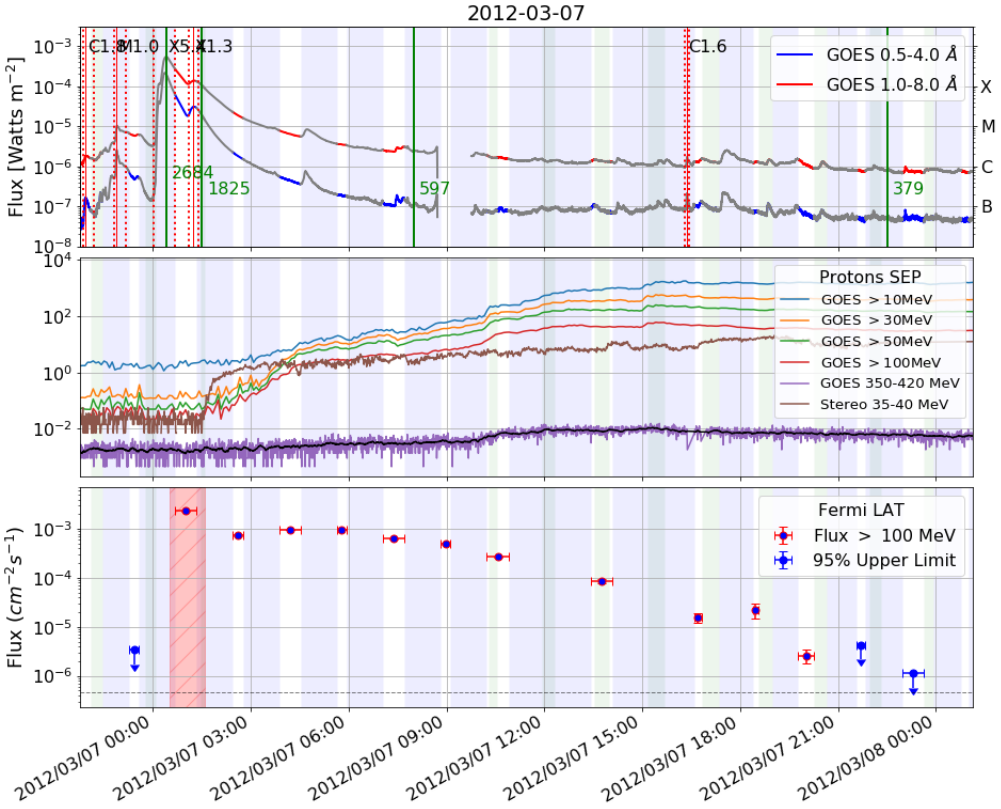

Figure A.12.2: Composite light curve for SEP event associated with 2012-03-07. Panels from top to bottom: GOES X-rays, GOES SEP count rate (ACE and STEREO data when available), Fermi-LAT >100 MeV flux.

A.13 2012-03-09

Type of Gamma-ray Flare: **Delayed only**.

Associated with a M6.3 GOES flare which started on 2012-03-09 03:22 and a CME with speed 950 km/s.

Fermi-LAT detected gamma-ray emission above 60 MeV starting on 2012-03-09 05:12 and ending on 2012-03-09 10:41, lasting 5.5 hours.

Comments: Delayed emission with a rise and fall pattern, but no gamma-ray emission detected above 60 MeV from the Sun while in the FoV during the impulsive phase of the flare with HXR reaching the 100-300 keV channel of NaI (coverage of the very first part of the GOES flare might be missing). This is one of the cases described as Delayed-only.

Date and Time	Exposure (minutes)	Flux (10^{-5} cm^{-2}s^{-1})	TS	ΔTS	Photon Index	Proton Index
2012-03-09 05:12 - 05:55	43	0.27 ± 0.08	32	-0.2	-2.24 ± 0.25	-
2012-03-09 06:47 - 07:30	43	0.96 ± 0.12	139	20	0.09 ± 0.92	5.49 ± 0.74
2012-03-09 08:22 - 09:05	43	0.89 ± 0.12	140	28	1.78 ± 1.21	5.61 ± 0.78
2012-03-09 09:58 - 10:41	22	0.43 ± 0.13	25	0.3	-2.51 ± 0.32	-

Table A.13.1: `SunMonitor` maximum likelihood results for 2012-03-09 (see Appendix A for description).

GOES	Class M6.3	Start 2012-03-09 03:22	Peak 2012-03-09 03:53	Stop 2012-03-09 04:18	Dur. (min) 56	AR position N17W13
CME	Speed 950 km/s	Width Halo	C2 time 2012-03-09 04:26			
SEP	Instrument GOES	Emax 100 MeV present				
HXR	Instrument NaI5	Emax > 100 kev				

Table A.13.2: Properties of the events associated with 2012-03-09: GOES X-ray flare, CME, SEPs, HXRs (HXR coverage incomplete).

Date and Time	Helio X,Y	ERR 68%	ERR 95%	Angular Distance	Relative Distance (95)	Average Boresight (°)
2012-03-09 05:12 - 05:55	-932,381	406	883	1141	1	48

Table A.13.3: The GOES X-ray flare associated with the FLSF originated from AR 11429 whose position at the time of the GOES flare was N17W13 (see Appendix A for description).

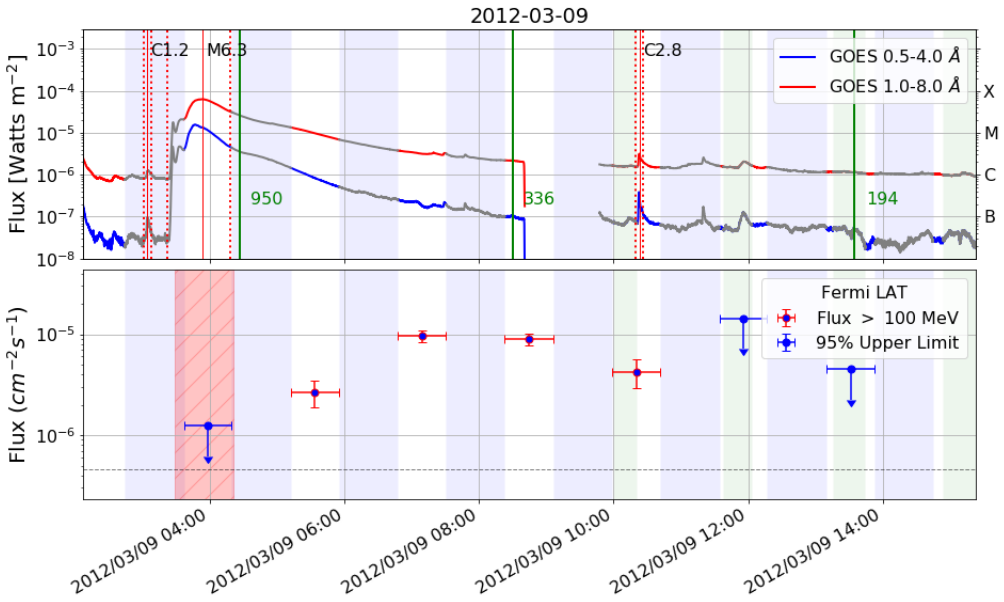

Figure A.13.1: Light curve for 2012-03-09. Top panel: GOES X-rays, bottom panel: Fermi-LAT flux > 100 MeV.

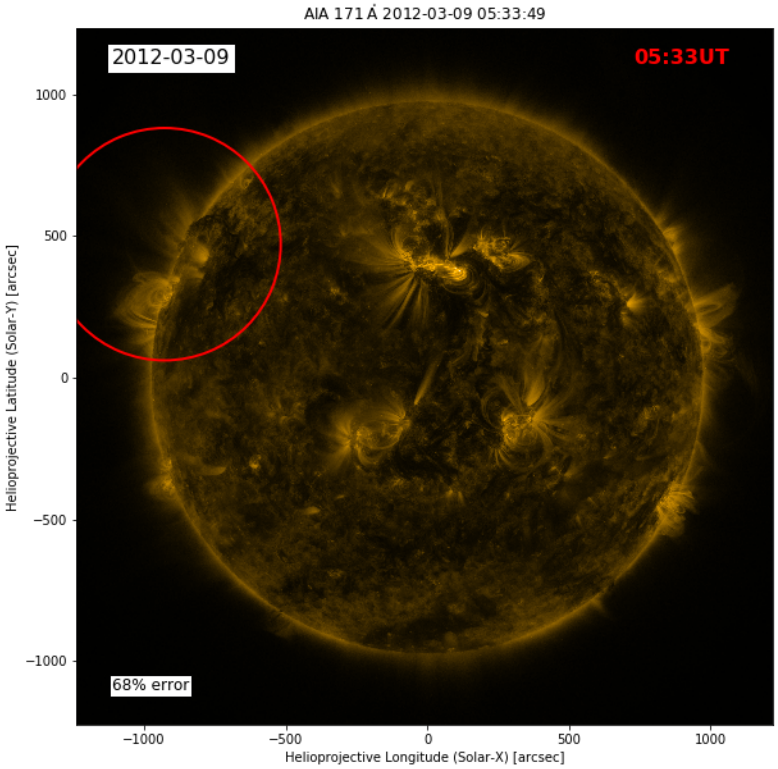

Figure A.13.2: Time resolved localization of the > 60 MeV emission from the 2012-03-09 flare. The mean time of each window is annotated in the upper right hand corner of each panel. The circles are the 68% source location uncertainty regions (results in Table A.13.3).

A.14 2012-03-10

Type of Gamma-ray Flare: **Delayed**.
Associated with a M8.4 GOES flare which started on 2012-03-10 17:15 and a CME with speed 1296 km/s.
Fermi-LAT detected gamma-ray emission above 60 MeV starting on 2012-03-10 21:00 and ending on 2012-03-10 23:15, lasting 2.3 hours.
Comments: The prompt phase of the M8.4 flare is most likely outside of the FoV (no coverage of Rhessi or GBM for the start of the GOES flare, but the peak of the derivative of the SXR peaks is outside of the FoV).

Date and Time	Exposure (minutes)	Flux (10^{-5} cm^{-2}s^{-1})	TS	ΔTS	Photon Index	Proton Index
2012-03-10 21:00 - 21:34	34	0.23 $\pm$ 0.06	25	2	-2.50 $\pm$ 0.30	-
2012-03-10 22:35 - 23:15	40	0.19 $\pm$ 0.06	18	3	-3.04 $\pm$ 0.40	-

Table A.14.1: `SunMonitor` maximum likelihood results for 2012-03-10 (see Appendix A for description).

GOES	Class M8.4	Start 2012-03-10 17:15	Peak 2012-03-10 17:44	Stop 2012-03-10 18:30	Dur. (min) 75	AR position N18W27
CME	Speed 1296 km/s	Width Halo	C2 time 2012-03-10 18:00			
SEP	Instrument GOES	Emax 100 MeV present				
HXR	Instrument NaI5	Emax $>$ 50 kev				

Table A.14.2: Properties of the events associated with 2012-03-10: GOES X-ray flare, CME, SEPs, HXRs (HXR coverage incomplete).

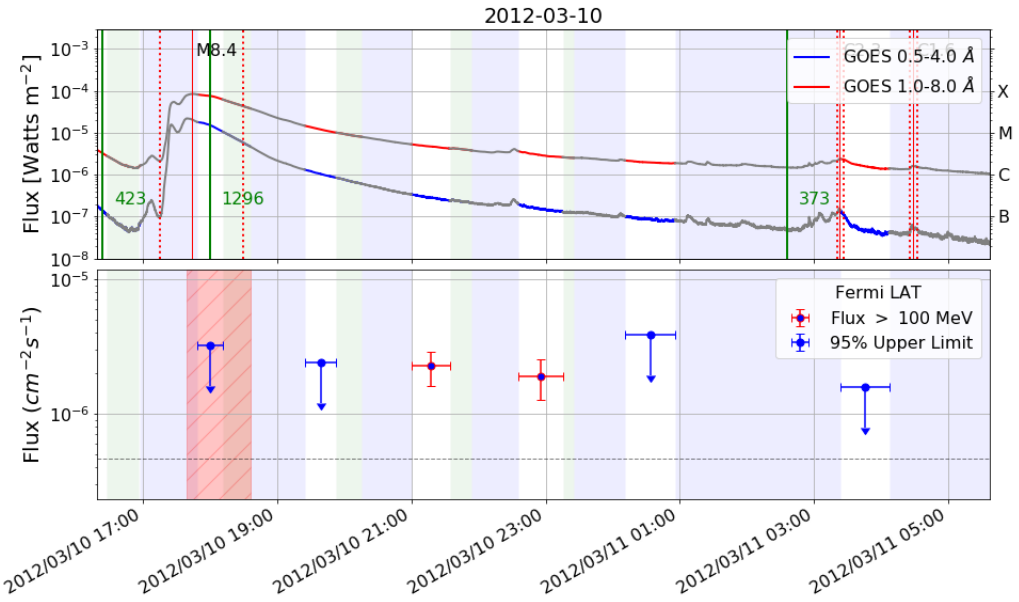

Figure A.14.1: Light curve for 2012-03-10. Top panel: GOES X-rays, bottom panel: Fermi-LAT flux > 100 MeV.

A.15 2012-05-17

Type of Gamma-ray Flare: **Delayed**.

Associated with a M5.1 GOES flare which started on 2012-05-17 01:25 and a CME with speed 1582 km/s.

Fermi-LAT detected gamma-ray emission above 60 MeV starting on 2012-05-17 02:12 and ending on 2012-05-17 04:18, lasting 2.1 hours.

Comments: Associated with the first GLE of Solar Cycle 24 (see Section 7.3).

Date and Time	Exposure (minutes)	Flux (10^{-5} cm^{-2}s^{-1})	TS	ΔTS	Photon Index	Proton Index
2012-05-17 02:12 - 02:44	32	1.19 $\pm$ 0.19	100	10	-0.72 $\pm$ 0.77	3.69 $\pm$ 0.49
2012-05-17 03:49 - 04:18	30	0.44 $\pm$ 0.13	29	7	-2.30 $\pm$ 0.28	-

Table A.15.1: `SunMonitor` maximum likelihood results for 2012-05-17 (see Appendix A for description).

GOES	Class M5.1	Start 2012-05-17 01:25	Peak 2012-05-17 01:47	Stop 2012-05-17 02:14	Dur. (min) 49	AR position N13W87
CME	Speed 1582 km/s	Width Halo	C2 time 2012-05-17 01:48			
SEP	Instrument GOES	Emax 605 MeV				
HXR	Instrument Rhessi	Emax > 100 kev				

Table A.15.2: Properties of the events associated with 2012-05-17: GOES X-ray flare, CME, SEPs, HXRs (HXR coverage incomplete).

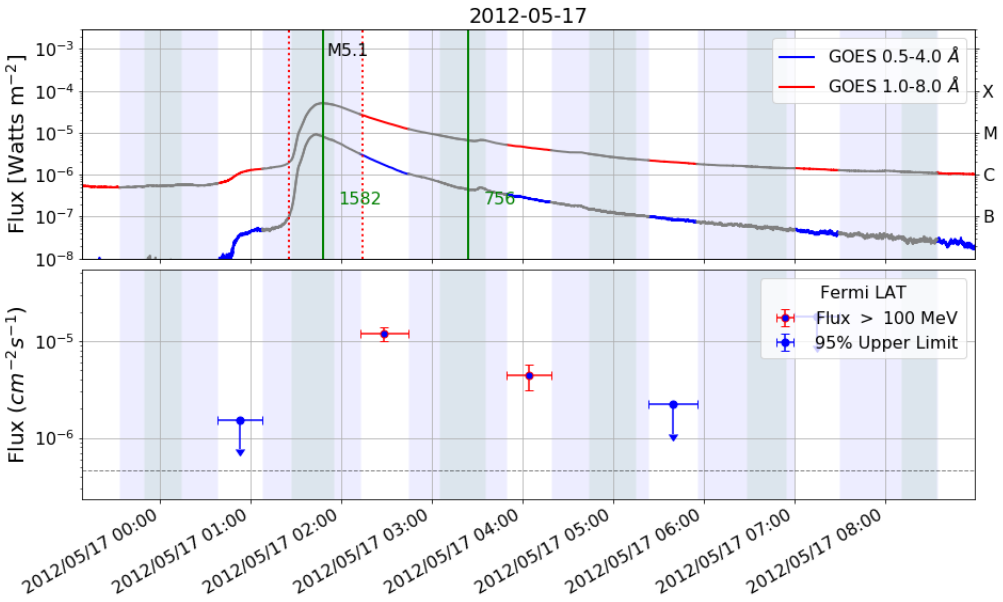

Figure A.15.1: Light curve for 2012-05-17. Top panel: GOES X-rays, bottom panel: Fermi-LAT flux > 100 MeV.

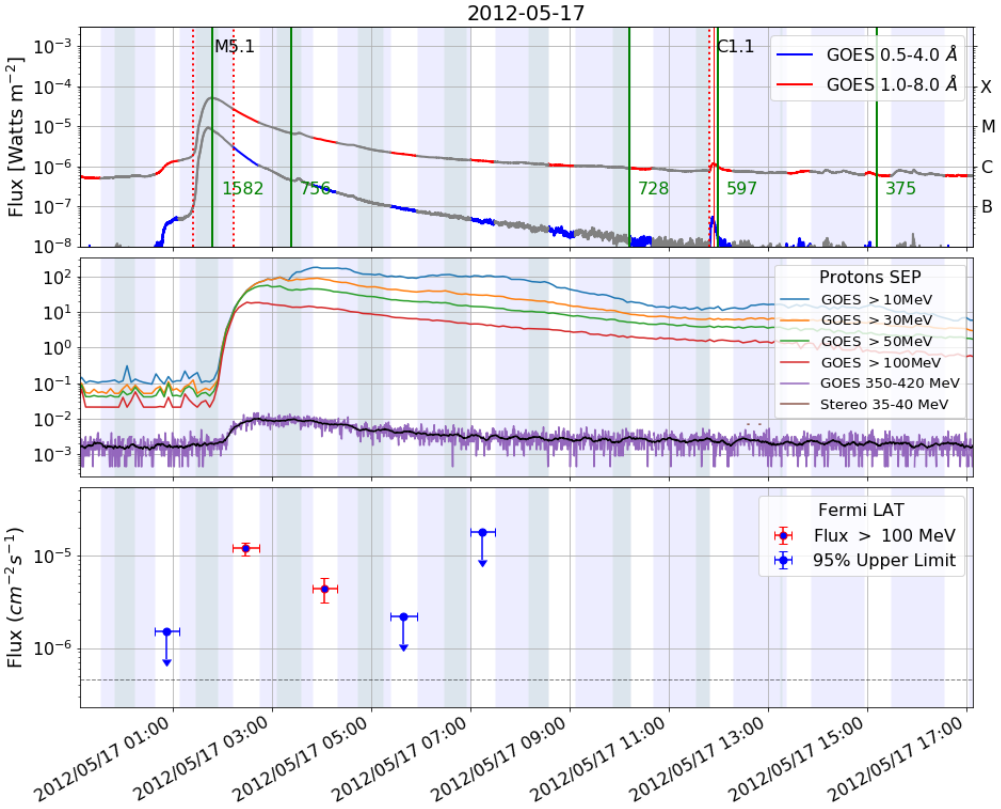

Figure A.15.2: Composite light curve for SEP event associated with 2012-05-17. Panels from top to bottom: GOES X-rays, GOES SEP count rate (ACE and STEREO data when available), Fermi-LAT >100 MeV flux.

A.16 2012-06-03

Type of Gamma-ray Flare: **Prompt Delayed**.

Associated with a M3.3 GOES flare which started on 2012-06-03 17:48 and a CME with speed 605 km/s.

Fermi-LAT detected gamma-ray emission above 60 MeV starting on 2012-06-03 17:53 and ending on 2012-06-03 18:02, lasting 9 minutes. The prompt phase of 2012-06-03 is also associated with a LLE detection. The emission detected by the LLE approach started on 2012-06-03 at 17:53:20 and ended at 17:53:40 with a total duration of 20 seconds.

Comments: LLE detection coincident with HXR peak and detected above 100 MeV, followed by short delayed emission over 23 minutes.

Start Time	Duration (sec)	$Flux_{30}$	$Flux_{100}$	TS	`SunMon` detected	Out of FoV
2012-06-03 17:53:20	20	110.54 ± 5.28	49.66± 4.54	120	X	

Table A.16.1: LLE Spectral results for flare 2012-06-03. $Flux_{30}$ and $Flux_{100}$ indicate the flux computed from 30 MeV to 10 GeV and from 100 MeV to 10 GeV respectively (in units of 10^{-5} $cm^{-2}s^{-1}$).

Date and Time	Exposure (minutes)	Flux (10^{-5} $cm^{-2}s^{-1}$)	TS	ΔTS	Photon Index	Proton Index
2012-06-03 17:38 - 18:02	24	3.06 ± 0.25	395	39	-0.19 ± 0.63	4.96 ± 0.42

Table A.16.2: `SunMonitor` maximum likelihood results for 2012-06-03 (see Appendix A for description).

GOES	Class M3.3	Start 2012-06-03 17:48	Peak 2012-06-03 17:55	Stop 2012-06-03 17:57	Dur. (min) 9	AR position N16E33
CME	Speed 605 km/s	Width 71	C2 time 2012-06-03 18:12			
HXR	Instrument Rhessi	Emax 100 kev				

Table A.16.3: Properties of the events associated with 2012-06-03: GOES X-ray flare, CME, SEPs, HXRs .

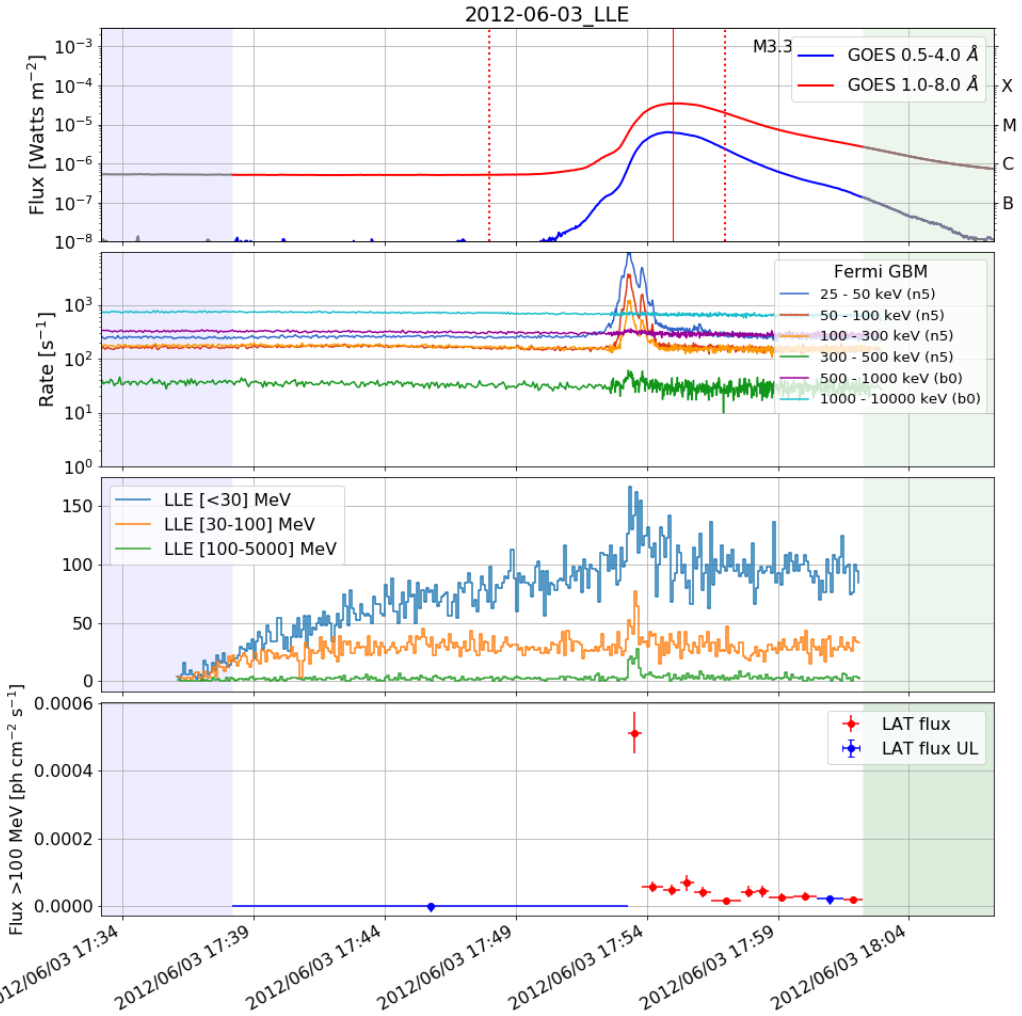

Figure A.16.1: Light curve for FLSF 2012-06-03. Panels from top to bottom: GOES X-rays; Fermi-GBM; Fermi-LAT LLE; Binned Fermi-LAT flux > 100 MeV.

Date and Time	Helio X,Y	ERR 68%	ERR 95%	Angular Distance	Relative Distance (95)	Average Boresight (°)
2012-06-03 17:38 - 18:02	-457,181	507	825	94	0.1	39

Table A.16.4: The GOES X-ray flare associated with the FLSF originated from AR 11496 whose position at the time of the GOES flare was N16E33 (see Appendix A for description).

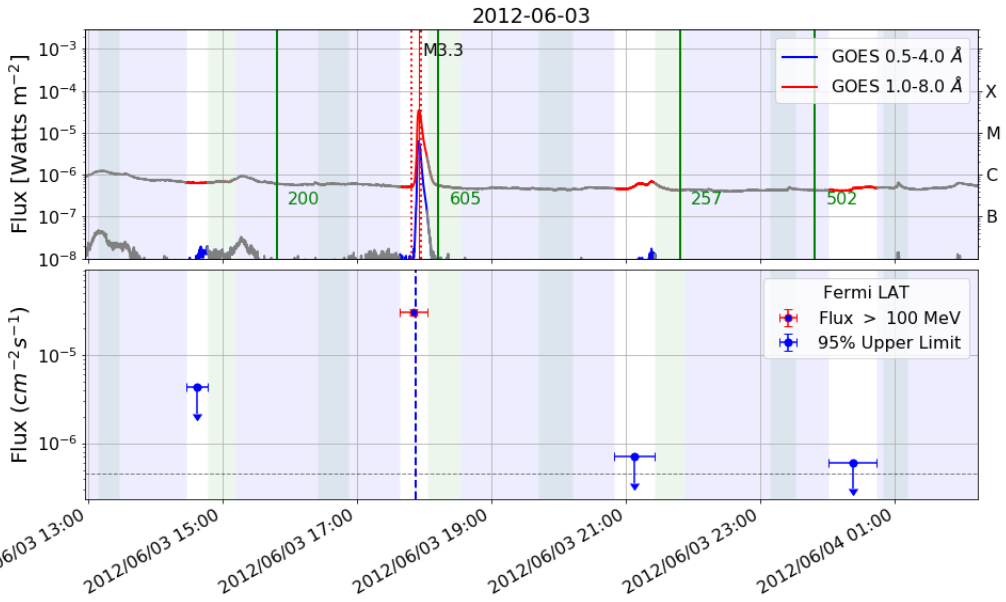

Figure A.16.2: Light curve for 2012-06-03. Top panel: GOES X-rays, bottom panel: Fermi-LAT flux > 100 MeV. Vertical blue line marks the start time of the LLE flare.

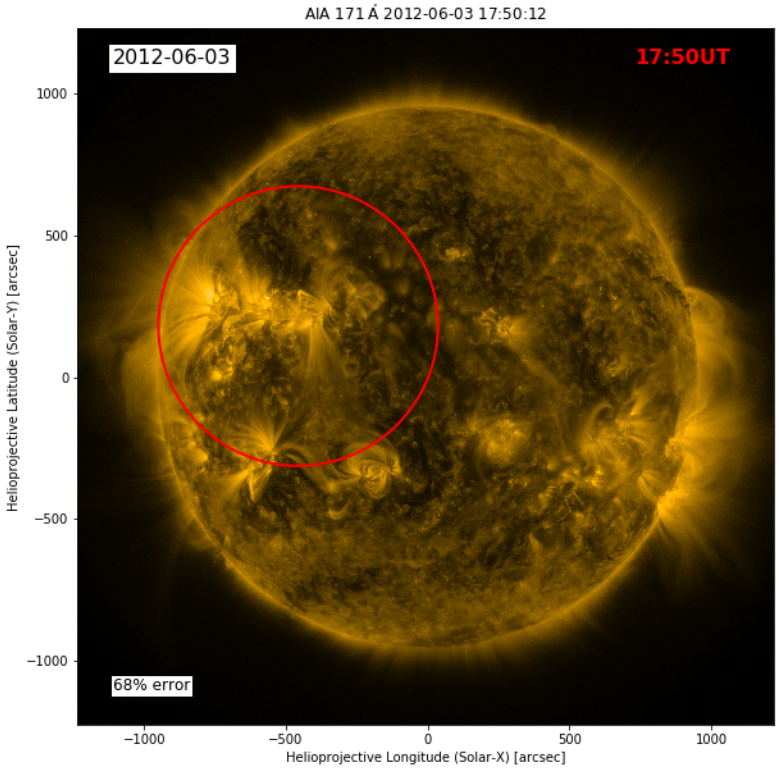

Figure A.16.3: Time resolved localization of the > 60 MeV emission from the 2012-06-03 flare. The mean time of each window is annotated in the upper right hand corner of each panel. The circles are the 68% source location uncertainty regions (results in Table A.16.4).

A.17 2012-07-06

Type of Gamma-ray Flare: **Delayed**.

Associated with a X1.1 GOES flare which started on 2012-07-06 23:01 and a CME with speed 1828 km/s.

Fermi-LAT detected gamma-ray emission above 60 MeV starting on 2012-07-06 23:20 and ending on 2012-07-07 00:08, lasting 48 minutes.

Comments: nan

Date and Time	Exposure (minutes)	Flux (10^{-5} cm^{-2}s^{-1})	TS	ΔTS	Photon Index	Proton Index
2012-07-06 23:20 - 00:08	48	3.06 $\pm$ 0.15	1173	143	0.40 $\pm$ 0.35	5.75 $\pm$ 0.29

Table A.17.1: `SunMonitor` maximum likelihood results for 2012-07-06 (see Appendix A for description).

GOES	Class X1.1	Start 2012-07-06 23:01	Peak 2012-07-06 23:08	Stop 2012-07-06 23:14	Dur. (min) 13	AR position S18W64
CME	Speed 1828 km/s	Width Halo	C2 time 2012-07-06 23:24			
SEP	Instrument GOES	Emax 100 MeV				

Table A.17.2: Properties of the events associated with 2012-07-06: GOES X-ray flare, CME, SEPs, HXRs .

Date and Time	Helio X,Y	ERR 68%	ERR 95%	Angular Distance	Relative Distance (95)	Average Boresight ($^\circ$)
2012-07-06 23:20 - 00:08	530,-433	372	586	302	0.5	25

Table A.17.3: The GOES X-ray flare associated with the FLSF originated from AR 11515 whose position at the time of the GOES flare was S18W64 (see Appendix A for description).

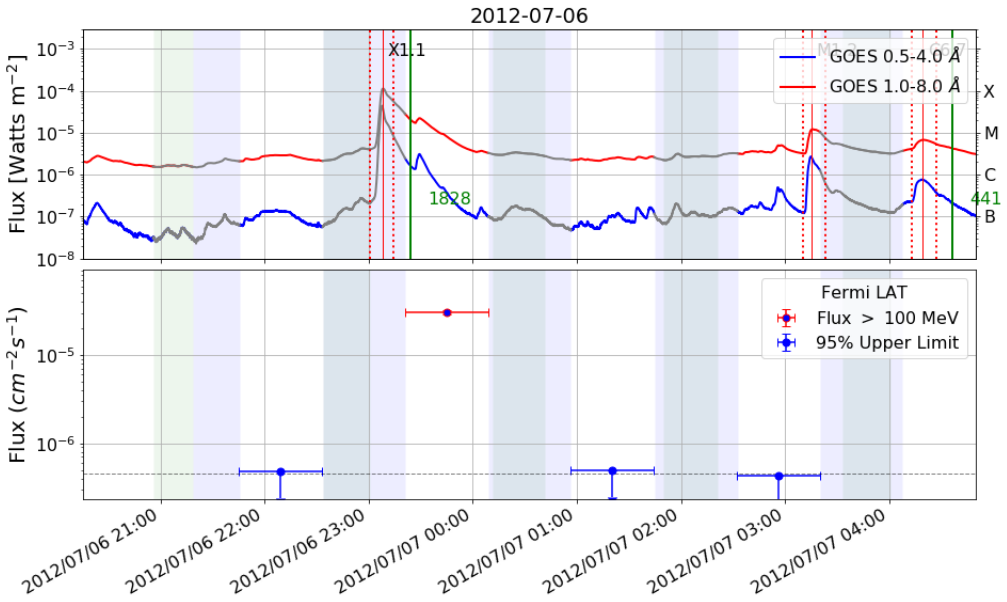

Figure A.17.1: Light curve for 2012-07-06. Top panel: GOES X-rays, bottom panel: Fermi-LAT flux > 100 MeV.

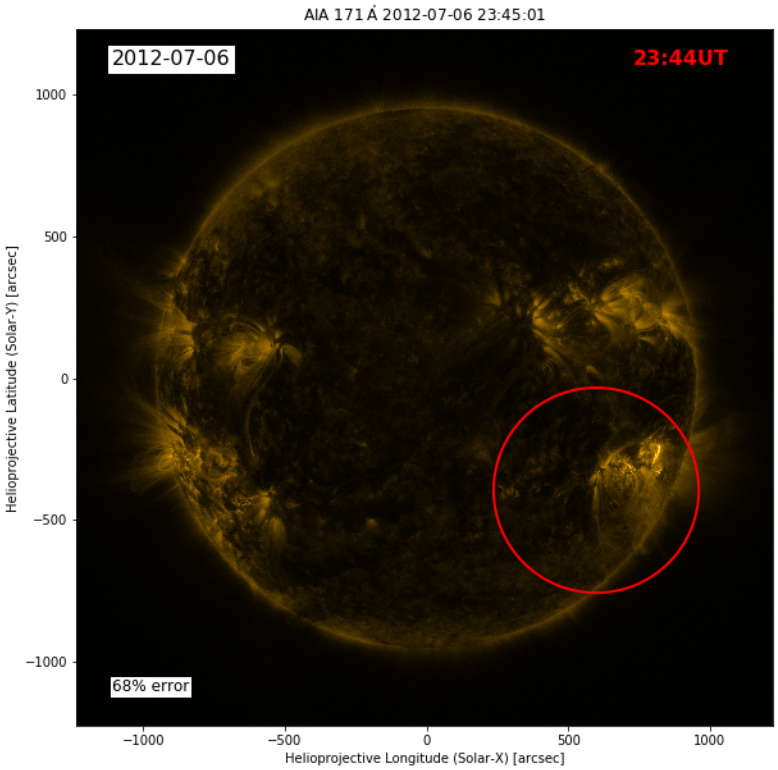

Figure A.17.2: Time resolved localization of the > 60 MeV emission from the 2012-07-06 flare. The mean time of each window is annotated in the upper right hand corner of each panel. The circles are the 68% source location uncertainty regions (results in Table A.17.3).

A.18 2012-08-06

Type of Gamma-ray Flare: **Prompt**.

Associated with a M1.6 GOES flare which started on 2012-08-06 04:33 and a CME with speed 198 km/s.

Fermi-LAT detected gamma-ray emission with the LLE approach only. Emission started on 2012-08-06 at 04:36:01 and ended at 04:36:31 with a total duration of 30 seconds.

Comments: Likely associated with a very slow CME (slowest of the FLSF catalog: the CME detection is described poor in the LASCO catalog.

Start Time	Duration (sec)	$Flux_{30}$	$Flux_{100}$	TS	`SunMon` detected	Out of FoV
2012-08-06 04:36:01	30	204.73 $\pm$ 4.73	1.79$\pm$ 0.12	0		

Table A.18.1: LLE Spectral results for flare 2012-08-06. $Flux_{30}$ and $Flux_{100}$ indicate the flux computed from 30 MeV to 10 GeV and from 100 MeV to 10 GeV respectively (in units of 10^{-5} $cm^{-2}s^{-1}$).

GOES	Class M1.6	Start 2012-08-06 04:33	Peak 2012-08-06 04:38	Stop 2012-08-06 04:41	Dur. (min) 8	AR position S14E88
CME	Speed 198 km/s	Width 81	C2 time 2012-08-06 05:12			
HXR	Instrument NaI5	Emax 100 kev				

Table A.18.2: Properties of the events associated with 2012-08-06: GOES X-ray flare, CME, SEPs, HXRs .

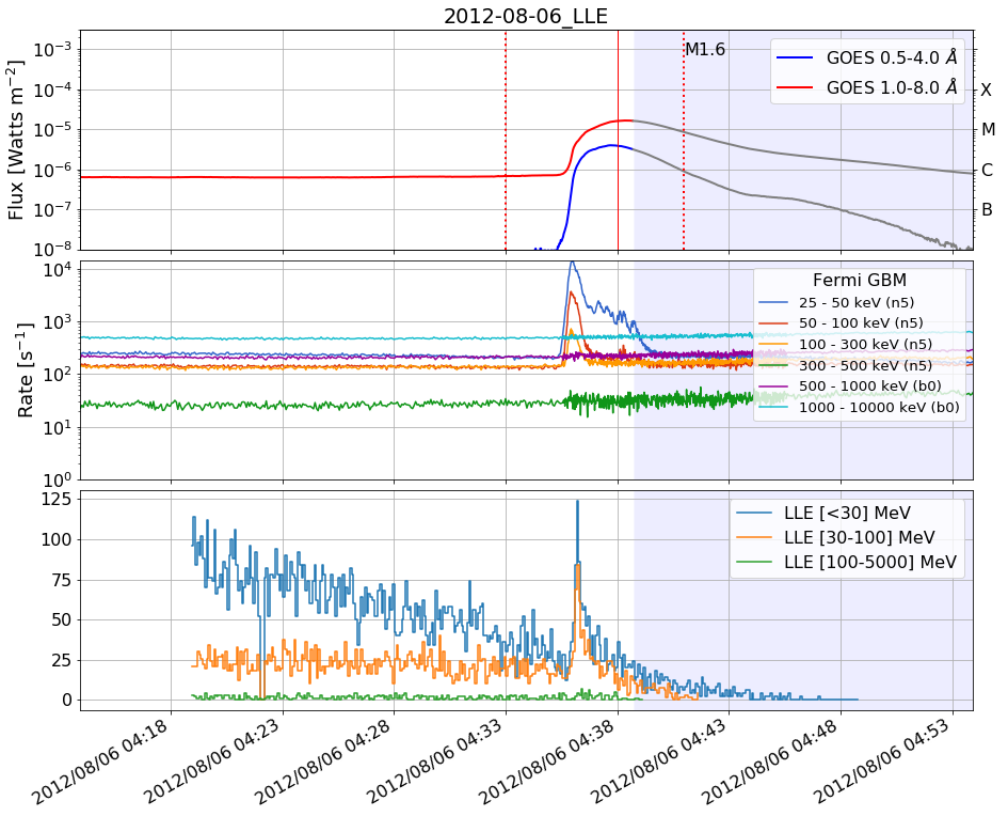

Figure A.18.1: Light curve for FLSF 2012-08-06. Panels from top to bottom: GOES X-rays; Fermi-GBM; Fermi-LAT LLE.

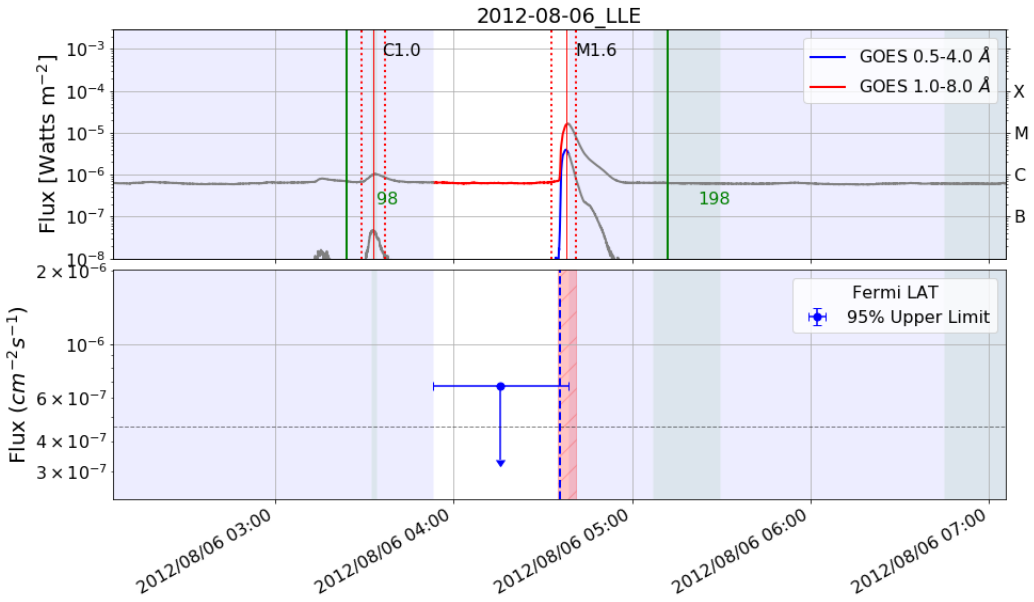

Figure A.18.2: Light curve for 2012-08-06. Top panel: GOES X-rays, bottom panel: Fermi-LAT flux > 100 MeV. Vertical blue line marks the start time of the LLE flare.

A.19 2012-10-23

Type of Gamma-ray Flare: **Prompt Delayed**.
Associated with a X1.8 GOES flare which started on 2012-10-23 03:13 (no significant CME associated).
Fermi-LAT detected gamma-ray emission above 60 MeV starting on 2012-10-23 03:15 and ending on 2012-10-23 04:20, lasting 65 minutes. The prompt phase of 2012-10-23 is also associated with a LLE detection. The emission detected by the LLE approach started on 2012-10-23 at 03:15:33 and ended at 03:15:53 with a total duration of 20 seconds.
Comments: Very interesting case of Delayed gamma-ray emission, with no CME. A possible explanation could be the large eruptive behavior and sunquake observed but failed at developing a CME (see Section 7.1 for context). LLE detection of the prompt phase up to 100 MeV (HXR up to 1 MeV), followed by a `SunMonitor` detection about an hour later (GOES lightcurve not available for this time range).

Start Time	Duration (sec)	$Flux_{30}$	$Flux_{100}$	TS	`SunMon` detected	Out of FoV
2012-10-23 03:15:33	20	3078.96 ± 272.89	105.04± 20.24	4	X	X

Table A.19.1: LLE Spectral results for flare 2012-10-23. $Flux_{30}$ and $Flux_{100}$ indicate the flux computed from 30 MeV to 10 GeV and from 100 MeV to 10 GeV respectively (in units of 10^{-5} $cm^{-2}s^{-1}$).

Date and Time	Exposure (minutes)	Flux (10^{-5} $cm^{-2}s^{-1}$)	TS	ΔTS	Photon Index	Proton Index
2012-10-23 04:13 - 04:43	30	0.73 ± 0.18	39	9	-2.73 ± 0.27	-

Table A.19.2: `SunMonitor` maximum likelihood results for 2012-10-23 (see Appendix A for description).

GOES	Class	Start	Peak	Stop	Dur. (min)	AR position
	X1.8	2012-10-23 03:13	2012-10-23 03:17	2012-10-23 03:21	8	S10E42
HXR	Instrument	Emax				
	BGO	1000 kev				

Table A.19.3: Properties of the events associated with 2012-10-23: GOES X-ray flare, CME, SEPs, HXRs .

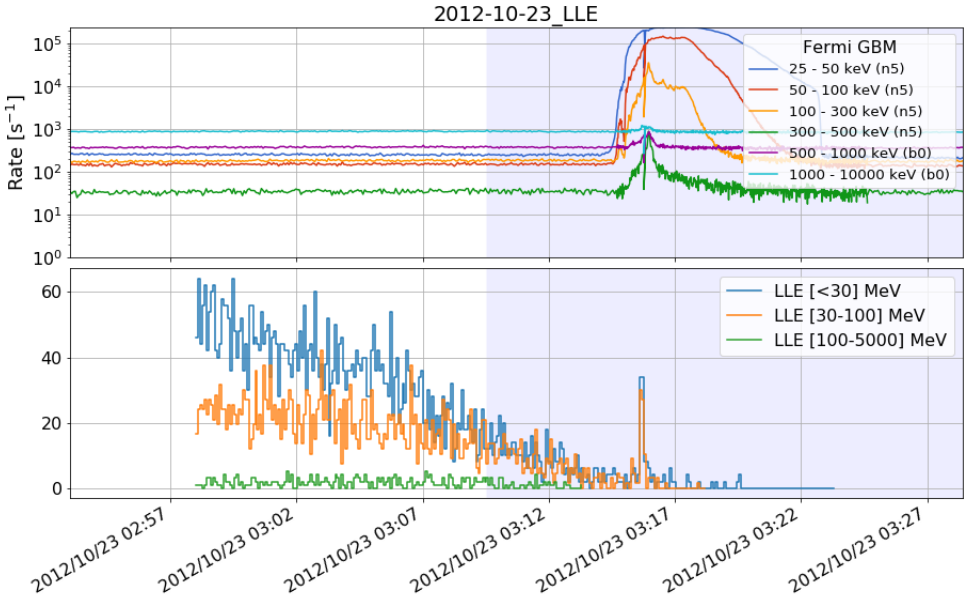

Figure A.19.1: Light curve for FLSF 2012-10-23. Panels from top to bottom: GOES X-rays; Fermi-GBM; Fermi-LAT LLE.

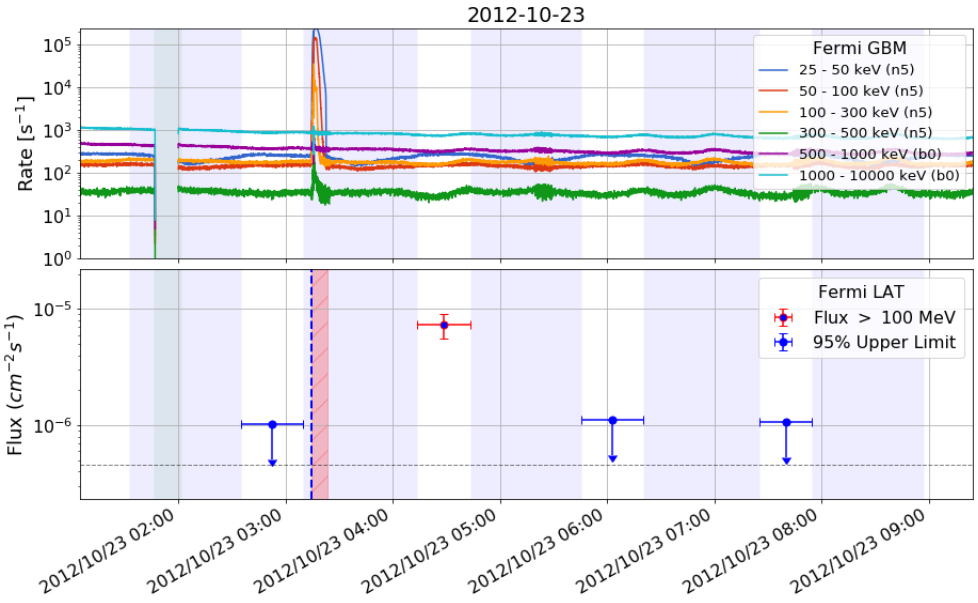

Figure A.19.2: Light curve for 2012-10-23. Top panel: GOES X-rays, bottom panel: Fermi-LAT flux > 100 MeV. Vertical blue line marks the start time of the LLE flare.

A.20 2012-11-13

Type of Gamma-ray Flare: **Prompt**.

Associated with a M6.0 GOES flare which started on 2012-11-13 01:58 and a CME with speed 851 km/s.

Fermi-LAT detected gamma-ray emission above 60 MeV starting on 2012-11-13 02:01 and ending on 2012-11-13 02:04, lasting 2 minutes.

Comments: Binned LAT analysis shows the gamma-ray emission does not extend beyond HXR (GOES lightcurve not available for this time range).

Date and Time	Exposure (minutes)	Flux (10^{-5} cm^{-2}s^{-1})	TS	ΔTS	Photon Index	Proton Index
2012-11-13 01:34 - 02:14	40	0.46 ± 0.09*	60	7	-2.61 ± 0.21	-

Table A.20.1: `SunMonitor` maximum likelihood results for 2012-11-13 (see Appendix A for description).

GOES	Class M6.0	Start 2012-11-13 01:58	Peak 2012-11-13 02:04	Stop 2012-11-13 02:04	Dur. (min) 8	AR position S25E46
CME	Speed 851 km/s	Width 119	C2 time 2012-11-13 02:24			
HXR	Instrument NaI5	Emax 100 kev				

Table A.20.2: Properties of the events associated with 2012-11-13: GOES X-ray flare, CME, SEPs, HXRs .

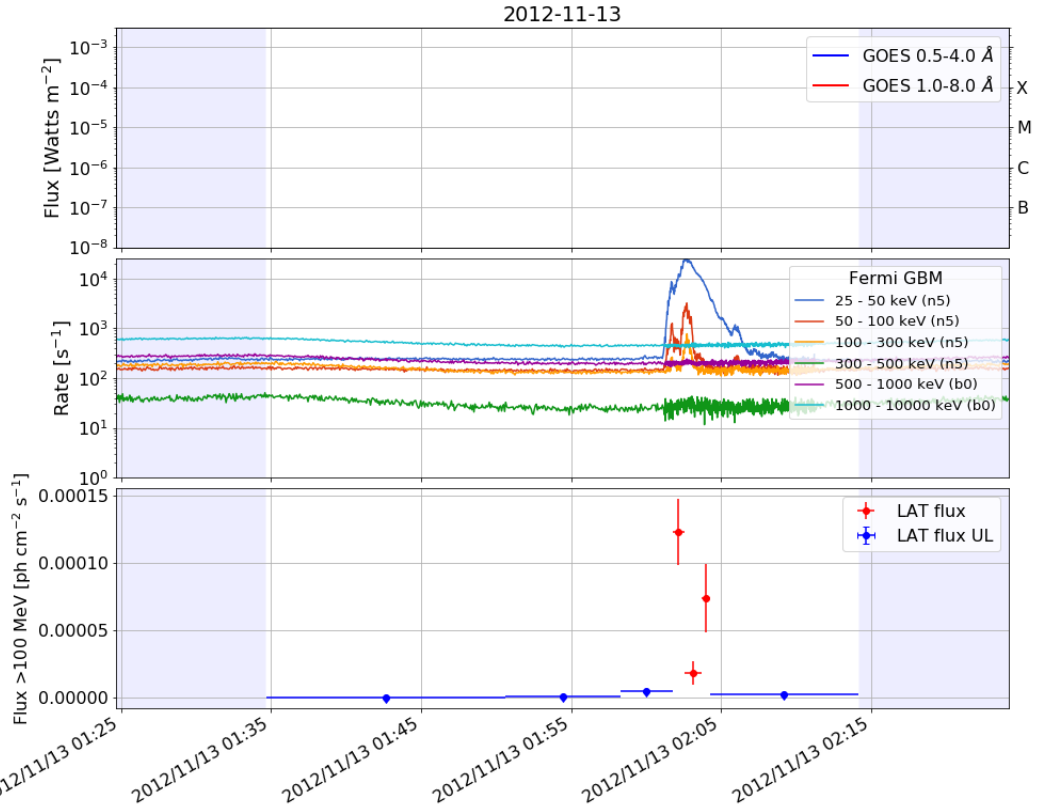

Figure A.20.1: Light curve for FLSF 2012-11-13. Panels from top to bottom: GOES X-rays; Fermi-GBM; Binned Fermi-LAT flux > 100 MeV.

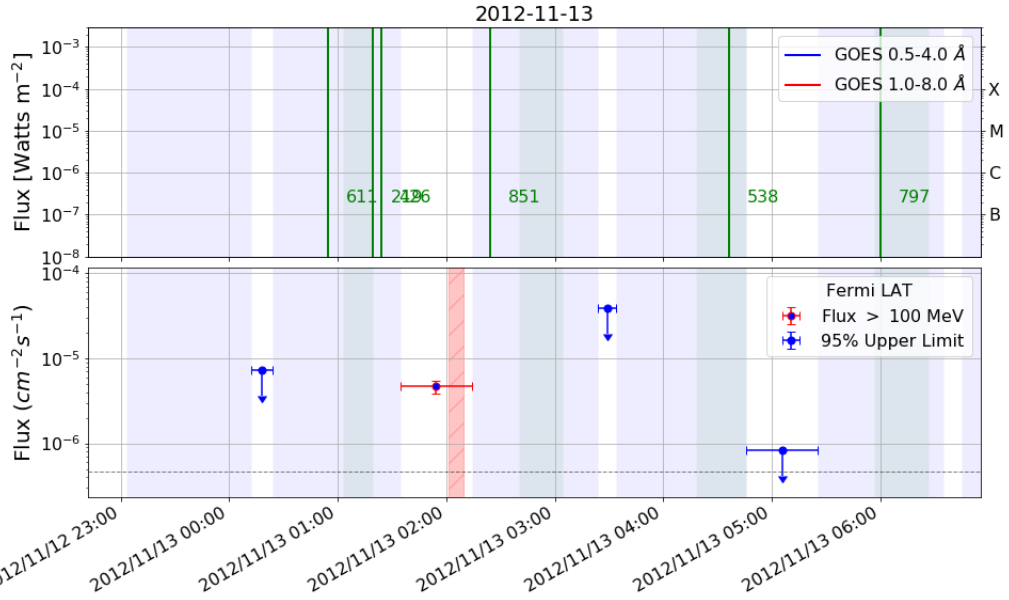

Figure A.20.2: Light curve for 2012-11-13. Top panel: GOES X-rays, bottom panel: Fermi-LAT flux > 100 MeV.

A.21 2012-11-27

Type of Gamma-ray Flare: **Prompt Delayed**.
Associated with a M1.6 GOES flare which started on 2012-11-27 15:52 (no significant CME associated).
Fermi-LAT detected gamma-ray emission above 60 MeV starting on 2012-11-27 15:55 and ending on 2012-11-27 16:05, lasting 10 minutes.
Comments: Gamma rays starting at the time of the HXR and lasting about 10 minutes beyond the HXR peak. From SOHO movie, it seems that the flare is associated with a filament eruption.

Date and Time	Exposure (minutes)	Flux (10^{-5} cm^{-2}s^{-1})	TS	ΔTS	Photon Index	Proton Index
2012-11-27 15:48 - 16:34	46	0.27 $\pm$ 0.07	44	2	-2.22 $\pm$ 0.21	-

Table A.21.1: `SunMonitor` maximum likelihood results for 2012-11-27 (see Appendix A for description).

GOES	Class	Start	Peak	Stop	Dur. (min)	AR position
	M1.6	2012-11-27 15:52	2012-11-27 15:57	2012-11-27 16:03	11	N08W83
HXR	Instrument	Emax				
	BGO	500 kev				

Table A.21.2: Properties of the events associated with 2012-11-27: GOES X-ray flare, CME, SEPs, HXRs .

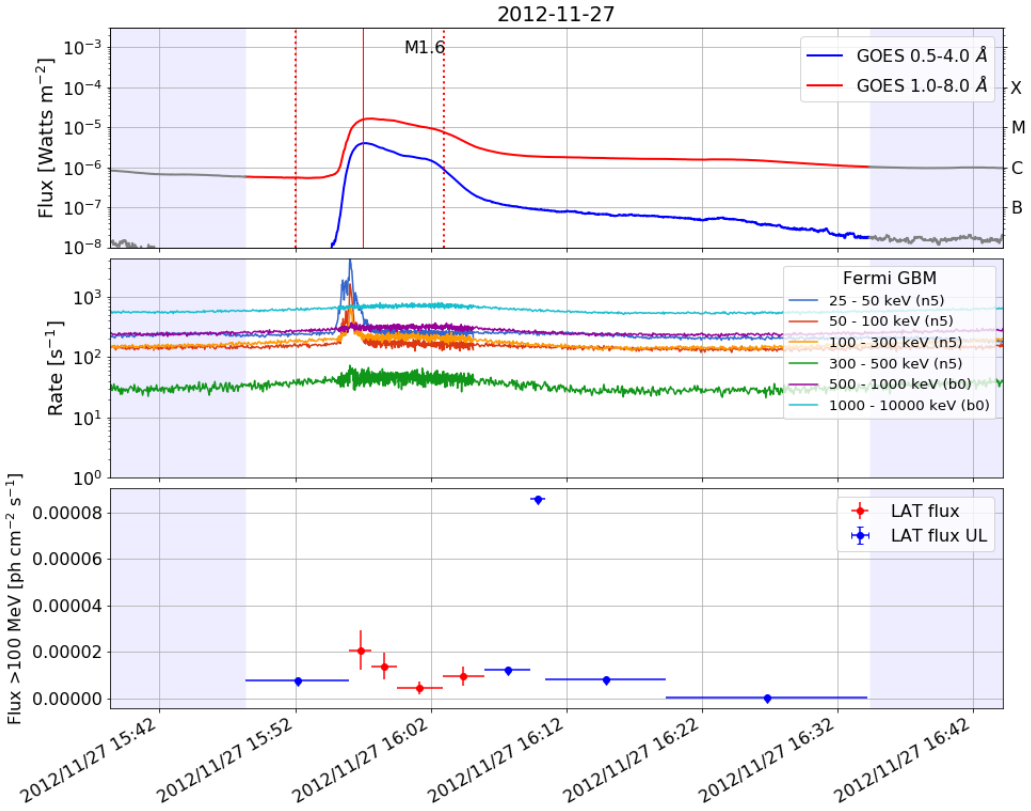

Figure A.21.1: Light curve for FLSF 2012-11-27. Panels from top to bottom: GOES X-rays; Fermi-GBM; Binned Fermi-LAT flux > 100 MeV.

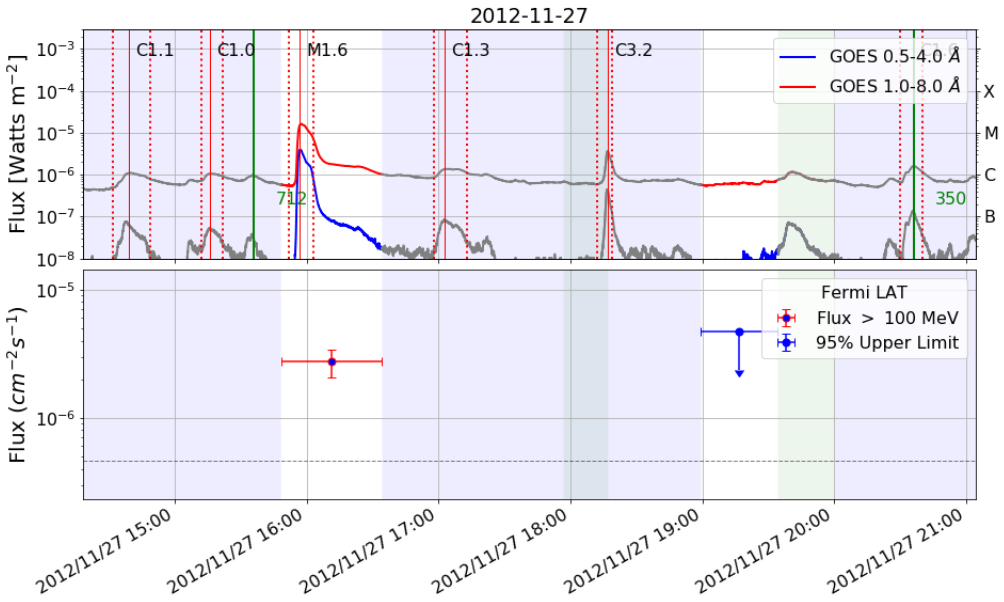

Figure A.21.2: Light curve for 2012-11-27. Top panel: GOES X-rays, bottom panel: Fermi-LAT flux > 100 MeV.

A.22 2013-04-11

Type of Gamma-ray Flare: **Delayed only**.

Associated with a M6.5 GOES flare which started on 2013-04-11 06:55 and a CME with speed 861 km/s.

Fermi-LAT detected gamma-ray emission above 60 MeV starting on 2013-04-11 07:10 and ending on 2013-04-11 07:33, lasting 23 minutes.

Comments: HXRs show a series of peaks but there is no gamma-ray detection at that time. It shows a delayed onset lasting for 23 minutes.

Date and Time	Exposure (minutes)	Flux (10^{-5} cm^{-2}s^{-1})	TS	ΔTS	Photon Index	Proton Index
2013-04-11 07:00 - 07:39	39	5.71 ± 0.24*	1422	120	-0.43 ± 0.27	5.67 ± 0.27

Table A.22.1: `SunMonitor` maximum likelihood results for 2013-04-11 (see Appendix A for description).

GOES	Class M6.5	Start 2013-04-11 06:55	Peak 2013-04-11 07:16	Stop 2013-04-11 07:29	Dur. (min) 34	AR position N07E13
CME	Speed 861 km/s	Width Halo	C2 time 2013-04-11 07:24			
SEP	Instrument GOES	Emax 100 MeV				
HXR	Instrument NaI5	Emax 100 kev				

Table A.22.2: Properties of the events associated with 2013-04-11: GOES X-ray flare, CME, SEPs, HXRs .

Date and Time	Helio X,Y	ERR 68%	ERR 95%	Angular Distance	Relative Distance (95)	Average Boresight (°)
2013-04-11 07:00 - 07:39	255,-517	406	624	867	1	47

Table A.22.3: The GOES X-ray flare associated with the FLSF originated from AR 11719 whose position at the time of the GOES flare was N07E13 (see Appendix A for description).

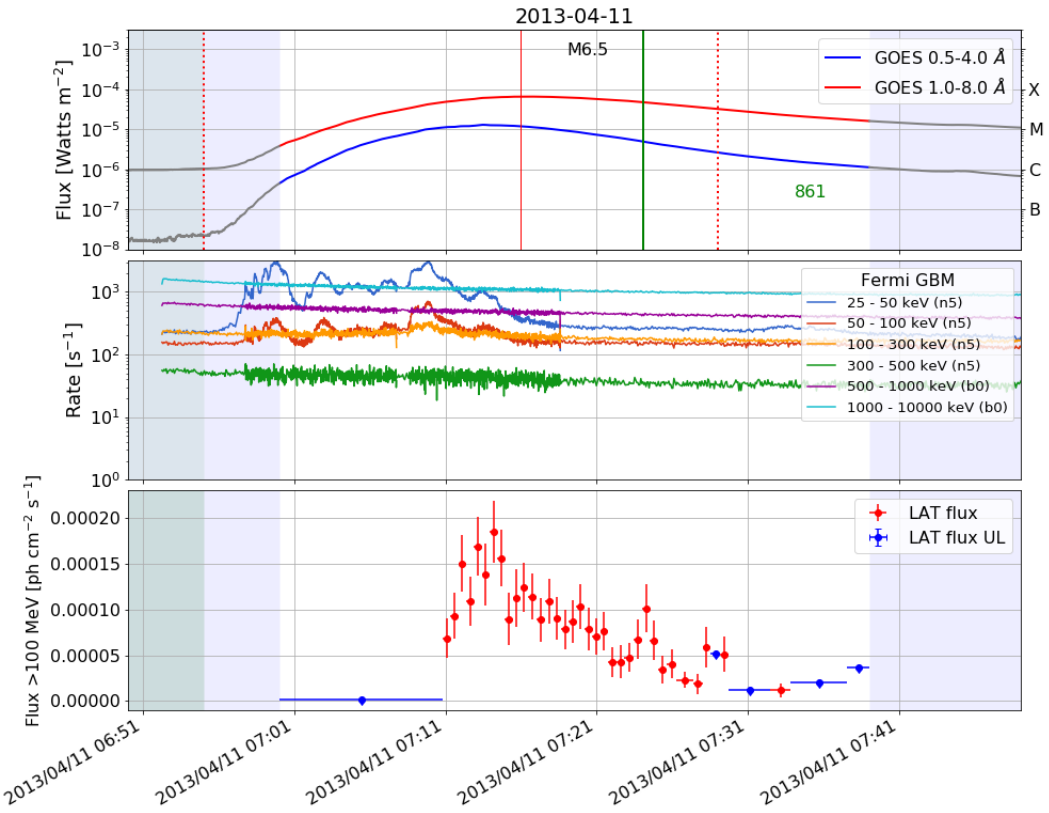

Figure A.22.1: Light curve for FLSF 2013-04-11. Panels from top to bottom: GOES X-rays; Fermi-GBM; Binned Fermi-LAT flux > 100 MeV.

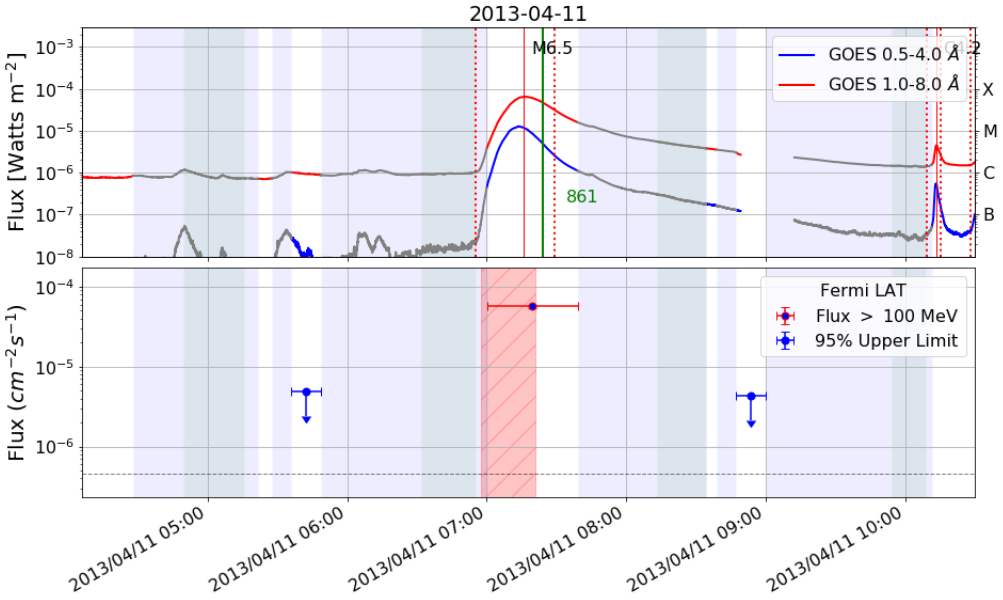

Figure A.22.2: Light curve for 2013-04-11. Top panel: GOES X-rays, bottom panel: Fermi-LAT flux > 100 MeV.

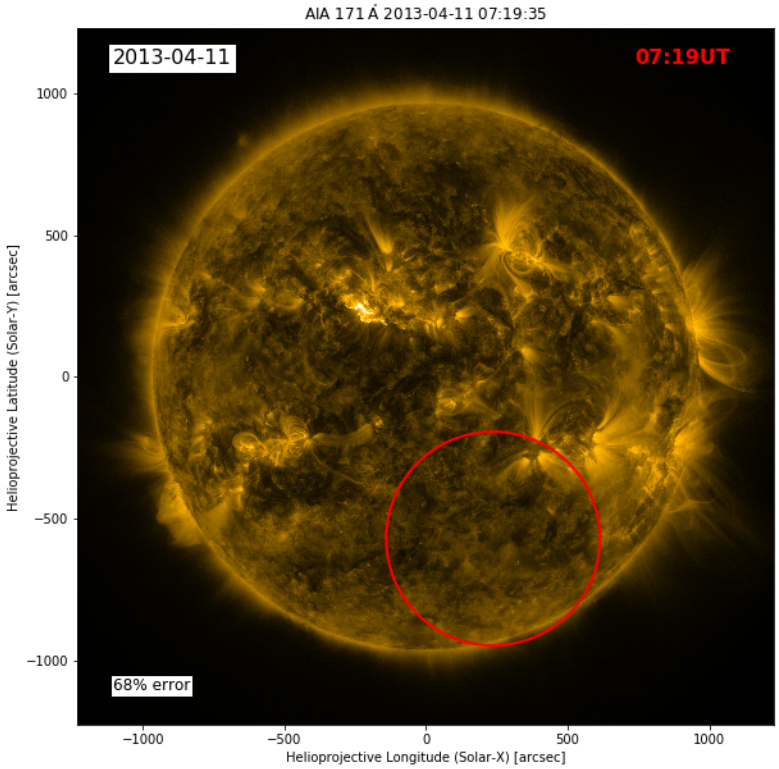

Figure A.22.3: Time resolved localization of the > 60 MeV emission from the 2013-04-11 flare. The mean time of each window is annotated in the upper right hand corner of each panel. The circles are the 68% source location uncertainty regions (results in Table A.22.3).

A.23 2013-05-13a

Type of Gamma-ray Flare: **Delayed**.

Associated with a X1.7 GOES flare which started on 2013-05-13 01:53 and a CME with speed 1270 km/s.

Fermi-LAT detected gamma-ray emission above 60 MeV starting on 2013-05-13 04:31 and ending on 2013-05-13 05:14, lasting 43 minutes.

Comments: Single window detection. No gamma-ray detection during the early phase of the X1.7 GOES flare.

Date and Time	Exposure (minutes)	Flux (10^{-5} cm^{-2}s^{-1})	TS	ΔTS	Photon Index	Proton Index
2013-05-13 04:31 - 05:14	43	0.96 $\pm$ 0.11	188	36	3.00 $\pm$ 0.14	>6

Table A.23.1: `SunMonitor` maximum likelihood results for 2013-05-13a (see Appendix A for description).

GOES	Class X1.7	Start 2013-05-13 01:53	Peak 2013-05-13 02:17	Stop 2013-05-13 02:32	Dur. (min) 39	AR position N12E67
CME	Speed 1270 km/s	Width Halo	C2 time 2013-05-13 02:00			
SEP	Instrument STEREO	Emax 60 MeV				
HXR	Instrument NaI5	Emax > 300 kev				

Table A.23.2: Properties of the events associated with 2013-05-13a: GOES X-ray flare, CME, SEPs, HXRs (HXR coverage incomplete).

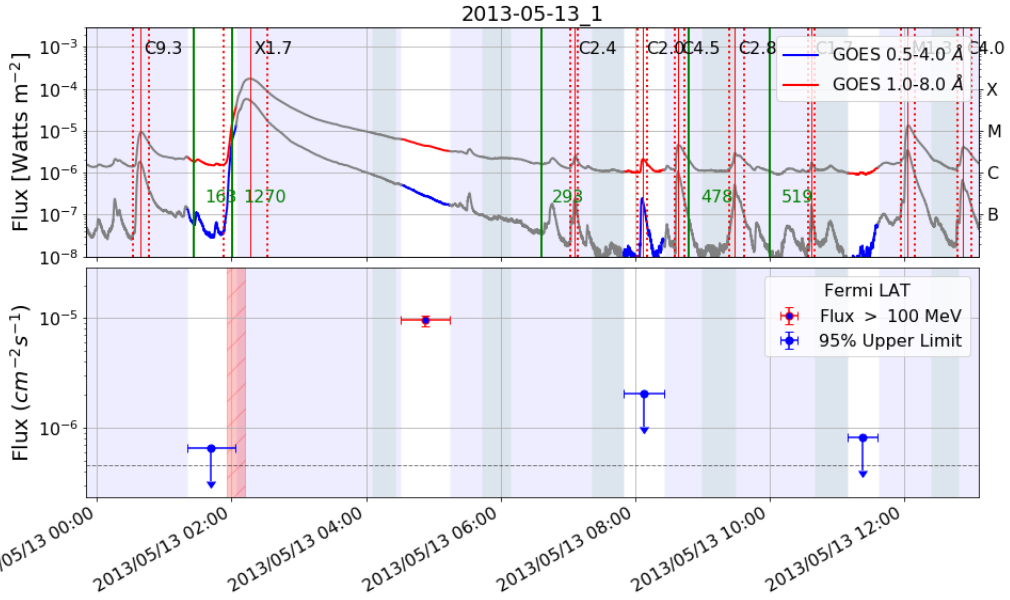

Figure A.23.1: Light curve for 2013-05-13a. Top panel: GOES X-rays, bottom panel: Fermi-LAT flux > 100 MeV.

A.24 2013-05-13b

Type of Gamma-ray Flare: **Delayed**.

Associated with a X2.8 GOES flare which started on 2013-05-13 15:48 and a CME with speed 1850 km/s.

Fermi-LAT detected gamma-ray emission above 60 MeV starting on 2013-05-13 17:15 and ending on 2013-05-13 21:09, lasting 3.9 hours.

Comments: Second CME (speed 849 km/s) is unrelated (different AR).

Date and Time	Exposure (minutes)	Flux (10^{-5} cm^{-2}s^{-1})	TS	ΔTS	Photon Index	Proton Index
2013-05-13 17:15 - 17:58	30	2.41 $\pm$ 0.21	371	43	-0.24 $\pm$ 0.48	3.91 $\pm$ 0.31
2013-05-13 20:26 - 21:09	43	1.72 $\pm$ 0.14	371	43	0.21 $\pm$ 0.73	5.55 $\pm$ 0.51

Table A.24.1: `SunMonitor` maximum likelihood results for 2013-05-13b (see Appendix A for description).

GOES	Class X2.8	Start 2013-05-13 15:48	Peak 2013-05-13 16:05	Stop 2013-05-13 16:16	Dur. (min) 28	AR position N12E67
CME	Speed 1850 km/s	Width Halo	C2 time 2013-05-13 16:07			
SEP	Instrument STEREO	Emax 60 MeV				
HXR	Instrument Rhessi	Emax 800 kev				

Table A.24.2: Properties of the events associated with 2013-05-13b: GOES X-ray flare, CME, SEPs, HXRs .

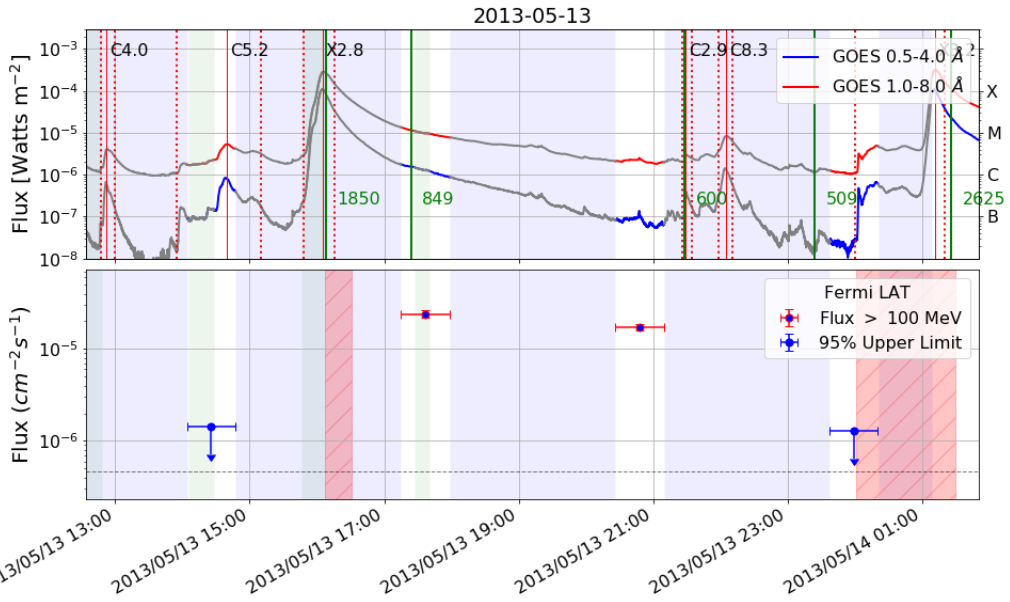

Figure A.24.1: Light curve for 2013-05-13b. Top panel: GOES X-rays, bottom panel: Fermi-LAT flux > 100 MeV.

A.25 2013-05-14

Type of Gamma-ray Flare: **Delayed only**.

Associated with a X3.2 GOES flare which started on 2013-05-14 00:00 and a CME with speed 2625 km/s.

Fermi-LAT detected gamma-ray emission above 60 MeV starting on 2013-05-14 01:17 and ending on 2013-05-14 06:42, lasting 5.4 hours.

Comments: Impulsive phase with HXR mostly observed in the first time window but a binned analysis points to the gamma-ray emission starting after the end of the HXR. FLSF is tentatively classified Delayed Only. Possible SEP event associated with this flare, but strong previous SEP event still ongoing.

Date and Time	Exposure (minutes)	Flux (10^{-5} cm^{-2}s^{-1})	TS	ΔTS	Photon Index	Proton Index
2013-05-14 01:08 - 01:55	47	1.02 ± 0.09*	292	46	0.55 ± 0.67	>6
2013-05-14 02:43 - 03:31	47	3.30 ± 0.15	1518	193	0.62 ± 0.32	4.95 ± 0.24
2013-05-14 04:19 - 05:06	47	2.32 ± 0.16	546	87	1.26 ± 0.61	5.91 ± 0.43
2013-05-14 05:59 - 06:42	42	0.59 ± 0.09	105	19	1.05 ± 1.43	>6

Table A.25.1: `SunMonitor` maximum likelihood results for 2013-05-14 (see Appendix A for description).

GOES	Class X3.2	Start 2013-05-14 00:00	Peak 2013-05-14 01:11	Stop 2013-05-14 01:20	Dur. (min) 80	AR position N12E67
CME	Speed 2625 km/s	Width Halo	C2 time 2013-05-14 01:25			
SEP	Instrument STEREO	Emax 60 MeV				
HXR	Instrument BGO	Emax 500 kev				

Table A.25.2: Properties of the events associated with 2013-05-14: GOES X-ray flare, CME, SEPs, HXRs .

Date and Time	Helio X,Y	ERR 68%	ERR 95%	Angular Distance	Relative Distance (95)	Average Boresight (°)
2013-05-14 02:43 - 03:31	-1137,333	315	507	305	0.6	12

Table A.25.3: The GOES X-ray flare associated with the FLSF originated from AR 11748 whose position at the time of the GOES flare was N12E67 (see Appendix A for description).

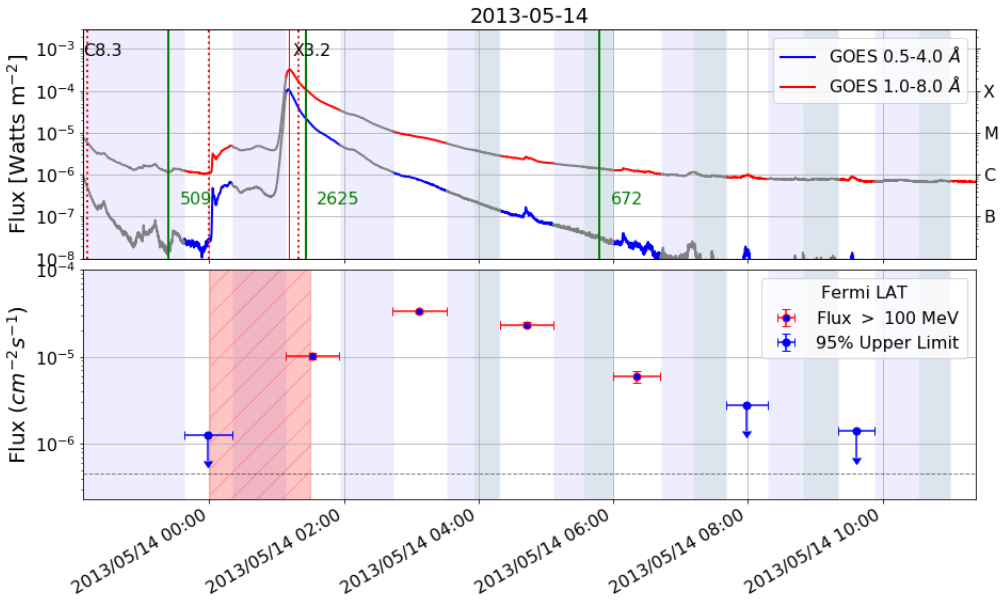

Figure A.25.1: Light curve for 2013-05-14. Top panel: GOES X-rays, bottom panel: Fermi-LAT flux > 100 MeV.

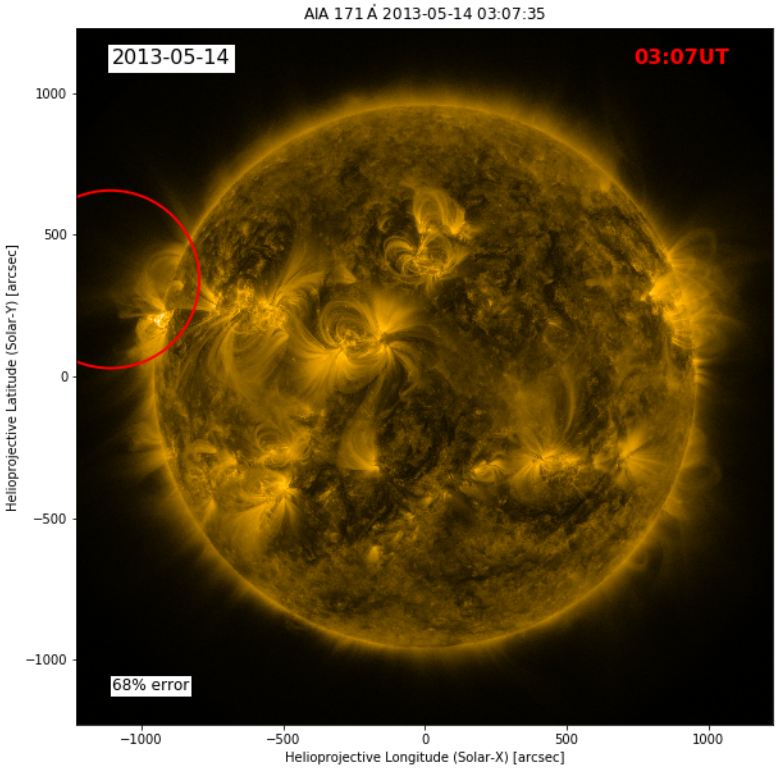

Figure A.25.2: Time resolved localization of the > 60 MeV emission from the 2013-05-14 flare. The mean time of each window is annotated in the upper right hand corner of each panel. The circles are the 68% source location uncertainty regions (results in Table A.25.3).

A.26 2013-05-15

Type of Gamma-ray Flare: **Delayed only**.
Associated with a X1.2 GOES flare which started on 2013-05-15 01:25 and a CME with speed 1366 km/s.
Fermi-LAT detected gamma-ray emission above 60 MeV starting on 2013-05-15 04:12 and ending on 2013-05-15 04:58, lasting 46 minutes.
Comments: Entire impulsive phase observed in HXR with the Sun in the FoV, but no gamma-ray detection (maximum energy reached in HXR is in the 100-300 keV channel). The fact that the Fermi-LAT detection follows an upper limit is consistent with a rise and fall behavior, with the peak reached around 4:30UT.

Date and Time	Exposure (minutes)	Flux (10^{-5} cm^{-2}s^{-1})	TS	ΔTS	Photon Index	Proton Index
2013-05-15 04:12 - 04:58	46	0.36 $\pm$ 0.07	51	9	-2.62 $\pm$ 0.22	-

Table A.26.1: `SunMonitor` maximum likelihood results for 2013-05-15 (see Appendix A for description).

GOES	Class X1.2	Start 2013-05-15 01:25	Peak 2013-05-15 01:48	Stop 2013-05-15 01:58	Dur. (min) 33	AR position N11E49
CME	Speed 1366 km/s	Width Halo	C2 time 2013-05-15 01:48			
SEP	Instrument GOES	Emax 50 MeV				
HXR	Instrument NaI5	Emax 100 kev				

Table A.26.2: Properties of the events associated with 2013-05-15: GOES X-ray flare, CME, SEPs, HXRs .

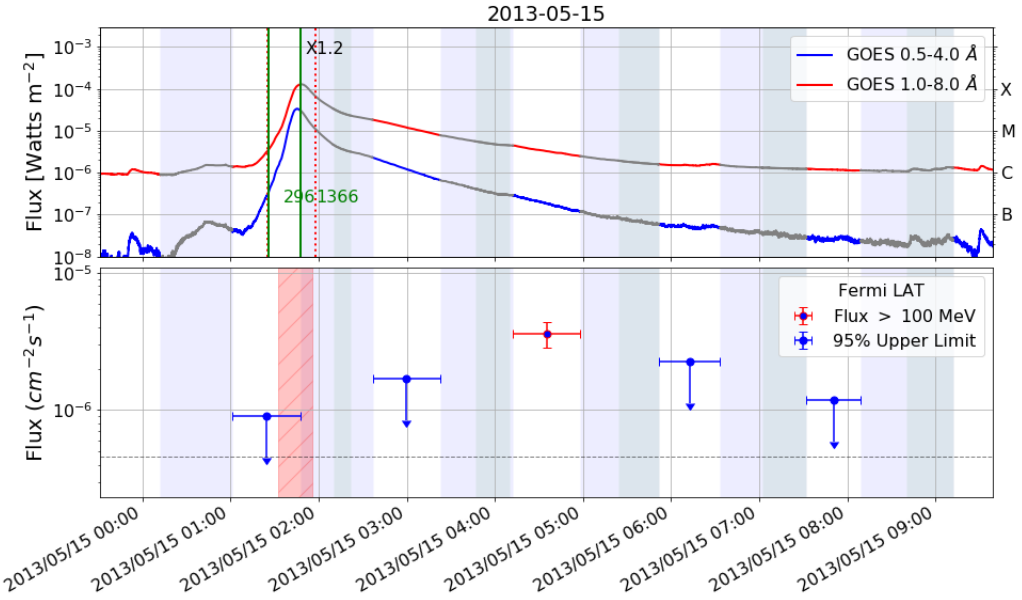

Figure A.26.1: Light curve for 2013-05-15. Top panel: GOES X-rays, bottom panel: Fermi-LAT flux > 100 MeV.

A.27 2013-10-11

Type of Gamma-ray Flare: **BTL Delayed**.
Associated with a M4.9 equivalent flare from STEREO observations which started on 2013-10-11 07:01 and a CME with speed 1200 km/s.
Fermi-LAT detected gamma-ray emission above 60 MeV starting on 2013-10-11 07:13 and ending on 2013-10-11 07:36, lasting 23 minutes.
Comments: BTL flare behind the East limb (see analysis of this flare in Pesce-Rollins et al. 2015).

Date and Time	Exposure (minutes)	Flux (10^{-5} cm^{-2}s^{-1})	TS	ΔTS	Photon Index	Proton Index
2013-10-11 06:56 - 07:39	42	12.55 $\pm$ 0.36	3949	317	-0.34 $\pm$ 0.16	4.33 $\pm$ 0.12

Table A.27.1: `SunMonitor` maximum likelihood results for 2013-10-11 (see Appendix A for description).

GOES	Class M4.9*	Start 2013-10-11 07:01	Peak 2013-10-11 07:25	Stop 2013-10-11 07:45	Dur. (min) 44	AR position N21E103
CME	Speed 1200 km/s	Width Halo	C2 time 2013-10-11 07:24			
SEP	Instrument STEREO	Emax 60 MeV				
HXR	Instrument NaI5	Emax 10 kev				

Table A.27.2: Properties of the events associated with 2013-10-11: GOES X-ray flare, CME, SEPs, HXRs .

Date and Time	Helio X,Y	ERR 68%	ERR 95%	Angular Distance	Relative Distance (95)	Average Boresight (°)
2013-10-11 06:56 - 07:39	-930,311	141	257	77	0.3	40

Table A.27.3: Localization results for the BTL gamma-ray flare 2013-10-11. Position behind the limb estimated by STEREO as N21E103.

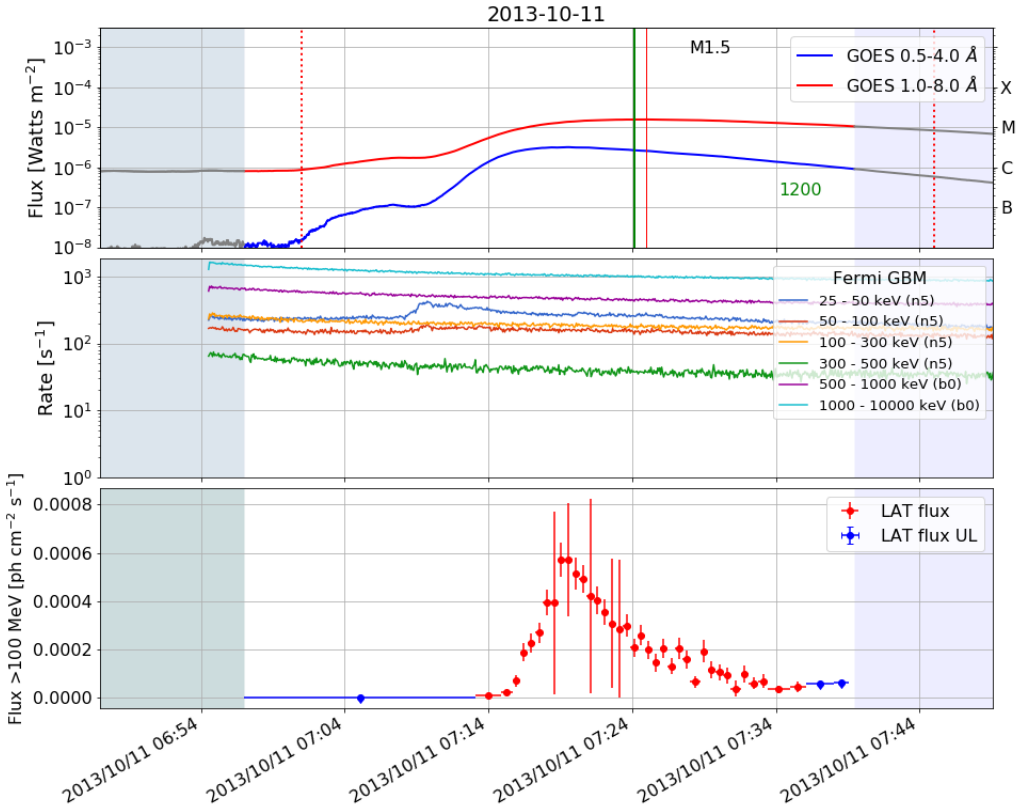

Figure A.27.1: Light curve for FLSF 2013-10-11. Panels from top to bottom: GOES X-rays; Fermi-GBM; Binned Fermi-LAT flux > 100 MeV.

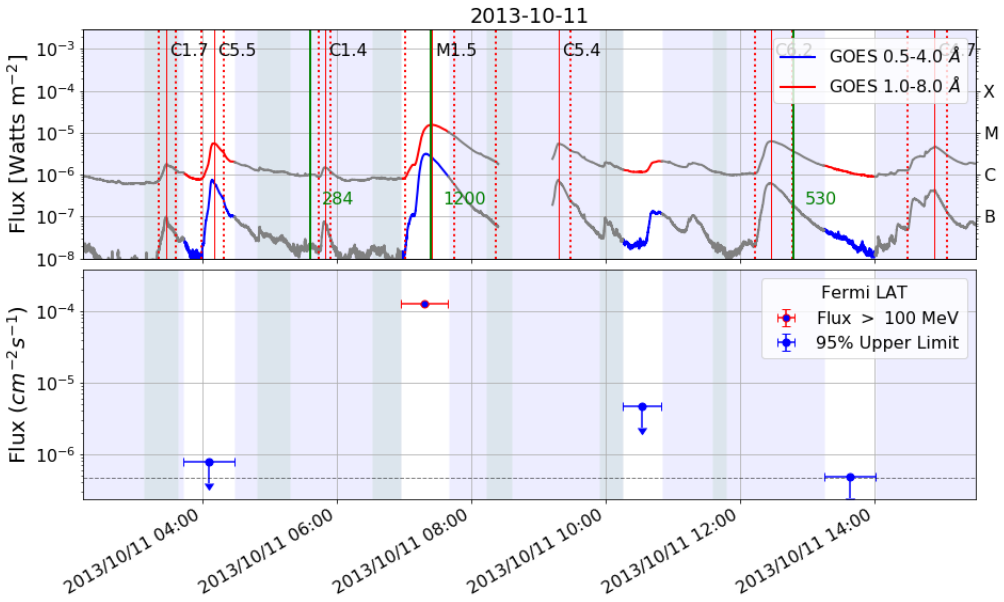

Figure A.27.2: Light curve for 2013-10-11. Top panel: GOES X-rays, bottom panel: Fermi-LAT flux > 100 MeV.

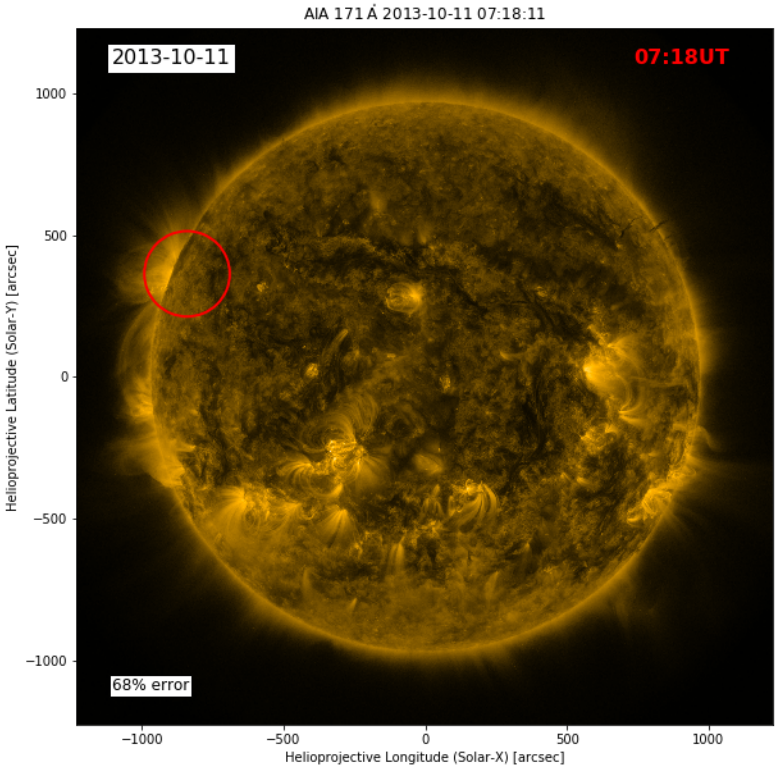

Figure A.27.3: Time resolved localization of the > 60 MeV emission from the 2013-10-11 flare. The mean time of each window is annotated in the upper right hand corner of each panel. The circles are the 68% source location uncertainty regions (results in Table A.27.3).

A.28 2013-10-25a

Type of Gamma-ray Flare: **Delayed**.
Associated with a X1.7 GOES flare which started on 2013-10-25 07:53 and a CME with speed 587 km/s.
Fermi-LAT detected gamma-ray emission above 60 MeV starting on 2013-10-25 08:15 and ending on 2013-10-25 08:57, lasting 42 minutes.
Comments: Gamma rays detected after the end of the X-ray flare (Sun was out of the FoV during the X-ray flare).

Date and Time	Exposure (minutes)	Flux (10^{-5} cm^{-2}s^{-1})	TS	ΔTS	Photon Index	Proton Index
2013-10-25 08:15 - 08:57	42	1.15 ± 0.12*	211	21	0.07 ± 0.88	6.00 ± 3.61

Table A.28.1: `SunMonitor` maximum likelihood results for 2013-10-25a (see Appendix A for description).

GOES	Class X1.7	Start 2013-10-25 07:53	Peak 2013-10-25 08:01	Stop 2013-10-25 08:09	Dur. (min) 16	AR position S08E59
CME	Speed 587 km/s	Width Halo	C2 time 2013-10-25 08:12			
SEP	Instrument STEREO	Emax 60 MeV				
HXR	Instrument Rhessi	Emax 300 kev				

Table A.28.2: Properties of the events associated with 2013-10-25a: GOES X-ray flare, CME, SEPs, HXRs .

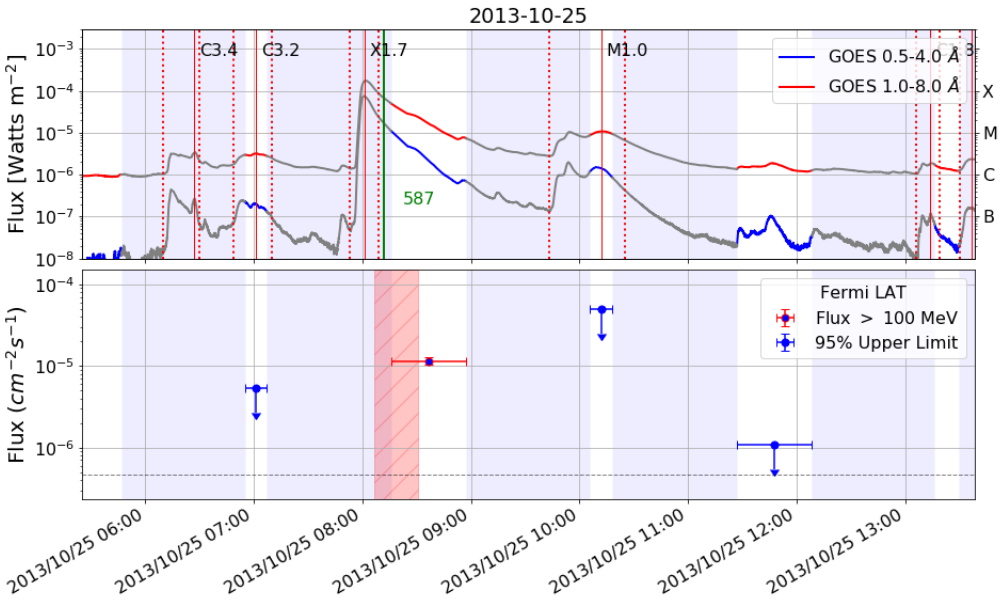

Figure A.28.1: Light curve for 2013-10-25a. Top panel: GOES X-rays, bottom panel: Fermi-LAT flux > 100 MeV.

A.29 2013-10-25b

Type of Gamma-ray Flare: **Prompt**.

Associated with a M1.9 GOES flare which started on 2013-10-25 20:54 (no significant CME associated).

Fermi-LAT detected gamma-ray emission with the LLE approach only. Emission started on 2013-10-25 at 20:56:52 and ended at 20:57:02 with a total duration of 10 seconds.

Comments: LLE flare only with no gamma rays detected above 100 MeV.

Start Time	Duration (sec)	$Flux_{30}$	$Flux_{100}$	TS	SunMon detected	Out of FoV
2013-10-25 20:56:52	10	38.90 ± 0.97	1.13± 0.09	0		

Table A.29.1: LLE Spectral results for flare 2013-10-25b. $Flux_{30}$ and $Flux_{100}$ indicate the flux computed from 30 MeV to 10 GeV and from 100 MeV to 10 GeV respectively (in units of 10^{-5} $cm^{-2}s^{-1}$).

GOES	Class M1.9	Start 2013-10-25 20:54	Peak 2013-10-25 20:58	Stop 2013-10-25 21:13	Dur. (min) 19	AR position S08E59
SEP	Instrument STEREO	Emax 60 MeV present				
HXR	Instrument NaI5	Emax 100 kev				

Table A.29.2: Properties of the events associated with 2013-10-25b: GOES X-ray flare, CME, SEPs, HXRs .

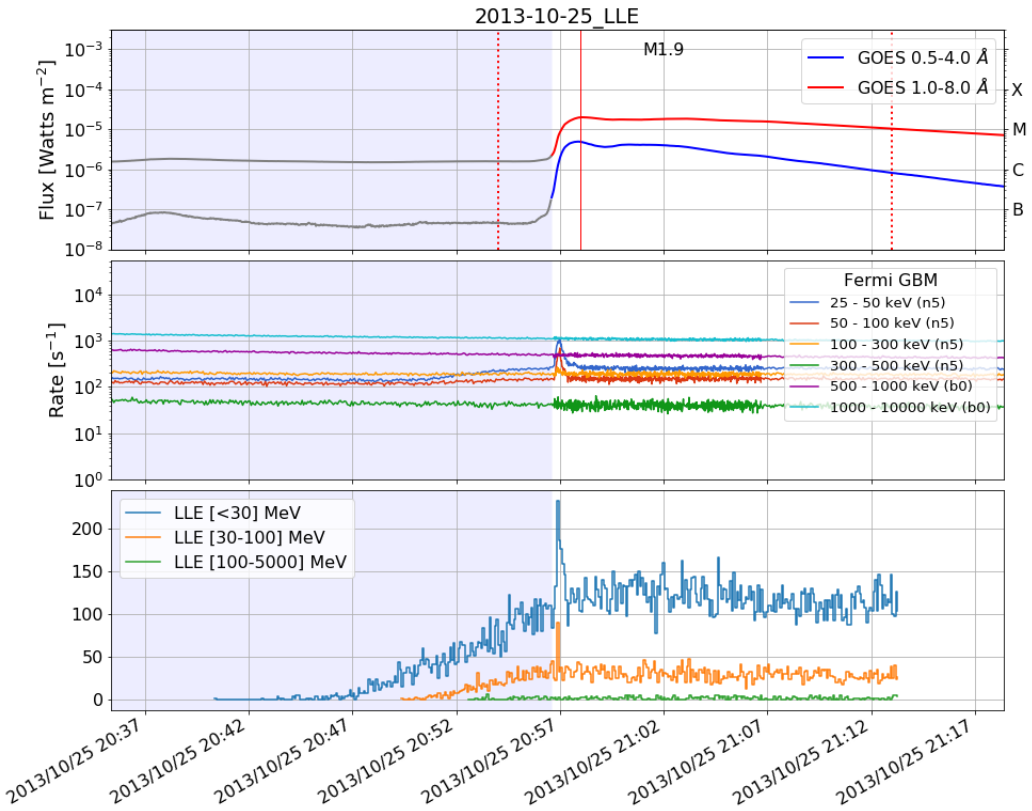

Figure A.29.1: Light curve for FLSF 2013-10-25b. Panels from top to bottom: GOES X-rays; Fermi-GBM; Fermi-LAT LLE.

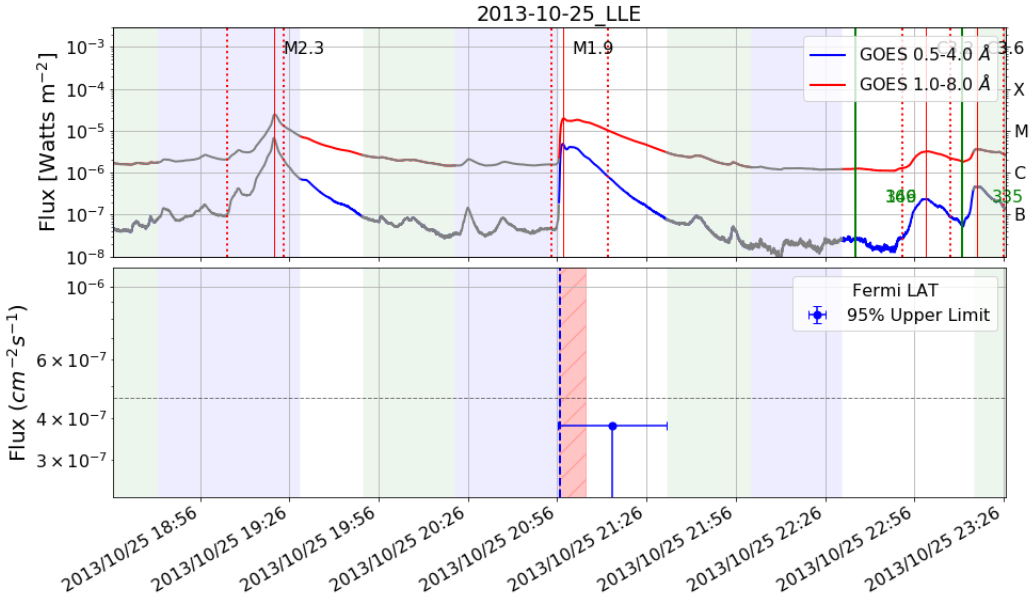

Figure A.29.2: Light curve for 2013-10-25b. Top panel: GOES X-rays, bottom panel: Fermi-LAT flux > 100 MeV. Vertical blue line marks the start time of the LLE flare.

A.30 2013-10-28a

Type of Gamma-ray Flare: **Prompt**.

Associated with a X1.0 GOES flare which started on 2013-10-28 01:41 and a CME with speed 695 km/s.

Fermi-LAT detected gamma-ray emission with the LLE approach only. Emission started on 2013-10-28 at 01:59:15 and ended at 02:00:26 with a total duration of 70 seconds.

Comments: LLE flare only with no gamma rays detected above 100 MeV.

Start Time	Duration (sec)	$Flux_{30}$	$Flux_{100}$	TS	SunMon detected	Out of FoV
2013-10-28 01:59:15	70	0.45 ± 0.03	0.00± 0.00	5		

Table A.30.1: LLE Spectral results for flare 2013-10-28a. $Flux_{30}$ and $Flux_{100}$ indicate the flux computed from 30 MeV to 10 GeV and from 100 MeV to 10 GeV respectively (in units of 10^{-5} $cm^{-2}s^{-1}$).

GOES	Class X1.0	Start 2013-10-28 01:41	Peak 2013-10-28 02:03	Stop 2013-10-28 02:12	Dur. (min) 31	AR position N05W72
CME	Speed 695 km/s	Width Halo	C2 time 2013-10-28 02:24			
HXR	Instrument BGO	Emax 1000 kev				

Table A.30.2: Properties of the events associated with 2013-10-28a: GOES X-ray flare, CME, SEPs, HXRs .

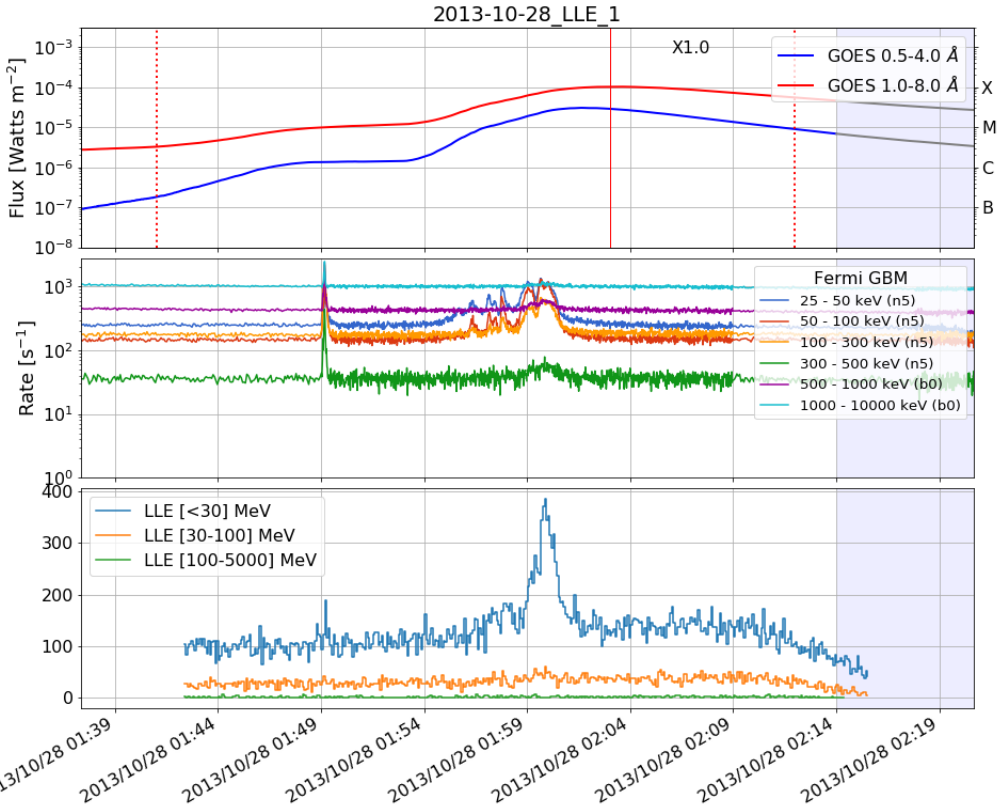

Figure A.30.1: Light curve for FLSF 2013-10-28a. Panels from top to bottom: GOES X-rays; Fermi-GBM; Fermi-LAT LLE.

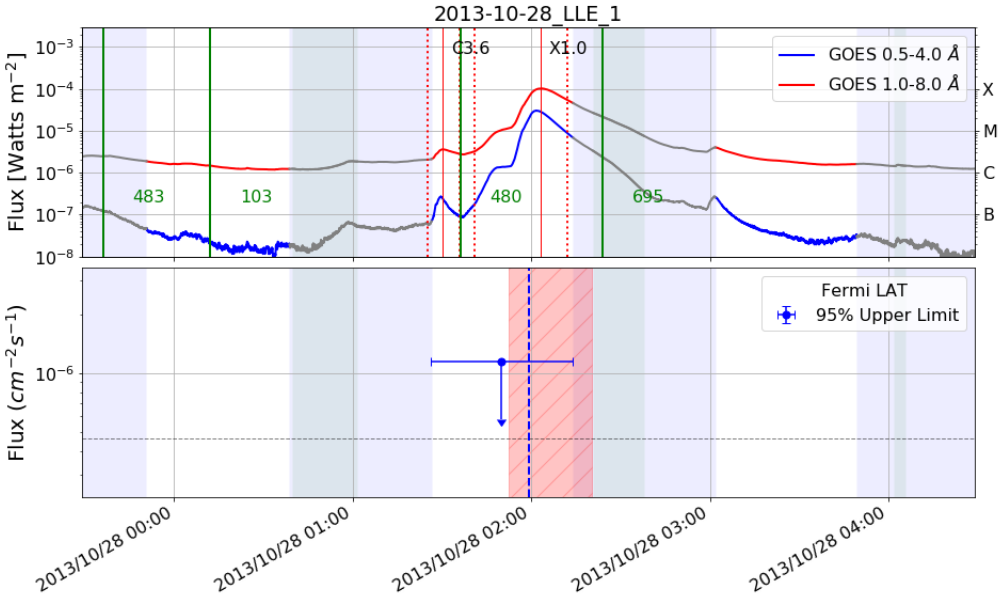

Figure A.30.2: Light curve for 2013-10-28a. Top panel: GOES X-rays, bottom panel: Fermi-LAT flux > 100 MeV. Vertical blue line marks the start time of the LLE flare.

A.31 2013-10-28b

Type of Gamma-ray Flare: **Prompt**.

Associated with a M5.1 GOES flare which started on 2013-10-28 04:32 and a CME with speed 1201 km/s.

Fermi-LAT detected gamma-ray emission with the LLE approach only. Emission started on 2013-10-28 at 04:37:48 and ended at 04:38:38 with a total duration of 50 seconds.

Comments: LLE flare only with no gamma rays detected above 100 MeV. Associated with a rather fast CME with a partial Halo.

Start Time	Duration (sec)	$Flux_{30}$	$Flux_{100}$	TS	SunMon detected	Out of FoV
2013-10-28 04:37:48	50	25.93 ± 1.27	0.00± 0.00	3		

Table A.31.1: LLE Spectral results for flare 2013-10-28b. $Flux_{30}$ and $Flux_{100}$ indicate the flux computed from 30 MeV to 10 GeV and from 100 MeV to 10 GeV respectively (in units of 10^{-5} $cm^{-2}s^{-1}$).

GOES	Class M5.1	Start 2013-10-28 04:32	Peak 2013-10-28 04:41	Stop 2013-10-28 04:46	Dur. (min) 14	AR position N08W72
CME	Speed 1201 km/s	Width 315	C2 time 2013-10-28 04:48			
HXR	Instrument BGO	Emax 1000 kev				

Table A.31.2: Properties of the events associated with 2013-10-28b: GOES X-ray flare, CME, SEPs, HXRs .

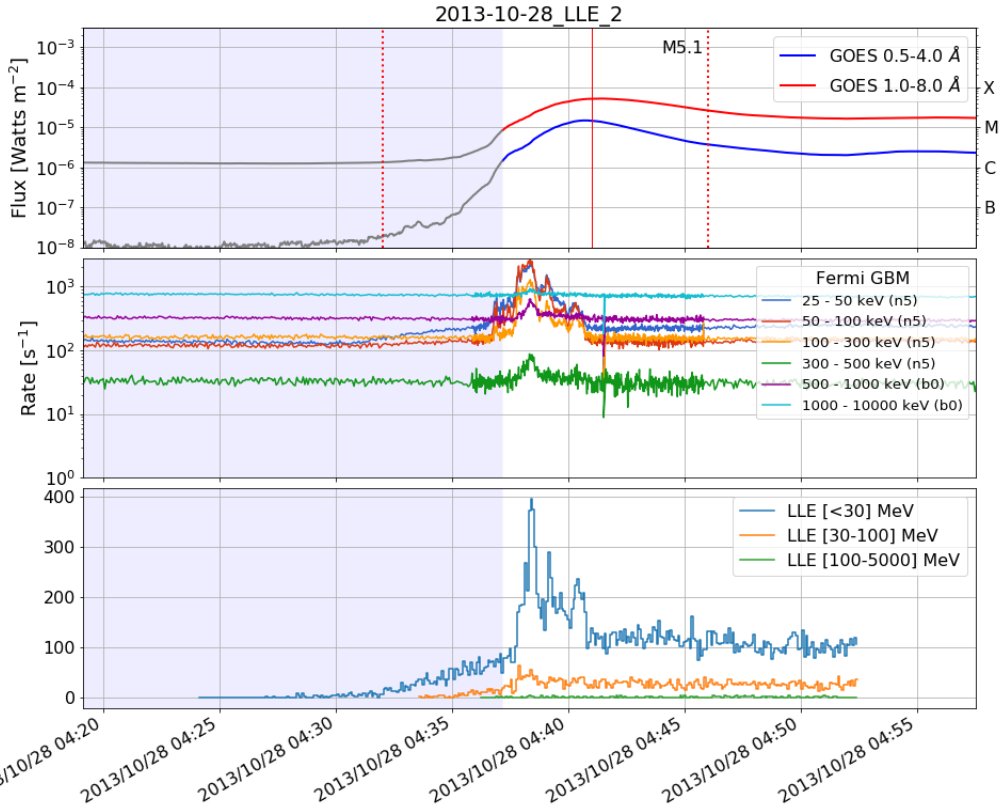

Figure A.31.1: Light curve for FLSF 2013-10-28b. Panels from top to bottom: GOES X-rays; Fermi-GBM; Fermi-LAT LLE.

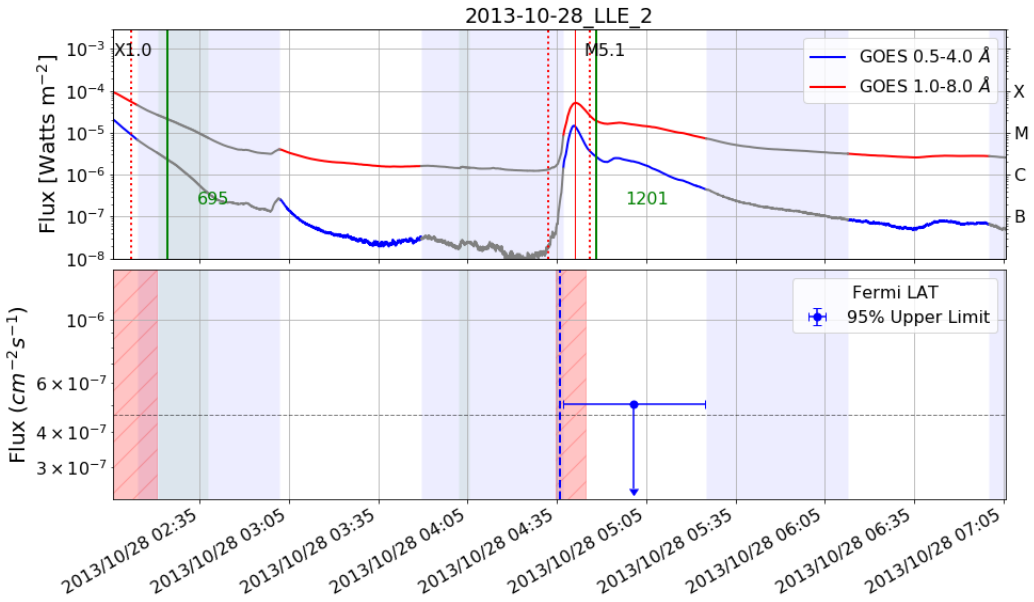

Figure A.31.2: Light curve for 2013-10-28b. Top panel: GOES X-rays, bottom panel: Fermi-LAT flux > 100 MeV. Vertical blue line marks the start time of the LLE flare.

A.32 2013-10-28c

Type of Gamma-ray Flare: **Delayed**.

Associated with a M2.7 GOES flare which started on 2013-10-28 14:46 and a CME with speed 812 km/s.

Fermi-LAT detected gamma-ray emission above 60 MeV starting on 2013-10-28 15:45 and ending on 2013-10-28 16:05, lasting 21 minutes.

Comments: Multiple flaring activity before the start of the gamma-rays with a pair of M-class flares from the same region M2.7 and M4.4.

Date and Time	Exposure (minutes)	Flux (10^{-5} cm^{-2}s^{-1})	TS	ΔTS	Photon Index	Proton Index
2013-10-28 15:45 - 16:05	21	0.81 $\pm$ 0.12	120	8	-2.32 $\pm$ 0.15	-

Table A.32.1: `SunMonitor` maximum likelihood results for 2013-10-28c (see Appendix A for description).

GOES	Class M2.7	Start 2013-10-28 14:46	Peak 2013-10-28 15:01	Stop 2013-10-28 15:04	Dur. (min) 18	AR position S08E21
CME	Speed 812 km/s	Width Halo	C2 time 2013-10-28 15:36			
SEP	Instrument STEREO	Emax 60 MeV				
HXR	Instrument Rhessi	Emax 50 kev				

Table A.32.2: Properties of the events associated with 2013-10-28c: GOES X-ray flare, CME, SEPs, HXRs .

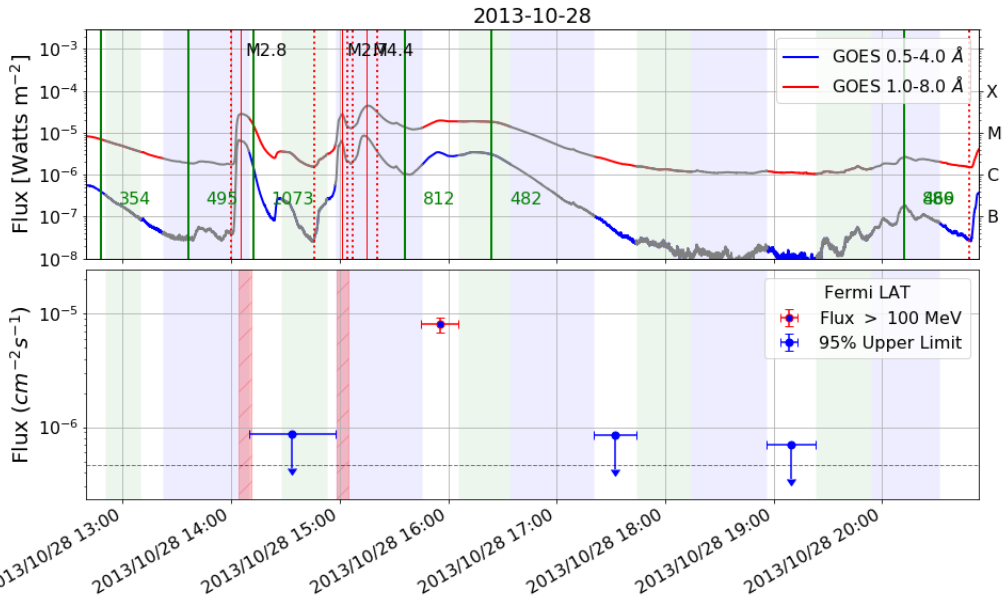

Figure A.32.1: Light curve for 2013-10-28c. Top panel: GOES X-rays, bottom panel: Fermi-LAT flux > 100 MeV.

A.33 2013-10-28d

Type of Gamma-ray Flare: **Prompt**.

Associated with a M1.5 GOES flare which started on 2013-10-28 20:48 and a CME with speed 771 km/s.

Fermi-LAT detected gamma-ray emission with the LLE approach only. Emission started on 2013-10-28 at 20:54:47 and ended at 20:55:37 with a total duration of 50 seconds.

Comments: LLE flare only with no gamma rays detected above 100 MeV.

Start Time	Duration (sec)	$Flux_{30}$	$Flux_{100}$	TS	SunMon detected	Out of FoV
2013-10-28 20:54:47	50	9.82 ± 0.55	0.33 ± 0.05	7		

Table A.33.1: LLE Spectral results for flare 2013-10-28d. $Flux_{30}$ and $Flux_{100}$ indicate the flux computed from 30 MeV to 10 GeV and from 100 MeV to 10 GeV respectively (in units of 10^{-5} $cm^{-2}s^{-1}$).

GOES	Class M1.5	Start 2013-10-28 20:48	Peak 2013-10-28 20:57	Stop 2013-10-28 21:02	Dur. (min) 14	AR position N07W83
CME	Speed 771 km/s	Width 284	C2 time 2013-10-28 21:25			
SEP	Instrument GOES	Emax 100 MeV present				
HXR	Instrument NaI5	Emax 100 kev				

Table A.33.2: Properties of the events associated with 2013-10-28d: GOES X-ray flare, CME, SEPs, HXRs .

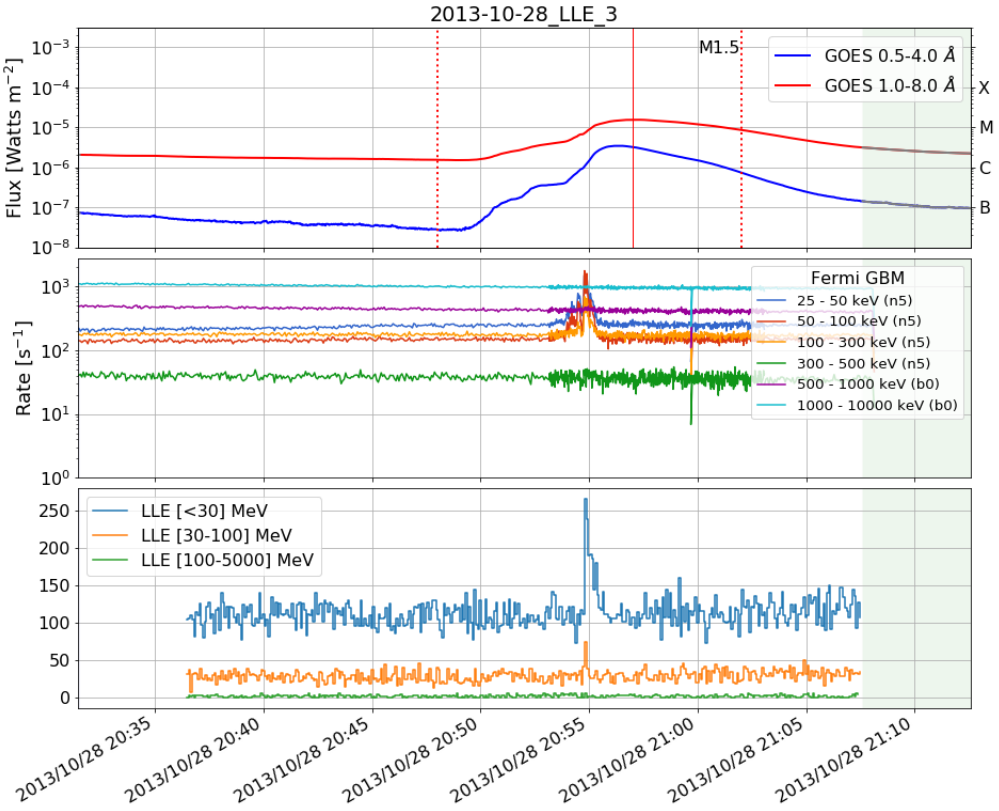

Figure A.33.1: Light curve for FLSF 2013-10-28d. Panels from top to bottom: GOES X-rays; Fermi-GBM; Fermi-LAT LLE.

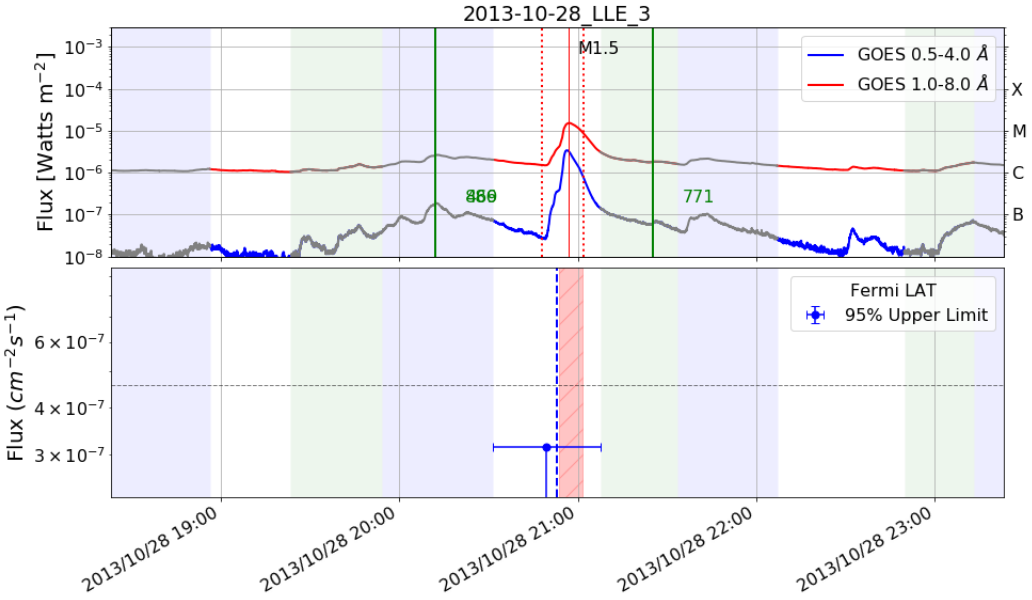

Figure A.33.2: Light curve for 2013-10-28d. Top panel: GOES X-rays, bottom panel: Fermi-LAT flux > 100 MeV. Vertical blue line marks the start time of the LLE flare.

A.34 2014-01-06

Type of Gamma-ray Flare: **BTL**.
Associated with a X3.5 equivalent flare from STEREO observations which started on 2014-01-06 07:40 and a CME with speed 1402 km/s.
Fermi-LAT detected gamma-ray emission above 60 MeV starting on 2014-01-06 07:55 and ending on 2014-01-06 08:11, lasting 16 minutes.
Comments: No GOES X-ray flare at all for this BTL flare behind the West limb. Associated with a fast Halo CME and a strong SEP event.

Date and Time	Exposure (minutes)	Flux (10^{-5} cm^{-2}s^{-1})	TS	ΔTS	Photon Index	Proton Index
2014-01-06 07:55 - 08:30	34	0.42 ± 0.09	52	13	1.84 ± 2.16	5.77 ± 1.94

Table A.34.1: `SunMonitor` maximum likelihood results for 2014-01-06 (see Appendix A for description).

GOES	Class X3.5*	Start 2014-01-06 07:40	Peak 2014-01-06 07:50	Stop 2014-01-06 08:08	Dur. (min) 28	AR position S08W110
CME	Speed 1402 km/s	Width Halo	C2 time 2014-01-06 08:00			
SEP	Instrument GOES	Emax 605 MeV				
HXR	Instrument Rhessi	Emax 6 kev				

Table A.34.2: Properties of the events associated with 2014-01-06: GOES X-ray flare, CME, SEPs, HXRs .

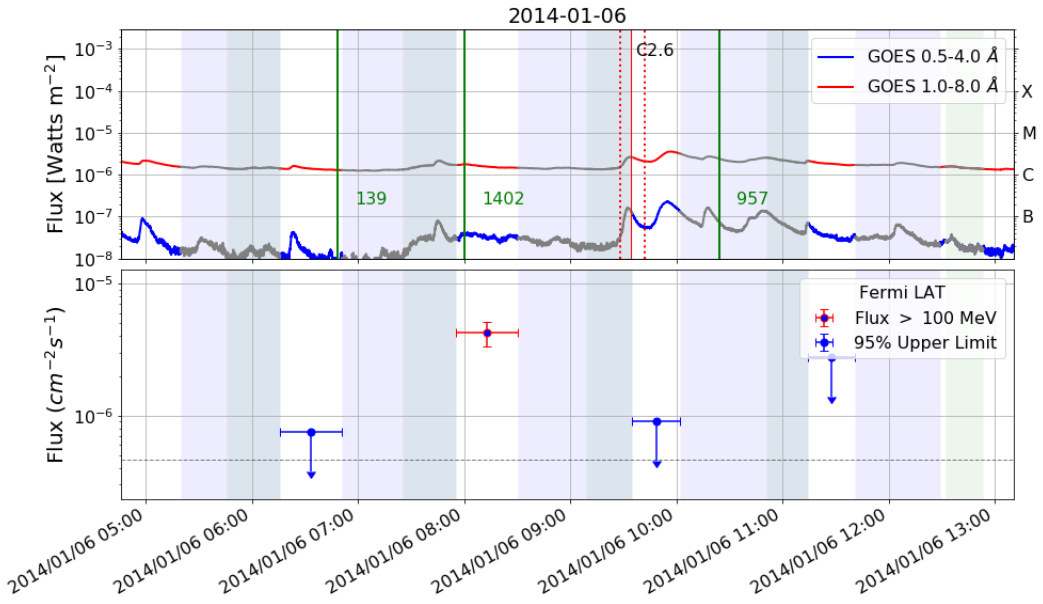

Figure A.34.1: Light curve for 2014-01-06. Top panel: GOES X-rays, bottom panel: Fermi-LAT flux > 100 MeV.

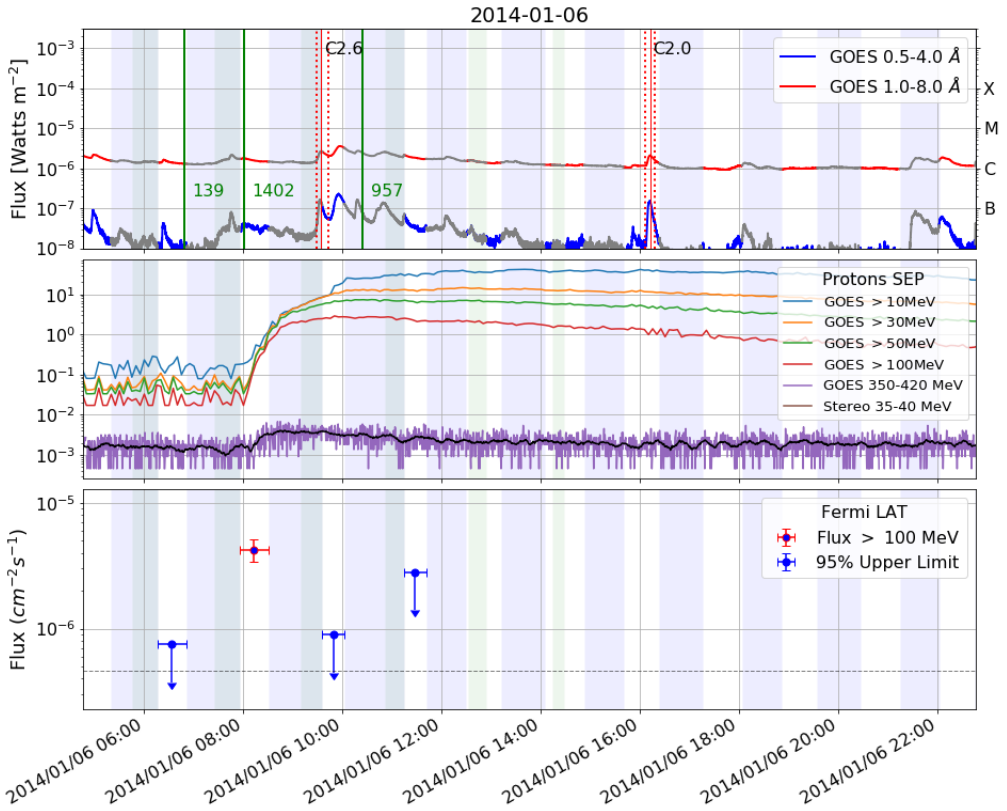

Figure A.34.2: Composite light curve for SEP event associated with 2014-01-06. Panels from top to bottom: GOES X-rays, GOES SEP count rate (ACE and STEREO data when available), Fermi-LAT >100 MeV flux.

A.35 2014-01-07

Type of Gamma-ray Flare: **Delayed**.

Associated with a X1.2 GOES flare which started on 2014-01-07 18:04 and a CME with speed 1830 km/s.

Fermi-LAT detected gamma-ray emission above 60 MeV starting on 2014-01-07 18:41 and ending on 2014-01-07 19:29, lasting 48 minutes.

Comments: nan

Date and Time	Exposure (minutes)	Flux (10^{-5} cm^{-2}s^{-1})	TS	ΔTS	Photon Index	Proton Index
2014-01-07 18:41 - 19:29	48	0.29 ± 0.07	32	5	-2.68 ± 0.27	-

Table A.35.1: `SunMonitor` maximum likelihood results for 2014-01-07 (see Appendix A for description).

GOES	Class X1.2	Start 2014-01-07 18:04	Peak 2014-01-07 18:32	Stop 2014-01-07 18:58	Dur. (min) 54	AR position S15W10
CME	Speed 1830 km/s	Width Halo	C2 time 2014-01-07 18:24			
SEP	Instrument GOES	Emax 100 MeV				
HXR	Instrument NaI5	Emax > 20 kev				

Table A.35.2: Properties of the events associated with 2014-01-07: GOES X-ray flare, CME, SEPs, HXRs (HXR coverage incomplete).

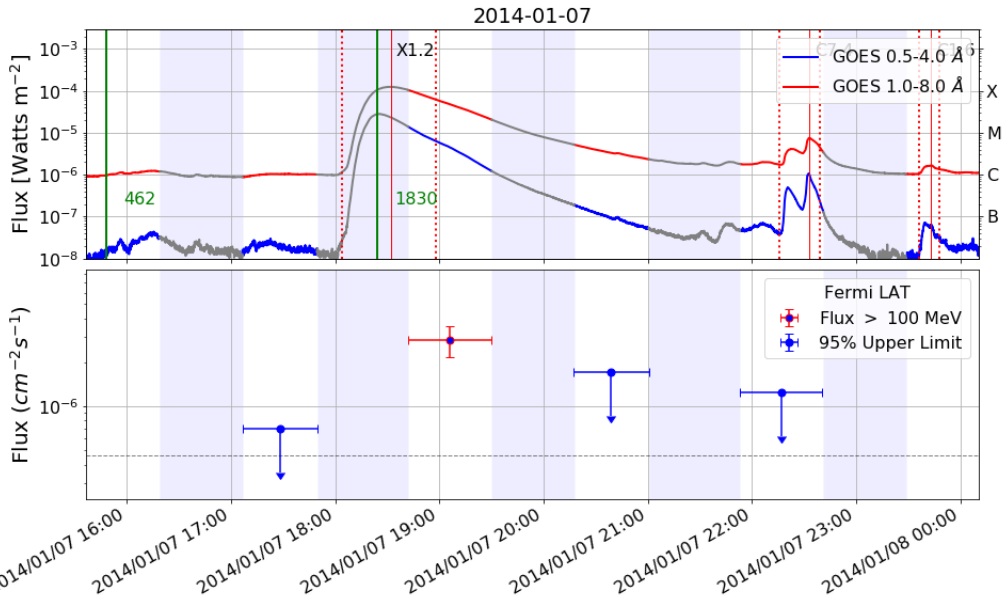

Figure A.35.1: Light curve for 2014-01-07. Top panel: GOES X-rays, bottom panel: Fermi-LAT flux > 100 MeV.

A.36 2014-02-25

Type of Gamma-ray Flare: **Prompt Delayed**.

Associated with a X4.9 GOES flare which started on 2014-02-25 00:39 and a CME with speed 2147 km/s.

Fermi-LAT detected gamma-ray emission above 60 MeV starting on 2014-02-25 00:44 and ending on 2014-02-25 07:51, lasting 7.1 hours. The prompt phase of 2014-02-25 is also associated with a LLE detection. The emission detected by the LLE approach started on 2014-02-25 at 00:44:47 and ended at 00:51:27 with a total duration of 400 seconds.

Comments: Interesting flare with a LLE detection of the prompt phase of the flare when Sun is out of the FoV: two peaks observed with very different spectra (> 100 MeV detected for only the second peak in Figure A.36.2). A binned analysis shows a rise in the first `SunMonitor` time window followed by a fast decay.

Start Time	Duration (sec)	$Flux_{30}$	$Flux_{100}$	TS	`SunMon` detected	Out of FoV
2014-02-25 00:44:47	400	1406.93 ± 24.95	631.28± 26.22	2652	X	X

Table A.36.1: LLE Spectral results for flare 2014-02-25. $Flux_{30}$ and $Flux_{100}$ indicate the flux computed from 30 MeV to 10 GeV and from 100 MeV to 10 GeV respectively (in units of 10^{-5} $cm^{-2}s^{-1}$).

Date and Time	Exposure (minutes)	Flux (10^{-5} $cm^{-2}s^{-1}$)	TS	ΔTS	Photon Index	Proton Index
2014-02-25 01:09 - 01:29	20	169.60 ± 1.97*	24030	2121	-0.33 ± 0.06	3.78 ± 0.04
2014-02-25 04:20 - 04:40	20	28.34 ± 0.91	2707	370	1.17 ± 0.28	>6
2014-02-25 07:30 - 07:51	21	0.87 ± 0.17	74	11	2.39 ± 2.53	>6

Table A.36.2: `SunMonitor` maximum likelihood results for 2014-02-25 (see Appendix A for description).

GOES	Class X4.9	Start 2014-02-25 00:39	Peak 2014-02-25 00:49	Stop 2014-02-25 01:03	Dur. (min) 24	AR position S15E65
CME	Speed 2147 km/s	Width Halo	C2 time 2014-02-25 01:25			
SEP	Instrument GOES	Emax 100 MeV				
HXR	Instrument BGO	Emax 7000 kev				

Table A.36.3: Properties of the events associated with 2014-02-25: GOES X-ray flare, CME, SEPs, HXRs .

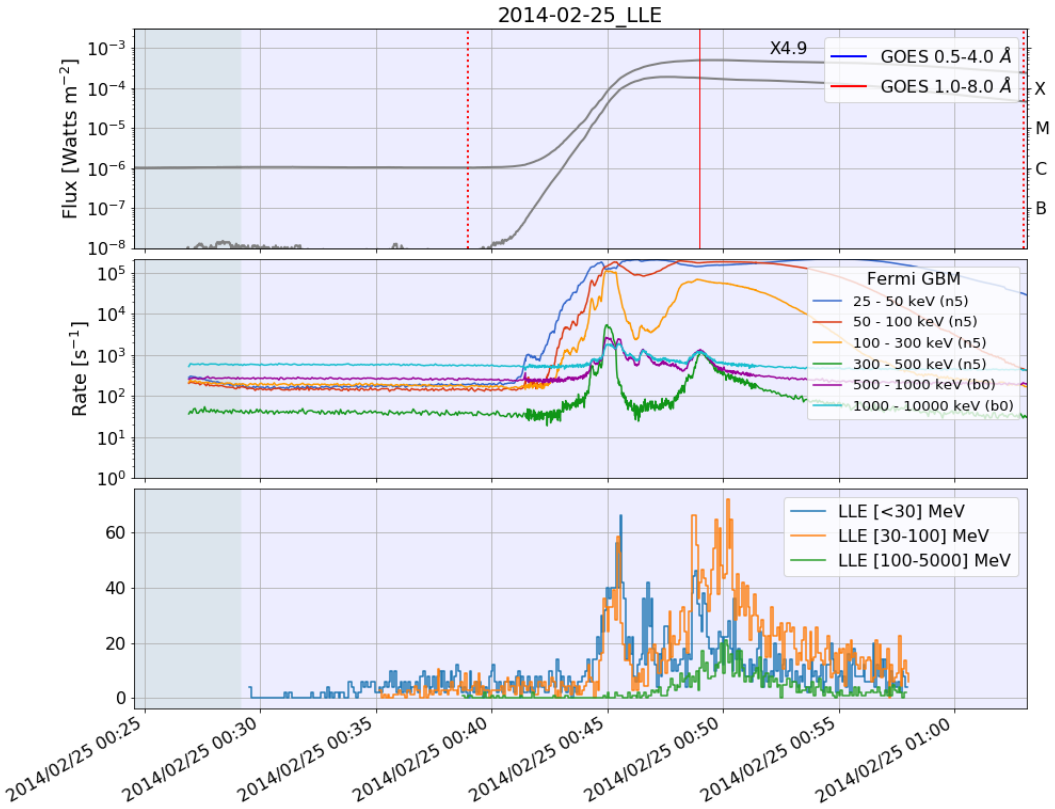

Figure A.36.1: Light curve for FLSF 2014-02-25. Panels from top to bottom: GOES X-rays; Fermi-GBM; Fermi-LAT LLE.

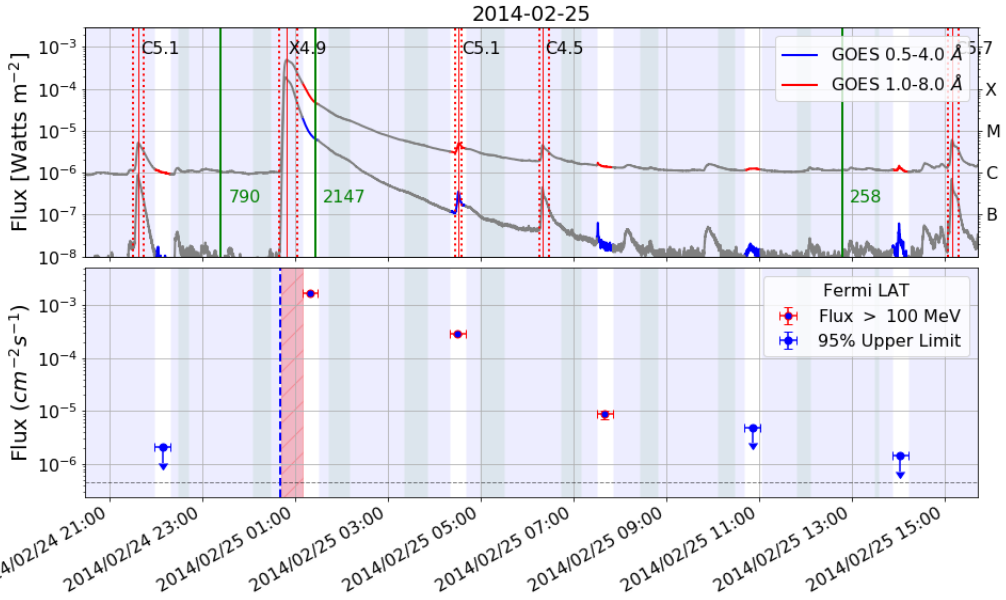

Figure A.36.2: Light curve for 2014-02-25. Top panel: GOES X-rays, bottom panel: Fermi-LAT flux > 100 MeV. Vertical blue line marks the start time of the LLE flare.

Date and Time	Helio X,Y	ERR 68%	ERR 95%	Angular Distance	Relative Distance (95)	Average Boresight (°)
2014-02-25 01:09 - 01:29	-933,-347	162	162	169	1	50
2014-02-25 04:20 - 04:40	-982,-213	363	574	133	0.2	50

Table A.36.4: The GOES X-ray flare associated with the FLSF originated from AR 11990 whose position at the time of the GOES flare was S15E65 (see Appendix A for description).

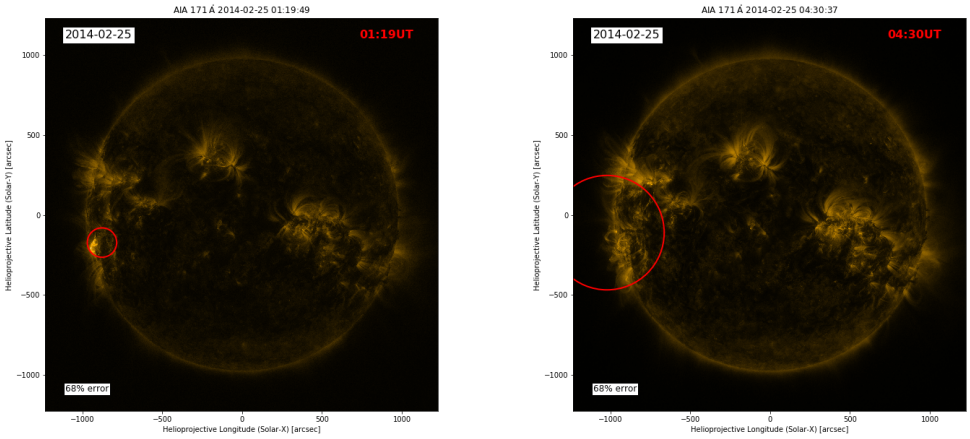

Figure A.36.3: Time resolved localization of the > 60 MeV emission from the 2014-02-25 flare. The mean time of each window is annotated in the upper right hand corner of each panel. The circles are the 68% source location uncertainty regions (results in Table A.36.4).

A.37 2014-06-10

Type of Gamma-ray Flare: **Prompt Delayed**.

Associated with a X1.5 GOES flare which started on 2014-06-10 12:36 and a CME with speed 1469 km/s.

Fermi-LAT detected gamma-ray emission above 60 MeV starting on 2014-06-10 12:47 and ending on 2014-06-10 14:26, lasting 1.6 hours. The prompt phase of 2014-06-10 is also associated with a LLE detection. The emission detected by the LLE approach started on 2014-06-10 at 12:47:18 and ended at 12:47:43 with a total duration of 25 seconds.

Comments: Prompt phase of the flare happening with the Sun in the FoV detected with LLE, but no higher than 100 MeV. In the next time window more than an hour later, gamma-ray detected above 60 MeV.

Start Time	Duration (sec)	$Flux_{30}$	$Flux_{100}$	TS	`SunMon` detected	Out of FoV
2014-06-10 12:47:18	25	6.73 ± 1.26	2.86± 1.06	18	X	

Table A.37.1: LLE Spectral results for flare 2014-06-10. $Flux_{30}$ and $Flux_{100}$ indicate the flux computed from 30 MeV to 10 GeV and from 100 MeV to 10 GeV respectively (in units of 10^{-5} $cm^{-2}s^{-1}$).

Date and Time	Exposure (minutes)	Flux (10^{-5} $cm^{-2}s^{-1}$)	TS	ΔTS	Photon Index	Proton Index
2014-06-10 14:00 - 14:26	25	1.17 ± 0.26	49	5	-2.47 ± 0.22	-

Table A.37.2: `SunMonitor` maximum likelihood results for 2014-06-10 (see Appendix A for description).

GOES	Class X1.5	Start 2014-06-10 12:36	Peak 2014-06-10 12:52	Stop 2014-06-10 13:03	Dur. (min) 27	AR position S19E89
CME	Speed 1469 km/s	Width Halo	C2 time 2014-06-10 13:30			
SEP	Instrument STEREO	Emax 60 MeV				
HXR	Instrument BGO	Emax 1000 kev				

Table A.37.3: Properties of the events associated with 2014-06-10: GOES X-ray flare, CME, SEPs, HXRs .

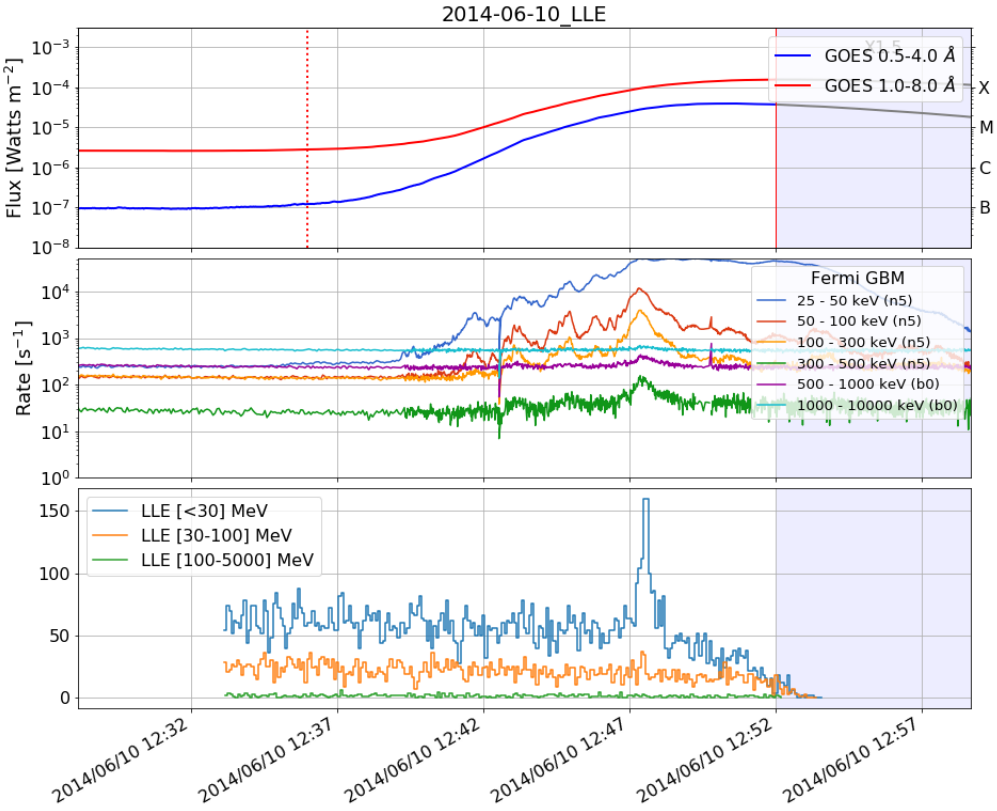

Figure A.37.1: Light curve for FLSF 2014-06-10. Panels from top to bottom: GOES X-rays; Fermi-GBM; Fermi-LAT LLE.

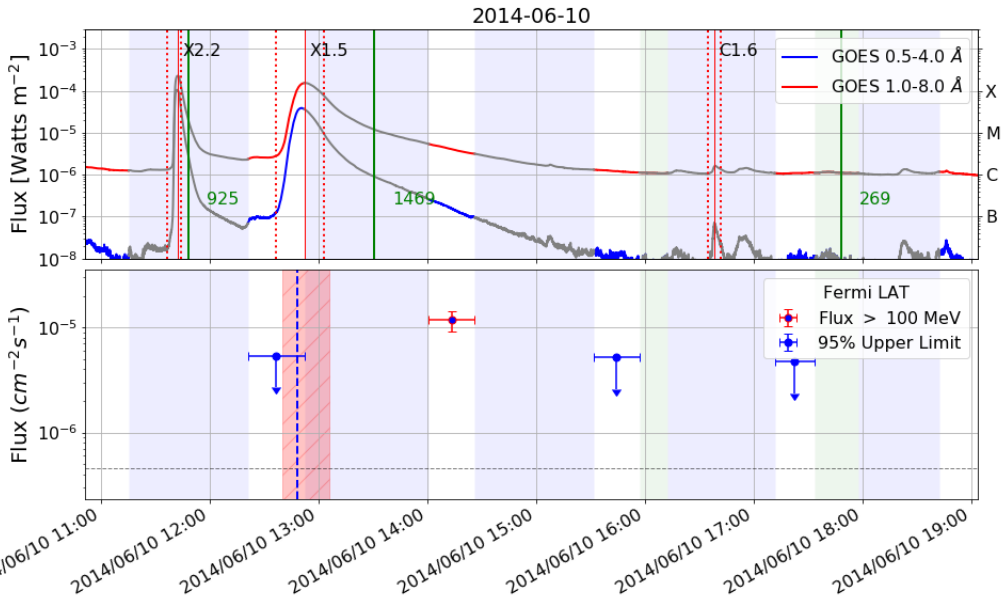

Figure A.37.2: Light curve for 2014-06-10. Top panel: GOES X-rays, bottom panel: Fermi-LAT flux > 100 MeV. Vertical blue line marks the start time of the LLE flare.

A.38 2014-06-11

Type of Gamma-ray Flare: **Delayed**.

Associated with a X1.0 GOES flare which started on 2014-06-11 08:59 and a CME with speed 829 km/s.

Fermi-LAT detected gamma-ray emission above 60 MeV starting on 2014-06-11 09:06 and ending on 2014-06-11 09:30, lasting 24 minutes.

Comments: Most of the non-thermal activity of the X1.0 flare happened before the Sun came into the FoV, so there is evidence of delayed emission.

Date and Time	Exposure (minutes)	Flux (10^{-5} cm^{-2}s^{-1})	TS	ΔTS	Photon Index	Proton Index
2014-06-11 09:06 - 09:30	24	0.99 $\pm$ 0.26*	30	3	-2.77 $\pm$ 0.30	-

Table A.38.1: `SunMonitor` maximum likelihood results for 2014-06-11 (see Appendix A for description).

GOES	Class X1.0	Start 2014-06-11 08:59	Peak 2014-06-11 09:06	Stop 2014-06-11 09:10	Dur. (min) 11	AR position S18E57
CME	Speed 829 km/s	Width 130	C2 time 2014-06-11 09:24			
HXR	Instrument BGO	Emax 1000 kev				

Table A.38.2: Properties of the events associated with 2014-06-11: GOES X-ray flare, CME, SEPs, HXRs .

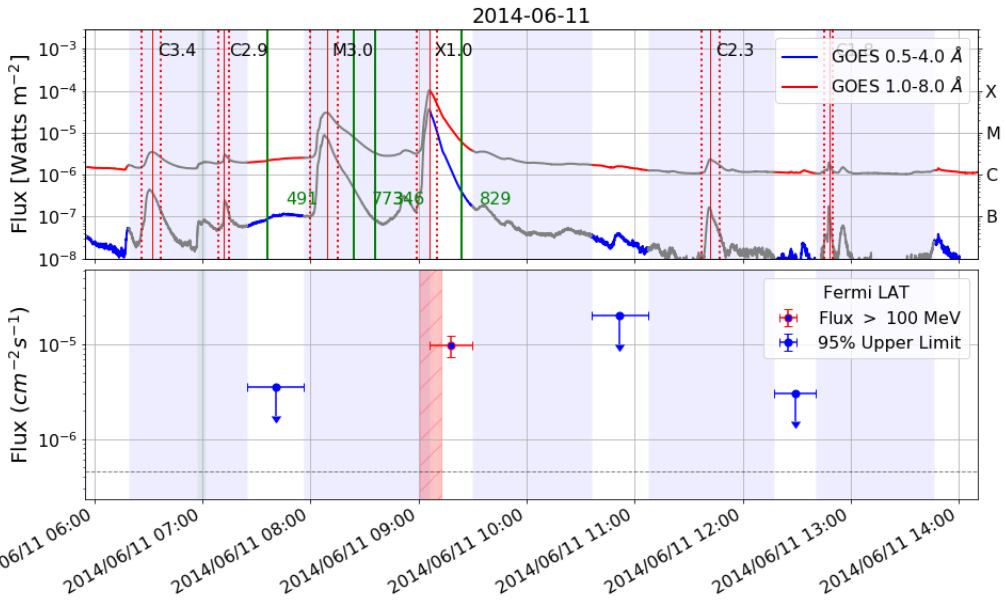

Figure A.38.1: Light curve for 2014-06-11. Top panel: GOES X-rays, bottom panel: Fermi-LAT flux > 100 MeV.

A.39 2014-09-01

Type of Gamma-ray Flare: **BTL Delayed**.

Associated with a X2.4 equivalent flare from STEREO observations which started on 2014-09-01 10:58 and a CME with speed 1901 km/s.

Fermi-LAT detected gamma-ray emission above 60 MeV starting on 2014-09-01 11:02 and ending on 2014-09-01 12:57, lasting 1.9 hours.

Comments: BTL flare 40° behind the East limb (see Section 5.3 for details).

Date and Time	Exposure (minutes)	Flux (10^{-5} cm^{-2}s^{-1})	TS	ΔTS	Photon Index	Proton Index
2014-09-01 11:02 - 11:18	16	378.66 ± 6.63	41620	-5590	-1.03 ± 0.09	4.70 ± 0.07
2014-09-01 12:25 - 12:57	32	2.98 ± 0.22	545	31	-1.16 ± 0.29	3.72 ± 0.24

Table A.39.1: `SunMonitor` maximum likelihood results for 2014-09-01 (see Appendix A for description).

GOES	Class X2.4*	Start 2014-09-01 10:58	Peak 2014-09-01 11:12	Stop 2014-09-01 11:40	Dur. (min) 42	AR position N14E126
CME	Speed 1901 km/s	Width Halo	C2 time 2014-09-01 11:12			
SEP	Instrument GOES	Emax 100 MeV				
HXR	Instrument NaI5	Emax 100 kev				

Table A.39.2: Properties of the events associated with 2014-09-01: GOES X-ray flare, CME, SEPs, HXRs .

Date and Time	Helio X,Y	ERR 68%	ERR 95%	Angular Distance	Relative Distance (95)	Average Boresight (°)
2014-09-01 11:02 - 11:18	-1126,-182	215	325	612	2	67
2014-09-01 12:25 - 12:57	-664,257	452	740	88	0.1	47

Table A.39.3: Localization results for the BTL gamma-ray flare 2014-09-01. Position behind the limb estimated by STEREO as N14E126.

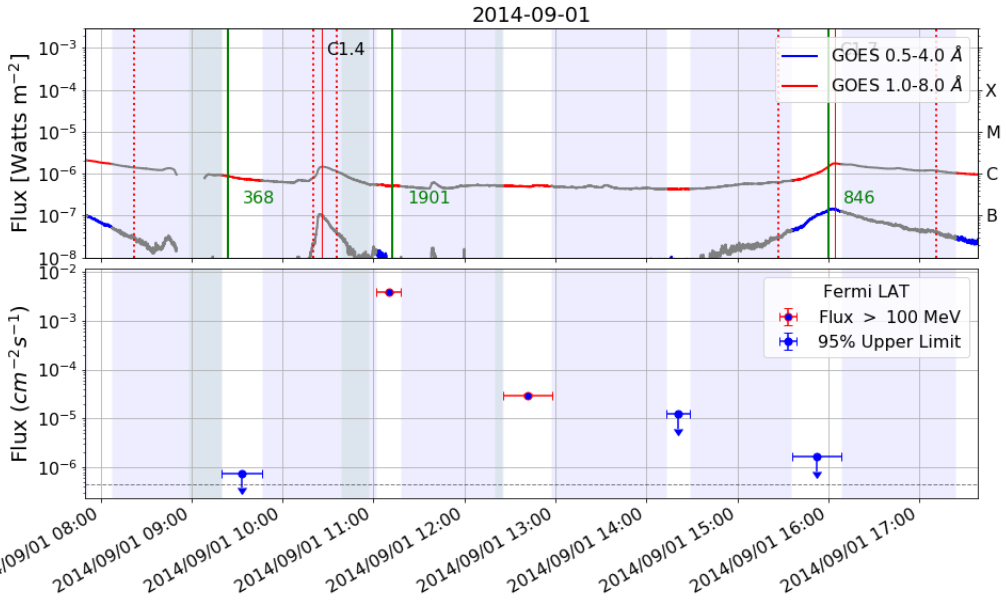

Figure A.39.1: Light curve for 2014-09-01. Top panel: GOES X-rays, bottom panel: Fermi-LAT flux > 100 MeV.

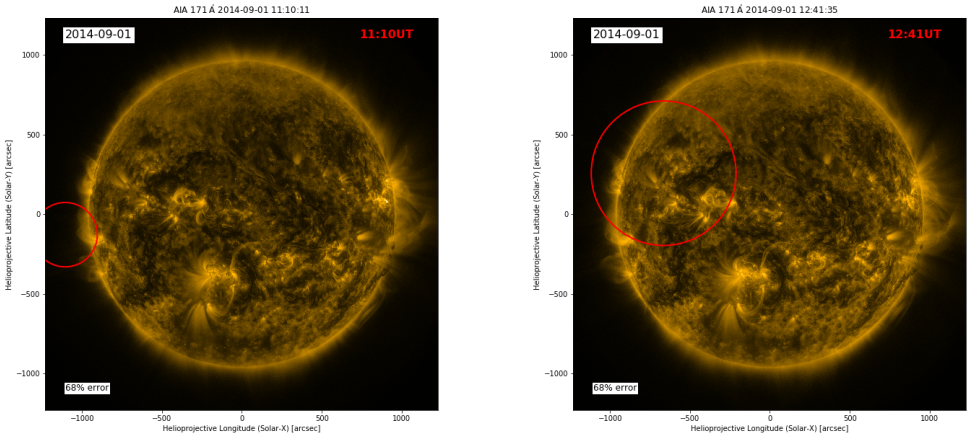

Figure A.39.2: Time resolved localization of the > 60 MeV emission from the 2014-09-01 flare. The mean time of each window is annotated in the upper right hand corner of each panel. The circles are the 68% source location uncertainty regions (results in Table A.39.3).

A.40 2014-09-10

Type of Gamma-ray Flare: **Delayed**.

Associated with a X1.6 GOES flare which started on 2014-09-10 17:21 and a CME with speed 1071 km/s.

Fermi-LAT detected gamma-ray emission above 60 MeV starting on 2014-09-10 17:35 and ending on 2014-09-10 17:53, lasting 18 minutes.

Comments: Gamma-ray detected during the later part of the X1.6 flare impulsive phase, but lasting beyond the end of it, makind it delayed emission.

Date and Time	Exposure (minutes)	Flux (10^{-5} cm^{-2}s^{-1})	TS	ΔTS	Photon Index	Proton Index
2014-09-10 17:35 - 17:53	18	7.44 ± 0.51*	559	66	0.35 ± 0.54	4.66 ± 0.34

Table A.40.1: `SunMonitor` maximum likelihood results for 2014-09-10 (see Appendix A for description).

GOES	Class X1.6	Start 2014-09-10 17:21	Peak 2014-09-10 17:45	Stop 2014-09-10 18:20	Dur. (min) 59	AR position N15E02
CME	Speed 1071 km/s	Width 331	C2 time 2014-09-10 17:24			
SEP	Instrument GOES	Emax 100 MeV				
HXR	Instrument NaI5	Emax 100 kev				

Table A.40.2: Properties of the events associated with 2014-09-10: GOES X-ray flare, CME, SEPs, HXRs .

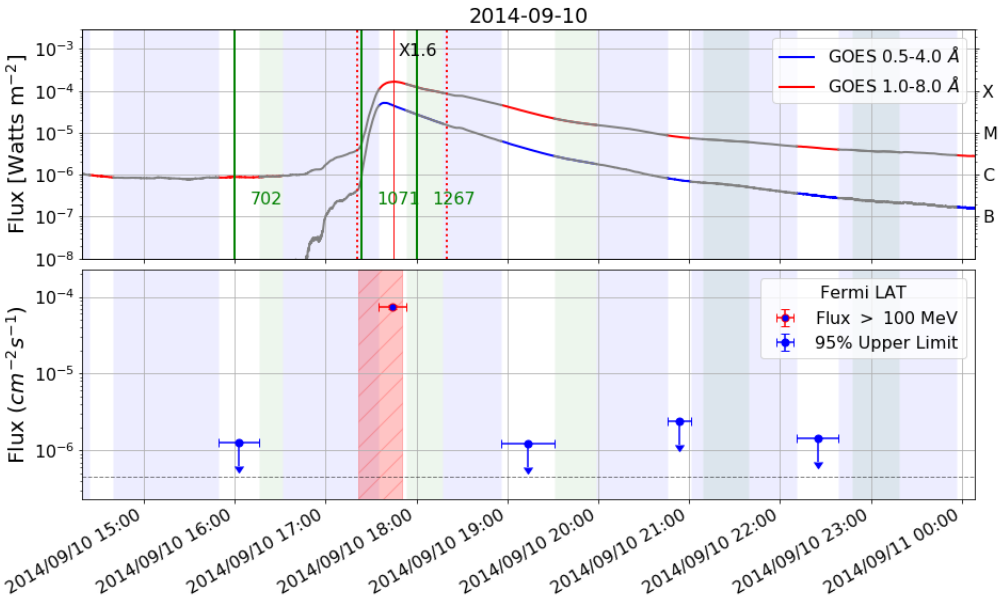

Figure A.40.1: Light curve for 2014-09-10. Top panel: GOES X-rays, bottom panel: Fermi-LAT flux > 100 MeV.

A.41 2015-06-21

Type of Gamma-ray Flare: **Prompt Delayed**.

Associated with a M2.7 GOES flare which started on 2015-06-21 02:04 and a CME with speed 1366 km/s.

Fermi-LAT detected gamma-ray emission above 60 MeV starting on 2015-06-21 02:09 and ending on 2015-06-21 12:14, lasting 10.1 hours.

Comments: FSF lasting more than 10 hours with a rise and fall behavior. The first time window is coincident with M2.7 flare with some of the HXR activity up to 50 - 100 keV. The gamma-ray detection is faint and it is not possible to distinguish between Prompt or short-delay emission. This flare is categorizes as Prompt - Delayed.

Date and Time	Exposure (minutes)	Flux (10^{-5} cm^{-2}s^{-1})	TS	ΔTS	Photon Index	Proton Index
2015-06-21 02:09 - 02:42	33	0.25 $\pm$ 0.08	23	5	-3.05 $\pm$ 0.39	-
2015-06-21 05:19 - 05:53	33	1.26 $\pm$ 0.15	162	16	-0.18 $\pm$ 0.74	4.29 $\pm$ 0.56
2015-06-21 08:30 - 09:03	33	0.81 $\pm$ 0.13	101	12	0.03 $\pm$ 1.14	4.24 $\pm$ 0.67
2015-06-21 11:40 - 12:14	33	0.38 $\pm$ 0.10	31	10	2.05 $\pm$ 2.61	>6

Table A.41.1: `SunMonitor` maximum likelihood results for 2015-06-21 (see Appendix A for description).

GOES	Class M2.7	Start 2015-06-21 02:04	Peak 2015-06-21 02:34	Stop 2015-06-21 03:15	Dur. (min) 71	AR position N12E16
CME	Speed 1366 km/s	Width Halo	C2 time 2015-06-21 02:36			
SEP	Instrument GOES	Emax 10 MeV				
HXR	Instrument NaI5	Emax > 50 kev				

Table A.41.2: Properties of the events associated with 2015-06-21: GOES X-ray flare, CME, SEPs, HXRs (HXR coverage incomplete).

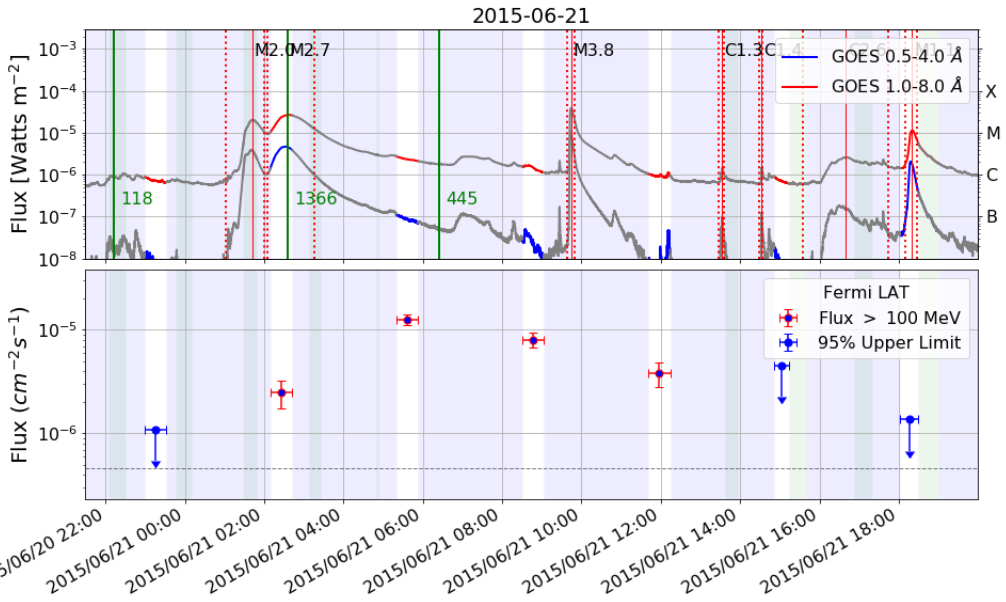

Figure A.41.1: Light curve for 2015-06-21. Top panel: GOES X-rays, bottom panel: Fermi-LAT flux > 100 MeV.

A.42 2015-06-25

Type of Gamma-ray Flare: **Delayed**.

Associated with a M7.9 GOES flare which started on 2015-06-25 08:02 and a CME with speed 1627 km/s.

Fermi-LAT detected gamma-ray emission above 60 MeV starting on 2015-06-25 09:24 and ending on 2015-06-25 10:09, lasting 45 minutes.

Comments: nan

Date and Time	Exposure (minutes)	Flux (10^{-5} cm^{-2}s^{-1})	TS	ΔTS	Photon Index	Proton Index
2015-06-25 09:24 - 10:09	45	0.40 ± 0.08	48	6	-2.72 ± 0.22	-

Table A.42.1: `SunMonitor` maximum likelihood results for 2015-06-25 (see Appendix A for description).

GOES	Class M7.9	Start 2015-06-25 08:02	Peak 2015-06-25 08:16	Stop 2015-06-25 09:05	Dur. (min) 63	AR position N11W45
CME	Speed 1627 km/s	Width Halo	C2 time 2015-06-25 08:36			
SEP	Instrument GOES	Emax 10 MeV				
HXR	Instrument BGO	Emax 1000 kev				

Table A.42.2: Properties of the events associated with 2015-06-25: GOES X-ray flare, CME, SEPs, HXRs .

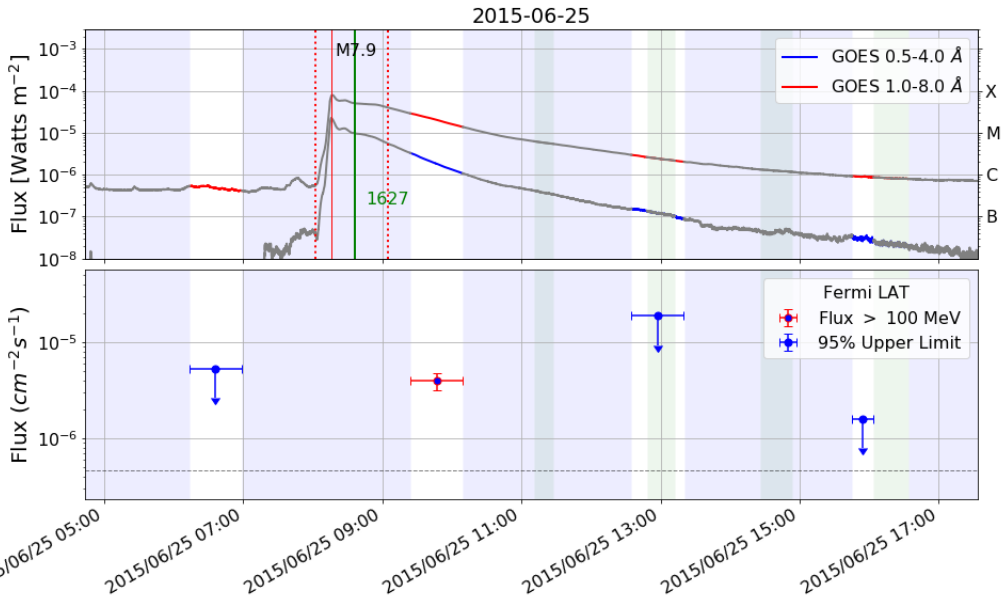

Figure A.42.1: Light curve for 2015-06-25. Top panel: GOES X-rays, bottom panel: Fermi-LAT flux > 100 MeV.

A.43 2017-09-06a

Type of Gamma-ray Flare: **Prompt**.
Associated with a X2.2 GOES flare which started on 2017-09-06 08:57 and a CME with speed 391 km/s.
Fermi-LAT detected gamma-ray emission above 60 MeV starting on 2017-09-06 09:05 and ending on 2017-09-06 09:16, lasting 10 minutes.
Comments: Gamma rays following about the same evolution as the HXRs (might be some very short delay). Associated with a weak CME detection.

Date and Time	Exposure (minutes)	Flux (10^{-5} cm^{-2}s^{-1})	TS	ΔTS	Photon Index	Proton Index
2017-09-06 08:51 - 09:19	28	1.31 $\pm$ 0.16*	130	21	0.59 $\pm$ 1.05	>6

Table A.43.1: `SunMonitor` maximum likelihood results for 2017-09-06a (see Appendix A for description).

GOES	Class X2.2	Start 2017-09-06 08:57	Peak 2017-09-06 09:10	Stop 2017-09-06 09:17	Dur. (min) 20	AR position S09W42
CME	Speed 391 km/s	Width 245	C2 time 2017-09-06 09:48			
HXR	Instrument NaI5	Emax 300 kev				

Table A.43.2: Properties of the events associated with 2017-09-06a: GOES X-ray flare, CME, SEPs, HXRs .

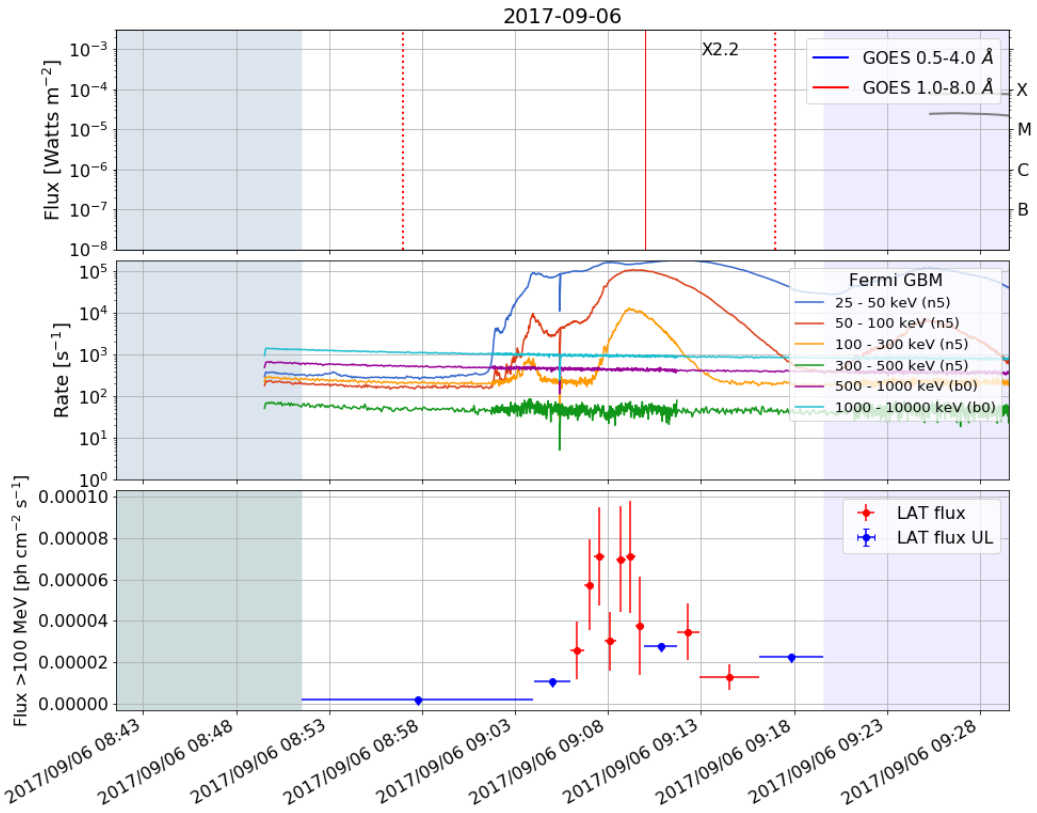

Figure A.43.1: Light curve for FLSF 2017-09-06a. Panels from top to bottom: GOES X-rays; Fermi-GBM; Binned Fermi-LAT flux > 100 MeV.

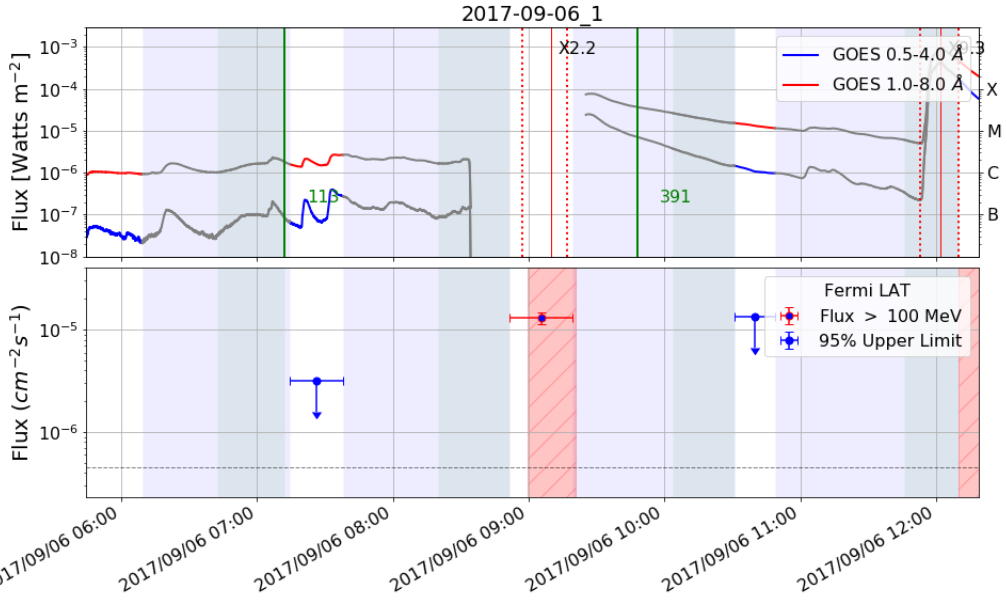

Figure A.43.2: Light curve for 2017-09-06a. Top panel: GOES X-rays, bottom panel: Fermi-LAT flux > 100 MeV.

A.44 2017-09-06b

Type of Gamma-ray Flare: **Delayed**.

Associated with a X9.3 GOES flare which started on 2017-09-06 11:53 and a CME with speed 1571 km/s.

Fermi-LAT detected gamma-ray emission above 60 MeV starting on 2017-09-06 12:10 and ending on 2017-09-07 01:11, lasting 13.0 hours.

Comments: X9.3 flare: brightest X-ray flare of the Cycle 24. The most energetic part of the prompt phase of the flare is not in the FoV and there is no HXR coverage at the peak. Additional solar flares occured during the 13 hours duration which could contribute the overall gamma-ray emission, making it appear longer.

Date and Time	Exposure (minutes)	Flux (10^{-5} cm^{-2}s^{-1})	TS	ΔTS	Photon Index	Proton Index
2017-09-06 12:10 - 12:35	25	0.96 ± 0.11*	156	17	0.05 ± 1.06	>6
2017-09-06 13:23 - 14:10	26	2.63 ± 0.17*	604	66	0.39 ± 0.55	>6
2017-09-06 15:03 - 15:40	18	2.93 ± 0.41	137	24	1.20 ± 1.29	5.61 ± 0.79
2017-09-06 16:45 - 17:09	19	3.56 ± 0.52	130	24	1.24 ± 1.24	5.16 ± 0.69
2017-09-06 18:14 - 18:50	36	2.73 ± 0.24	337	49	0.67 ± 0.68	5.36 ± 0.48
2017-09-06 19:55 - 20:20	25	2.27 ± 0.35	96	17	0.74 ± 1.33	>6
2017-09-06 21:25 - 22:00	35	2.56 ± 0.24	318	36	0.11 ± 0.67	5.51 ± 0.54
2017-09-06 23:05 - 23:31	26	0.96 ± 0.22	43	4	-3.06 ± 0.30	-
2017-09-07 00:36 - 01:11	35	0.62 ± 0.13	52	4	-2.63 ± 0.22	-

Table A.44.1: `SunMonitor` maximum likelihood results for 2017-09-06b (see Appendix A for description).

GOES	Class X9.3	Start 2017-09-06 11:53	Peak 2017-09-06 12:02	Stop 2017-09-06 12:10	Dur. (min) 17	AR position S09W42
CME	Speed 1571 km/s	Width Halo	C2 time 2017-09-06 12:24			
SEP	Instrument GOES	Emax 100 MeV				
HXR	Instrument Rhessi	Emax > 300 kev				

Table A.44.2: Properties of the events associated with 2017-09-06b: GOES X-ray flare, CME, SEPs, HXRs (HXR coverage incomplete).

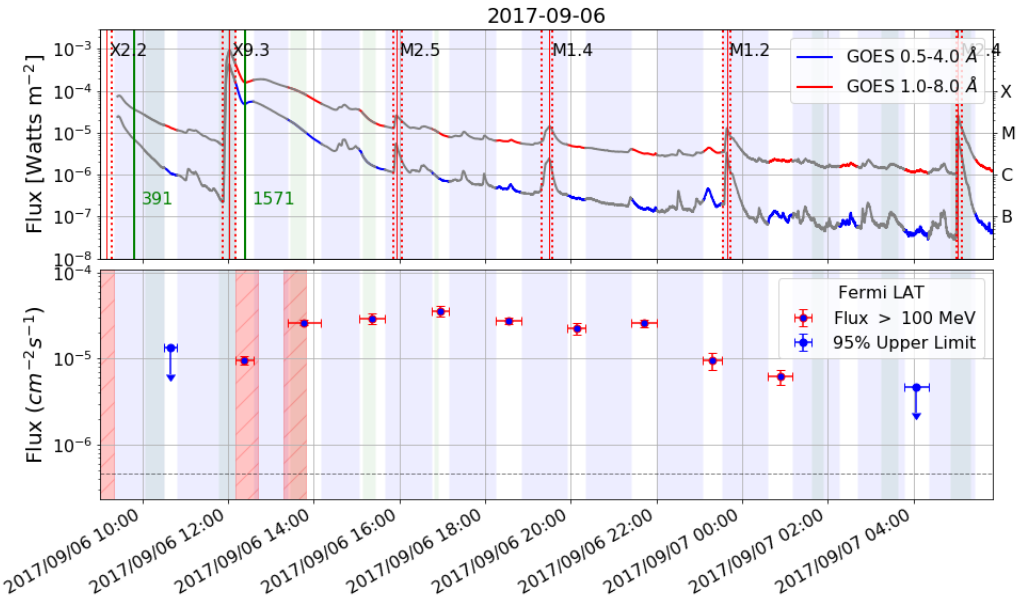

Figure A.44.1: Light curve for 2017-09-06b. Top panel: GOES X-rays, bottom panel: Fermi-LAT flux > 100 MeV.

A.45 2017-09-10

Type of Gamma-ray Flare: **Prompt Delayed**.

Associated with a X8.2 GOES flare which started on 2017-09-10 15:35 and a CME with speed 3163 km/s.

Fermi-LAT detected gamma-ray emission above 60 MeV starting on 2017-09-10 15:57 and ending on 2017-09-11 05:11, lasting 13.2 hours. The prompt phase of 2017-09-10 is also associated with a LLE detection. The emission detected by the LLE approach started on 2017-09-10 at 15:57:47 and ended at 16:03:12 with a total duration of 325 seconds.

Comments: See Section 5.2 for detailed analysis.

Start Time	Duration (sec)	$Flux_{30}$	$Flux_{100}$	TS	`SunMon` detected	Out of FoV
2017-09-10 15:57:47	325	1059.78 ± 8.84	600.62± 6.59	13338	X	

Table A.45.1: LLE Spectral results for flare 2017-09-10. $Flux_{30}$ and $Flux_{100}$ indicate the flux computed from 30 MeV to 10 GeV and from 100 MeV to 10 GeV respectively (in units of 10^{-5} $cm^{-2}s^{-1}$).

Date and Time	Exposure (minutes)	Flux (10^{-5} $cm^{-2}s^{-1}$)	TS	ΔTS	Photon Index	Proton Index
2017-09-10 15:52 - 16:28	35	290.96 ± 2.10*	61725	4429	-0.67 ± 0.03	3.74 ± 0.03
2017-09-10 17:33 - 17:58	24	76.44 ± 1.87	6112	469	-0.70 ± 0.30	3.30 ± 0.06
2017-09-10 19:03 - 19:39	36	88.31 ± 1.30	16954	1819	-0.02 ± 0.07	3.70 ± 0.05
2017-09-10 20:44 - 21:08	24	35.81 ± 1.34	2311	276	0.07 ± 0.22	4.18 ± 0.14
2017-09-10 22:13 - 22:49	36	15.01 ± 0.53	2559	315	0.35 ± 0.22	4.67 ± 0.16
2017-09-10 23:54 - 00:18	24	5.60 ± 0.54	310	68	2.03 ± 0.84	4.92 ± 0.43
2017-09-11 01:23 - 02:00	36	2.38 ± 0.22	284	55	1.69 ± 0.83	5.97 ± 0.54
2017-09-11 03:05 - 03:29	24	1.39 ± 0.28	59	12	1.00 ± 1.58	5.02 ± 0.97
2017-09-11 04:34 - 05:11	37	0.49 ± 0.11	43	2	-2.65 ± 0.24	-

Table A.45.2: `SunMonitor` maximum likelihood results for 2017-09-10 (see Appendix A for description).

GOES	Class X8.2	Start 2017-09-10 15:35	Peak 2017-09-10 16:06	Stop 2017-09-10 16:31	Dur. (min) 56	AR position S08W88
CME	Speed 3163 km/s	Width Halo	C2 time 2017-09-10 16:00			
SEP	Instrument GOES	Emax 605 MeV				
HXR	Instrument BGO	Emax 3000 kev				

Table A.45.3: Properties of the events associated with 2017-09-10: GOES X-ray flare, CME, SEPs, HXRs .

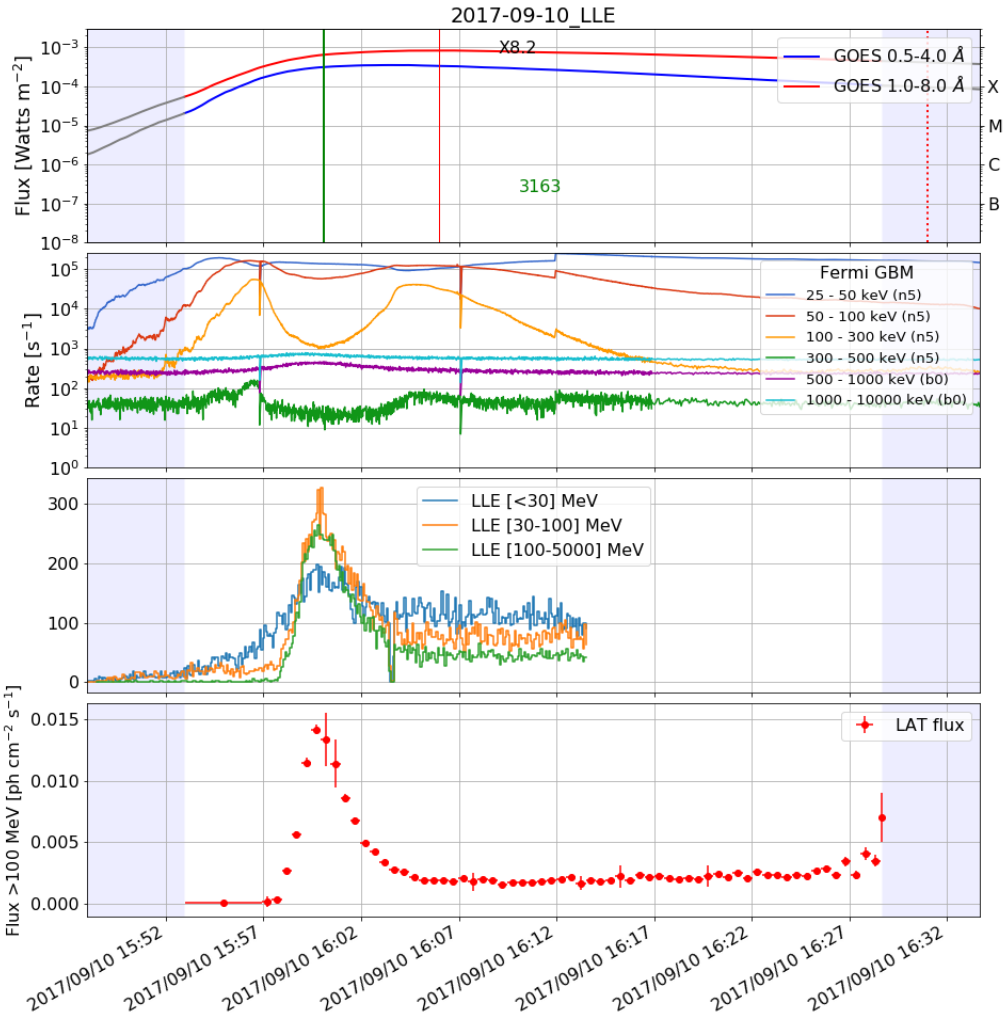

Figure A.45.1: Light curve for FLSF 2017-09-10. Panels from top to bottom: GOES X-rays; Fermi-GBM; Fermi-LAT LLE; Binned Fermi-LAT flux > 100 MeV.

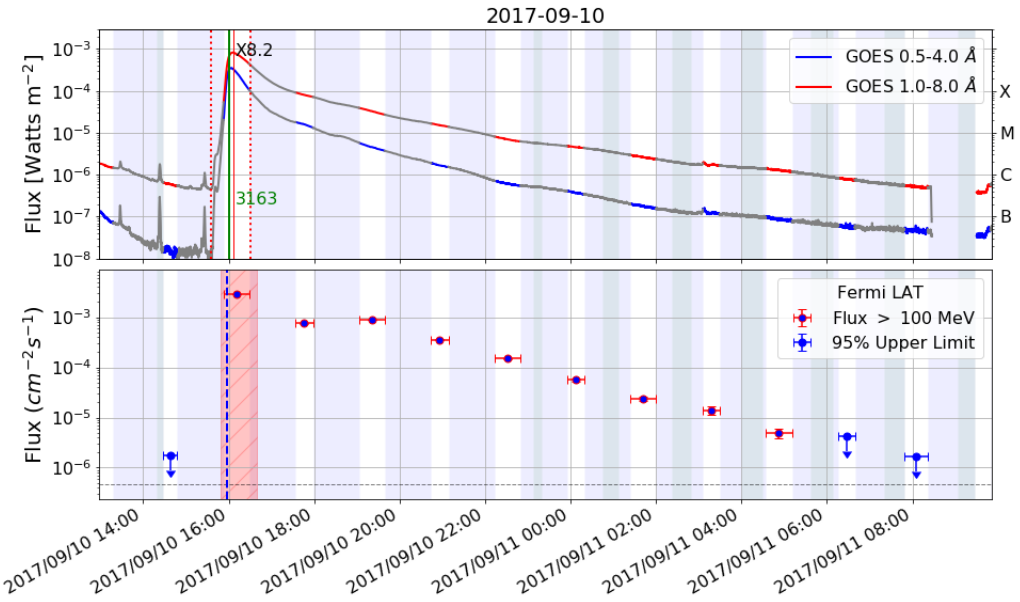

Figure A.45.2: Light curve for 2017-09-10. Top panel: GOES X-rays, bottom panel: Fermi-LAT flux > 100 MeV. Vertical blue line marks the start time of the LLE flare.

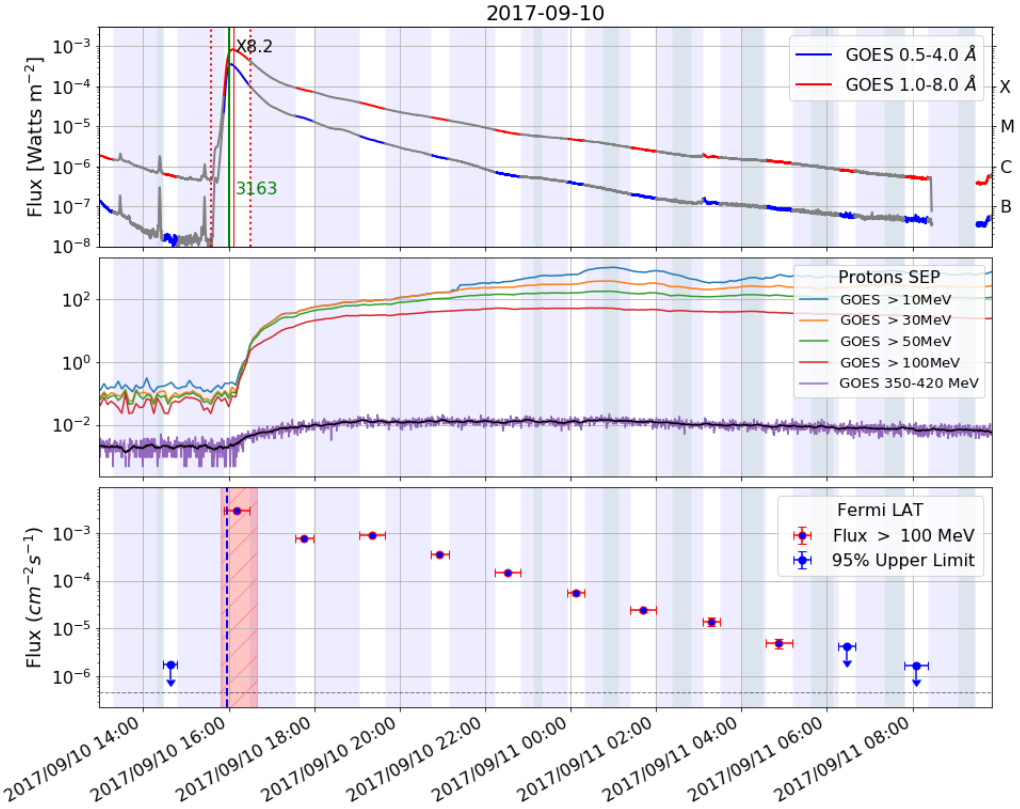

Figure A.45.3: Composite light curve for SEP event associated with 2017-09-10. Panels from top to bottom: GOES X-rays, GOES SEP count rate (ACE and STEREO data when available), Fermi-LAT >100 MeV flux.

Appendix B

Credits

- Fermi-LAT collaboration

The Fermi-LAT collaboration is supported by the National Aeronautics and Space Administration and the Department of Energy in the United States, the Commissariat a l'Energie Atomique and the Centre National de la Recherche Scientifique / Institut National de Physique Nucleaire et de Physique des Particules in France, the Agenzia Spaziale Italiana and the Istituto Nazionale di Fisica Nucleare in Italy, the Ministry of Education, Culture, Sports, Science and Technology (MEXT), High Energy Accelerator Research Organization (KEK) and Japan Aerospace Exploration Agency (JAXA) in Japan, and the K. A. Wallenberg Foundation, the Swedish Research Council and the Swedish National Space Board in Sweden. Additional support for science analysis during the operations phase is gratefully acknowledged from the Istituto Nazionale di Astrofisica in Italy and the Centre National d'Etudes Spatiales in France.

- Photo Credit

Figure 1.1 credit: NASA/DOE/Fermi-LAT Collaboration

Figure 2.5 credit: TRACE, Stanford-Lockheed ISR, NASA. TRACE LOOPS AR9077: Solar Magnetic Arcade[1].

Figure 3.1, Figure 3.2 and Figure 3.3 credits: NASA - Goddard Space Flight Center - Fermi Science Support Center

Figure 3.4 credit: Elizabeth Hays for the Fermi-LAT Collaboration[2]

Figure 3.5 credit: NASA - Sonoma State University portal.

Figure 3.6 credit: Hartman, R.C. for for the Fermi-LAT Collaboration[3].

[1] http://apod.nasa.gov/apod/ap120315.html

[2] http://spie.org/newsroom/3370-fermi-large-area-telescope-locates-unexpected-gamma-ray-outbursts

[3] http://fermi.gsfc.nasa.gov/ssc/library/conferences/207aas/ACD_AAS207.pdf

Figure 5.1 credit: NASA, DOE, International Fermi LAT Collaboration. Solar Flare in the Gamma-ray Sky, illustrated by Astronomical Picture of the Day on March 15, 2012[4].

[4] http://apod.nasa.gov/apod/ap120315.html

Bibliography

Abdo, A., Ackermann, M., Ajello, M., et al. 2009, Astroparticle Physics, 32, 193

Abdo, A. A., Ackermann, M., Ajello, M., et al. 2010, Ap. J. Supp., 188, 405

Abdo, A. A., Ackermann, M., Ajello, M., et al. 2011, Ap. J., 734, 116

Acero, F., Ackermann, M., Ajello, M., et al. 2015, The Astrophysical Journal Supplement Series, 218, 23

Ackermann, M., Ajello, M., Albert, A., et al. 2012a, Ap. J. Supp., 203, 4

Ackermann, M., Ajello, M., Albert, A., et al. 2014, Ap. J., 787, 15

Ackermann, M., Ajello, M., Allafort, A., et al. 2012b, Ap. J., 745, 144

Ackermann, M., Allafort, A., Baldini, L., et al. 2017, Ap. J., 835, 219

Ajello, M., Albert, A., Allafort, A., et al. 2014, Ap. J., 789, 20

Akimov, V. V., Ambrož, P., Belov, A. V., et al. 1996, Solar Physics, 166, 107

Akimov, V. V., Leikov, N. G., Kurt, V. G., & Chertok, I. M. 1994, in American Institute of Physics Conference Series, Vol. 294, High-Energy Solar Phenomena - a New Era of Spacecraft Measurements, ed. J. Ryan & W. T. Vestrand, 130–133

Aschwanden, M. J. 2005, Physics of the Solar Corona. An Introduction with Problems and Solutions (2nd edition)

Aschwanden, M. J., Hudson, H., Kosugi, T., & Schwartz, R. A. 1996, Ap. J., 464, 985

Atwood, W., Albert, A., Baldini, L., et al. 2013, ArXiv e-prints

Atwood, W. B., Abdo, A. A., Ackermann, M., et al. 2009, Ap. J., 697, 1071

Atwood, W. B., Bagagli, R., Baldini, L., et al. 2007, Astroparticle Physics, 28, 422

Augusto, C. R. A., Navia, C. E., de Oliveira, M. N., et al. 2018, ArXiv e-prints

Barat, C., Trottet, G., Vilmer, N., et al. 1994, Ap. J. Lett., 425, L109

Benz, A. O. 2008, Living Reviews in Solar Physics, 5, 1

Cash, W. 1979, The Astrophysical Journal, 228, 939

Chen, B. & Bastian, T. S. 2012, The Astrophysical Journal, 750, 35

Chupp, E. L., Forrest, D. J., Ryan, J. M., et al. 1982, Ap. J. Lett., 263, L95

Chupp, E. L. & Ryan, J. M. 2009, Research in Astronomy and Astrophysics, 9, 11

Dolan, J. F. & Fazio, G. G. 1965, Reviews of Geophysics and Space Physics, 3, 319

Dunphy, P. P. & Chupp, E. L. 1994, in American Institute of Physics Conference Series, Vol. 294, High-Energy Solar Phenomena - a New Era of Spacecraft Measurements, ed. J. Ryan & W. T. Vestrand, 112–117

Emslie, A. G. 1978, The Astrophysical Journal, 224, 241

Esposito, J. A., Bertsch, D. L., Chen, A. W., et al. 1999, Ap. J. Supp., 123, 203

Fletcher, L., Dennis, B. R., Hudson, H. S., et al. 2011, Space Science Reviews, 159, 19

Forrest, D. J., Chupp, E. L., Ryan, J. M., et al. 1980, Sol Phys, 65, 15

Gary, D. E., Chen, B., Dennis, B. R., et al. 2018, The Astrophysical Journal, 863, 83

Gopalswamy, N., Mäkelä, P., Yashiro, S., et al. 2018, The Astrophysical Journal, 868, L19

Grechnev, V. V., Kiselev, V. I., Kashapova, L. K., et al. 2018, Sol Phys, 293, 133

Grove, J. E. & Johnson, W. N. 2010, in SPIE proceedings series, Vol. 7732, Space Telescopes and Instrumentation 2010: Ultraviolet to Gamma Ray, 77320J

Hartman, R. C., Bertsch, D. L., Bloom, S. D., et al. 1999, Ap. J. Supp., 123, 79

Hathaway, D. H. 2015, Living Reviews in Solar Physics, 12

Howard, T. A. & Tappin, S. J. 2009, Space Science Reviews, 147, 31

Hua, X. M. & Lingenfelter, R. E. 1987, Solar Physics, 107, 351

Hudson, H. S. 1978, Ap. J., 224, 235

Hurford, G. J., Krucker, S., Lin, R. P., et al. 2006, Ap. J. Lett., 644, L93

Illarionov, E., Sokoloff, D., Arlt, R., & Khlystova, A. 2011, Astronomische Nachrichten, 332, 590

Kanbach, G., Bertsch, D. L., Fichtel, C. E., et al. 1988, Space Science Reviews, 49, 69

Kanbach, G., Bertsch, D. L., Fichtel, C. E., et al. 1993, Astron. & Astrophys. Supp., 97, 349

Krucker, S., Battaglia, M., Cargill, P. J., et al. 2008, The Astronomy and Astrophysics Review, 16, 155

Krucker, S., Hudson, H. S., Glesener, L., et al. 2010, Ap. J., 714, 1108

Krucker, S., Hurford, G. J., MacKinnon, A. L., Shih, A. Y., & Lin, R. P. 2008, Ap. J. Lett., 678, L63

Krucker, S., White, S. M., & Lin, R. P. 2007, Ap. J. Lett., 669, L49

Kuznetsov, S. N., Kurt, V. G., Yushkov, B. Y., Kudela, K., & Galkin, V. I. 2010, Solar Physics, 268, 175

Lande, J., Ackermann, M., Allafort, A., et al. 2012, Ap. J., 756, 5

Lee, J. & Gary, D. E. 2000, in Astronomical Society of the Pacific Conference Series, Vol. 206, High Energy Solar Physics Workshop - Anticipating Hess!, ed. R. Ramaty & N. Mandzhavidze, 323

Lin, R. P. 2011, Space Science Reviews, 159, 421

Lin, R. P., Krucker, S., Hurford, G. J., et al. 2003, Ap. J. Lett., 595, L69

Liu, W., Jin, M., Downs, C., et al. 2018, The Astrophysical Journal, 864, L24

Liu, W., Petrosian, V., Dennis, B. R., & Jiang, Y. W. 2008, The Astrophysical Journal, 676, 704

Longo, F., Omodei, N., & Digel, S. 2017, The Astronomer's Telegram, 10720

Longo, F. & Pesce-Rollins, M. 2017, The Astronomer's Telegram, 10735

Masuda, S., Kosugi, T., Hara, H., Tsuneta, S., & Ogawara, Y. 1994, Nature, 371, 495

Mattox, J. R., Bertsch, D. L., Chiang, J., et al. 1996, Ap. J., 461, 396

Meegan, C., Lichti, G., Bhat, P. N., et al. 2009, The Astrophysical Journal, 702, 791

Michelson, P. F., Atwood, W. B., & Ritz, S. 2010, Reports on Progress in Physics, 73, 074901

Miller, J. A. 2000, in IAU Symposium, Vol. 195, Highly Energetic Physical Processes and Mechanisms for Emission from Astrophysical Plasmas, ed. P. C. H. Martens, S. Tsuruta, & M. A. Weber, 277

Moiseev, A. A., Hartman, R. C., Ormes, J. F., et al. 2007, Astroparticle Physics, 27, 339

Moskalenko, I. V., Porter, T. A., & Digel, S. W. 2006, The Astrophysical Journal, 652, L65

Murphy, R. J., Dermer, C. D., & Ramaty, R. 1987, Ap. J. Supp., 63, 721

Murphy, R. J., Kozlovsky, B., Share, G. H., Hua, X.-M., & Lingenfelter, R. E. 2007, Ap. J. Supp., 168, 167

Murphy, R. J., Share, G. H., Grove, J. E., et al. 1997, Ap. J., 490, 883

Nitta, N. V., Aschwanden, M. J., Boerner, P. F., et al. 2013, Sol Phys, 288, 241

Nolan, P. L., Abdo, A. A., Ackermann, M., et al. 2012, Ap. J. Supp., 199, 31

Omodei, N., Pesce-Rollins, M., Longo, F., Allafort, A., & Krucker, S. 2018, The Astrophysical Journal, 865, L7

Park, B. T., Petrosian, V., & Schwartz, R. A. 1997, Ap. J., 489, 358

Parker, E. N. 1958, The Astrophysical Journal, 128, 664

Pelassa, V., Preece, R., Piron, F., et al. 2010, ArXiv e-prints

Pesce-Rollins, M., Omodei, N., Petrosian, V., et al. 2015, Ap. J. Lett., 805, L15

Petrosian, V. 2012, Space Science Reviews, 173, 535

Petrosian, V. & Liu, S. 2004, Ap. J., 610, 550

Petrosian, V., McTiernan, J. M., & Marschhauser, H. 1994, Ap. J., 434, 747

Poluianov, S. V., Usoskin, I. G., Mishev, A. L., Shea, M. A., & Smart, D. F. 2017, Solar Physics, 292

Rainó, S., Giglietto, N., Moskalenko, I., Orlando, E., & Strong, A. 2017, EPJ Web of Conferences, 136, 03007

Ramaty, R. & Mandzhavidze, N. 1994, in American Institute of Physics Conference Series, Vol. 294, High-Energy Solar Phenomena - a New Era of Spacecraft Measurements, ed. J. Ryan & W. T. Vestrand, 26–44

Ramaty, R., Schwartz, R. A., Enome, S., & Nakajima, H. 1994, Ap. J., 436, 941

Rank, G., Ryan, J., Debrunner, H., McConnell, M., & Schönfelder, V. 2001, Astron. & Astrophys., 378, 1046

Raymond, J. C., Krucker, S., Lin, R. P., & Petrosian, V. 2012, Space Science Reviews, 173, 197

Reames, D. V. 1995, Advances in Space Research, 15, 41

Ryan, J. M. 2000, Space Science Reviews, 93, 581

Schneid, E. J., Bertsch, D. L., Dingus, B. L., et al. 1996, Astron. & Astrophys. Supp., 120, 299

Share, G. H., Chupp, E. L., Forrest, D. J., & Rieger, E. 1983, AIP Conference Proceedings

Share, G. H., Murphy, R. J., Tolbert, A. K., et al. 2017, ArXiv e-prints

Shih, A. Y., Lin, R. P., & Smith, D. M. 2009, Ap. J. Lett., 698, L152

Trottet, G. 1994, in American Institute of Physics Conference Series, Vol. 294, High-Energy Solar Phenomena - a New Era of Spacecraft Measurements, ed. J. Ryan & W. T. Vestrand, 3–14

Trottet, G., Barat, C., Ramaty, R., et al. 1996, in American Institute of Physics Conference Series, Vol. 374, American Institute of Physics Conference Series, ed. R. Ramaty, N. Mandzhavidze, & X.-M. Hua, 153–161

Trottet, G., Vilmer, N., Barat, C., et al. 1998, Astron. & Astrophys., 334, 1099

Veronig, A. M. & Brown, J. C. 2004, The Astrophysical Journal, 603, L117

Vestrand, W. T. & Forrest, D. J. 1993, The Astrophysical Journal, 409, L69

Vestrand, W. T. & Forrest, D. J. 1994, AIP Conference Proceedings

Vestrand, W. T., Share, G. H., J. Murphy, R., et al. 1999, Ap. J. Supp., 120, 409

Vilmer, N., MacKinnon, A. L., Trottet, G., & Barat, C. 2003, Astron. & Astrophys., 412, 865

Webb, D. F. & Howard, T. A. 2012, Living Reviews in Solar Physics, 9

Wilks, S. S. 1938, Ann. Math. Statist., 9, 60

Yashiro, S., Gopalswamy, N., Akiyama, S., Michalek, G., & Howard, R. A. 2005, Journal of Geophysical Research (Space Physics), 110, A12S05